STRUCTURAL MEMBERS PRODUCED FROM UNREFINED LUNAR

REGOLITH, A STRUCTURAL ASSESSMENT

By

STEPHEN JOSEPH INDYK

A thesis submitted to the

Graduate School-New Brunswick

Rutgers, The State University of New Jersey

In partial fulfillment of the requirements

For the degree of

Master of Science

Graduate Program in Mechanical and Aerospace Engineering

Written under the direction of

Dr. Haym Benaroya

And approved by

_____

_____

_____

New Brunswick, New Jersey

October, 2015

ABSTRACT OF THE THESIS

STRUCTURAL MEMBERS PRODUCED FROM UNREFINED LUNAR

REGOLITH, A STRUCTURAL ASSESSMENT

By Stephen Indyk
Thesis Director: Prof. Haym Benaroya

The potential of utilizing lunar regolith as the raw material for manufacturing structural members is very appealing for future exploration of the Moon. Future lunar missions will depend on in-situ resource utilization (ISRU) for structural components. Manufacturing structural components directly from unrefined lunar regolith would have the advantage of needing less specialized material processing equipment in comparison with refining the lunar regolith for its raw elements. Sintering lunar regolith has been proposed as a structural material by previous researchers but has not been evaluated for its elastic material properties. Sintering can be a highly variable process and only with the knowledge of the material constants can a structure be designed using this material.

Quantification of the material properties was performed for sintered lunar regolith by testing sintered lunar regolith simulant. Two batches of sintered lunar regolith simulant JSC-1A samples with porosities 1.44% and 11.78% underwent compression testing using an Instron series 4500 Universal Test System machine. Material properties were evaluated from the load vs. deflection data acquired. Stress, strain, modulus of elasticity, toughness, the compression strength, bulk modulus, Poisson's ratio and compressive strength were evaluated as a function of porosity and data were aggregated as probability density functions. The average compressive strengths of the low porosity

material were 202 MPa, and 84 MPa for the high porosity material. By comparing these values with other ISRU derived structural materials, sintered lunar regolith is expected to be one of the strongest material derived from lunar sources.

Acknowledgements

First and foremost, I would like to thank my research advisor, Professor Haym Benaroya for offering his gracious guidance and sharing his wisdom over many years. This research is simply a small component of the lunar base vision he has advocated for many years, a vision well worth perusing and which I am honored to be a small part of.

Assistance for this research was provided to me by many people and groups, all of whom deserve my gratitude and thanks. The material samples used in the research were generously provided by Professor Amit Bandyopadhyay and Thomas Gualtieri of Washington State University. These samples were an integral component of this research, and without them this work would not have existed. The lunar simulant used in creating these samples was donated by Honeybee Robotics. Joe Vanderveer, John Petroski and Terence Whalen of Rutgers University all played important roles in assisting me with setting up the equipment used to test the material samples. My colleagues and officemates were all supportive and helpful in offering direction along various aspects of this research as well; this includes Elan Borenstein, Sohrob Mottaghi, Yuri Gulak and Paul Bonness of Rutgers University. From the Caltech Jet Propulsion Laboratory, Ashley Chandler, Mark Balzer and Lori Shiraishi all offered their time and assistance with the testing of the material samples.

Finally, I would like to express my gratitude to my very supportive family for the years of encouragement and fostering my interests. To my grandparents William and Gladys Smith, my great uncles Joseph Finelli and George Muller, to all my aunts, my sisters Theresa and Susie Indyk and especially my mother Felicia Indyk, thank you all so much.

Table of Contents

List of Tables

List of Figures

Chapter 1.   Background

1.1 Introduction to Topic

From the log cabins built from trees felled by settlers of the American Pacific Northwest to the reinforced concrete, steel and glass skyscrapers towering over Manhattan and other modern cities, humans have been constructing progressively complex structures for centuries. The lime and clay processed into cement and the iron ore forged into steel share the same humble beginnings as the timber harvested by logging - they originated from Earth. Making use of indigenous materials to construct dwellings has been a human activity for millennia. Of course, human-inhabited structures are simply a convenient example of what has and can be constructed from indigenous materials. Structural materials comprise a majority of man-made objects, such as underground pipes, smart phone housings, aircraft fuselages and many more. They all share a thread of being constructed from indigenous, processed and, of course, refined materials. Determining the strength and capabilities of structures depends heavily on the material used to create the structure, as well as the application envisioned. Through testing and statistical analysis, the strength of materials has become a fundamental field. With information available about common materials only a click away on the Internet, and with finite element analysis (FEA) software readily available, the real difficulty in assessing structural materials becomes apparent when investigating new materials.

An entire celestial body that has yet to be evaluated for its structural materials is Earth's closet neighbor, the Moon. Colonizing the Moon has been a human dream since mankind first looked up to it in the night sky. Before any such dream can become a

reality, it is necessary to first learn how to use the existing lunar resources. However, the difficult environment of the Moon does not afford its first settlers the luxury of simply chopping down trees to construct shelter. Instead, these intrepid settlers will have to rely on deliberately constructed habitats transported from Earth for a considerable period of time. These domiciles will be well thought out, having exact placements on the Lunar surface decided well in advance by Moon surveying satellites. Considerations will be made in order to maximize or minimize the effects of the Sun, ensure constant communication with Earth and allow spacecraft to ferry goods to and from this home away from home. It is the later, second or third generation lunar structures that will likely be constructed mostly, if not entirely, out of indigenous materials.

The potential utilization of lunar regolith as a raw material for manufacturing structural members is very promising for future exploration and settlement. For economic and practical reasons, future lunar missions will eventually depend on in-situ resource utilization (ISRU) for lunar structural components. Manufacturing structural components directly from unrefined lunar regolith would advantageously require less specialized terrestrial equipment. One method to forge structural material from unrefined lunar regolith is a process known as sintering. A possible issue with sintering from a structural perspective is the pores created in the sintering process. 'The more vacuum a thing contains within it, the more readily it yields…,' words written in the first century B.C. by the Roman philosopher Lucretius in his work entitled, *On the Nature of the Universe*. The effects of porosity on material strength are not a new concept.

It is the question of what could be constructed from sintered lunar regolith that is the motivation of the research work presented here.

1.2   Research Goals

In order to further explore and develop the Moon, future long-duration surface missions will increasingly depend on ISRU. Otherwise, everything necessary for building inhabitable structures on the Moon would have to be transported from Earth, which is economically unsustainable. Fortunately, the Moon itself provides a promising and easily accessible raw material via its regolith that may be used to construct housing and other structures. Lunar regolith is a granular substance that is not only plentiful on the Moon, but can also be easily extracted, allowing for sintered lunar regolith to be used for large load bearing structures potentially designed to house astronauts.

It is expected that lunar settlement would take place in three phases; the first phase would require prefabricated structures to be transported from Earth to the Moon. Phase two would consist of creating a combination of terrestrially and lunar manufactured structures. Finally, the third phase would see structures that are primarily composed of lunar-derived structural material. Two of the three phases will depend on using lunar-derived ISRU structural material. So it will be important to develop a path to raise the maturity of the technologies needed to manufacture, inspect and construct these indigenous lunar structures.

Several types of lunar regolith derived structural materials have been proposed and studied in the past, each depending on various methods of manipulating the lunar regolith. Some processes refine the lunar regolith into raw ore, where others form more conventional construction materials by combining additives to produce lunar concrete. Raw materials and even lunar concrete have been investigated thoroughly to determine their elastic material constants. The practicality of these materials has been extensively

evaluated in other research works such as Lin (1987) and Houssam et al. (2012). To a lesser extent, qualitative evaluations of the structural potential of sintered lunar regolith have been performed. However, sintered lunar regolith material properties require further investigation. Therefore, a central aspect of this research is to determine whether sintered lunar regolith is a viable lunar ISRU structural material.

Sintering, the process of applying heat to a powder compact to increase strength and integrity, has previously been shown by researchers such as Taylor and Meek (2005), to be a possible method of converting raw lunar regolith to solid components. However, the sintering process itself contains many variables to control. The foremost is controlling and understanding the effect of the material's porosity. A composite material's porosity greatly affects its strength and is a significant factor in the properties of sintered materials. Developing an understanding of how porosity affects the elastic material constants of sintered lunar regolith is another goal of this research project. To accomplish this, two separate sample sets of high and low porosity sintered lunar simulant were investigated.

The effects of porosity on basic material properties, such as bulk modulus, Young's modulus, Poisson's ratio, toughness and compressive strength, were investigated. To evaluate the desired material properties as functions of porosity, an experiment was developed. Compression testing of the sintered lunar simulant was performed, and then stress and strain values were computed from load and deflection data recorded. These collected material properties were also compared with similar terrestrial values to evaluate their accuracy and relevance. In addition to terrestrial materials, the data was also compared to potential lunar ISRU derived material properties. To collect

information on previously researched lunar materials, a literature review conducted. Special attention was paid to experimental research that quantified elastic material constants of lunar ISRU materials. Suggestions are also made on how sintered lunar regolith can be utilized on the Moon.

Our overarching motivation has been whether structures can be constructed on the Moon using unrefined sintered lunar regolith. Our primary contribution is the examination of sintered lunar regolith properties via experiments and our assessment of that data. The short answer is: yes, it will be possible to erect surface lunar structures using unrefined sintered lunar regolith.

Understanding the natural environment is especially important for developing a new structural material from indigenous sources. Determining how a structural material could be used depends heavily on the environmental conditions in which it is expected to operate. This is discussed next.

1.3   Description and Constraints of the Lunar Environment

A definition of the lunar environment is needed before any system that is expected to operate on the Moon is designed. For comparison and understanding, certain lunar parameters are cited from *Lunar Sourcebook* by Heiken et al. (1991) about the Moon in this section and compared to those of Earth. The Moon is Earth's nearest celestial body at 284,400 km away. To date the only man-made vehicles to reach lunar orbit, or the lunar surface have been transported by means of a rocket. This places additional constraints on any manned or unmanned system to reach the Moon. These systems must be compact and portable to be transported by a rocket, as well as survive the demanding acceleration, altitude, pressure, temperature and radiation conditions

associated with rocket flight from the Earth to the Moon. The lunar gravitational constant is 1.622 m/s^2, Earth's gravitational constant is 9.81 m/s^2, making lunar gravity approximately 1/6th that of the Earth. Lunar regolith is abundant and coats the surface of the Moon. Median depths of the lunar regolith have been estimated to be 2-4 m in the mare regions and 6-8 m on the far side and non-mare nearside areas. The increase in density with depth leads to significant difficulties in excavation. The dust environment is another engineering concern. Regolith is very fine-grained, and its mean grain size ranges from 40 to 900 μm with most mean values being between 45 and 100 μm. Particles below 20 μm in size have also been found. Materially, regolith contains heavy metals with many minerals common to those on Earth. This includes hard rocks and minerals such as basalt, anorthosite and olivine. Once disturbed, the regolith is electrostatically charged and can remain suspended 1-2 m above the surface. All of these properties make the regolith a serious threat to any mechanical system, leading to accelerated wear due to the regolith's abrasiveness. The lunar surface has low thermal capacity and very low thermal conductivity, making heat retention difficult. Surface temperatures between 374 and 92 K have been measured at the Apollo 15 landing site. Intense solar radiation exists between 1,316 W/m^2 and 1,421 W/m^2, depending on the distance from the Earth to the Sun, at the lunar surface. For comparison, radiation at the Earth's surface is about 0.095 W/m^2. The lunar surface has a high vacuum with a pressure of 2.667e-13 kPa (2e-12 Torr) at night. For comparison, average sea-level pressure on the Earth's surface is 101.325 kPa (760 Torr).

1.4 Literature Review

There are four main reasons why sintering lunar regolith is an efficient and viable option for use as a structural material. First, there is a need for in-situ resource utilization (ISRU). Secondly, there are limited alternative materials that could be made from ISRU without extensive refinement. Third, the current state of manufacturing process technology available would allow for effective sintering manufacturing. And finally, there are a multitude of useful structures that could be produced with sintered lunar regolith. Relevant research work is listed below and evaluated on these four criteria. Our research is focused on sintering of unprocessed lunar regolith.

Our review of research is organized in the manner of how previous work is relevant to this research project. Special attention is given to experimental material properties. Relevance of the literature reviewed is evaluated on four fundamental classifications; the need for ISRU, alternative ISRU materials, manufacturing processes, and what could be constructed.

1.4.1 The Need for ISRU

Duke et al. (2006) developed a strategy for exploration and development of the Moon. A main focus is the economics of going to the Moon. The cost of transporting material from the Earth into orbit was cited as a main problem with commercializing space. Development of the Moon would allow for natural resource access and a space transportation infrastructure. ISRU was discussed as a key factor in the development of the Moon. Resources that could come directly from the Moon included power, propellants, life support consumables and structural materials. Sintering regolith, cast

basalt, concrete and microwave processing of regolith were discussed as potential structural materials.

1.4.2   Alternative Materials from ISRU

There have been investigations into utilizing the lunar regolith to make concrete. Testing of both actual lunar regolith and lunar simulant has been conducted resulting in compressive strength measurements. Two works of note involve actual lunar material, and an additive laden lunar concrete.

Researchers led by Lin (1987) created lunar concrete using 40 g of a sample of regolith. The sample was acquired by Apollo 16, and is from the lunar mare, the large dark basaltic plains on the Moon formed by ancient volcanic activity. Testing of the samples found a compressive strength of 74 MPa (10,000 psi), a tensile strength of 8.3 MPa (1,200 psi), a modulus of elasticity of 21,400 MPa (3.1 $x10^6$ psi) and a thermal expansion coefficient of 5.4 $x10^{-6}$ cm/cm/°C (2.9x10^{-6} in/in/deg F).

Houssam et al. (2012) created cast blocks of lunar concrete using JSC-1 mixed with sulfur powder in a 65% to 35% ratio and measured the compressive strength to be 31 MPa. Sulfur, previously shown to be on the Moon, is another viable ISRU option for lunar concrete.

Landis (2007) developed refining processes that could produce several heavy metals from lunar ISRU. Aluminum, iron, calcium and magnesium were among those elements that could be reacted with fluorine. Material properties of these metals would be expected to be the same as those on Earth and depend on the quality of the refining and material processing.

Benaroya et al. (2012) specifically advocated the use of magnesium as an ISRU-derived structural material. High strength to weight ratio, high impact resistance and vibration damping 30 times that of aluminum were cited as favorable characteristics for refining magnesium for use in structures.

In addition to cements and metals, utilizing the raw lunar regolith, with or without additives, has also been proposed as structural materials. Specific manufacturing processes have been suggested and are discussed in the next section.

1.4.3   Manufacturing Processes

Several novel means of manufacturing materials derived from lunar sources have been researched and tested. Processes involving additive manufacturing, casting, microwaving and thermite reactions have been investigated previously. A majority of research projects have tested simulant and one has tested with actual lunar material.

Allen et al. (1994) demonstrated the possibility of producing cast-sintered bricks of lunar simulant. Using radiant heating, microwave heating, and a combination of both, cast brick-sized blocks of sintered lunar simulant were generated. The main purpose of this work was to develop practical methods of sintering to produce lunar bricks. Two simulants were used in their tests, MLS-1 and the venerable JSC-1. A recommended sintering temperature of 1,100 °C was concluded to be the most effective to produce solid bricks. Since quality was of main concern, sintering behavior is significantly improved by compaction of the simulant. This is because of a decrease in porosity and an increase of grain-to-grain contact. Incorporating vibratory compacting into the manufacturing process was also suggested. Since crushed rock effectively is an insulator, thermal cracking could be an issue. Thermal cracking could be minimized by allowing for

relatively long heating and cooling periods. During some of their manufacturing tests, the bricks were stuck to the mold and had to be chipped out. Difficulties of casting large blocks of sintered lunar simulant were acknowledged and it should be expected that actual lunar regolith would behave similarly. Different environments for sintering were also used, for example, conducting sintering in argon and hydrogen atmospheres, but not in a vacuum.

While this research excelled in manufacturing process development, it stopped short of performing material property investigations. One important difference with the cast sintering process investigated was the atmospheric conditions. Their testing was conducted under atmospheric conditions, it is expected that manufacture on the Moon would produce better quality material due to using vacuum sintering. The operational use of molds form blocks is a factor let to be thoroughly investigated in the lunar manufacturing process. Some concerns with molds involve how big they have to be, or whether they are fabricated on site or transported from Earth.

Microwave sintering was investigated utilizing actual lunar regolith. Taylor and Meek (2005) showed that one critical property was the presence of native nanophase Fe^0, which was formed as a result the auto-reduction of the FeO in the silicate melts formed by micrometeorite impacts. Since nanophase Fe^0 was caused by meteoritic impacts, the more mature the lunar soil, the higher the nanophase Fe^0 concentration found. Nanophase Fe^0 are particles of iron with grain sizes less than 100 nanometers. Because of this iron inclusion, lunar regolith can be melted with a common household microwave in a matter of minutes. Microwaving allows the regolith to heat rapidly to temperatures of between 1200 °C and 1500 °C. Also identified was that at that time, no lunar simulants contained

nanophase Fe^0. Hence, this microwavability property of lunar regolith was not discovered earlier since so much work regarding lunar regolith had to be done with simulants. Also emphasized was the importance of working with actual lunar material.

Taylor and Meek (2005) also suggested some applications of their discovery; microwave sintering could result in a smooth surface, one that could be used for producing an antenna dish or other surfaces that would benefit from a glass-like finish.

The exact manufacturing process is not discussed in this paper, making it difficult to quantitatively evaluate parameters such as rate of manufacture or energy consumption. Material excavation and post processing are required of any structural material fabricated by microwave sintered lunar regolith. Material properties were not investigated quantitatively, leaving an uncertainty in the quality of material produced from this process or its structural capacity. However, this research has created a demand for the investigation of this microwavability property further. Hung and McNatt (2010) have been since able to file for a patent on the process of adding nanophase Fe^0 to lunar simulants.

Faierson et al. (2010) studied a lunar structure constructed from ISRU resources. A geothermite reaction was tested using a mixture of JSC-1AF and JSC-1A lunar simulants and aluminum powder. The structural components were fabricated using a geothermite reaction with a mixture of JSC-1AF and JSC-1A lunar simulants and aluminum powder. A geothermite reaction is a reaction between minerals and a reducing agent exhibiting a thermite type of reaction behavior. In this case the minerals were the lunar simulant and the reducing agent was the aluminum powder. The process involves oxidation-reduction reactions between the constituents of the reactant mixture. Similar to

casting, molds were used to form sintered blocks in a few carefully selected shapes. Once assembled, the blocks would form a voussoir dome. A voussoir is a wedge shaped element used in constructing an arch or vault, and a voussoir dome is a three dimensional surface comprised of these wedge shaped elements. Fabrication of the blocks was performed under standard terrestrial atmospheric conditions and used NiCr wire to initiate the reaction. Compression tests were conducted on samples of about 5 cm in height and about 2.5 cm in diameter. Experimental data indicated an ultimate strength range of 10-18 MPa depending on particle size and the ratio of aluminum to lunar simulant. For their calculations, a hypothetical value of 13.8 MPa was used. The dome shape was feasible and suggested an upper bound to the size of the dome possible in the lunar environment. Loading conditions on the voussoir dome were investigated to ensure that the structure could support itself. Also calculated was the potential of a voussoir dome structure from bricks fabricated though geothermic reactions.

The work of Faierson et al. (2010) was one of the few research efforts to investigate the material properties of the created sintered material. They highlight that material strength is a function of the ratio of simulant to aluminum, as well as the grain size of the simulant used. However, there was little investigation into the differences in material strength as a function of the material composition. There was no study of the material's porosity. A main focus was to determine if the selected voussoir dome was suitable for manufacture from this sintered regolith and aluminum reaction. One feature of the voussoir dome is that it is compression stabilized. This structure is comprised of individual blocks, and for the dome to work, a variety of blocks and molds are needed, increasing the complexity of manufacture and assembly. Furthermore, an assembly

procedure for the structure would need to be developed for either autonomous or manned construction. There would be considerable effort needed to make this completely ISRU based. Researchers would need to import equipment to refine aluminum and supply NiCr wire or develop a lunar resource-based alternative to complete the fabrication process.

Hobosyan and Marturosyan (2012) investigated another type of thermitic reaction that produced structural material. JSC-1A lunar regolith simulant was mixed with aluminum and Teflon and tested in 10^{-3} Torr vacuum conditions. The samples were prepared using a uniaxial press and measured at 13 mm in diameter and 3 mm in height. Material properties collected included Knoop Hardness, a microhardness test typically used for thin sheets or very brittle materials where only a small indentation may be made for testing purposes. A pyramidal diamond point is pressed into the polished surface of the test material with a known, often 100 gram-force, load. Knoop Hardness measurements of 750 (100 gf) to 850 (1 kgf) were reported. Porosity was calculated for the end material at between 40% and 60%. Findings included a maximum combustion temperature of 1400 °C and a very rapid temperature rise of 500 K/s. A self-sustaining reaction could be achieved from a minimum concentration of aluminum with 12% by weight and with adding 1.5% of Teflon by weight. Higher Teflon concentrations lead to higher porosity, where inter-connected pore sizes varied in the range of 20 - 200 μm. The chemical reaction and thermal conditions of the reaction are the main focus of this research.

This thesis offers further insights about the possibilities of an additive-based sintered material. This work did not fully investigate the material properties of the final structural material. No compression testing was performed or other material properties

investigated. Porosity was calculated but no correlation between porosity and material strength or other material properties were performed. No comparisons of hardness were made, however the reported Knoop Hardness is comparable to Quartz, 820, or Feldspar, 560. Notably, the combustion reaction took place under vacuum conditions, allowing for a more accurate lunar fabricated material sample. However, no investigation was done of the equipment required or for the operational difficulty of fabricating structural material on the lunar surface.

Demonstration of direct laser fabrication using JSC-1AC as a viable additive manufacturing method was conducted by Balla et al. (2012). The additive manufacturing technology tested in this research was Laser Engineering Net Shaping (LENS). Typically used in metal sintering, this process results in net-shaped parts ready for cleaning with minimal post-fabrication finishing. Net-shaped part is an industrial manufacturing term meaning that the initial product is very close to the final product, reducing the need for extensive finishing work such as machining or grinding. This system focused a laser beam on lunar simulant with a spot size of 1.65 mm, causing its complete melting and solidification. Screening of particles suitable for their equipment to a range of 50 -150 μm was required. Dense solid cylindrical parts, 8-10 mm in diameter and with a height of 25-30 mm, were produced using a laser power of 50 W, at a scan of 20 mm/s and a powder feed rate of 12.36 g/min, the powder feed rate is the rate at which the regolith is deposited onto the work plane. The work plane may also be called the construction surface in other additive manufacturing processes. A laser energy density of 2.12 J/mm appeared to be ideal for generating the melt pool necessary for lunar regolith powder deposition without excessive liquid pool spreading or cracking of solidified parts. While this testing was

performed in ambient, non-vacuum conditions, the authors did suggest that parts made on the Moon should be stronger as the process performs better in a vacuum.

This work was a very detailed investigation of the parameters needed to produce a solid usable material from an additive manufacturing process. It offers insight into the energy requirements and the speed at which a LENS machine could produce useful material. While mentioned, this work does not include a thorough overview of what it would require to operate a system like this on the Moon. Regarding implementation using ISRU, the LENS system would need to be exported to the Moon for production. Material properties were not investigated, opting to leave this as future work. Since the simulant was completely melted, no porosity was computed.

A large-scale additives manufacturing system was investigated by Cesaretti et al. (2013) to produce 1:1 scale structures using lunar regolith simulant. The goal was to design a preliminary lunar outpost structure, develop a lunar simulant and to demonstrate the construction process. Using a 3D-printing system called D-shape, samples and sizable structures were constructed with the machine's systems evaluated in both ambient and vacuum conditions of $1x10^6$ mbar. A total of six liquid ink injections were tested with the nozzle buried in the simulant at vacuum conditions. This was performed to test if injections below a simulant layer could prevent the fluid from vaporizing. This differed from the terrestrial printing fabrication since the printer does not bury the nozzle in the working material. The simulant development was motivated for economic reasons, as the costs associated with procuring such a large quantity of JSC-1A or CAS-1 was greater than budgets allowed. The simulant developed was named DNA-1 and was based on natural volcanic material found close to the Bolsena Lake in Italy. DNA-1 simulant was

also compared to JSC-1A and a lunar soil sample 14163. Of note, DNA-1 contains a larger mass percentage of MgO than JSC-1A but less than the lunar soil sample 14163, and a smaller mass percentage of Fe_2O_3 as compared to JSC-1A. High amounts of MgO was also an important inclusion for the simulant used in testing as MgO is required as one of the reactants which allowed the D-shape printing process to occur. The D-shape printer had a square work area of 6 m by 6 m and the printer head was 6 m long and used 300 nozzles in a line spaced 20 mm apart. Binding liquid is dropped onto the surface after a fresh layer of working material has been moved atop the work plane. Suitable for terrestrial construction, the authors state that this system would have to be reengineered before it would be functional on the Moon. Measurements of some mechanical material properties were performed for the fabricated samples, most notably: compressive strength of 20.35 MPa (2951 psi), total open porosity 13%, density 1855.33 kg/m^3, and Young's modulus 2350 MPa (340.8 ksi). In addition to structural use, an alternative use for solar radiation or micrometeoroid protection was also suggested.

The successful demonstration of constructing a large-scale structure using an additive manufacturing process from lunar simulant is a notable milestone for lunar structures technology. The system was proven to work in ambient conditions; the binding agent could work in a vacuum with some process modification. The details of the vacuum testing would need to be elaborated on in more detail and structure construction tested in a larger format. The vacuum testing performed served the purpose of validating that the binding agent could bind the simulant in a vacuum environment. Some details of this process need to be elaborated for proper comparison with ISRU based manufacturing systems, such as how much binding liquid is required to produce the structures presented

in their work. We will further discuss material property values discussed in this work in subsequent sections.

Cardiff and Hall (2008) sintered JSC-1A / JSC-1AF lunar simulants using concentrated solar energy through a Fresnel lens. Based on a rolling chassis, the Fresnel lens achieved a maximum sintering rate of 13 cm^2/min, sintered to about 0.5 cm deep. This test was also performed in a high vacuum on Earth, utilizing terrestrial solar rays; lunar solar rays would be more powerful as they do not have atmospheric obstructions. The maximum depth achieved was about 2.5 cm using this system. The Fresnel lens system, as demonstrated, served to prove the concept of a dust mitigations system. Extrapolating on the sintering rate measured, a construction rate was calculated. Within approximately a 55-day period, 100 m^2 of lunar regolith could be converted into a landing pad. This system could be almost entirely constructed using ISRU, making this process highly efficient. Sintering benefits from a vacuum environment, solar energy is readily available and raw lunar regolith is of course plentiful. With some additional complexity, similar to a 3D printing machine, it is possible to imagine a system utilizing a 3D printing base and a Fresnel lens to produce complex sintered lunar regolith structural components.

Gualtieri and Bandyopadhyay (2015) investigated sintered lunar regolith material properties concurrently with this research project. The samples used in their testing were the same type of samples that they provided to us for testing. The simulant they used was a mix of JSC-1, JSC-1AF, and JSC-1AC lunar mare regolith simulant. The simulant powder was sieved and separated into different sizes of greater than and less than 212 μm particles. Using 12.7 mm and 7 mm diameter cylindrical dies, samples with a height to

diameter ratio of between 2:1 and 1.5:1 were pressed up to ~145 MPa. After pressing, the samples were fired for 20 minutes at 1200 °C. The phases of the sintered samples were analyzed and compared to the phases in the original powder using X-ray diffraction. The microstructure was observed using a field emission scanning electron microscope. The density of the samples was calculated using Archimedes' method. Compression tests were performed on a universal testing machine with a constant stroke rate of 0.5 mm per min until fracture. Hardness tests were conducted using a Vickers micro-hardness tester at a load of 100 g with a dwell time of 15 s. Melting was not noticed, however, liquid phase sintering was observed. They hypothesized that the variation of porosity is a result of the different green densities of the starting state of the samples. Green density is defined as the weight per unit volume of an unsintered compact. Gualtieri and Bandyopadhyay also noted that it is common for ceramic bodies being pressed by a die to have higher porosity near the edges of the sample due to frictional forces which cause a porosity gradient from the surface to the inside. The material properties they reported were averaged from at least ten tests. The average hardness was 1030.2 $HV_{0.1}$ ± 69.73 $HV_{0.1}$. The hardness results were stated to be quite high and were compared to commercial grade zirconia. Their 99.0 ± 0.5% dense samples had a failure stress that averaged 232 MPa and an average modulus of elasticity of 10.9 GPa. The 92 ± 2% dense samples exhibited a failure stress of 103.2 MPa and an average modulus of elasticity of 5.98 GPa. The Ryshkewitch equation was also used to calculate zero porosity compressive strength value of ~ 140.7 MPa. Also suggested was the feasibility of pressing a sample, then firing it in an oven.

Happel et al. (1992) arrived at the conclusion that cast basalt would be the most suitable material to construct a lunar base from native lunar materials. Several considerations were made in their selection of cast basalt including internal pressurization, radiation shielding, construction ease, and manufacturing process size constraints of components. Their cited reason for using indigenous lunar materials was the high cost of transporting structural materials from Earth. An ideal lunar construction material is one that is readily available in large quantities on the lunar surface and requires minimal processing. Also cited was the fact that lunar regolith is greater than 5 m deep on the surface at most locations. Desirable mechanical properties for such a material include high tensile and compressive strengths, fatigue and crack resistance and resistance to radiation damage. Concrete is good in compression, but requires reinforcing for tensile strength. Lunar concrete needs to be cured in a pressurized environment. Metal ores require refinement from raw regolith. Cast basalt can be readily manufactured on the Moon from regolith. Minimal material preparation is needed except for filtering of lunar rocks greater than 18 cm. Once placed in a furnace, the basalt could be melted and poured into molds to cool. However, aside from its workability, a primary disadvantage of cast basalt is that it is brittle. Corrective measures of reinforcing cast basalt were discussed. Calculations based on an assumption that cast basalt has a mass density of 3 g/cm^3 showed an ultimate compressive strength of 538 MPa (78,000 psi) and a modulus of elasticity 100 GPa ($14x10^6$ psi). A process of manufacturing a cylindrical habitat from cast basalt was proposed.

The use of cast basalt as a lunar construction material is very appealing. The assumed compressive strength values are extremely high and require further verification.

The biggest uncertainty about cast basalt is the actual material properties, and so terrestrial values of cast basalt are used. Further testing in a reduced gravity environment should be conducted to verify the accuracy of terrestrial values. Gravity could play a role in crystallization during cooling and solidification of a cast material and was not noted to this effect. From an implementation perspective, the ease of construction is an important consideration. If cast basalt were selected as the primary lunar construction material there are certain structures that benefit from casting and certain ones that do not from a manufacturing perspective. It would be difficult to imagine casting a road surface on the Moon, but it would be easier, if not more labor intensive, to cast and lay bricks as the road surface. Structurally, cast basalt is very strong, so strong that it might be over engineered and even wasteful regarding the energy used to melt and pour the basalt. An alternative to melting the lunar regolith is sintering, which would require less energy. Even if sintering produced a weaker material, it should be sufficient from a structural point of view in the reduced-gravity lunar environment.

The earliest test of sintering lunar regolith simulant by rapid prototyping methods was performed by McLemore et al. (2008). This work was performed at NASA Marshall Space Flight Center using an electron beam melting (EBM) process. This technology uses an electron beam in a vacuum to melt metal powders layer-by-layer. The focus of the work was to produce metallic parts in situ. Testing was performed with granular titanium to produce mechanical components successfully before proceeding to lunar simulant. Only qualitative testing was performed using Geological Survey Lunar Highland Type Medium NU-LHT-1M lunar regolith simulant. Light sintering of the simulant was observed, but no mechanical evaluation of the produced sintered material

was reported. Nondestructive evaluation (NDE) techniques were also cited as a requirement for any part produced in situ for post-production quality inspection and certification. Laser ultrasonics was one potential NDE method proposed for post manufacturing certification. A combination of additive and more traditional subtractive manufacturing techniques will be needed for fabricating parts on the Moon.

1.4.4 What Could Be Constructed from ISRU Lunar Materials

A thorough structural engineering design and analysis of a lunar structure was first investigated by Ruess et al. (2006). Reasons to go to the Moon were cited. A definition of the lunar environment was given. A detailed set of structural requirements was established; structural adequacy, material properties, maintenance, functionality, compatibility, transportation, ease of construction, excavation, foundations and use of local materials. Potential lunar materials were compiled from previous research works and included; metals, fabrics, composites, indigenous materials and concretes. Material selection was cited as being a subjective process and mentions that cast regolith appears to have the best combination of material and manufacturing properties for ISRU materials. Types of lunar assembled structures were evaluated and compared. A design was settled upon with loading requirements established and finally, a detailed structural analysis was completed for a modular second generation lunar structure.

Wilson and Wilson (2005) proposed sintering regolith or using epoxy paving as methods of mitigating lunar dust in the context of protecting a proposed lunar based, 20-meter liquid mirror telescope. Coating the lunar regolith surface in either the epoxy or sintering the lunar regolith surface directly was discussed as a dust mitigation method. Where it was mentioned to be an interim solution to the lunar dust problem, long-term

issues of creating this structure were identified. These issues include, surface erosion, wear resistance, maintenance and damage repair from cosmic rays and/or micrometeoroid impacts.

Hintze et al. (2009) investigated the potential of using two methods for dust mitigation on the lunar surface. The first was by sintering the regolith simulant into a solid with a solar concentrator. The second was by using heat or UV cured polymers to stabilize the surface.

A solar concentrator comprised of a Fresnel lens with a 1 m^2 collection area mounted on a moveable frame was constructed. Temperatures achieved by concentrating the Sun's rays through the Fresnel lens system were measured at 1350 °C, which was more than sufficient to melt the JSC-1A upon which it was focused. A main goal for the study was to measure the maximum depth the lunar simulant solidifies. A maximum depth of about 6 mm was achieved through a combination of melting and sintering. Decreasing density of the JSC-1A was observed during melting and the melted area seemed to contract on itself as well, resulting in a weak bond between successive passes of the solar concentrator. Two difficulties were identified; a single lens solar concentrator must move to follow the sun if it is to maintain a focal point on a select spot, and it proved difficult to heat the lunar simulant to great depths or wide areas. Their solutions to these observed problems were to decouple the solar collector and the applicator from each other. Greater depth could be achieved by sintering the surface layer by layer, or continuously adding regolith on top of a heater area. They also suggested regulating the sintering rate as a function of the measured sintered surface temperature. To provide an

idea of the speed of which this process could construct, the time needed to sinter a specific size launch pad was calculated.

Load bearing tests were also conducted using the sintered and the polymer cured materials in the study by Hintze. To accomplish this, the solidified test samples were backed and loaded against the lunar simulant. The sintered specimen was sintered in a crucible and then placed on a bed of lunar simulant, where the polymers tested were applied and cured directly on the simulant. The test system comprised of a six inch diameter dish filled with JSC-1A lunar simulant with the test specimen on top having force applied to it by a ¾ in diameter piston. The sintered samples' strengths ranged from 130 psi for 2.5 mm thick samples, 290 psi for 4.2 mm samples and 310 psi for 6.0 mm samples. The polymer mixtures were able to reach strengths from 20 psi to 80 psi. Abrasion resistance tests were also performed to investigate the potential of a rocket launching or landing on the dust mitigated surfaces.

The most important outcome of this experimental research was the creation of a solid surface on top of the lunar simulant, proving that this dust mitigation method may be an option. More conceptually and not discussed in their research, these manufacturing methods have potential to manufacture structural components as well. On the Moon, it should be expected that sintering is more effective due to the vacuum conditions. This work was performed in the Earth atmosphere, and from the Earth's solar concentration of the sun. The more intense solar energy of the lunar surface should also provide higher temperatures, allowing for increased rates of sintering if the temperature can be properly regulated. Too high temperatures, if not properly regulated, would melt the lunar regolith. Sintered surfaces would be preferable to melted surfaces as melting caused contracting

and cracking in the formed material. The number of load bearing tests were not mentioned, but assumed to be small due to the laborious nature of manufacturing the sintered components. For more accurate load bearing values, more specimens should be tested. The measurements from the load bearing tests should not be considered a maximum material strength value of the sintered material. Additional tests should be performed without the lunar simulant as a backing to understand the compressive strength of the material. Other mechanical material properties were not evaluated in this research. The aspect of UV based polymers adds complexity and a consumable non-in-situ resource, making UV polymers a less favorable option. Long term thermal analysis of such a large solid structure was also not considered in the work. Presumably, a large solid sintered ceramic would undergo the thermal gradients of the standard lunar cycle and suffer from thermal fatigue.

1.5   Sintering Background

The information summarized in this section is from *Sintering Theory and Practice* by German (1996) and is provided as background for understanding the sintering process.

Sintering is a thermal treatment for bonding particles into a coherent, predominantly solid structure via mass transport events that often occur at the atomic scale. The bonding from sintering leads to improved strength and lowers the system energy. This is not to be confused with melting which results in a phase transition of the material from a solid to a liquid. For a lunar application where resources would be limited, sintering would be more efficient at producing solid material than melting, require less energy since sintering occurs at about 50-70% of the melting temperature, depending on the material.

Sintering is divided into four stages; each representative of the geometric progression involved in transforming the powder compact into a strong, dense object. Depending on the conditions at which sintering is initiated, the sintering stages might begin with loose powder or nearly full density deformed particles. There are four main stages of sintering, with a graphical representation of each in Figure 1-1:

- Adhesion, rearrangement and repacking,

- Initial-stage neck growth,

- Intermediate stage,

- Final stage.

Through adhesion, rearrangement and repacking (A), loose particles form contacts with each other at random orientations. Adhesion occurs due to weak forces, including van der Waals forces and agglomeration forces from liquids. The closer the particles approach one another, the greater the bonding force. The adhesion stage occurs spontaneously with the formation of an emerging sinter bond.

Figure 1-1 – Phases of sintering: A- Adhesion, rearrangement and repacking. B- Initial-stage neck growth. C- Intermediate stage. D- Final stage. The grains are black, white is empty space or pores and the white lines are grain boundaries.
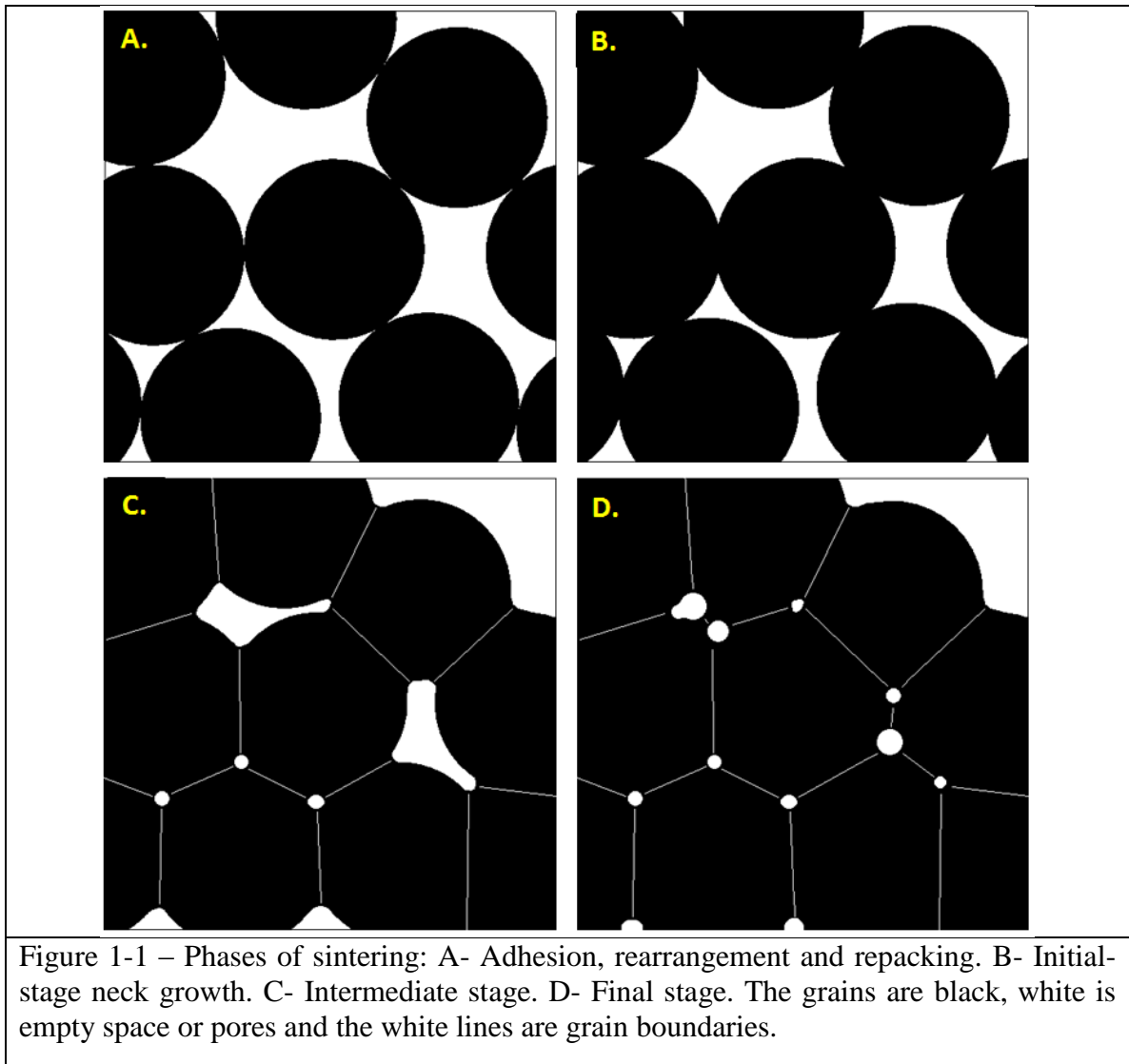
During the initial-stage neck growth (B), growth of the sinter bond from an initial loose powder contact occurs. The neck size is sufficiently small that neighboring necks grow independently of one another. The initial stage concludes when the neck size ratio of neck diameter over particle diameter is approximately 0.3.

The intermediate stage (C) is characterized by simultaneous pore rounding, densification, and grain growth. The driving force is the elimination of the remaining

surface energy since the curvature gradients have largely been smoothed prior to the intermediate stage.

The final stage (D) is generalized by closed pores becoming unstable due to coarsening, as grain growth elongates the pores and they close. The final stage is slow compared to the initial and intermediate stages. Simultaneous coarsening events occur which impede densification. During coarsening events, there are no net dimensional changes but there is a considerable reduction in surface area, increase in grain size and compact strengthening occurs with changes in pore shape and size. If grain growth is rapid in comparison with the pore mobility, the pores are isolated away from the grain boundaries, resulting in slow densification from long-range volume diffusion. Alternatively, if pore mobility is high, via surface diffusion or evaporation–condensation, the pores can remain attached to the moving grain boundaries and continue to shrink. Grain boundary mobility depends on diffusion rates within the grain boundary, while pore mobility depends on the pore curvature. Typically, pores move by surface diffusion and grain boundary motion depends on the temperature, grain size, and grain boundary energy. Pore mobility is important in sintering as it helps dictate the size, shape and location of pores in the medium. If pores contain a trapped gas, solubility of the gas in the matrix affects both coarsening and densification of the medium during the final stage.

One aspect that was not detailed in Sintering Theory and Practice is gravity's effect on sintering. The Moon's reduced gravity should be expected to influence sintering in a different way than terrestrial sintering. However, a detailed investigation of this affect it is beyond the scope of this research and this section. Instead a short literature review and discussion on sintering results from microgravity experiments follows.

Park et al. (2006) analyzed data collected aboard the space shuttle Columbia during STS-65, STS-83 and STS-94 to study the gravitational effects on liquid phase sintering (LPS). Densification and distortion of liquid phase sintered tungsten heavy alloys were reviewed. Tungsten contents range from 35 to 93 percent by weight with the matrix phase consisting of nickel and iron in a 7:3 ratio, respectively. Tests were conducted in microgravity and terrestrial gravity. Lunar and Martian gravity conditions were investigated by means of interpolation between these two data points. Constructing a finite element program based on mass and momentum conservation was used in their analysis. Full three-dimensional simulations were used to demonstrate the gravitational effect on sintering. Sintering stress relations, bulk viscosity, shear viscosity, grain growth formulas were incorporated in a finite element program, boundary conditions were set, and the effect of friction and surface tension were also incorporated. The simulation results showed that gravitational forces are dominant in stronger gravity fields and surface tension effects are dominant in weaker gravity fields. The material composition also plays a role in distortion. Notably, with an increasing amount of tungsten (solid), the shape distortion was reduced in both microgravity and at terrestrial gravity but with less effect under microgravity.

The finite element program developed serves to provide interpolated data on a lunar environment. This is based on the assumption that the effects of lunar gravity scale linearly between terrestrial gravity and microgravity. So long as this is correct, this finite element tool could be used to approximate sintering effects on the Moon. The validity of this assumption requires further investigation.

Upadhyaya and German (2001) investigated data on liquid phase sintering (LPS) collected onboard space shuttle Columbia during STS-65, STS-83 and STS-94 to study gravitational effects on tungsten heavy alloys. Tungsten contents range from 35 to 93 percent by weight with the matrix phase consisting of nickel and iron in a 7:3 ratio, respectively. Tests were conducted in microgravity and terrestrial gravity. Tungsten heavy alloys are particularly sensitive to gravitation effects since the liquid-solid density difference is large. Using tungsten heavy alloys, samples were isostatically cold pressed, pre-sintered and then dry machined to cylindrical pellets.

Terrestrially, gravity induced grain settling results in solid-solid contacts that lead to coalesced grains. One recognizable problem in compacts sintered terrestrially is gravity induced solid-liquid separation and compact slumping when excess liquid is present. In LPS, an excess of liquid causes shape loss, consequently only alloys with small quantities of liquid, less than 20 percent by volume, are fabricated on Earth. The factors causing distortion in LPS are not understood.

Ideally, when high liquid content alloy is sintered in microgravity it will try to minimize its energy by attaining a spherical shape. During microgravity sintering, the cylindrical pre-sintered sample underwent reshaping and completely spheroidized. Spheroidizing is a type of heat treatment for heavy metal-based alloys typically used to increase ductility. It is conducted at elevated temperatures just below the melting point of the material and is followed by a slow cooling. In terrestrial gravity the sintering alloy slumps and attains a 'bullet' shape. Pore evolution proved stable in microgravity. When sintered on Earth, pores are located on the top of the sample, whereas in microgravity pores are localized at the center of the sample. Conditions during sintering that cause the

loss in structural rigidity prevail in microgravity. Microgravity sintered tungsten alloys disprove the premise that absence of gravity will lead to homogeneous microstructure during sintering. When low solid content alloys are sintered in microgravity they exhibit microstructural gradients from the periphery to the center of the compact. Under terrestrial conditions, distortion is accompanied by solid-liquid segregation, whereas in microgravity, the compacts tend to spheroidize. This implies that the conditions that cause the loss of structural rigidity prevail even in a microgravity environment.

Whereas the microgravity research of Upadhyaya and German (2001) was conducted using a very dense metal, the JSC-1A analyzed in our research is neither metal rich nor comparatively high density. Tungsten's density is about 19 g/cm^3 whereas solid basalt, which can be comparable to JSC-1A lunar simulant, has a density of about 3 g/cm^3. Samples fabricated on the Moon instead of terrestrially would result in shape and structural differences. There could be more shape distortion and different pore migration. Where the samples tested were all deemed cylindrical enough to test, it is possible that samples manufactured in a lunar gravity environment could have a pore structure localized at the center of the sample, and potentially more shape distortion. It appears that much of the microgravity sintering research to date was based on metallic sintering due to the large density gradients achievable. So long as metallic sintering is comparable to ceramic sintering, the metallic sintering microgravity based research should scale appropriately for a lunar regolith analogue.

German (2003) commented on distortion due to the effects of gravity on LPS. Seventy-seven powder compacts have been processed in microgravity conditions with the following general observations: terrestrial gravity compacts always densify prior to

distorting; gravity induces grain settling, with top-bottom grain size, solid volume fraction and contiguity gradients; grain settling does not occur in microgravity, rather surface to core gradients arise; pore elimination (densification) is essentially impossible in microgravity; pore coarsening and coalescence produce large pores in microgravity; green body homogeneity is a dominant factor with respect to distortion on Earth; grain settling induces structural rigidity that helps minimize distortion on Earth, without grain settling microgravity sintering results in more distortion. The overall observation was made that samples are more porous and more distorted when compared to Earth-based sintering. Microgravity results in a lower strength compact since there is no grain compression to form a solid skeleton. As pores cluster and coalesce, they become closed but not eliminated. As a consequence, microgravity compacts are weaker with more distortion and less densification. Table 1-1 shows the general differences between terrestrial and microgravity sintering.

Attribute	Terrestrial Gravity	Microgravity
Densification	Yes	No
Distortion	Some	Considerable
Porosity	Little	Considerable
Pore Size	Small	Large
Buoyancy	Yes	No
Contiguity	High	Low

Table 1-1 – Summary of sintering differences between terrestrial gravity and microgravity conditions from German (2003). It would be expected that sintering on the Moon would produce conditions between terrestrial gravity and microgravity.

Sintering tests have been conducted in terrestrial gravity and microgravity environments in an attempt to study gravitational affects. To date, only interpolation between these two data points have been used to predict the effects of sintering in the lunar gravity. The exact effects of lunar gravity sintering are not well understood and would require further testing to have quantifiable values. ISRU based sintering on the Moon would rely on ceramic sintering not metallic sintering, as has been studied in microgravity. Samples tested in this research project have been fabricated in terrestrial gravity and may have stronger characteristics than if the samples were to be sintered under lunar gravity. To what degree terrestrial sintering may have made these samples stronger than their lunar analogue is difficult to predict. This serves to highlight that further work is required to understand manufacturing by sintering in lunar gravity. Liquid phase sintering occurs as a result of sintering lunar regolith. However, it is currently unclear how the potential effects of centralized pore concentration and increased shape distortion on components sintered on the lunar surface could affect material properties and material strength. However, once these effects are better understood, it is surely possible to correct for pore concentration and distortion effects to regain or enhance lunar sintered component strength.

After reviewing the literature on the process of sintering and gravitational effects on sintering, we conclude that sintering can be a favorable manufacturing method for forming solid material in the lunar environment. Since sintering utilizes a granular medium, performs well in vacuum conditions and can be accomplished by applying heat to the granular medium, sintering lends itself to lunar ISRU quite well. The lunar surface is already equipped with the fundamental requirements for sintering: the surface is

covered in lunar regolith that is an extremely fine and granular material, the atmosphere is a vacuum and the Sun provides plenty of solar radiation. Solar radiation can be a significant source of the thermal energy required for sintering.

Solar energy could be converted to thermal energy by methods such as solar panels to power heaters or solar ray concentration though optics. Lunar regolith in its raw form is already a viable candidate for sintering. As previously reviewed, geothermic reactions with lunar simulant require adding additional material to forge structural material. Similar in method is the creation of lunar concrete, which again requires additional processing. Sintering can be accomplished with or without additional material and requires only heat.

Sintering also has the advantage of being a relatively simple process in comparison to other manufacturing processes that may require high precision or very specialized machinery. This is not to say that sintering cannot be used to create complex structural components. Like many other manufacturing methods, sintering can become complicated if the demand is for complex or complicated components. This could include specialized molds for complex shapes or very large workspaces for very large shapes. However for simplicity, only basic sintering methods will be assumed for this research in application to the lunar surface. Questions to be addressed are how structurally viable could this sintered lunar regolith be. This will be addressed in the rest of this research.

Chapter 2.　　Sample Preparation and Description

2.1　Design of the Experiment

To evaluate the material properties of sintered lunar regolith, testing must be performed. Compression testing was selected as opposed to tensile testing due to the brittle nature of rocks and ceramics. The destructive nature of compressive testing means that each test can only be performed once. Any quantifiable values of the sample will need to be measured before testing. Samples would need to be created of two different porosities to evaluate the effect of porosity on material strength. Material choices need to be made.

2.2　Lunar Simulant Selection

To evaluate material properties of sintered lunar regolith, material samples must first be created for testing. The first step in creating samples for testing is to select the proper material. Ideally, obtaining actual lunar regolith would be preferred. But the inherent problem in testing actual lunar regolith is the very limited quantity available for research, let alone destructive testing.

Across the entire American Apollo and Soviet lunar sample return missions, 382 kg and 300 grams, respectively, of lunar material have been brought to Earth. Of this mass, a very small portion was lunar regolith, making it a highly valued material. Another option for lunar material is by lunar asteroids, ejecta from impacts on the lunar surface that have escaped the Moon's gravity field into that of Earth. Testing using ejecta was not an option since it would not be likely or verifiable that lunar regolith could

survive entry into the Earth's atmosphere. Fortunately, the difficulty of testing with actual lunar material is not a unique problem.

Due to the scarce supply of lunar regolith, many lunar regolith simulants have been created. Simulants are just as the name implies. They simulate certain properties of the original medium, in this case lunar regolith. Over the years, many different lunar simulants have been created for various research projects. A table of various lunar regolith simulants can be seen in Table 2-1. A simulant must replicate the lunar surface as well as possible. Lunar regolith is substantially unlike any terrestrial material because of the lack of observed weathering effects from wind, water and erosion on the Moon. The difficulty in constructing a simulant that perfectly replicates all of the original materials properties cannot be overstated. Depending on the application, a simulant is developed to mimic certain traits such as chemical composition, geotechnical properties or bulk properties. Simulants are typically developed off of the best information available on the original medium. In the case of lunar regolith, this is mostly from the returned Apollo samples. Thus, there are many specialized simulants.

Simulant Name	Information	Type
ALS	Arizonal Lunar Simulant	Low-Ti mare (geotechnical)
BP-1	KSC/ Arizona Black point quarry waste (basalt); used for large excavation exercises with BLADE. *Rahmatian and Metzger. (2010)*	Low-Ti mare (geotechnical)
CSM-CL	Colorado School of Mines - Colorado Lava. Unpublished	Geotechnical
DNA-1	*Cesaretti et al. (2013)*	Low-Ti mare (general use), similar to JSC-1, higher MgO content
GCA-1	Goddard Space Center. *Taylor et al. (2008)*	Low-Ti mare (geotechnical)
GRC-1 & GRC-3	Glenn Research Center (Sandy, clay mixture used in SLOPE Facility for mobility/ excevation. *Oravec et al. (2010)*	Geotechnical: Standard vehicle mobility Lunar simulant
GSC-1	Goddard 'simulant''; material from local site that is being used for drilling testing	-
JSC-1	Johnson Space Center. *McKay et al. (1994)*	Low-Ti mare (general use)
JSC-1A, JSC-1AF, JSC-1C	Orbitec created under a NASA contract	Low-Ti mare (general use). Produced from the same source material as JSC-1
MKS-1	*Carpenter. (2005)*	Low-Ti mare (inended use unknown)
MLS-1	Minnesota Lunar Simulant *Weiblen et al. (1990)*	High-Ilimenite mare (general use)
MLS-1P	*Weilblen et al. (1990)*	High -Ti mare (experimental, not produced in bulk although small quantities were distributed)
MLS-2	*Tucker et al. (1992)*	Highlands (general use)
NU-LHT-1M, NU-LHT-2M, NU-LHT-1D, NU-LHT-2C	NASA/USGS Highland type simulant (chemical/Mineralogical & physical properties) *Stoeser et al. (2009)*	Highlands (general use)
CAS-1	China (chinese Academyu of Sciences) a basic simulant made to represent Apollo 14	Low-Ti mare (general use)
CLRS-1	Chinese Lunar Regolith Simulant. *Chinese Academy of Sciences (2009)*	Low-Ti mare (general use?)
CLRS-2	*Chinese Academy of Sciences (2009)*	Low-Ti mare (general use?)
CUG-1	China. *He et al. (2010)*	Low-Ti mare (geotechnical)
NAO-1	NAO-1, National Astromical Observatories, Chiese Academy of Sciences. *Li et al. (2009)*	Highlands (general use)
TJ-1, TJ-2	China (Torgji University); a basaltic ash feedstock with olivine and glass. *Jiang et al. (2011)*	Low-Ti mare (geotechnical)
CHENOBI	Canada (physical a& chemical properties simulant)	Highlands (geotechnical)
OB-1	Canada, Olivine-Bytownite. *Battler and Spray (2009)*	Highlands (general use geotechnical)
FJS-1 (type 1), FJS-1 (type 2), FJS-1 (type 3),	Fuji Japanese Simulant. *Kanamori et al. (1998)*	Low-Ti Mare, Low-Ti Mare, High-Ti Mare, (general use)
Oshima base simulant	*Syeyoshi et al. (2008)*	High-Ti mare (general use)
Kohyama base simiulant	*Syeyoshi et al. (2008)*	Intermediat between highlands and mare (general use)
KOHLS-1	Korea. Koh Lunar simulant. *Jiang et al. (2010)*	Low-Ti mare (geotechnical)

Table 2-1 – Listing of known lunar simulants from Marshal Space Flight Center (2010) with additional, more recent, simulants included.

With so many simulants available from so many different countries and of various base materials, it can be difficult to select the most appropriate simulant for an individual research problem. Another difficulty is accurately comparing results with similar research

in the literature when different lunar simulants are used. To assist in evaluating lunar simulants, Rickman et al. (2013) sought to create a set of four standards: particle size-distributions, particle-shape distributions, density of the bulk material, and the relative abundance of minerals rocks and glass. In its ideal form, a researcher should be able to determine which of the four criteria are of most importance to their work, and then review the literature for the simulant that matches their need.

One concern with lunar simulants, as indicated by Rickman et al. (2013), is the sampling bias of the lunar samples. The average regolith is a mathematical construct and has no physical reality. However, the rocks and regolith returned from the Moon were handpicked by astronauts, typically favoring the geology training they received. That is, the samples were deliberately selected, not randomly selected, and thus are not statistically representative of the general population. When applying data from lunar sample measurements, statistical parameters are used the most.

Another limitation is the lack of data available for regolith particles of very small values, especially less than 5 μm. Simulants may have accurate averages of grain size, however, when matching grain size distribution of actual samples to simulant samples, this distribution does not always follow the same formula.

In evaluating the relevance of the four standards for this research project, the distribution of particle size is the most important factor for the sintering investigation, especially since it factors into the green density of the compact which impacts porosity.

In the sintering process, the particle-shape distribution was assumed to be secondary to particle size, meaning that size would play a far greater factor than particle shape for this research project.

The density of the bulk material was of less concern since it was treated as a controlled variable. Sieving the simulant of choice would filter its material density, in effect altering the undisturbed density of the simulant, but allowing for post-sintering porosity to be evaluated.

Material composition is of considerable importance as different ratios and types of materials can lead to different melting temperatures, which could impact the sintering process. Also impacted are the types of sintering possible, as mentioned previously, inclusions of nanophase Fe^0 allowed microwave sintering to take place. For this research microwave sintering was not to be investigated, making this addition not necessary. Rickman et al. (2013) point out that the regolith is very different between the mare and the highland areas. And even within the mare or highlands, it is not uniform. It was not the scope of this research to investigate sintering in all regions of the Moon. So the selection of which lunar region would be best for ISRU of structural regolith was not a deciding factor in lunar simulant selection.

Ultimately the driving factor for lunar simulant selection became a function of availability and economics. Honeybee Robotics graciously donated about 5 lb of JSC-1A low-Ti mare lunar regolith simulant. In the United States, JSC-1 has become the industry standard. After the original supply of JSC-1, JSC-1A was produced and took its place due to its availability and general use properties. The selection of JSC-1A means that the results from this research would be most relevant for ISRU structures located in the lunar mare regions. JSC-1A was designed to be as similar as possible to its predecessor JSC-1 and was produced from the same source material.

Next, samples would need to be fabricated from the simulant. And once samples were obtained and catalogued, compression testing could be conducted to measure forces applied to, and deflections of, each individual sample. Afterwards, the data collected could be computed and analyzed to evaluate relevant material properties of the sintered material.

2.3 Sample Production

Lacking the expertise or the right equipment to create sintered lunar samples of various porosities, we reached out to other researchers, in particular Professor Amit Bandyopadhyay of Washington State University, to learn more and to enquire about the possibility of collaboration. Professor Bandyopadhyay is also a Rutgers Alumnus of the Department of Material and Ceramic Engineering. In part because of his connection to Rutgers, he was willing to collaborate with our research. We asked whether using the same Laser Engineering Net Shaping (LENS) additive manufacturing capability that was presented in their paper, Balla et al. (2012), was a possibility. The conclusion from this discussion was, it would be too time and resource consuming to construct the requested number of compression samples. The alternate solution proposed by Professor Bandyopadhyay was to have one of his students press and oven-fire samples from a simulant material that we would provide. We investigated the cost of purchasing lunar simulant for this research and solicited institutions that could donate simulant for this research. Honeybee Robotics in Pasadena, California was willing to provide 5 lb of JSC-1A lunar simulant that was packaged and sent to Professor Bandyopadhyay's laboratory at Washington State University in Pullman, Washington, where the sintered samples were made. The manufacturing of the sintered samples was done by Thomas Gualtieri, a

student of Professor Bandyopadhyay. Thomas Gualtieri's account of the details of the sintering process can be found in Appendix B. From this point on, the manufacturing of the samples was led by Gualtieri and included regular correspondence of the status of the samples production. Two sample sets of eight each were produced to evaluate the effect of porosity on the material properties. The sample set size was determined by a balance of labor of manufacturing, and the number of samples required for significant statistical correlation. A summary of the sintering process is provided below.

For preparing the samples, the first step used a No. 70 sift to separate out any grains that were larger than 212 μm. Without this initial sifting step, it was observed that larger grain powder would collect together upon the pouring of the powder into the mold. This produced samples with inconsistent porosity across the specimen. By sifting the powder, there was a more consistent size of powder, which resulted in more homogeneous porosity across the sample.

Secondly, six grams of the powder was measured out and poured into a 12 mm wide cylinder mold. It was found through trial and error that when six grams of powder was pressed it produced a sample that had a height to width ratio of 2:1.

Next, the powder was subjected to a pressure of 4 MPa for a minute and then removed. The difficult part of this step was that upon removal from the mold, the packed cylinders would frequently break apart due to the powder being very dry and lacking in adhesion to itself. Additionally, once the samples were removed from the mold, they were still very fragile and ran the risk of being broken during transportation from the mold to the furnace.

The samples were then put in a furnace where they were sintered. A graph of the temperature vs. time for the sintering process can be seen in Figure 2-1. It was found that at 1125 °C the powder would start to melt and not retain its cylinder shape. The time to sinter was determined by trial and error once the maximum shape retaining temperature was discovered.

Figure 2-1 – Temperature was ramped up to 1120 °C. At 1125 °C the cylinders would lose their shape.
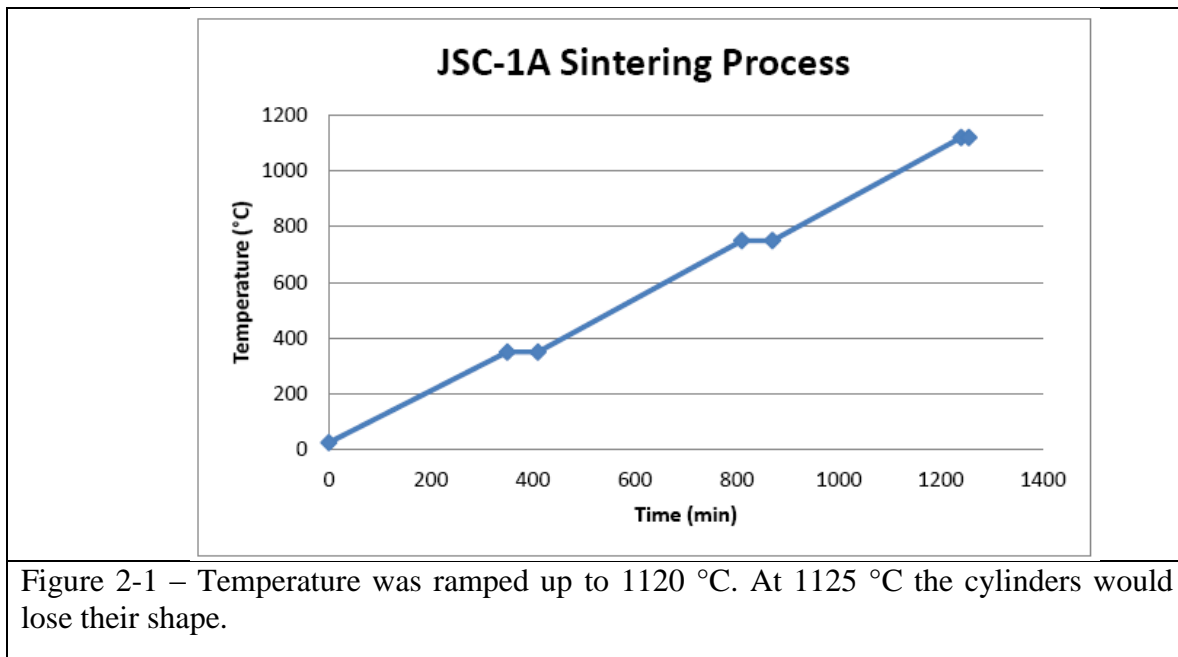
Finally, the sample was inspected to ensure that the cylindrical shape was retained and the cylinder ends remained flat.

Two batches of samples were produced from the simulant, the first from the powder that made it through the No. 70 sift (low porosity), and the second from the powder that did not pass through the No. 70 sift (high porosity). The low porosity sample set was comprised of the JSC-1A lunar simulant and was sifted for particles < 212 micron, then processed at 1,120 °C for 15 min. The calculated average porosity of this sample set was 1.44% (s=1.91, n=8) where 's' is the standard deviation and 'n' is the sample size. The high porosity sample set was the JSC-1A lunar simulant, which was

sifted for particles > 212 micron, then processed at 1,120 °C for 15min. The calculated average porosity of this sample set was 11.78% (s=3.30, n=8).

Sintering Temperature (°C)	Sintering Time (min)	Powder Size (µm)	Average Porosity (%)
1120	15	< 212	1.44
1120	15	> 212	11.78

Table 2-2 – Sintering parameters and porosity resulting from the sample production process.

2.4 Physical Attributes of the Samples

As shown in Table 2-3, the average sample from the low porosity group weighed 5.339 g, had a height of 19.238 mm and a diameter of 11.744 mm. From Table 2-4, the average sample from the high porosity group weighed 4.879 g, had a height of 18.693 mm and a diameter of 12.262 mm. Upon measuring all of the samples, the samples were visually inspected. All samples were very similar in concentricity of shape with the exception of sample number 8 that had a slight curve to its cylindrical shape.

Low Porosity, < 212 μm						
Sample Number	Mass (grams)	Average Height (mm)	Height STD (n=3)	Average Diameter (mm)	Diameter STD (n=5)	Average Density (g/cm³)
1	5.430	19.5850	0.0352	11.5718	0.0556	2.6363
2	5.346	19.0213	0.0019	11.6934	0.0537	2.6170
3	5.391	19.3590	0.0137	11.7222	0.0743	2.5805
4	5.650	20.5380	0.0067	11.6624	0.0840	2.5755
5	5.488	19.4240	0.0297	11.7292	0.0255	2.6151
6	4.724	16.9083	0.0597	11.6844	0.0380	2.6055
7	5.249	18.8930	0.0373	11.8100	0.0731	2.5361
8	5.437	20.1753	0.1531	12.0806	0.0927	2.3509
Mean	5.339	19.238		11.744		2.565
STD	0.257	1.021		0.142		0.086
Variance	0.066	1.041		0.020		0.007

Table 2-3 – Sample physical dimension statistics for the low porosity set of samples 1 through 8.

High Porosity, > 212 μm						
Sample Number	Mass (grams)	Average Height (mm)	Height STD (n=3)	Average Diameter (mm)	Diameter STD (n=5)	Average Density (g/cm³)
9	5.093	19.4050	0.0594	12.1356	0.0487	2.2692
10	4.180	16.5760	0.0430	12.5176	0.0484	2.0489
11	4.938	18.7863	0.0347	12.1434	0.0331	2.2694
12	5.106	19.8533	0.0399	12.1742	0.0999	2.2095
13	5.106	19.1503	0.0158	12.1378	0.0475	2.3043
14	5.048	18.7807	0.0194	12.1096	0.0293	2.3337
15	5.002	19.2723	0.0485	12.5304	0.0191	2.1049
16	4.555	17.7170	0.0343	12.3468	0.0347	2.1475
Mean	4.879	18.693		12.262		2.211
STD	0.314	0.991		0.166		0.095
Variance	0.099	0.981		0.028		0.009

Table 2-4 – Sample physical dimension statistics for the high porosity set of samples 9 through 16.

Two samples can be seen in Figure 2-2, highlighting the textural differences between the high and low porosity samples. Whereas all samples had a dull reddish grey color, the most noticeable visual differences were in the surface roughness of the samples. The high porosity samples have noticeable voids on the surface and even fail to form a complete circle at the top of the cylinder. This inability of the samples to have a completely circular diameter is another possible reason for the several premature test failures.

Figure 2-2 – True color image of a low and high porosity sample. Samples have an approximate length of 19 mm and are 12 mm in diameter.
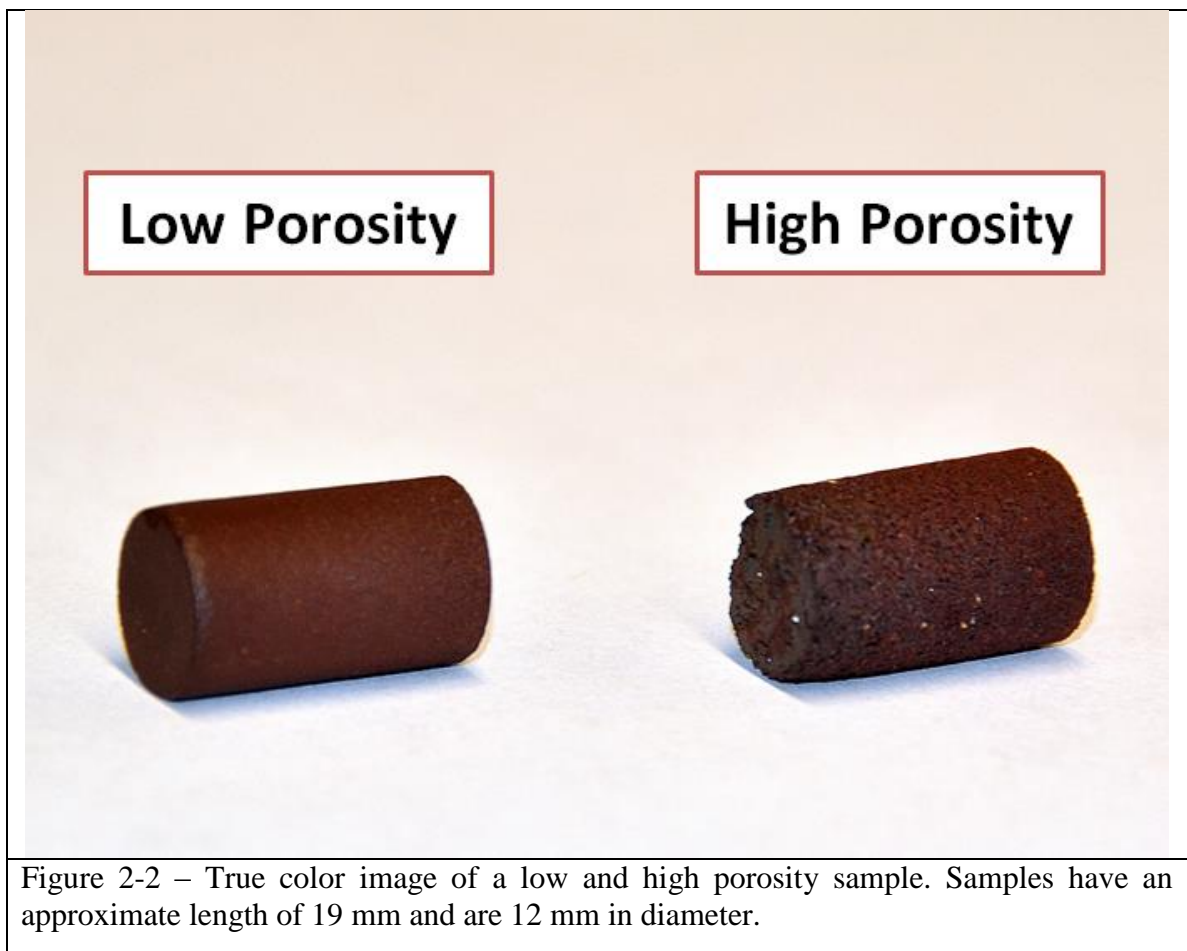
Figure 2-3 shows a close up of the post testing fractured surfaces. On the left is the remaining specimen from the low porosity test 4 and on the right is the remaining

specimen from test 9 of the high porosity set. The difference in grain size of each specimen is noticeable with the low porosity material being much finer than the coarse grains of the high porosity sample.

Figure 2-3 – Show is a close-up true color image of the fractured post compression tested samples. The low porosity fractured sample surface is on the left and the high porosity on the right.

Chapter 3.   Experimental Apparatus and Test Procedures

Proper safety protocols were followed throughout the duration of the testing. Personal safety equipment, goggles and respirator masks were used during the handling and testing of the lunar regolith and sintered specimens. Blast shields to prevent hazardous projectiles were implemented during destructive testing.

3.1   Testing Procedure

Measurements of the diameter, height and weight of each sample were performed and recorded prior to compressive testing. The diameter and height were both measured with a micrometer as seen in Figure 3-1. The height was measured at three different positions and averaged, and the diameter was measured at five different positions in order from the top to the bottom of sample and averaged. Weight was measured with a scale in grams accurate to three decimal places. The first eight samples tested were of the low porosity, < 212 micrometer particle size sample set, and the last eight samples were of the high porosity, > 212 micrometer particle size sample set.
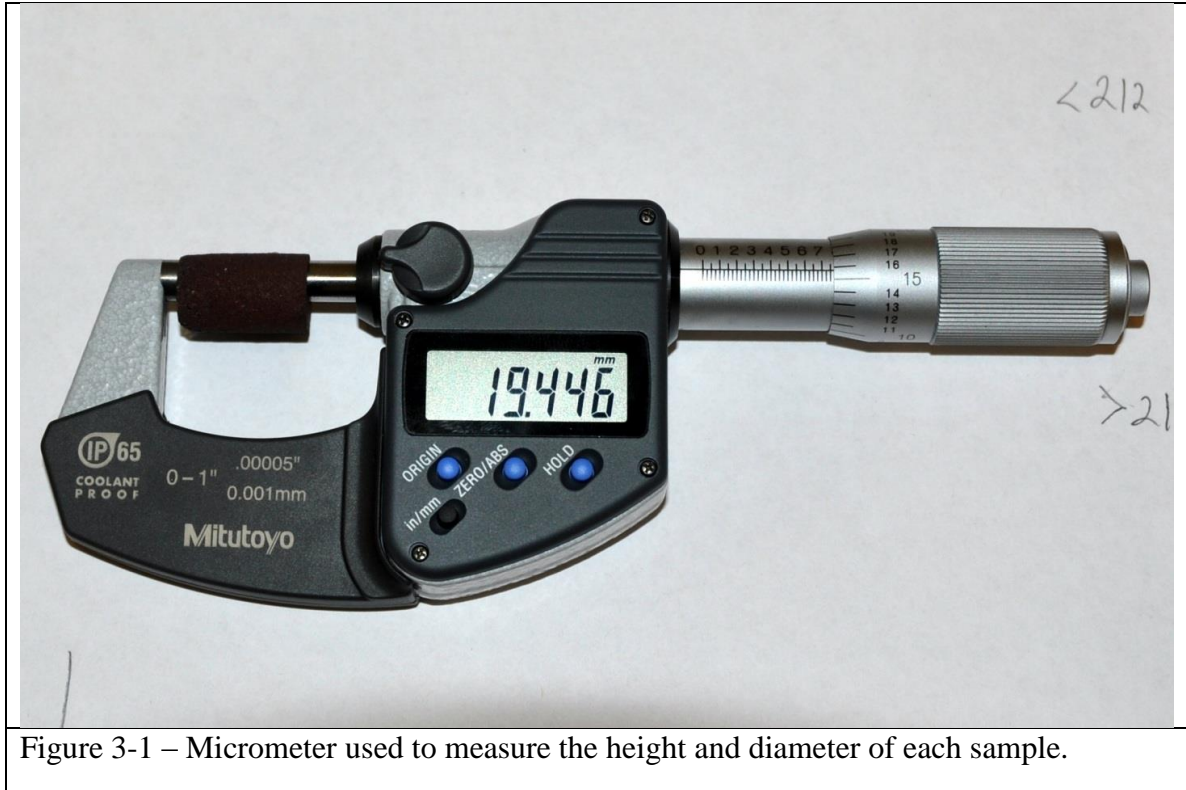
Figure 3-1 – Micrometer used to measure the height and diameter of each sample.

Compression testing was performed on May 20, 2014 in the Rutgers Material Science and Engineering Department in room CCR-137 with the assistance of graduate student Terence Whalen. Whalen instructed and showed me how to use the lab equipment and the proper safety procedure to follow for the tests. He provided assistance in selecting the parameters to use in the compression test, and after his guidance in setting up the first sample, I was allowed to conduct the remaining 17 tests on my own.

An Instron 4500 Series Universal Test System running Series IX version 8.04.00 software was used for the compression tests. This test apparatus can be seen in Figure 3-2 with a close-up of the sample between the plates seen in Figure 3-3. The software allowed for a few test parameters to be set. These parameters can change depending on the type of material used. Whalen aided in the selection of these parameters upon the first compression test and we decided to leave them the same for the duration of the testing.

Two parameters set were the crosshead speed of 1.000 mm/min and the break detection, which automatically stops the test if a sudden reduction of force was detected, set to 5 kN. Data was recorded by the universal test system at 10 points per second measured load in kN and displacement in mm for each test. The universal test system's maximum compression force was 95 kN. Video of each test was recorded from behind a clear shield using a Nikon D5000 DSLR camera on a tripod. Ambient room temperature and pressure conditions were observed for the duration of the tests. The tests were numbered in sequence from first to last test performed. To clamp the specimen the test operator manually jogged the clamps to the preload force. The preload force is required to hold the specimen in place on the clamps and is typically a trivial force in comparison to the maximum load the samples experience. The sample was placed between the compression plates of the universal test machine, and then preloaded to about 300 N. The test was then initiated via the software. The test was terminated either automatically by the software once the break detection value was triggered or manually by the operator.

Figure 3-2 – An annotated picture of the Instron Series 4500 Universal Test System used for testing. On the left is the computer shown with the software plotting the last test, in the center is the test unit with ball screws, cross head, universal joint, compression plates and load cell labeled, and to the right is the control panel for jogging the compression plates.

Figure 3-3 – A close-up view of the sample between the compression plates. The sample dimensions were approximately 19 mm tall and 12 mm in diameter.

Chapter 4.   Data Analysis

4.1 Load vs. Deflection Relations

The most fundamental data recorded during compression testing of the axially loaded specimens are deflection and load information. The load is the force applied by the compression machine to the specimen and the deflection is the deformation of the specimen. Along with the specimen dimensional measurements, all other calculations are based on this information, so inspecting this data for nuances is important. Interpreting this data first provides insight to the success and quality of the test.

A standard nomenclature is sought to portray important points during the specimen loading and is presented here. For each test performed, load and deflection data was collected; plots on a per test basis are provided in Appendices A.2, A.3 and A.4. Depicted in Figure 4-1 is an annotated example of such a plot, showing the load vs. deflection for the first test. Read left to right, the figure offers telling information on the progress of the test.

Figure 4-1 – A load vs. deflection plot for the first test conducted. Sample 1 withstood the highest loading of all the samples tested and did not demonstrate any premature failure.
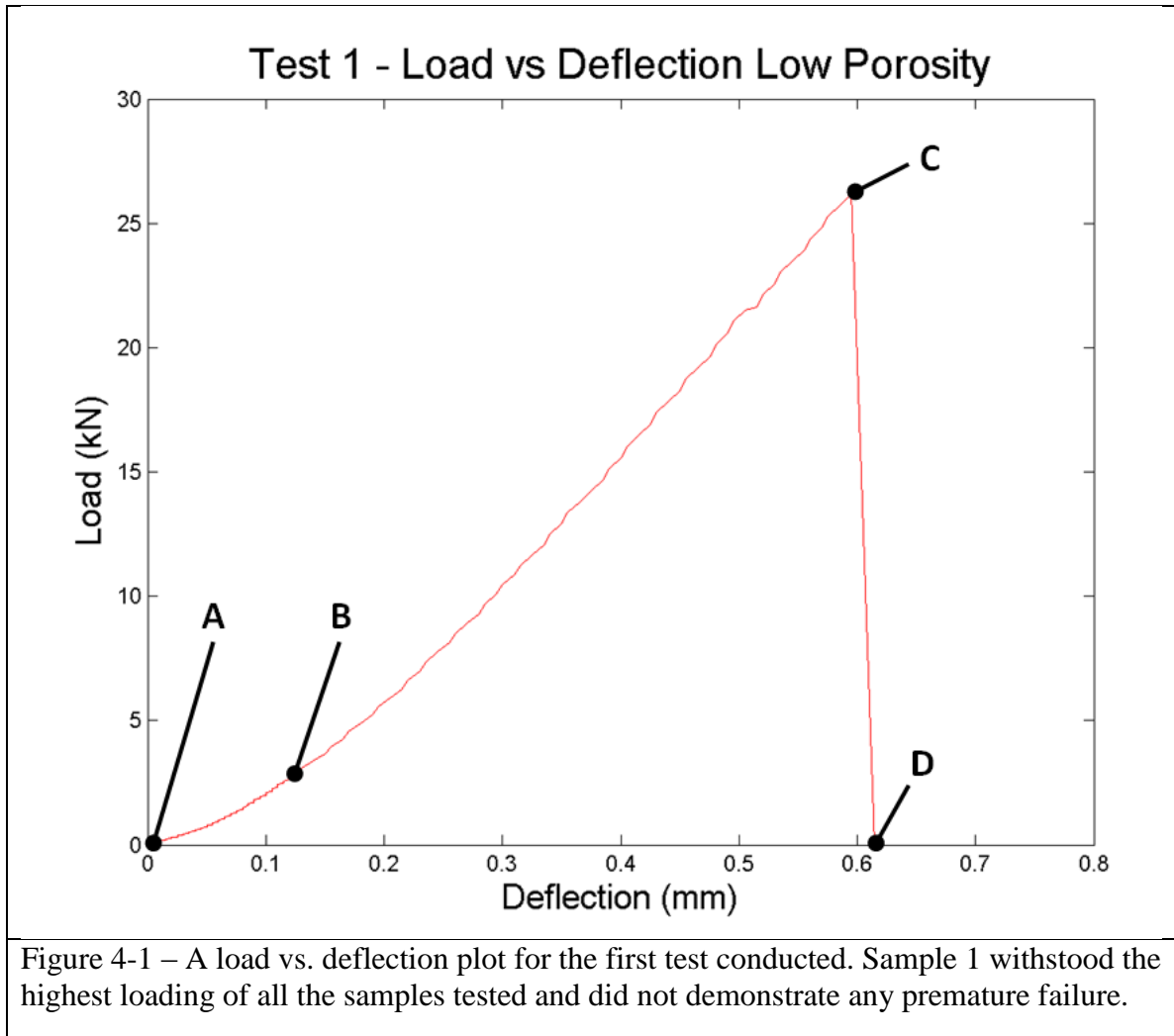
Label A is the beginning of the test and where 'Load Initial' occurs, which was the initial loading of the specimen by the Instron machine. The 'Load Initial' is not as important a value as it may seem. This is simply the value of the force used to hold the sample between the plates. Label B is the actual load start and denotes the point at which the sample ceases slipping and is firmly gripped between the two plates. Another feature common of compression tests is the load ramping up on the sample from the compression plates. This removing of any 'slack' in the machine setup is caused by the differences in sample placement and the interface between the sample and compression plates. This instance is denoted by inspecting the line in the load vs. deflection plot, where between

Label A and Label B the line is jumpier and more step-like, whereas the line between Label B and Label C is smoother.

After 0.2 mm deflection, we see that the load deflection relation is nearly linear. Location B is different for each test, but all instances occur below 0.2 mm of deflection without much variation. To simplify data reduction in the calculations, this instance was assumed to be at 0.2 mm of deflection and is denoted as 'Load 0.2 mm' or as 'Deflection 0.2 mm' depending on the value of interest. The most important data from these tests were the maximum load and deflection values. These are denoted as 'Load Final' or 'Deflection Final' and are indicated as Label C in Figure 4-1, which is the maximum of the test. This is where the sample failed and where the highest load value is measured by the Instron machine during the specimen's compression test. Label D is the point of test termination; this is where the machine or operator terminated the test after a steep decrease in load data following Label C. Label D is not important and does not appear in the presented datasets.

'Initial Failure' visually looks like the drop between Label C and Label D with less magnitude; however, it occurs between Label B and Label C. An example of an 'Initial Failure' is not depicted in Figure 4-1. 'Load Initial Failure' is the load at the first premature breakage of the specimen as the load increased; such breakage was less than the break detection of the Instron machine. Tests that demonstrated such initial failures were allowed to continue running until the maximum loading condition occurred. In several tests there were multiple early failures; however, only the first one, the lowest load where early failure occurred, was analyzed. 'Initial Failure' values were tracked with the goal of establishing a lower bound to the strength of the material. There is no

'Deflection Initial Failure' recorded since after any early failure, the maximum deflection values lose significance since it is not clear if the deflection recorded is due to actual deflection or a failure of the sample. This nomenclature is used consistently throughout the tables and figures.

The plot in Figure 4-1 is denoted as a complete plot since it includes the beginning, Label A, and continues until the termination, Label D, of the test. A majority of the figures presented are abridged and only show the start from Label B to the maximum at Label C. These figures are referred to in the plots as 'start to max.' Plots shown highlighting the importance of the initial failure are typically denoted as 'start to initial.'

Initial inspection of the data was performed to evaluate the quality and health of the data from each test. Each test figure can be found in Appendix A.3. Demonstrating the brittleness of the samples, multiple tests failed prematurely before reaching the maximum compressive load. These premature failures were easy to observe in the load vs. deflection plots, an example being test 5 with results shown in Figure 4-2. Of tests 1-8 for the low porosity set, three (tests 1, 3, & 6) ran to completion without an initial failure. One test (test 5) had one initial failure, and four tests (tests 2, 4, 7 & 8) had multiple premature failures. Of tests 9-17 of the high porosity set, three (tests 9, 12 & 13) ran to completion without an initial failure. Two (tests 11 & 14) had one initial failure, and three (tests 10, 15 & 16) had multiple premature failures. Because these initial failures were so common in the testing, two calculations were carried forward in the data analysis, one for the initial failure values, and one for the maximum failure values. The maximum failure values could be seen as the upper limit of the strength of the material if

a more refined and consistent manufacturing process were to be implemented. Both low and high porosity tests had five premature failures.

Figure 4-2 – A load vs. deflection plot for test 5, a low porosity test. Several samples exhibited an initial failure, clearly seen here at the initial peak at about 0.5 mm deflection. After the initial failure, the sample retains its integrity and was able to recover and withstand further loading until failing at the maximum load.
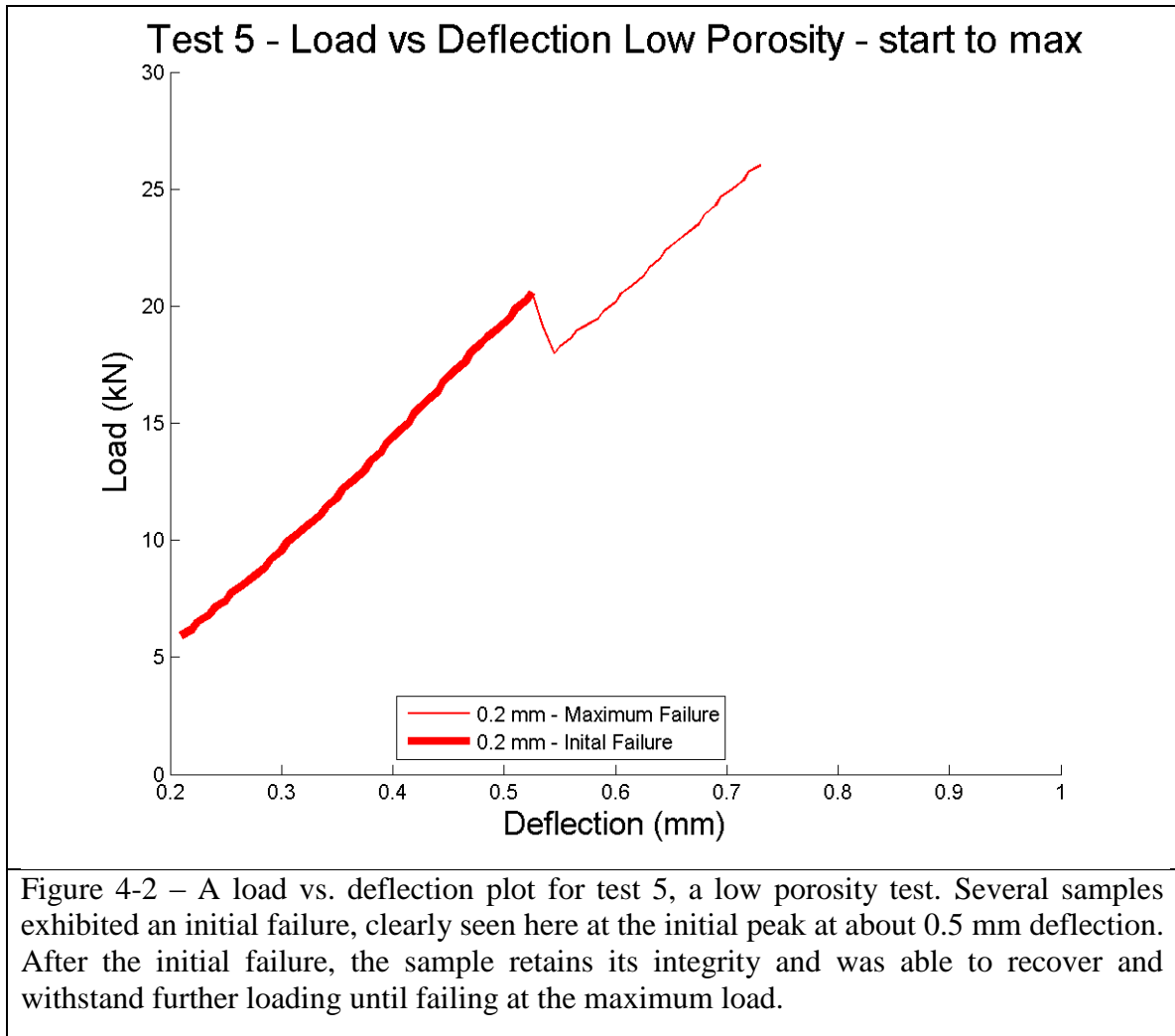
Investigating the effects of porosity on the loads and pressures achieved by each low and high porosity material is a key aspect of this research. Due to the initial failures of specimens during testing, the analysis could take on several stances since both low and high porosity data sets can include or ignore initial failures. The simplest approach to determine the effects of porosity is to average all the tests data regardless of the existence

of premature failures. The average maximum load for the low porosity data was 21.80 ± 5.02 kN, and 9.85 ± 4.16 kN for the high porosity data. The load achieved is unique to each sample and depended on the sample dimensions. This is a difference of about 12 kN between two porosity sets with only about 10% difference in porosity.

To take into consideration the dimensions of the samples, the average pressure should be calculated for more accurate comparisons. The average maximum pressure for the low porosity data was 202.23 ± 48.98 MPa, and 84.32 ± 36.98 MPa for the high porosity data. Here, a difference of about 118 MPa is observed. The low porosity material withstood over two times the pressure than the high porosity material. A direct and simple conclusion can be made that porosity does have a significant effect on the loads and pressures the sintered material was able to achieve. This was expected, but these results demonstrated how significant these differences can be.

For both the low and high porosity data sets, there were three tests that did not have initial or premature sample failures. From these tests without initial failures, the average maximum load withstood, or the 'Load Final,' was 25.31 ± 0.79 kN for the low porosity data and 11.68 ± 1.20 kN for the high porosity data. These values represent the highest loading withstood by the samples and, subsequently, the material. The averaged pressure withstood by the low porosity samples without initial failure was 237.166 ± 10.048 MPa and for the high porosity data without initial failure, 100.720 ± 10.511 MPa. It is interesting to note that the low porosity material withstood over two times the pressure than the high porosity material.

Inspecting the premature failure load data, there does not seem to be a correlation pointing to a common load that provoked an initial failure. Searching for a cause for the

premature failures, we considered the loading conditions. For both the low and high porosity data sets, five tests occurred with initial or premature failures of the sample. The 'Load Initial Failure' average for the low porosity data set was 19.689 ± 5.31 kN and 8.76 ± 4.87 kN for the high porosity data set. Loading ranges including the first standard deviation for both the low and high porosity data do not overlap, signifying there is no statistically significant load for which the samples should be expected to prematurely fail.

Just because a sample had a premature failure does not correlate to the sample reaching a significantly better or significantly worse maximum load value for either porosity set. There does not appear to be a relationship between premature failures and maximum loads achieved on a per test basis. For example, even though the low porosity specimen in test 5 experienced a premature failure at a high load, 20.57 kN, it was able to recover to a maximum load of 26.05 kN. This maximum load is comparable to that of test 1, 26.35 kN. Thus, sample 5 performed exceptionally well. Another low porosity specimen in test 2 reached about the same maximum load, 21.37 kN, as its premature failure load, 20.93 kN. An example from the high porosity sample set was the specimen of test 11, which was the best performing test in its set. Test 11 had a premature failure occur at 15.78 kN, which was less than 1 kN under its maximum load of 16.08 kN. Even after a premature failure, this specimen was able to achieve the best performance of the high porosity material, about 3 kN better than all other high porosity samples. Interestingly, *all tests in which initial failures occurred were still able to achieve the similar or greater maximum loads after the initial failure.* However, only in tests 5, 11 and 14 were the final load values able to match or exceed the final load values of their

non-premature failure counterparts. So more often than not, the tests without premature failures were still able to achieve the highest loads.

It was difficult to assess the magnitude of the premature failures for the samples during testing. No premature failures of the samples were all different and should not be expected to be the same. It is important to note that after an initial failure has occurred, the pressure distribution on the remaining sample is no longer known for certain. Two examples of sample premature failure can be seen in Figure 4-3. As an example, if a premature failure caused half of the sample to fracture and break away, the remaining cross-sectional area of the sample is now reduced to one half its original dimensions, effectively doubling the pressure on the remaining sample. After an initial failure occurred, the dimensional measurements of the sample are no longer known for certain, meaning that there is inaccuracy in the pressure calculations after a premature failure occurs. Premature failures can only weaken the sample and cause a reduction in load bearing material, effectively increasing the effective load, and subsequent the pressure, on the part of the sample remaining.

Test 3
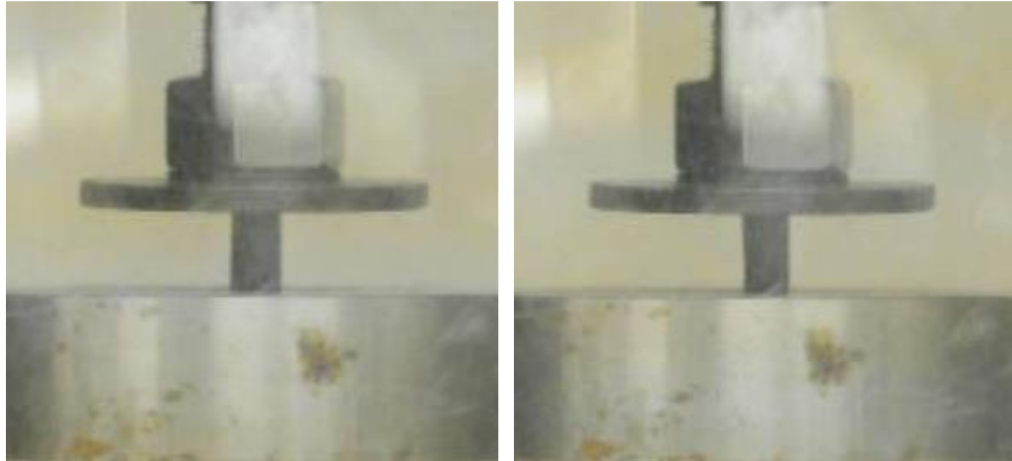
Test 5
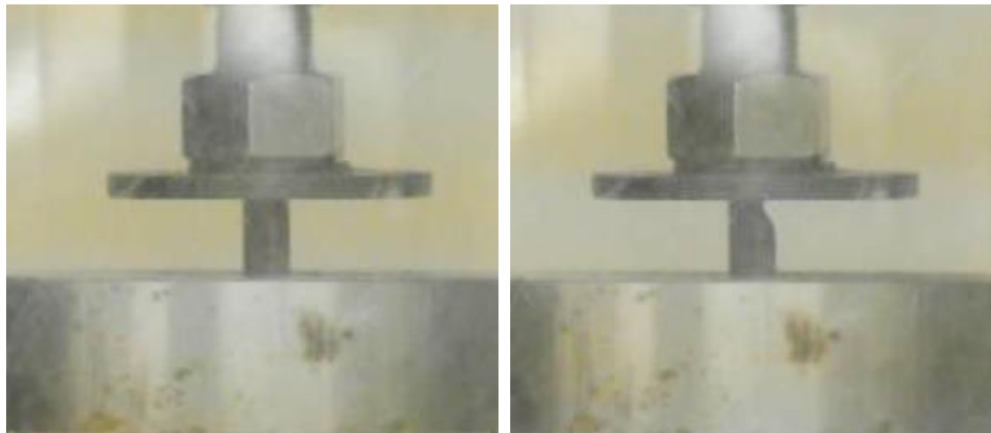
Figure 4-3 – Both image sets are from screenshots of video recorded for each test. The left images are before specimen failures and the right are after specimen failures. Looking at the top image set, at about 21 s into the video for test 3, a shard from the left flies off, and looking at the load and deflection plot for test 3, there is only a minor dip, not a negative deflection at about 0.4 mm. And for the bottom image set, at about 40 seconds into the video for test 5 a large fracture occurs at the upper right corner and flies off. This corresponds with the negative deflection at about 0.5 mm of the load and deflection plot for test 5.

Because of this, it should be expected that samples with premature failures should generally not reach the same maximum loading as un-fractured samples. In general, this was the case. The average final load for the three low porosity tests without initial failures was 25.31 ± 0.79 kN, and 11.67 ± 1.20 kN for the high porosity data set. Of the five low porosity tests with premature failures only test 5 was able to exceed the final average load set by the three non-premature failure low porosity tests. And for the five high porosity tests with premature failures, two tests, test 11 and 14, were able to exceed the final load average set by the three non-premature failure high porosity tests. Out of a total ten tests with premature failures, only three tests were able to exceed the load average set by the tests without premature failures. Still, six samples of both porosity grades experienced nominal compression tests without failing prematurely. Since the tests with initial failures were able to approach but not meet the maximum loads as those samples without initial failure, the manufacturing process, not the material itself, requires further investigation in order to control the quality of the sample produced. Again, even with premature failures, the low porosity material withstood over two times the pressure of the high porosity material. The results from the tests with premature failures provide evidence that *even though the material itself may be brittle, it can hold high compressive loads even after fracture.*

Pressures faced by the samples at failure were analyzed. As opposed analyzing the forces seen by each sample, calculating the pressure on the samples removes the minor dimensional differences across all of the samples. Making pressure more generalized for the material itself. Attempting to analyze the pressure experienced by the loads after an initial failure is difficult as mentioned above due to the unknown sample

dimensions after a premature failure. The averaged pressure at initial failure achieved by all the low porosity sample set was 176.570 ± 67.140 MPa and 76.717 ± 37.911 MPa for the high porosity data with initial failures. The averaged pressure at maximum failure achieved by the three low porosity samples without premature failures was 237.166 ± 4.558 MPa and 100.720 ± 10.511 MPa for the high porosity data. This is about a 35% pressure increase for the low porosity material between the average initial failure pressures, and the maximum obtainable pressure without initial failures, or about a 32% increase for the high porosity material. This is about a difference of about 61 MPa between the average initial and maximum failure for low porosity material and about a difference of 24 MPa for the high porosity material. The initial failures reduced the ability of ten specimens to reach their full potential before failing. These values for pressure are the most accurate values of pressure possible for the cumulative samples tested as the dimensions of the samples remained intact up to their failure. Less accurately due to sample dimensional information loss, the averaged pressure at maximum failure achieved by the low porosity sample set with initial failure was 181.302 ± 51.058 MPa and 74.479 ± 43.162 MPa for the high porosity data with initial failures. The average maximum failure pressure is about 56 MPa different between the data sets of with and without initial failures for low porosity material. For the high porosity material of the same comparison, this difference is about 27 MPa. However, it is once again important to note that these pressure deltas should be expected to be reduced if the actual sample dimensional information was known after the initial failure.

An investigation of the deflection data for both low and high porosity sintered lunar simulant was also performed. Final deflection values for tests without initial

failures denote the maximum compression of the samples. Table 4-1 summarizes loads and deflections for the low porosity data and Table 4-2 for the high porosity data. The average deflection at final loading for the low porosity data was 0.643 ± 0.034 mm and 0.463 ± 0.041 mm for the high porosity data. The specimen that experienced the greatest deflection without encountering an initial failure was a low porosity sample, test 6, which deflected 0.670 mm. The largest deflection without initial failure seen by the high porosity samples was test 9 which underwent 0.520 mm of deflection before maximum failure. On average, the low porosity material was able to sustain higher compression loads and deflection before failure than the high porosity material.

Low Porosity, < 212 μm						
Test Number	Load Initial (kN)	Load 0.2 mm (kN)	Load Intial Failure (kN)	Load Final (kN)	Deflection Initial (mm)	Deflection 0.2 mm (mm)	Deflection Final (mm)
1	0.06	5.91	-	26.35	0.205	0.595	0.595
2	0.62	6.25	20.93	21.37	0.205	0.530	0.655
3	0.33	4.84	-	24.43	0.210	0.665	0.665
4	0.01	3.59	15.17	20.08	0.205	0.470	0.590
5	0.56	5.93	20.57	26.05	0.210	0.525	0.730
6	0.27	3.98	-	25.15	0.205	0.670	0.670
7	3.71	11.22	15.98	21.03	0.205	0.345	0.575
8	0.21	2.40	3.21	9.92	0.200	0.265	0.925
Mean	0.72	5.52	18.97	21.80	0.206	0.508	0.643*
STD	1.15	2.49	7.08	5.02	0.003	0.135	0.034*
Variance	1.32	6.20	50.10	25.24	0.000	0.018	0.002*

*Only includes values from tests without intial failues, tests 1, 3 and 6

Table 4-1 – Table of loads and deflections for all low porosity tests.

High Porosity, > 212 μm						
Test Number	Load Initial (kN)	Load 0.2 mm (kN)	Load Initial Failure (kN)	Load Final (kN)	Deflection Initial (mm)	Deflection 0.2 mm (mm)	Deflection Final (mm)
9	0.19	2.59	-	10.76	0.205	0.520	0.520
10	0.06	0.77	3.32	4.38	0.205	0.580	0.775
11	1.50	8.95	15.78	16.08	0.200	0.355	0.375
12	0.24	4.74	-	10.90	0.210	0.425	0.425
13	1.26	5.35	-	13.37	0.200	0.445	0.445
14	0.84	6.21	8.91	13.12	0.205	0.285	0.405
15	0.30	1.72	4.92	5.23	0.200	0.450	0.590
16	0.20	2.34	3.74	4.99	0.205	0.330	0.495
Mean	0.57	4.08	8.96	9.85	0.204	0.424	0.463*
STD	0.52	2.55	4.31	4.16	0.003	0.092	0.041*
Variance	0.27	6.51	18.54	17.34	0.000	0.008	0.003*

* Only includes values from tests without intial failues, tests 9, 12 and 13

Table 4-2 – Table of loads and deflections for all high porosity tests.

Computing stress, strain and elastic moduli is the next step in quantifying the material properties.

4.2 Stress, Strain and Modulus of Elasticity

Of great importance to any material property investigation is an understanding of how well a material can handle and recover from stress and strain. Stress is measured in force per unit area whereas strain is a dimensionless value. The sintered lunar simulant specimens tested were more similar to ceramic materials, which typically fail due to small defections, than metals, which allow greater material deformation. No measurement device was available during testing to measure cross-sectional area change, but that was not a concern since the brittle nature of ceramics typically allow for minimal cross-sectional deformation before failure. Because of this, the difference in area is

expected to be minimal, and making engineering stress and engineering strain values relevant calculations.

Closely related to stress and strain, the modulus of elasticity was also determined. The modulus of elasticity is a measure of the material stiffness and expressed in terms of force per unit area. Experimentally, the modulus of elasticity can be calculated by the ratio of the stress over the strain calculated from sample testing.

Engineering stress Equation (1) and engineering strain Equation (2) were calculated using the common relations below. The modulus of elasticity, E, was calculated after rearranging Equation (3) from the linear best fit for each data set.

$$\sigma = \frac{F}{A} \qquad \textbf{(1)}$$

$$\varepsilon = \frac{\Delta L}{L} \qquad \textbf{(2)}$$

$$\sigma = E\varepsilon \qquad \textbf{(3)}$$

Stress and strain for the duration of the test was calculated for each sample. This used the averaged sample dimensions measured prior to testing as the initial lengths. Plots of the stress and strain calculations on a per test basis are available in Appendix A.5. A plot of the calculated stress strain relationship from test 1 can be seen in Figure 4-4.

Figure 4-4 – A stress vs. strain plot for the first test conducted. Sample 1 exhibited textbook behavior for a ceramic type material; the initial load ramping of the sample can be seen in the saw tooth segment below the 0.01 strain.
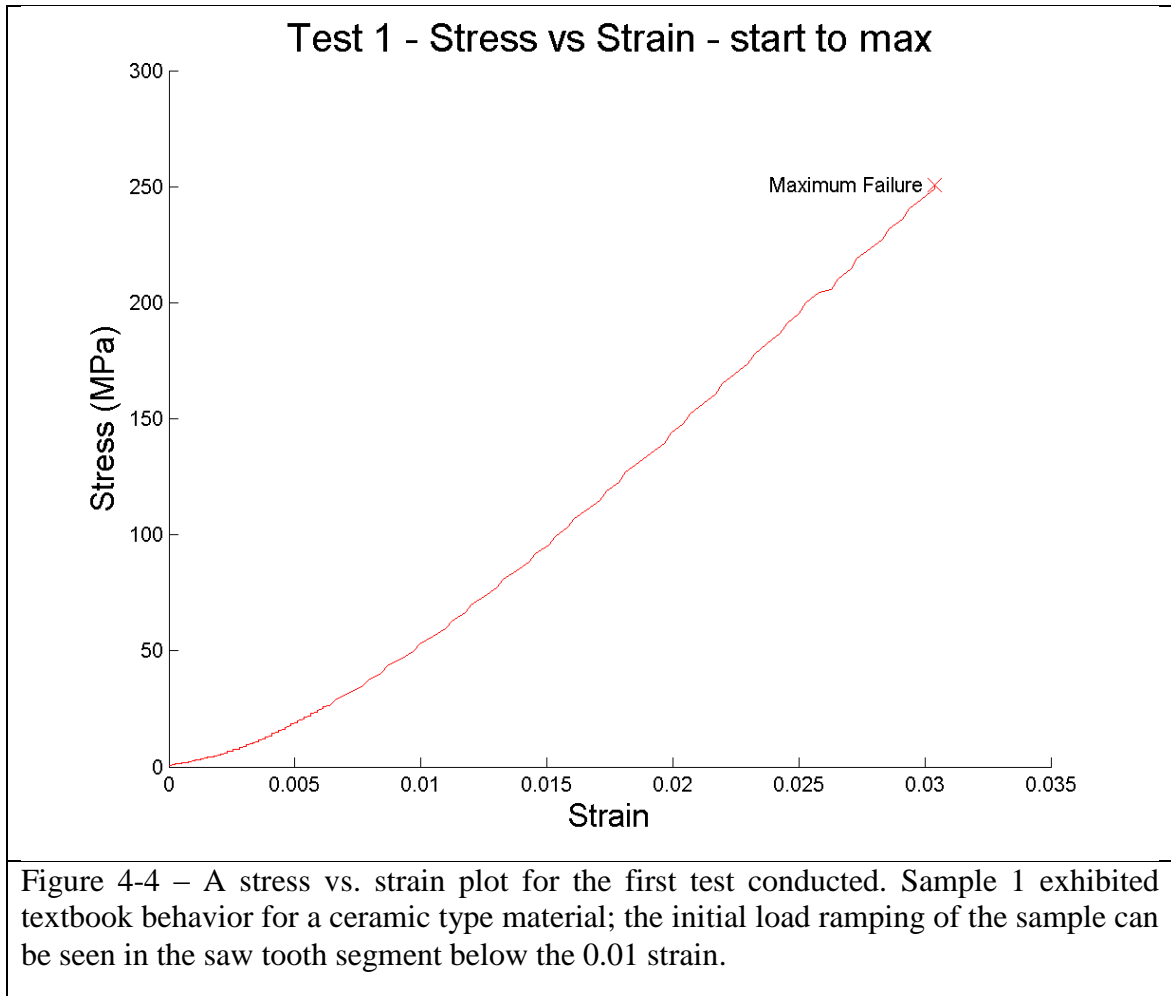
Several tests exhibited repeated premature sample failures before reaching their maximum compressive strengths. Figure 4-5 displays examples of these premature failures and labeled as 'Local Failure' in the stress strain plot. For computing the modulus of elasticity, several tests were removed due to poor stress strain data. The maximum failure point is identified as well as local failure points where appropriate.

Figure 4-5 – A stress vs. strain plot for test 7. Several tests demonstrated multiple premature failures of the sample before continuing to maximum failure. This plot is cut to display only data between the initial load ramping of the sample, the first 0.02 mm of compression, to the maximum failure of the sample.
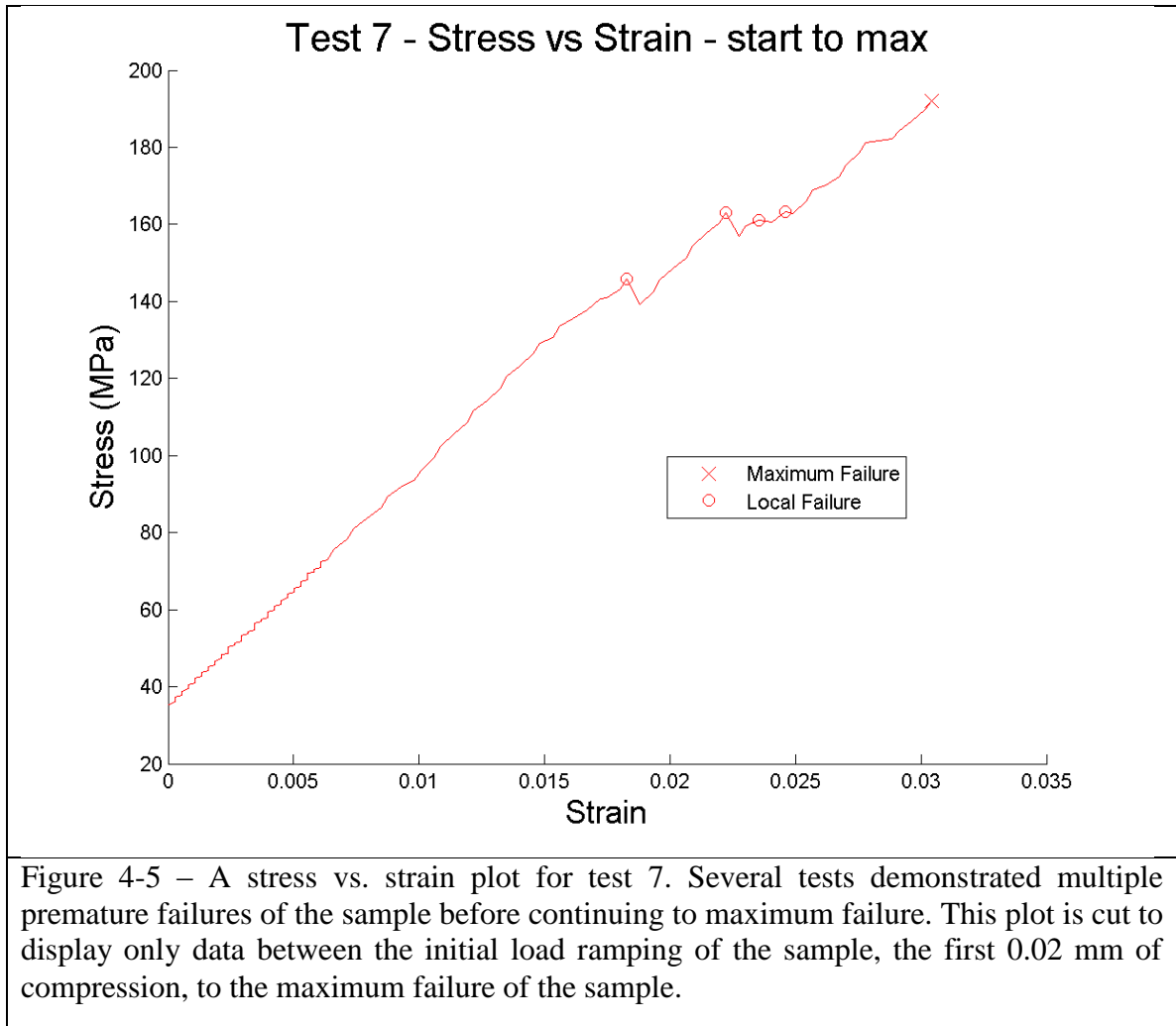
To calculate the modulus of elasticity for the samples, the slope of the stress strain line is calculated for each test. If no initial failure occurs, the maximum failure is used. Tests 7, 8, 10, 15 and 16 were removed from this calculation due to failures and poor stress strain data. This left six tests from the low porosity data set, and four tests from the high porosity data set. Shown in Table 4-3 are the calculated linear best-fit equations for each test.

Test 1	$y = 9841x - 51$	(4)
Test 2	$y = 8058x - 30$	(5)
Test 3	$y = 7924x - 45$	(6)
Test 4	$y = 8365x - 53$	(7)
Test 5	$y = 8525x - 42$	(8)
Test 6	$y = 7433x - 60$	(9)
Test 9	$y = 4477x - 25$	(10)
Test 11	$y = 6882x + 5$	(11)
Test 12	$y = 5203x - 13$	(12)
Test 13	$y = 5384x - 13$	(13)
Test 14	$y = 5430x - 5$	(14)

Table 4-3 – Linear stress vs. strain equations per test. Tests 1 through 6 were from the low porosity data. Tests 9 through 14 were from the high porosity data.

Figure 4-6 is an example of a test with the best-fit line and data-fitted equation. A plot of the best-fit line for each test can be found in Appendix A.7. Note that only the data in the highlighted blue region was used to calculate the slope. The results from the slope of each stress strain equation were averaged and standard deviations calculated. The low porosity modulus of elasticity was calculated to be 8358 ± 748 MPa and the high porosity sets modulus of elasticity calculated to be 5475 ± 782 MPa.

Figure 4-6 – A stress vs. strain plot for test 2 shown with the linear best fit line after the ramping and before the initial failure of the sample.
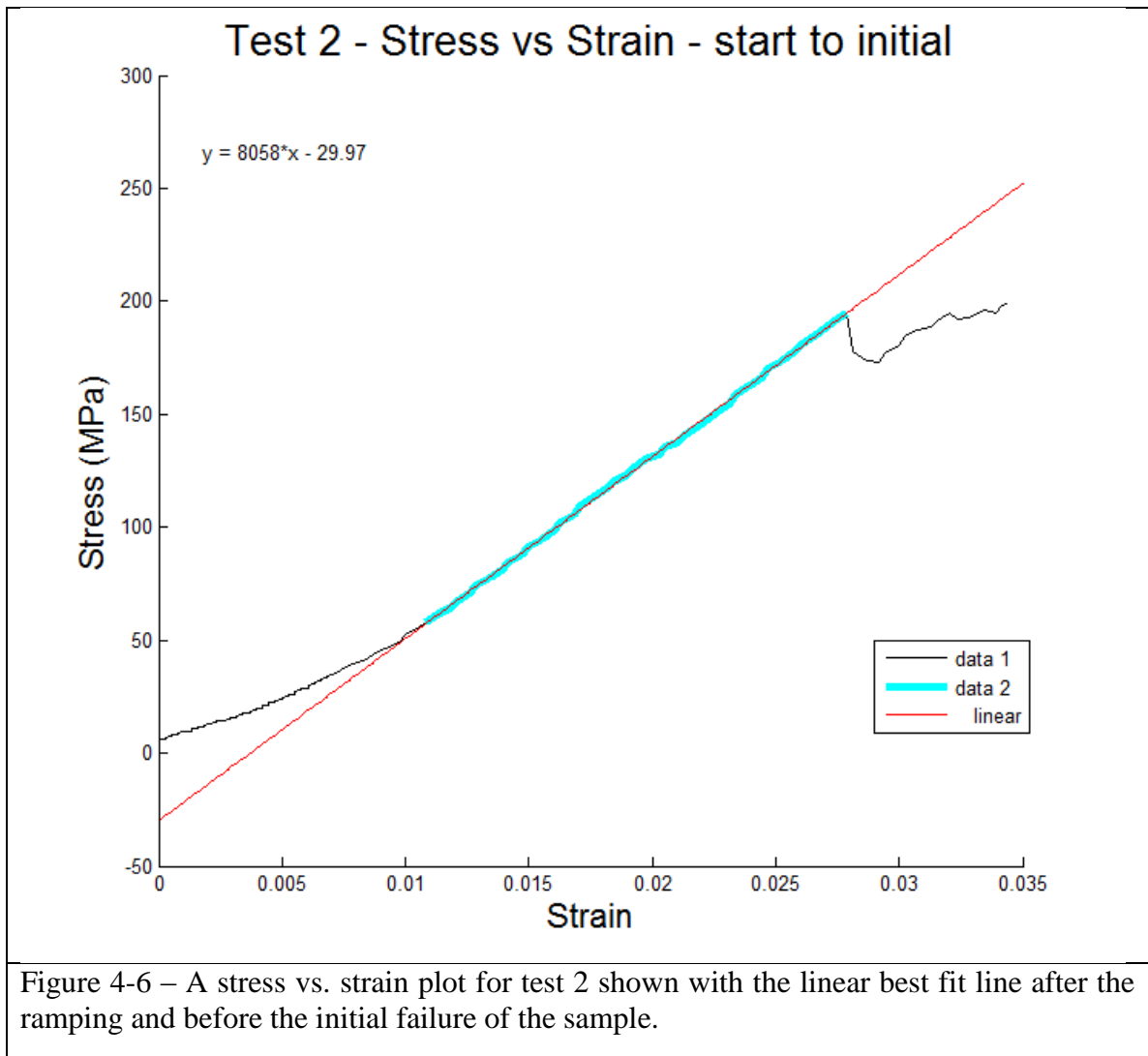
Additional mechanical material properties can be determined from stress and strain. By calculating the area beneath the stress strain plots, the mechanical material property toughness can be determined.

4.3 Toughness

Material toughness describes a material's ability to absorb energy and resist fracture. Tough materials can absorb a considerable amount of energy before fracture while brittle materials absorb very little. Toughness is not a single property but rather a

combination of strength and ductility. Materials with high yield strength and high ductility have high toughness. The toughness of a material can be determined by integrating the area under its stress-strain curve before fracture, as per Equation (15), where σ is stress, ϵ is strain and ϵ_f is the strain at failure. The energy of mechanical deformation per unit volume up to material fracture has units of joules per meter cubed.

$$\int_0^{\epsilon_f} \sigma \, d\epsilon = \frac{energy}{volume} \qquad (15)$$

Specifically for this testing the integration was performed numerically via the trapezoidal method in Matlab using the 'trapz' function. The stress strain data was used per test from the start of the ramping until the initial failure of the specimen. An example plot is shown in Figure 4-7 using test 1, with other tests shown in Appendix A.6. The early ramping region is expected to add a trivial amount of inaccuracy in the computed toughness values.

Figure 4-7 – Area under the stress vs. strain plot was calculated using numerical integration to provide the material toughness.
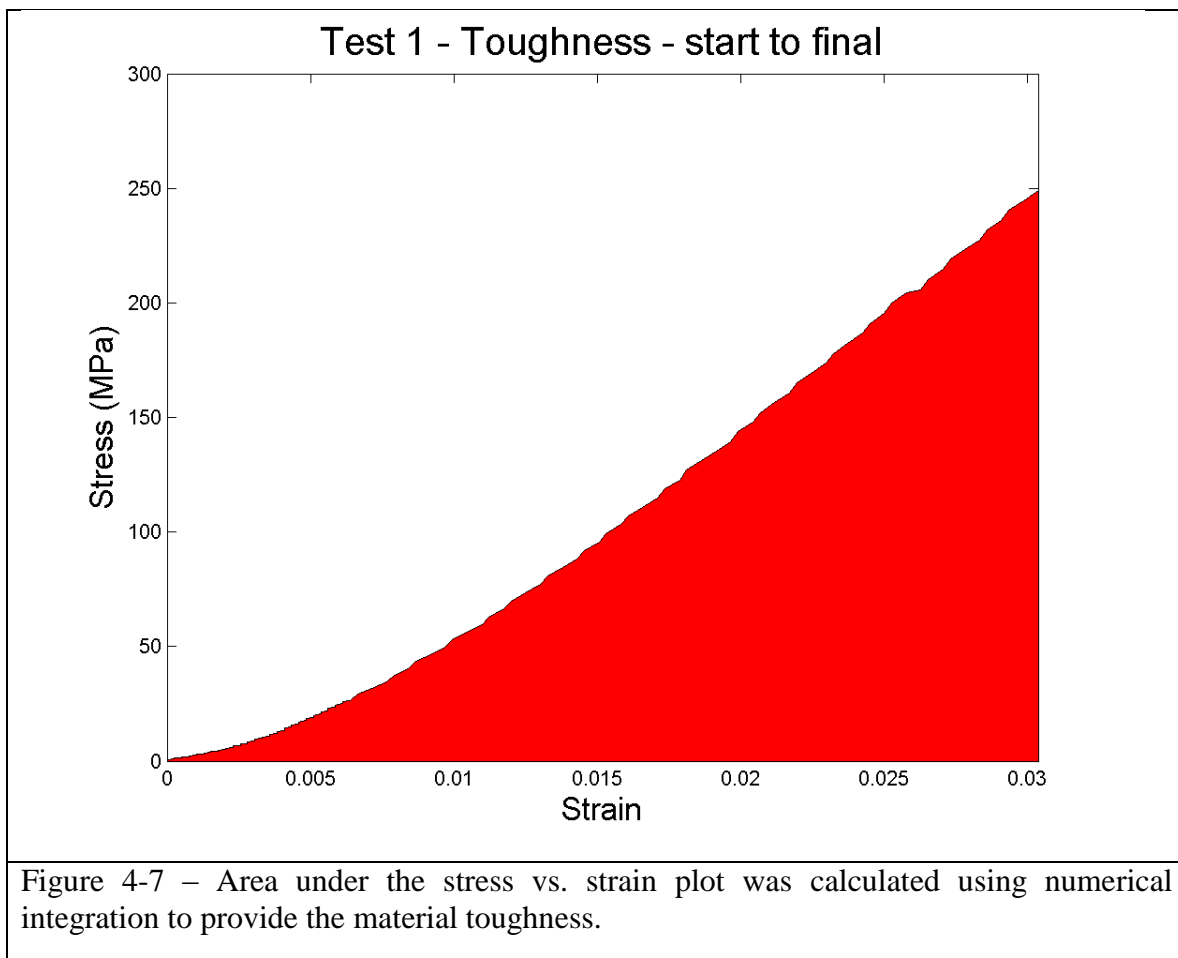
The calculated toughness values for each test are shown in Table 4-4. Averages with standard deviation for the error were calculated for both data sets. The low porosity data calculated average was 3.2 ± 0.9 MJ/m^3 and the high porosity data average was 1.0 ± 0.3 MJ/m^3. These results are not surprising. The low porosity samples were able to withstand higher loading conditions. What is interesting is that the low porosity samples demonstrated three times the toughness than the high porosity data.

The samples without initial failure and the greatest deflection and load ratio respectively was test 6, this is the second highest toughness value after test 5, which did incur an initial failure. For the high porosity tests, sample 11 had the greatest calculated toughness. Test 13, which did not experience an initial failure, had the second highest

toughness value of the high porosity data. Test 1 showed the greatest load bearing capacity but also the lowest deflection of the three low porosity non-initial failure tests. Sample 5 experienced the second highest loading of all the samples tested, but achieved the highest calculated toughness.

Toughness			
Test	MJ/m^3	Test	MJ/m^3
1	**3.2**	**9**	**1.1**
2	3.7	10	0.7
3	**3.4**	11	1.5
4	2.2	**12**	**1.0**
5	4.3	**13**	**1.3**
6	**3.8**	14	1.2
7	3.7	15	0.7
8	1.5	16	0.6
Mean	3.2		1.0
STD	0.9		0.3

Table 4-4 – Comparison of calculated toughness per test. The average for the low porosity data was 3.2 MJ/m^3 and 1.0 MJ/m^3 for the high porosity data. Bold test numbers and values indicate tests that performed without initial failures.

Material toughness is typically used to evaluate the ability of a material to withstand an impact. For lunar applications this would most likely take the form of meteoritic impacts.

4.4 Compressive Strength

Compressive strength is defined as the strength at which the sample fails. The mode of failure may be either brittle or plastic and corresponds to a dramatic increase in

strain given a small change in stress. Compressive strength is calculated by dividing the maximum load by the original cross-sectional area of a specimen in a compression test. Ultimate failure was the maximum load the sample could withstand, even if there was an initial failure. The low porosity samples showed about a 13% increase in compressive strength from the initial failure to the maximum failure. The high porosity samples demonstrated a 9% difference. With a refined manufacturing process, these initial failures should be fewer in sample testing.

Additionally the difference between 'all data' and 'best data' is that 'all data' includes all the samples of that set, whereas 'best data' only includes samples in that set that did not show an initial failure. Results showing the sample values for compressive strength are seen in Table 4-5. Of interest are the compressive strength values of the low porosity samples. An average compressive strength of the entire low porosity data set was 202.3 MPa (s=49, n=8). Samples without an initial failure in testing averaged 237.2 MPa (s=10.0, n=3). The highest compressive strength obtained was from sample 1, 250.6 MPa, and the lowest was from sample 8, 86.5 MPa. The set of high porosity samples proved to be more brittle and withstood a lower load than its sibling samples, however, the compressive strength values were still quite high. The average compressive strength of the entire high porosity data set was 84.3 MPa (s=39, n=8). Samples without an initial failure in testing averaged 100.7 MPa (s=10.5, n=3). The highest compressive strength obtained was from sample 11: 138.9 MPa and the lowest was from sample 16: 41.7 MPa. *It is worth noting that the worst performing low porosity sample performed better than the average high porosity sample set.*

		Compressive Strength			
		Initial Failure (MPa)	Initial Failure (ksi)	Max Failure (MPa)	Max Failure (ksi)
All Data (n=8) **Low Porosity**	**Mean**	**176.6**	**25.6**	**202.3**	**29.3**
	STD	67.1	9.7	49.0	7.1
	COV	0.4	0.4	0.2	0.2
	Variance	4,508	95	2,399	50
All Data (n=8) **High Porosity**	**Mean**	**76.7**	**11.1**	**84.3**	**12.2**
	STD	37.9	5.5	37.0	5.4
	COV	0.49	0.49	0.44	0.44
	Variance	1,437	30	1,367	29
Best Data (n=3) **Low Porosity**	**Mean**			**237.2**	**34.4**
	STD			10.0	1.5
	COV			0.04	0.04
	Variance			101	2
Best Data (n=3) **High Porosity**	**Mean**			**100.7**	**14.6**
	STD			10.5	5.6
	COV			0.10	0.38
	Variance			110	2

Table 4-5 – Summary table of compressive strength at initial failure and maximum failure for all samples tested.

The compressive strength values from the samples tested hold more significance when compared with the more common terrestrial structural materials as well as with better understood lunar concretes. Another appropriate comparison of sintered simulant is with basalt, as it is plentiful on the lunar mare regions. Basalt is also hailed as one of the strongest igneous rocks. Since the tested sintered lunar regolith simulant is also comprised mostly of basalt, the Dresser Basalt values can be seen as an expected upper strength limit for this sintered medium. Shown in Table 4-6 are the compressive strengths and selected tensile strengths for three grades of concrete, three common rocks and two proposed and tested lunar concretes.

Comparisons between Table 4-5 with Table 4-6 can be made. The strongest sample set, the low porosity samples, was able to reach 82% of the compressive strength of Dresser Basalt. We can also see from the Table 4-6 that concrete has a high range of compressive strengths, from 17 MPa (2500 psi) for residential concrete, to 28 MPa (4000 psi) for commercial structures, and to higher compressive strengths up to and exceeding 70 MPa (10,000 psi). The compressive strength of the single best low porosity sample, sample 1, is very strong in comparison to concrete. Sample 1 was able to achieve almost 15 times the compressive strength of terrestrial residential concretes. Even the worst performing individual high porosity sample, sample 16, was able to achieve almost 2.5 times the compressive strength of terrestrial residential concretes. Comparing the single best low porosity sample, sample 1, to lunar concrete showed the low porosity material was almost 3.5 times stronger. These results suggest that sintering is a viable option for high strength applications of lunar construction.

While tensile testing was not conducted, it would not be expected that sintered lunar regolith would have a high tensile strength. Ceramics, concretes and rocks are typically brittle materials, and as seen in Table 4-6, all the tensile strength values are relatively low in comparison to their compressive strength. Hence, sintered lunar regolith would be suitable for compressive loads; however, tensile loading could be investigated further if it is anticipated that sintered regolith can be reinforced.

	Compressive Strength		Tensile Strength	
	(Mpa)	(psi)	(Mpa)	(psi)
Lunar sulfur concrete[1]	31	4,500	-	-
Lunar concrete[2]	74	10,000	8.3	1200
Terrestrial concrete (residential)[3]	17	2,500	-	-
Terrestrial concrete (commercial)[3]	28	4,000	-	-
Terrestrial concrete (high strength)[3]	70	10,000	-	-
Kasota Sandstone[4]	102	14,750	6.3	915
Morton Granite Gneiss[4]	194	28,200	14	2,040
Dresser Basalt[4]	306	44,500	17	2,485

Houssam[1], Lin[2], National[3], Bridgeford[4]

Table 4-6 – Comparative compressive strength and tensile strength values for terrestrial concrete, lunar concrete and rock.

One of the key goals for this research project, again, was to investigate the effects of porosity on the sintered lunar simulant. Evaluating its compressive strength as a function of porosity provides interesting results in the next section.

4.5 Compressive Strength as a Function of Porosity

For sintered materials, porosity is a contributing factor to material strength. For the two sample sets analyzed, there was about a 10% difference in porosity caused by the manufacturing process. The high porosity samples had a porosity of 11.78 ± 3.30% and the low porosity samples 1.44 ± 1.91% porosity. To determine an upper and lower bound of compressive strength related to porosity, averages and standard deviations of these two data sets were calculated and linearly extrapolated. Initial and maximum failures of the samples were evaluated to gauge the upper and lower bounds of the material strength. Some of the initial failure data points are the same as the maximum data points since some samples did not have an initial failure, therefore being a better test specimen. Figure

4-8 shows the relation between compressive strength and porosity for initial failures of the samples.

Figure 4-8 – Porosity vs. compressive strength with all 8 data points per porosity shown. The dashed lines denote first standard deviations.
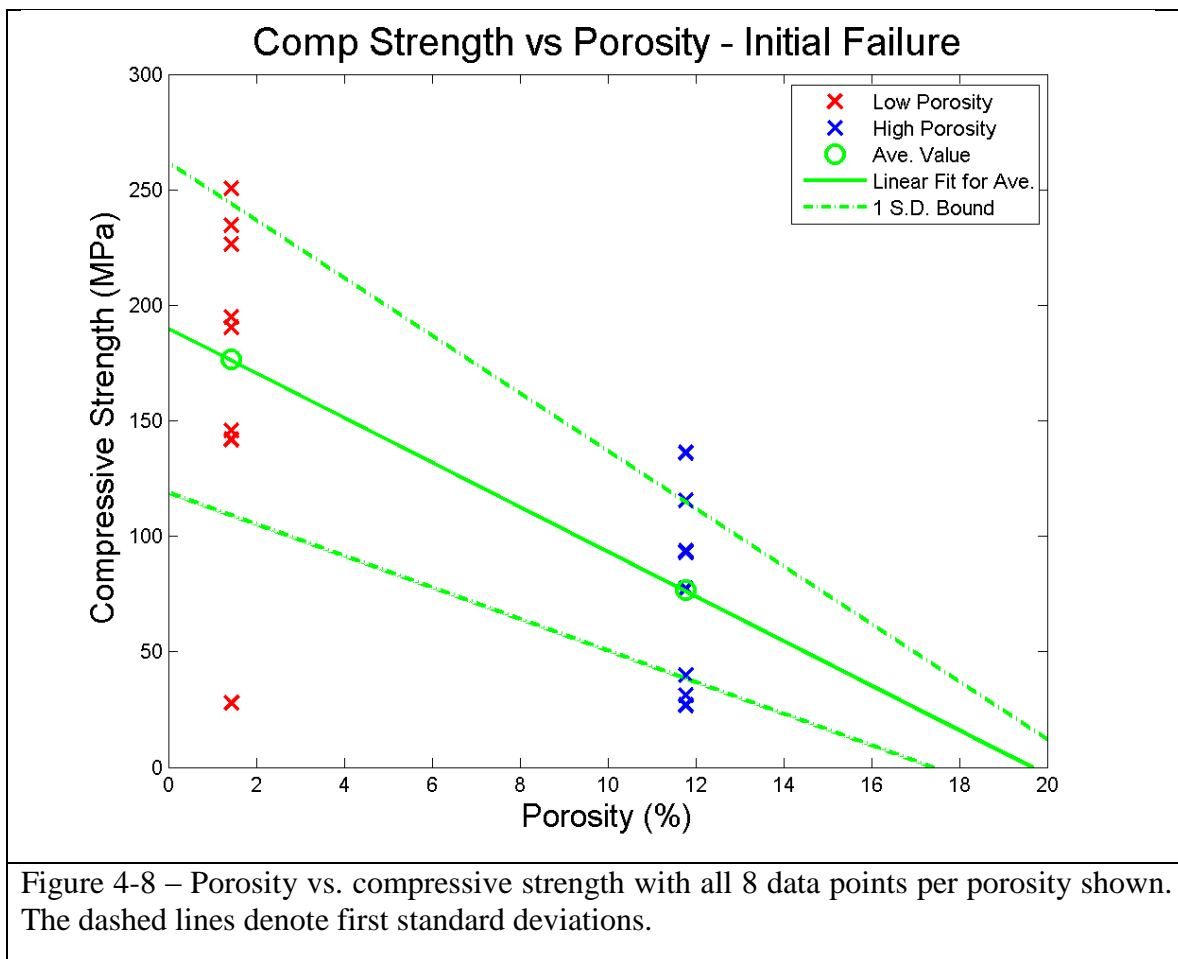
Mean values for both the low and high porosity data sets are calculated and shown with a linear fit. The extrapolated bound of the standard deviation of the data set is also displayed. The high porosity values produced more data points outside the first standard deviation bounds. This can be attributed to the greater brittleness of the high porosity material. The low porosity data set by comparison has a larger range of values, mainly attributed to the test 8 initial failure value at 28 MPa. Neglecting the 28 MPa value, the range of the low porosity data set becomes 108 MPa, this is closer to the high porosity

range of 88 MPa. Figure 4-9 shows the relation between compressive strength and porosity for maxium failures of the samples. The low porosity data set again suffers from the one outlier due to test 8 at 87 MPa. Still, the low porosity data sets had a higher compressive strength in both cases of initial and maximum failure.

Figure 4-9 – Porosity vs. compressive strength with all 8 data points per porosity shown. The dashed lines denote the first standard deviations.
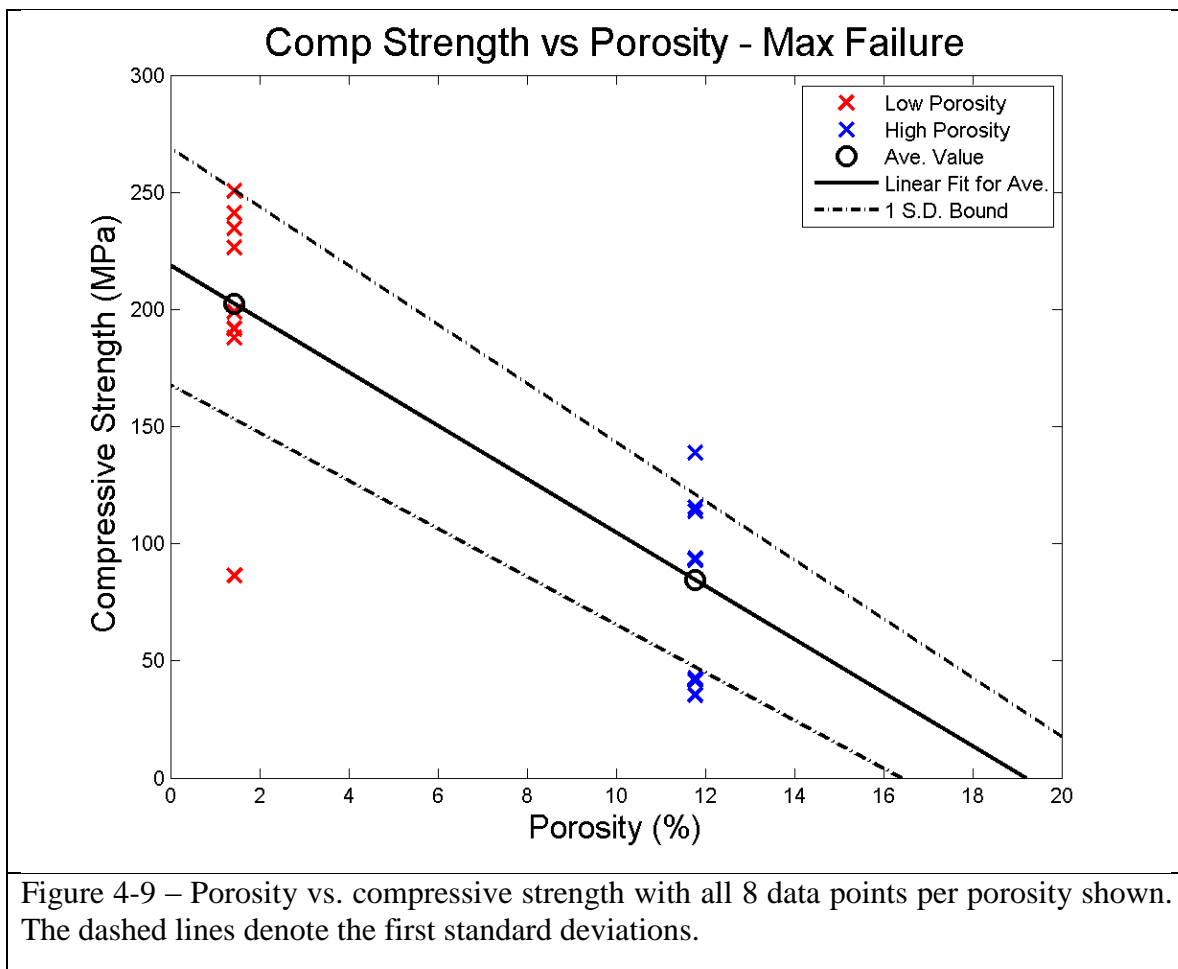
Computed from these two figures were the linear fits of the mean values and the standard deviation bounds. Equation (16) in Table 4-7 is the equation of the linear fit of the average values of the high and low porosity data sets for initial failure. The upper first standard deviation line for initial failure is given by Equation (17). Equation (18) is the equation for the lower first standard deviation for initial failure line.

Equation (19) in Table 4-7 is the equation of the linear fit of the average values of the high and low porosity data sets for maximum failure. The upper first standard deviation line for maximum failure is given by Equation (20). Equation (21) is the equation for the lower first standard deviation for maximum failure line.

$y = -9.66x + 190$	(16)
$y = -12.48x + 262$	(17)
$y = -6.829x + 1119$	(18)
$y = -11.40x + 219$	(19)
$y = -12.58x + 269$	(20)
$y = -10.24x + 168$	(21)

Table 4-7 – Equations (16) through (18) are for the compressive strength lines for initial failures. Equations (19) through (21) are for the compressive strength lines for maximum failure.

These equations are plotted in Figure 4-10, where we see an overlap. The trending of these equations is as expected, with the initial failures having lower mean values than the maximum failures. Graphically it is observable how close the initial and maximum mean failures of the high porosity data sets are. Also of interest is the close proximity of the first standard deviation upper bound. That both the initial and maximum failure linear equations share a very similar slope attest to the consistency of upper range of failure values. The lower bounds have more conflicting lines as expected since it is more common for a sample to fail prematurely as opposed to fail at an unusually high value.

Figure 4-10 – Porosity vs. compressive strength, matching color and matching dashed lines per initial and maximum failure data set.
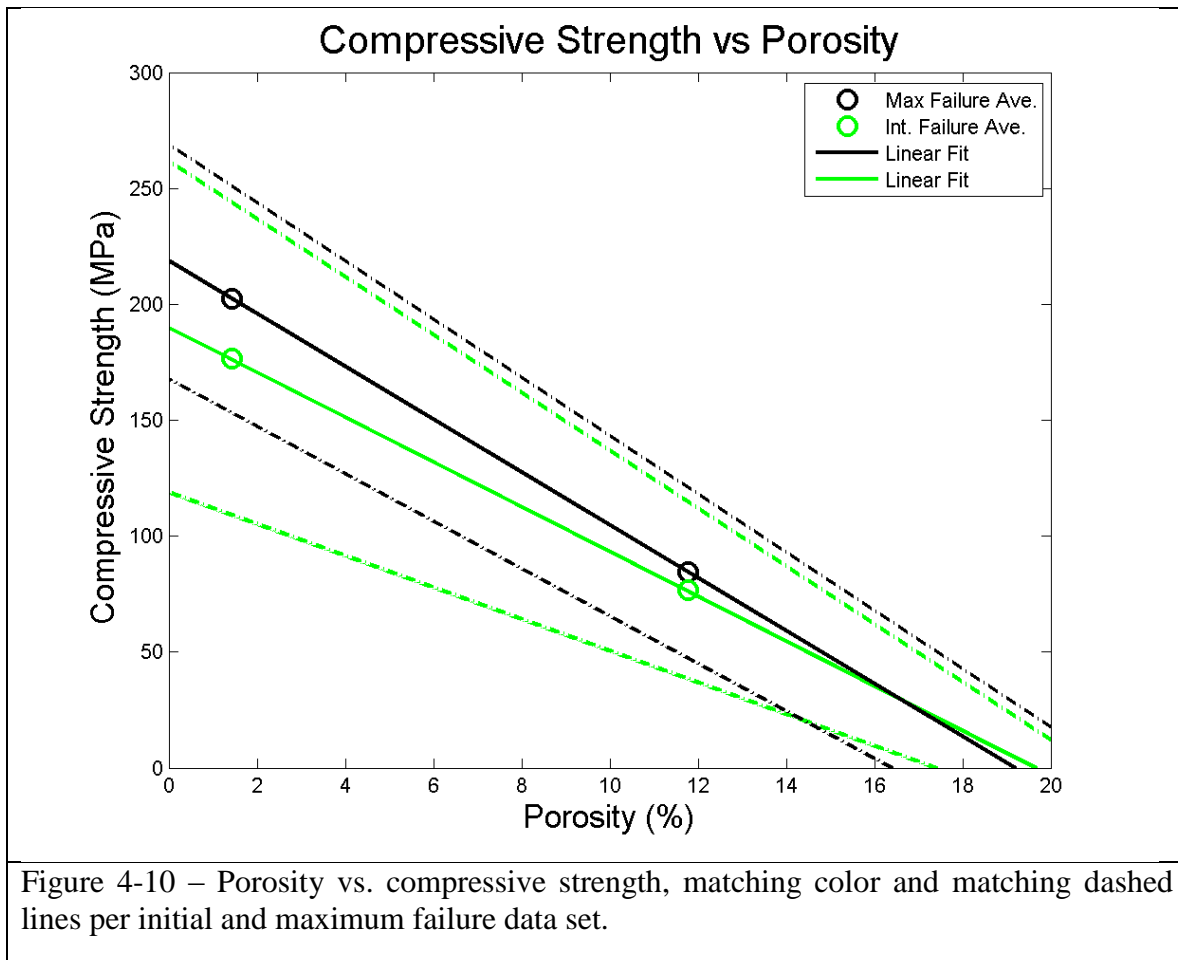
Investigating the upper bound of porosity at 0%, a solid material, we can compare with solid basalt since it is a major component of the JSC-1A simulant. Extrapolating the best-fit equation provides a 0% porosity compressive strength of about 190 ± 72 MPa for the initial failure data set, and an approximate value of 219 ± 51 MPa for the maximum failure data set. The value measured by Bridgford and Eustes (1999) for Dresser Basalt was 306 MPa. This extrapolated 0% porosity value is below the Dresser Basalt value but within two standard deviations.

Since porosity affects the structural quality of the sintered lunar simulant, there may be geographic limitations to where sintered lunar regolith could be manufactured on the Moon. The sample's achieved porosity is a function of the gain size of the lunar simulant used. This is an important observation as it is possible that different regions of the Moon contain higher concentrations of fine or large grained regolith. Fortunately, data returned from the Apollo missions provide insight into regolith particle size, and analyses of Lunar Reconnaissance Orbiter (LRO) data have provided regolith depth estimates across the lunar surface.

Table 4-8 shows a breakdown of grain size fractions of two lunar samples. Sample 71061,1 was a typical Apollo 17 mare soil and sample 72441,7 a typical South Massif soil, taken from the "light" mantle deposit. Taken as example regolith particle size distributions, it is possible to approximate the ratio of high and low porosity sintered material that could be found at each sample site. The high porosity material was sieved particles greater than 215 µm with the low porosity material being less than 215 µm. Since a higher resolution breakdown of particle size is not available, for this analysis the weight percentage of 150-250 µm will be conceded to the greater than 215 µm category. For sample 71061,1 a total 50.24% of particles were below 150 µm in size, with 40.61% being greater than 150 µm. For sample 72441,7, 71.66% of particles were below 150 µm in size, with 24.36% being greater than 150 µm. At both sites, over 50% of the material sampled was greater than 215 µm particle size. With sample 72441,7 being over 71.66% comprised of the less than 215 µm particles. At both of the sample sites, there is a greater proportion of higher quality raw regolith from which to produce the higher strength, low porosity sintered material.

	Weight % of Total Sample for Each Size Fraction									
Sample	<20 μm	20-45 μm	45-75 μm	75-90 μm	90-150 μm	150-250 μm	250-500 μm	0.5-1 mm	1-2 mm	2-4 mm	4-10 mm
71061,1	17.98	12.21	8.39	3.00	8.66	7.04	7.08	3.44	6.15	6.74	10.16
72441,7	25.84	18.79	12.00	4.01	11.02	8.37	8.55	x	3.67	2.76	1.01

Table 4-8 – Lunar sample particle size distribution sorted by weight percentage. This information was from p289-p290 of the *Lunar Sourcebook* by Heiken et al. (1991).

Part of premise for using sintered lunar regolith as a structural material is that there will be plentiful amounts of lunar regolith to harvest and process. A problem could arise if structures depended on ISRU lunar regolith were to be constructed in regions deprived of, or with a minimum of, regolith. The regolith depths across the lunar surface were calculated by Nickerson et al. (2011) and Bart et al. (2011). Using 143 different images from the Lunar Reconnaissance Orbiter Camera (LROC) and the Narrow Angle Camera (NAC) on LRO, regolith depth estimates were made. The maximum image size from LRO imagery is 2.5 x 26 km and it is possible to resolve meter-level detail. From these calculations, the median regolith depth in each region imaged ranges from 2.5 m to 8.7 m in depth. The shallowest lunar regolith depth occurs on the Moon's nearside maria. The Moon's far side and higher latitude regions showed the deepest lunar regolith.

The Apollo 17 landing site was at the Taurus-Littrow Valley on the eastern edge of Mare Serenitatis. This location was not directly measured for regolith depth by Nickerson et al. (2011) or Bart et al. (2011) but can be inferred by interpolation from their data. Using the known location of the Apollo 17 landing site, the regolith depth expected could be around 4 to 5 m. Combined with the previously discussed knowledge that regolith grain size in this region is favorable for producing low porosity sintered material, ample high quality sintered lunar regolith could be expected to be produced at

this site. Alternative locations would of course need to be evaluated further for regolith grain size and regolith depth to be able to reach the same conclusion.

4.6   Compressive Strength Histograms

Ideally, material properties are derived by testing a large number of samples, typically through destructive testing. Taking the mean and standard deviations of this large data set then defines the material properties. Due to the labor intensive nature of destructive testing, manufacturing a large quantity of samples for compression testing was not an option for this research project. Instead, our research plan required a small number of samples to be tested and analyzed. With the understanding that the sixteen total tests conducted would need to represent a larger number of samples, several histograms were constructed to understand the frequency of the compressive strength values measured.

From compression data collected on the 16 samples, four data sets were investigated using histograms: high porosity samples at maximum failure, high porosity samples at initial failure, low porosity samples at maximum failure and low porosity samples at initial failure. Additionally to these individual sets, a combined set of all initial failures and all maximum failures were also considered. All the histograms constructed used bins of 10 and ranged from the individual data sets minimum and maximum value. Table 4-9 shows the raw compressive strength data used to construct the histograms.

Compressive Strength					
Low Porosity, < 212 μm			High Porosity, > 212 μm		
Test Number	Initial Failure (MPa)	Maximum Failure (MPa)	Test Number	Initial Failure (MPa)	Maximum Failure (MPa)
1	**250.6**	**250.6**	9	**93.0**	**93.0**
2	194.9	199.0	10	27.0	35.6
3	**226.4**	**226.4**	11	136.2	138.9
4	142.0	188.0	12	**93.6**	**93.6**
5	190.3	241.1	13	**115.6**	**115.6**
6	**234.6**	**234.6**	14	77.3	113.9
7	145.9	191.9	15	39.9	42.4
8	28.0	86.5	16	31.2	41.7
Mean	176.6	202.3	**Mean**	76.7	84.3
STD	67.1	49.0	**STD**	37.9	37.0

Table 4-9 – Compressive strengths for all tests, means and standard deviations (STD) for each low porosity and high porosity data set are calculated and shown at the bottom. Values shown in bold are the same initial failure and maximum failure compressive strength for the respective test as no initial failure occurred.

The frequency of compressive strength values per sample was analyzed with the use of histograms. A histogram is a diagram that shows rectangles whose area is proportional to the frequency of a variable.

An optimistic maximum compressive strength value for sintered lunar simulant is from the upper limit of the first standard deviation of the samples once the outliers have been removed: 133 MPa for the high porosity and 242 MPa for the low porosity material. Analyzing the histograms for the compressive strength can provide a better idea whether that is a reasonable expectation of range. The most informative histogram showed all four data sets in one figure and can be seen in Figure 4-11. The bars displayed in red shades are from the low porosity data sets and the bars in blue are the high porosity data sets. It is clear that the low porosity samples consistently shows the highest compressive

strengths before experiencing failures; this sub-histogram is skewed to the right. On the other hand, the high porosity data set shows the highest frequency of compressive strength failures at the lower end of the scale. As expected, the initial failures exhibited the lowest values of compressive strength with maximum failures displaying the highest compressive strength.

Figure 4-11 – A histogram for the both high and low porosity samples at initial and maximum failures. Disregarding the set differences, this cumulative histogram shows a symmetric distribution.
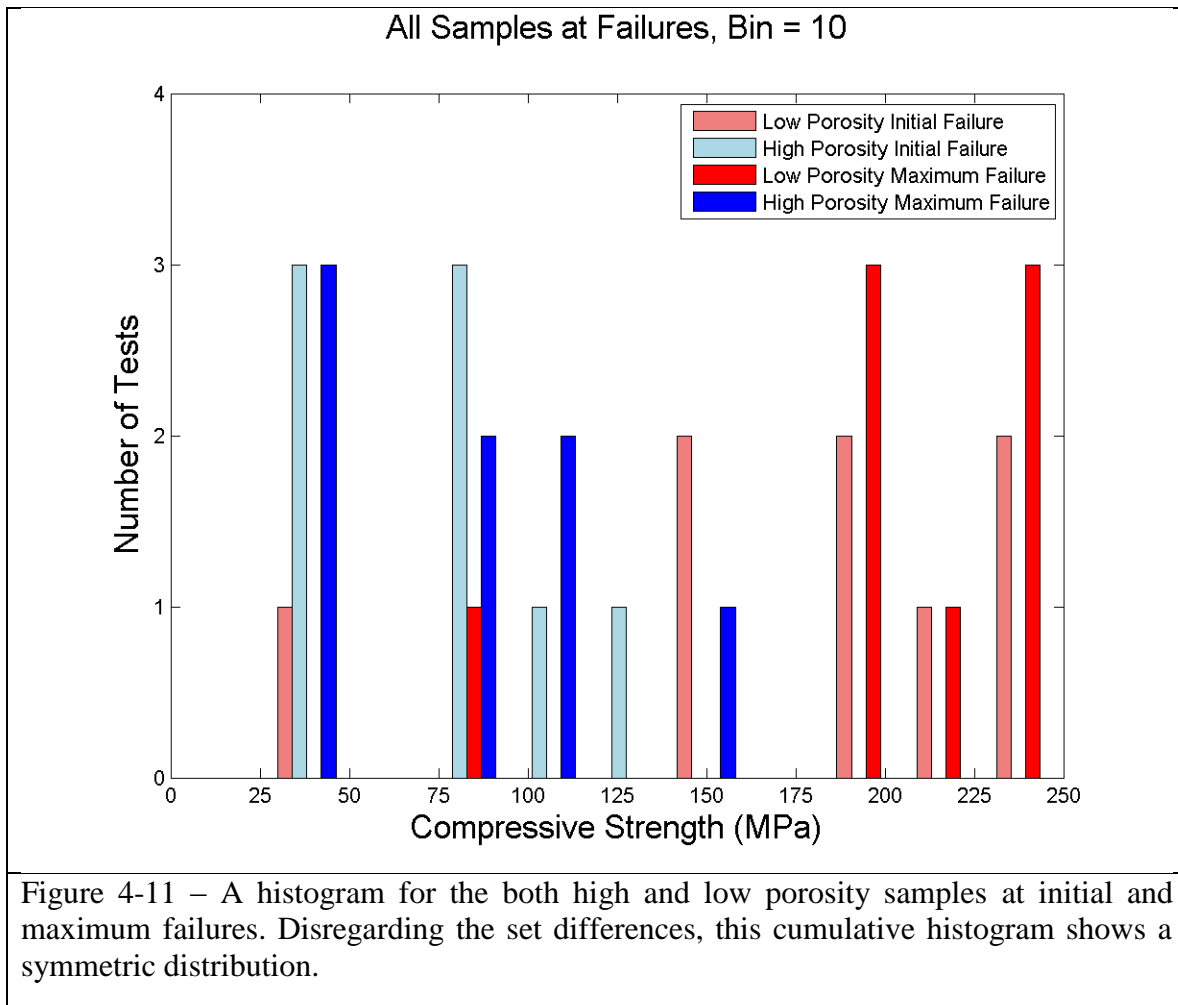
Notable outliers for the low porosity material experienced two failures below 100 MPa. Both of these failures are accredited to sample 8, which has been regarded as a lesser quality sample due to its cylindrical misshape that very likely contributed to its early failure. The three samples of high porosity material, which failed below 50 MPa,

can also be seen as outliers. These three values were from tests 10, 15 and 16, which were deemed poor samples that crumbled during the compressive testing. All three had both initial and maximum failures occurring at less than 50 MPa, providing the impression that the high porosity material is consistently weaker. It should be expected that with a better quality control process implemented after manufacturing, the samples could be made to higher standards and fewer outliers should be expected.

The histograms were created using the range of compressive strength values. These are then sorted into 10 equally spaced bins. The reason they are thicker or thinner in the various histograms and bins is because of the spread of the range; the high porosity histograms are narrower since the range was smaller, and the low porosity histograms appear wider since the range was larger.

The low porosity compressive strength histogram in Figure 4-12 shows the skewed shape favoring higher compressive strength values. In its current form the mean of the low porosity samples compressive strength is 202 MPa with a standard deviation of 49 MPa. Removing the previously discussed outlier of the crumbled sample number 8 increases the mean compressive strength to 219 MPa with a standard deviation of 24 MPa. This sets the statistical limit for the maximum compressive strength within the first standard deviation of 242 MPa, 66% of all high porosity samples should be expected to be below this compressive strength. It should be expected that with more compressive tests the shape of the histogram should take a bell curve shape centered at about the 219 MPa value.

Figure 4-12 – A histogram for the low porosity samples at maximum failure.
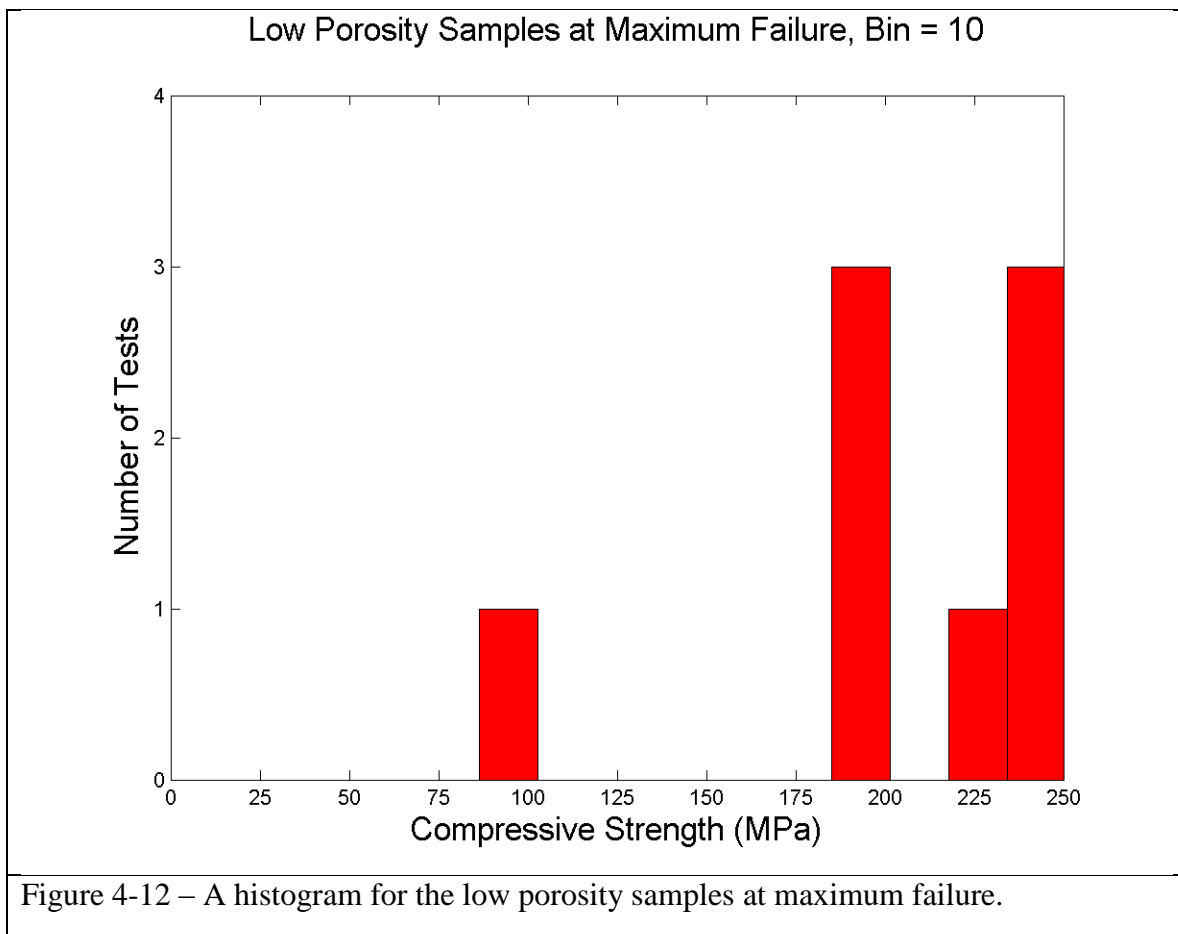
The high porosity compressive strength histogram in Figure 4-13 shows two local medians in the data centered at about 45 and 110 MPa. As previously discussed, the three values at about 45 MPa should be seen as outliers of compressive strength as the samples crumbled during compressive testing. Analyzing the five tests that performed nominally, tests 9, 11, 13, 14, and 15, which ranged between 93 MPa and 138 MPa, computes a mean of about 100 MPa for the material. This is about 15 MPa greater than the combined mean from the cumulative data set and provides a tighter first standard deviation of 33 MPa. This places the upper value for the first standard deviation for the compressive strength at an initial failure of 133 MPa, statistically.

Figure 4-13 – A histogram for the high porosity samples at maximum failure.
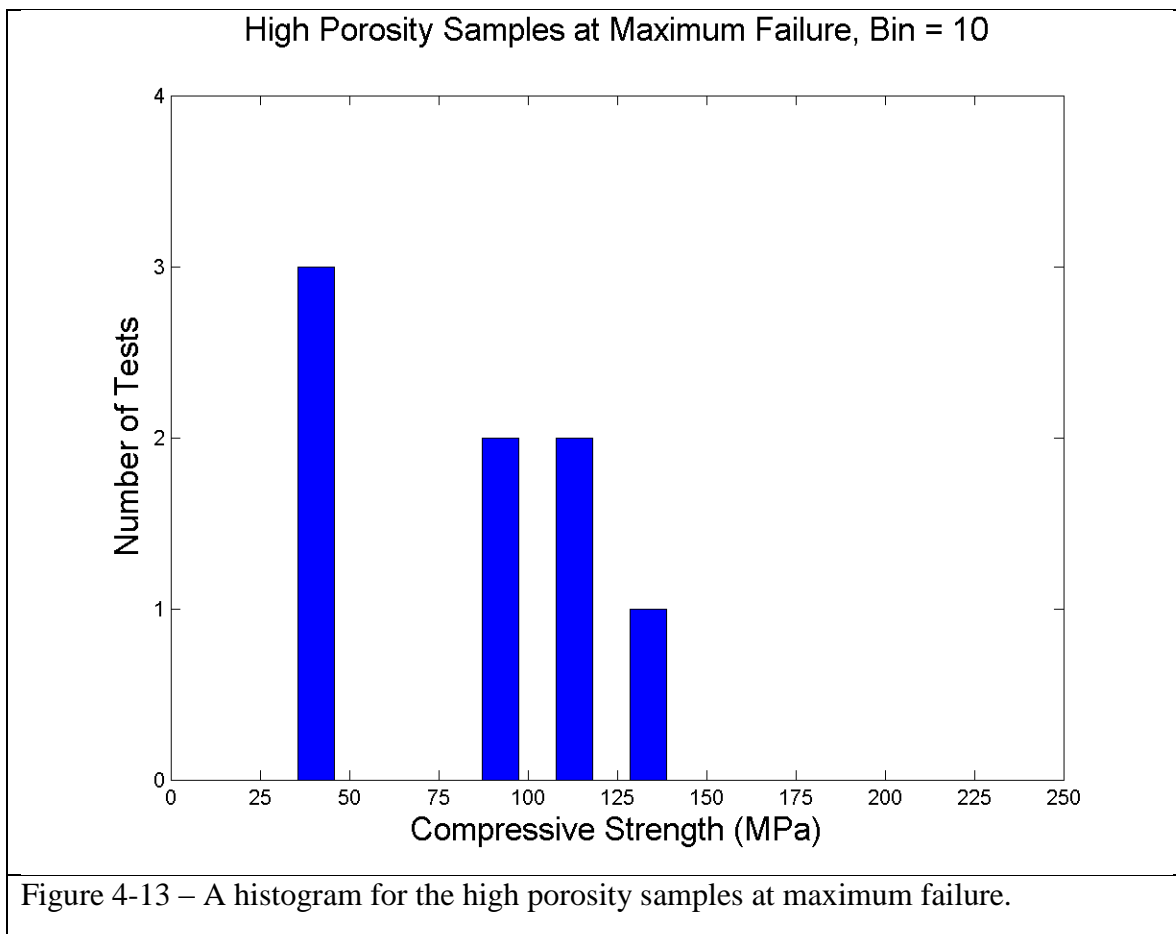
A combined data set of all compressive strength values measured at maximum failure was compiled into the histogram seen in Figure 4-14. For all sixteen tests, the mean value of compressive strength at maximum failure was 143 MPa with a standard deviation of 73 MPa. The local mean of the three outliers is 40 ± 3 MPa. Removing the four previously mentioned outlier samples that crumbled during compression testing increases the mean compressive strength to 170 MPa and tightens the standard deviation to 64 MPa. This reduction in the data set would not dramatically change the shape of the histogram. The histogram would still retain the two local mean configurations with the local means centered at the averages for both the low and high porosity data sets.

Figure 4-14 – A histogram for all the samples at maximum failure.
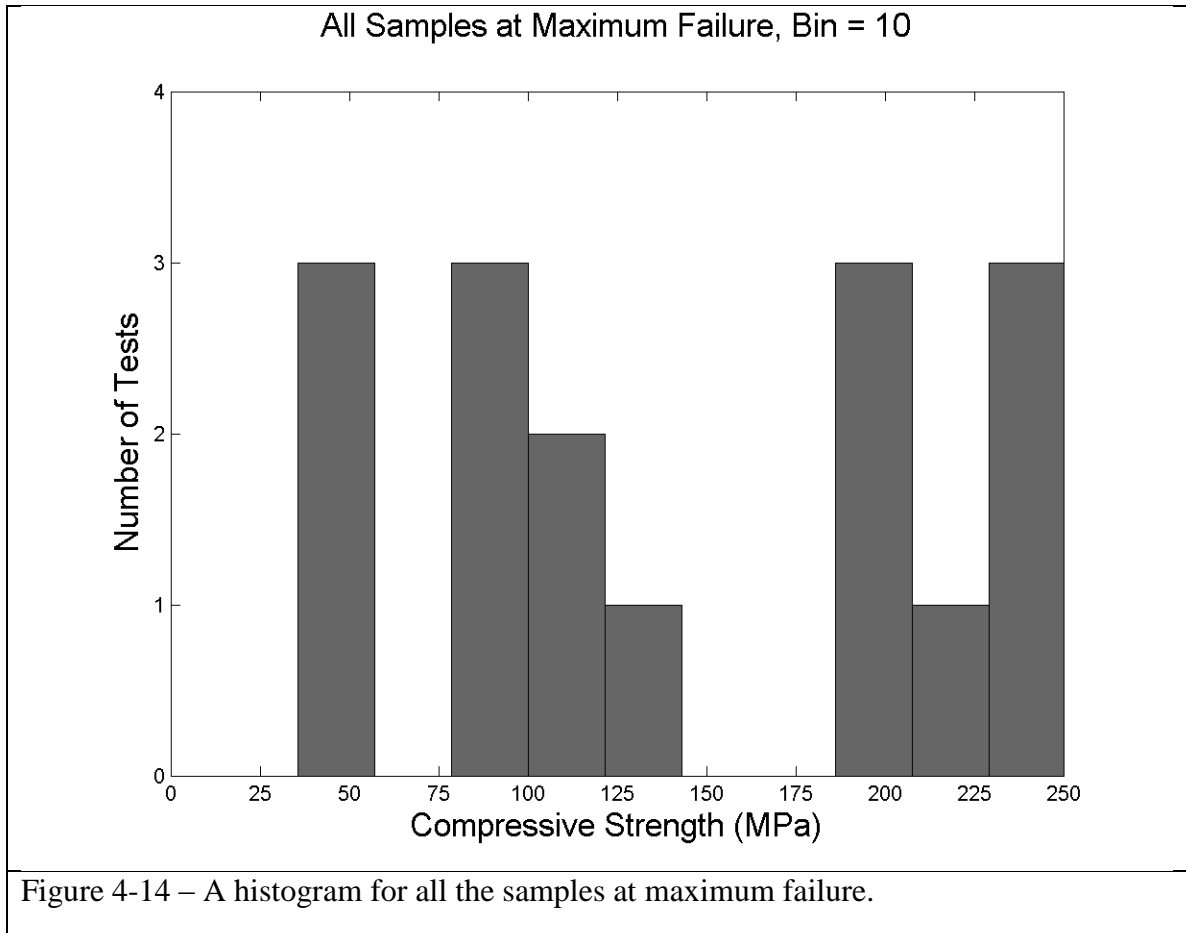
A combined data set of all compressive strength values measured at initial failure was compiled into the histogram seen in Figure 4-15. Inspecting the shape of this histogram, no significant correlation to compressive strength and initial failure can be identified. Of course, there is a larger frequency of initial failures at low compressive strength values due to the crumble-prone outliers. But across the full range of compressive strength values, there appears to be no consistent value for an initial failure of the sample. This lends credibility to the physical cause of an initial failure, a random imperfection in the sample resulting in a premature failure of the specimen, highlighting a manufacturing problem more than a material property problem.

Figure 4-15 – A histogram for all the samples at initial failure.
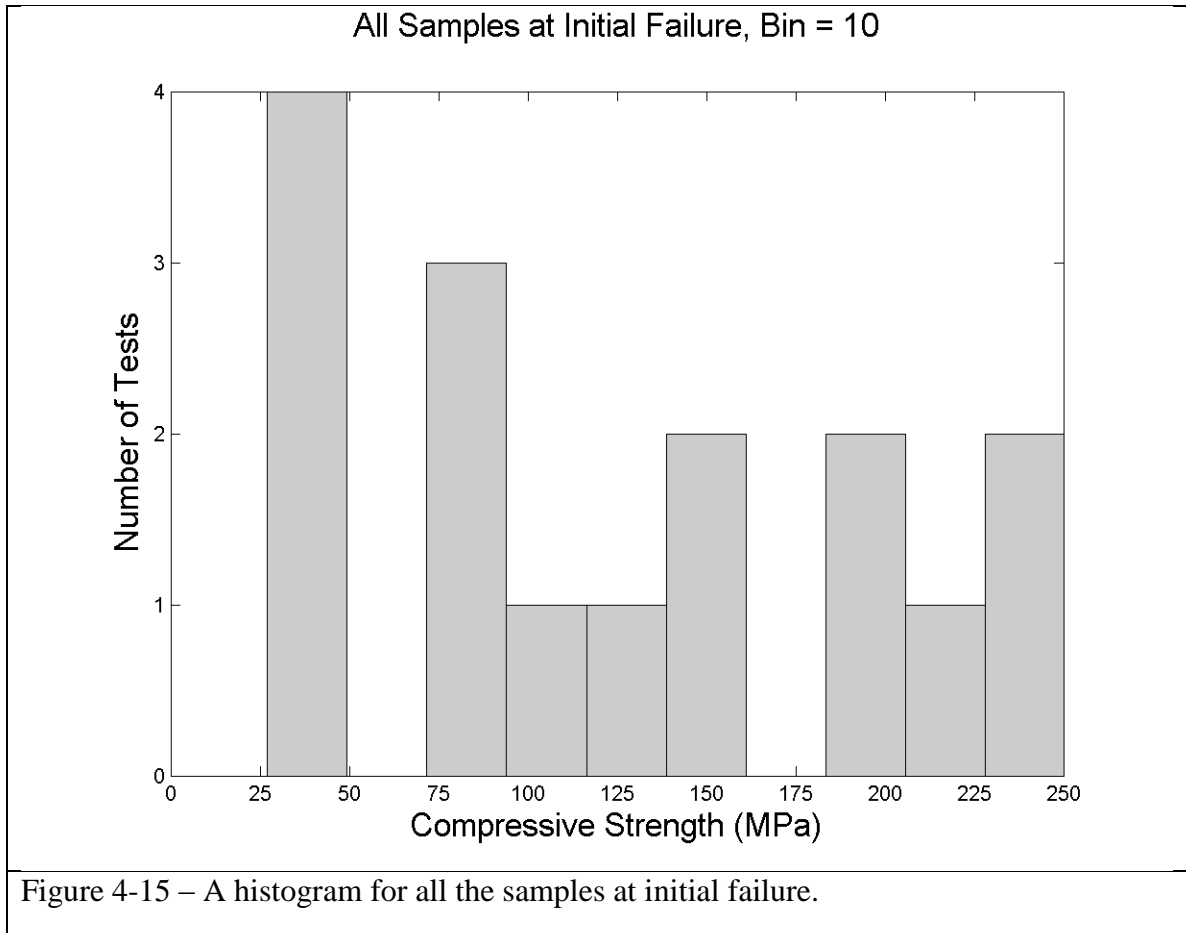
Additional histograms representing the initial failures are provided in Appendix A.8.

4.7 Bulk Modulus

One of the fundamental elastic moduli is the compression modulus, or bulk modulus. The bulk modulus is critical for evaluating a material's compressive loading capacity. The bulk modulus is the ratio of applied pressure to volumetric strain, as formulated in Equation (22).

$$K = -\frac{P}{\varepsilon_V} \qquad \textbf{(22)}$$

For this research, the bulk modulus was computed from the known pressure applied to the sample, an equation relating the measured diameter of the individual

sample, and the calculated strain from the deflection information on each experimental sample tested. The results of the bulk modulus calculations can be found in Table 4-10.

Due to the restricted, small size of the samples during compression testing, the change in diameter could not be measured. It is expected that during compression, the diameter of the sample would expand slightly under load, effectively altering the bulk modulus calculation.

The bulk modulus numbers presented here assumes an unchanging diameter during testing from the initial diameter measurements. Hence, the change in volume is only based on the change in height of the cylindrical specimen. The compression tests conducted were unconfined tests, meaning the specimen is expected to exhibit a lower bulk modulus than if tested under confined conditions.

		Bulk Modulus			
		Initial Failure (MPa)	Initial Failure (ksi)	Max Failure (MPa)	Max Failure (ksi)
All Data (n=8) Low Porosity	Mean	6,389.5	926.7	5,961.0	864.6
	STD	1,776	258	1,693	246
	COV	0.278	-	0.284	-
All Data (n=8) High Porosity	Mean	3,659.7	530.8	3,586.4	520.2
	STD	2,031	295	2,062	299
	COV	0.555	-	0.575	-
Best Data (n=3) Low Porosity	Mean			6,919.0	1,003.5
	STD			979	142
	COV			0.141	-
Best Data (n=3) High Porosity	Mean			4,272.0	619.6
	STD			621	90
	COV			0.145	-

Table 4-10 – Summary table of compressive strength values at initial failure and maximum failure. Means, standard deviations (STD) and coefficient of variation (COV) are tabulated per data set. COV is listed under the MPa columns, however, COV is dimensionless and the same for both MPa and ksi.

Coefficient of variation (COV) is used in Table 4-10 in place of variance since the variance was not providing useful information due to the wide range of data points. COV is defined as the ratio of standard deviation over the mean of the dataset. One advantage of using the COV is that the results are dimensionless, making it easier to compare between the datasets of different types, or in this case, data sets of very different values.

Making a comparison with the all data, the COV was statistically the same for the initial and maximum failures of low porosity or the initial and maximum failures of high porosity. However, the COV does not compare between the low and high porosity of the all data sets. Interestingly, the COV is statistically the same between the best data caparisons of low porosity and high porosity, meaning that there are three data sets that can be compared: (1) the all-data low porosity by initial and maximum failure, (2) the all-data high porosity by initial and maximum failure, and (3) the best-data low porosity with the best-data high porosity.

In both cases of initial and maximum failure for all data (1) and (2), the average bulk modulus for the low porosity samples was about 1.7 times greater than for the high porosity samples. This comparison also scaled similarly when comparing the maximum failure values from the best data set (3), indicating that the bulk modulus values scale between each individual data set (best data compared to best data or all data compared to all data).

Interestingly, the computed mean bulk modulus was greater for the initial failure than the maximum failure in both the low porosity (1) and high porosity (2) data sets, but it also had a greater standard deviation. This may be due to the experimental sample's

ability to withstand less compression after an initial failure, leading to a reduced overall change in volume and, subsequently, a lesser bulk modulus value.

The determination of the greatest averaged bulk modulus should be viewed by comparing data before a material failure occurred. This would be comparing the all-data, low porosity, initial failure with the all-data, high porosity, initial failure, and the best-data at maximum failure for both low and high porosity (3). These data sets do not have the effects of uncertainty caused by an initial failure on the computed strain data.

The largest average bulk modulus was exhibited by the low porosity samples at maximum failure for the best data (3). It is noteworthy that the all-data low porosity at initial failure showed the second highest average bulk modulus of 500 MPa, or about 7% less than the low porosity samples at maximum failure for the best data (3); leaving the impression that it was a correct assumption that bulk modulus is best computed with the data before the first failure of the experimental sample.

Comparing the bulk modulus between the low and high porosity average values, the high porosity samples had a bulk modulus 40% less than the low porosity samples. This comparison shows that porosity plays an important part in the bulk modulus of the sintered lunar regolith simulant material.

4.8   Poisson's Ratio

Poisson's ratio can be defined for solid materials as the negative ratio of the relative diameter change in the transverse direction (negative for compression) and the relative length change in the direction of tension (positive). After Poisson introduced this ratio, the conclusion he arrived at was 0.25 should be the value for all materials. This is the case when the solid is composed of particles, atoms or molecules governed by

spherically symmetric potentials. In this case the Cauchy relations hold and the elastic behavior of isotropic solids are governed by only one elastic constant, the Young's modulus. In general, however, isotropic materials are characterized by two elastic constants. Poisson's ratio of porous materials is of interest since in combination with one of the elastic moduli, typically the Young's modulus, it determines the linear elastic response of isotropic materials, making it practically useful. At present, there are still competing porosity dependences relating to which Poisson's ratio calculations are the most realistic.

Isotropic materials are characterized by two elastic constants, the rest can be calculated from the first two. Young's modulus E, the bulk modulus, also known as the compression modulus, K, the shear modulus or torsion modulus G, and Poisson's ratio v.

The following relation connects the elastic moduli to Poisson's ratio,

$$v = \frac{3K - 2G}{2(3K + G)} = \frac{E}{2G} - 1 = \frac{3K - E}{6K}. \qquad \textbf{(23)}$$

The stiffness ratio, K/G, can be expressed in terms of v by Equation (24),

$$\frac{K}{G} = \frac{2(1 - v)}{3(1 - 2v)}. \qquad \textbf{(24)}$$

Since all three elastic moduli are positive, it follows that

$$E = 2G(1 + v) \text{ and } E = 3K(1 - 2v). \qquad \textbf{(25)}$$

Poisson's ratio is bounded by the inequality in Equation (26) and for all materials microstructures might be found that lead to Poisson's ratios ranging from -1 (auxetic) to 0.5 (incompressible),

$$-1 < v < \frac{1}{2}. \qquad \textbf{(26)}$$

For this research project, the Poisson's ratio and the shear modulus were calculated using Equation (23). The computed averages for the Young's modulus and bulk modulus, separated by initial (init.) failure and the maximum (max.) failure, were used in this calculation. These results can be seen in Table 4-11 along with the computed elastic constants for three other select materials. Further explanation on the select materials is available in Section 4.9. The subscript 'o' denotes that elastic constant value is for the solid phase of that material. Comparing the values for the low and high porosity values, in both cases the initial failure sets have a higher calculated Poisson's ratio. The Young's modulus for both initial and maximum failure sets was the same in the computations, but the bulk modulus was for initial or maximum failure.

Material	K_o (MPa)	G_o (MPa)	v_o	E_o (MPa)	K_o/G_o	Porosity (%)
Terrestrial Basalt	62900	36500	0.257	91752	1.723	0
Terrestrial SiO2	36500	31200	0.167	72844	1.170	0
Lunar Basalt 12065 Model	105000	60500	0.258	152257	1.736	0
Sintered JSC-1A Mean Max. Failure	5961	3300	0.266	8358	1.806	1.44
Sintered JSC-1A Mean Init. Failure	6390	3260	0.282	8358	1.960	1.44
Sintered JSC-1A Mean Max. Failure	3586	2198	0.246	5475	1.632	11.78
Sintered JSC-1A Mean Init. Failure	3660	2189	0.251	5475	1.672	11.78

Table 4-11 – Computed bulk modulus, shear modulus, Poisson's ratio, Young's modulus, stiffness ratio (K/G) and porosity for two textbook materials, one computer model of lunar basalt and the sintered samples of high and low porosity.

4.9 Comparison of Lunar Analogue and Solid Material Properties

We wish to compare the properties of our lunar simulant to comparable materials used for structural applications. Young's modulus and bulk modulus were computed for two terrestrial rocks, basalt and plagioclase feldspar. The decision to evaluate basalt and plagioclase feldspar for comparison with lunar simulant was based on the composition of the lunar simulant used in our study, JSC-1A. Rickman et al. (2007) analyzed the JSC-1A series lunar simulant with electron-probe microanalysis to determine its mineralogy. An abridged selection of their data is shown in Table 4-12 where we see that plagioclase feldspar and basaltic glass are two major components of the JSC-1AF simulant. Because of this, terrestrial basalt and plagioclase feldspar were selected as lunar regolith simulant-comparable materials.

JSC-1AF Mineral Composition Oxide Weight %				
Oxide	Palagioclase	STD	Basaltic Glass	STD
SiO_2	49.80	0.63	46.11	0.53
TiO_2	0.10	0.03	2.80	0.22
Al_2O_3	31.87	0.71	14.92	0.65
Cr_2O_3	0.01	0.01	0.01	0.02
FeO*	0.85	0.11	12.66	1.08
MnO	0.02	0.02	0.22	0.02
MgO	0.15	0.06	0.51	0.49
CaO	14.19	0.54	9.98	0.63

* Total Fe calculated as FeO

Table 4-12 – Table of the major mineral composition by oxide weight percentage of JSC-1AF. Rickman et al. (2007)

A defining characteristic of a basaltic rock is the silicon dioxide (SiO_2) composition that typically ranges between 45% and 52% by weight. Plagioclase shares a similar mineral weight composition of SiO_2. However, the two rocks are very different in ways not of relevance here. For this series of calculations, SiO_2 is assumed to be the main component of plagioclase feldspar and thus all calculations use the properties of SiO_2 as representing plagioclase feldspar.

Material properties for basalt and SiO_2 were taken from Table 10 in *Elasticity of Minerals, Glasses, and Melts* (1995). Basalt glasses with density 2.77 kg/m^3 have an adiabatic bulk modulus of 62.9 GPa and a shear modulus of 36.5 GPa. SiO_2 with a density of 2.204 kg/m^3 has an adiabatic bulk modulus of 36.5 GPa and a shear modulus of 31.2 GPa.

Several types of lunar rock material properties were measured and computationally modeled by Warren et al. (1973) and Meyer et al. (2011), including lunar mare basalt sample number 12065 returned on Apollo 12. The bulk modulus, shear modulus and density were evaluated by measuring acoustic velocities, linear strain under uniaxial and hydrostatic pressures.

To best match the JSC-1A composition, the mare basalt sample number 12065 was selected since it was a median sample of the four mare basalts studied in Warren et al. (1973) for computations. The calculated composition is provided in Table 4-13. We thus use a bulk modulus of 105 GPa and shear modulus of 60.5 GPa after converting from Mbar. Values of bulk modulus and shear modulus are in percent volume and subsequently averaged for the entire rock composition.

Rock Model Compositons and Mineral Properties						
	Plagioclase	Peroxene	Olivine	"Opaques"	Silica	Total
Volume Percentage	17.44%	67.78%	2.76%	11.25%	0.78%	
Density (g/cm^3)	2.73	3.32	3.53	3.6	2.3	
Bulk Modulus (Megabar)	0.806	0.957	1.266	2.0	0.309	
Shear Modulus (Megabar)	0.376	0.58	0.729	1.1	0.266	
Bulk Modulus (Megabar Vol. % Composition)	0.141	0.649	0.035	0.225	0.002	1.052
Shear Modulus (Megabar Vol. % Composition)	0.066	0.393	0.020	0.124	0.002	0.605

Table 4-13 – Table of the modeled mineral composition by volume percentage of lunar mare basalt number 12065. Warren et al. (1973).

In the following paragraph we utilize equations for upper bounds of elastic properties given as functions of porosity percentage in order to develop a better comparison with our data. For a composite material comprised of two mediums, the elastic moduli have an upper and a lower bound from micromechanical bounds. For a porous material where one medium is filled by empty void, the elastic modulus lower bound degrades to zero.

In the following, our guide is Pabst and Gregorvá (2009), who summarized several relations for effective Poisson ratios of porous materials with different bounding theories. These equations are provided below where ϕ is the porosity percentage. We substituted the porosity values from our tests into these equations: 1.44% for the low porosity samples, and 11.78% for the high porosity samples.

The Hashin-Shtrikman bounds are the tightest bounds for the elastic moduli of two-phase composite materials. When the porous material has a Hashin-Shtrikman microstructure, the upper bounds are provided for bulk modulus by Equation (27) and for shear modulus by Equation (28),

$$K_{HS} = K_0 \frac{1 - \phi}{1 + A_{HS}\phi} \quad \text{with} \quad A_{HS} = \frac{1 + \nu_0}{2(1 - 2\nu_0)} \tag{27}$$

$$G_{HS} = K_0 \frac{1 - \phi}{1 + B_{HS}\phi} \quad \text{with} \quad B_{HS} = \frac{2(4 - 5\nu_0)}{(7 - 5\nu_0)} . \tag{28}$$

From the Nielsen relations, the porous bulk modulus and shear modulus upper bounds are related by Equation (29) and Equation (30), respectively,

$$K_N = K_0 \frac{(1 - \phi)^2}{1 + A_N\phi} \quad \text{with} \quad A_N = \frac{5\nu_0 - 1}{2(1 - 2\nu_0)} \tag{29}$$

$$G_N = G_0 \frac{(1 - \phi)^2}{1 + B_N\phi} \quad \text{with} \quad B_N = \frac{1 - 5\nu_0}{7 - 5\nu_0} . \tag{30}$$

Ramakrishnan and Arunachalam proposed another possible methodology of relating porosity to material properties, though it is incompatabile with the Nielsen solution. It is based on the relation of bulk and shear modulus upper bounds as seen in Equation (31) and Equation (32). The porous-inclusive derivation of Young's Modulus was used for calculations and is provided in Equation (33),

$$K_{RA} = K_0 \frac{(1 - \phi)^2}{1 + A_{RA}\phi} \quad \text{with} \quad A_{RA} = \frac{1 + \nu_0}{2(1 - 2\nu_0)} \tag{31}$$

$$G_{RA} = G_0 \frac{(1 - \phi)^2}{1 + B_{RA}\phi} \quad \text{with} \quad B_{RA} = \frac{11 - 19\nu_0}{4(1 + \nu_0)} \tag{32}$$

$$\frac{E}{E_0} = 1 - [E]\phi \quad \text{with} \quad [E] = \frac{3(1 - \nu_0)(9 + 5\nu_0)}{2(7 - 5\nu_0)} . \tag{33}$$

Our calculations for computing porosity were carried out using the nominal

elastic constants for basalt, SiO$_2$ and lunar basalt sample number 12065. The calculated

and averaged material constants for the experimental low and high porosity sintered

samples at both premature/initial and maximum failure were also calculated. The results

are summarized in Table 4-14. Notation used is as follows: the bulk modulus is denoted

by K, the torsion modulus by G, Poisson's ratio by v, and Young's modulus by E. Terms

in parentheses correspond to the equations used to compute that column's values. Hashin-

Shtrikman is abreviated with the subscript 'HS', Nielsen with 'N', and Ramakrishnan and

Arunachalam with the abreviation 'RA.'

	Material/Test	Porosity (%)	K$_{HS}$ (27) (MPa)	K$_N$ (29) (MPa)	K$_{RA}$ (31) (MPa)	v (23)	G$_{HS}$ (28) (MPa)	G$_N$ (30) (MPa)	G$_{RA}$ (32) (MPa)	E (33) (MPa)
Low Porosity	Basalt	1.44	60,862	60,845	59,985	0.222	35,489	35,482	34,846	89,102
	SiO2	1.44	35,526	35,519	35,014	0.187	30,303	30,296	29,594	70,753
	LunarBasalt12065	1.44	101,584	101,557	100,121	0.223	58,825	58,813	57,763	147,859
	Sintered Mean Max. Failure	0				0.226				
	Sintered Mean Init. Failure	0				0.232				
High Porosity	Basalt	11.78	48,158	47,323	42,485	0.222	28,959	28,575	24,845	70,074
	SiO2	11.78	29,184	28,823	25,746	0.187	24,555	24,207	20,281	55,739
	LunarBasalt12065	11.78	80,316	78,915	70,855	0.223	48,007	47,371	41,210	116,282
	Sintered Mean Max. Failure	0				0.218				
	Sintered Mean Init. Failure	0				0.220				

Table 4-14 – Computed porous elastic constants; bulk modulus, shear modulus, torsion modulus and Poisson's ratio, for five different materials. Parentheses denote the corresponding equation number used to calculate the columns value. Zero porosity refers to the equivalent solid.

When comparing the results of three methods for computing the elastic constants,

we see similar numbers. The Hashin-Shtrikman and Nielsen results were similar and the

Ramakrishnan and Arunachalam were further apart. It is interesting to see that Poisson's

ratio is essentially the same for low and high porosity materials whereas the other elastic

constants differ appreciably.

The porous elastic constants in Table 4-14 can also be compared with the solid elastic constant values from Table 4-11. The solid terrestrial values of basalt and plagioclase feldspar are still more than six times stronger than the low porosity sintered material, making both the high and low porosity sintered material considerably weaker than solid rock, which is not unexpected.

Of note is that the modeled lunar mare basalt of 12065 exhibited very high values for mechanical material properties. It is unclear if this is due to inaccuracies in the mathematical model for the material properties or if they are indeed that large.

In addition to the tabulated values for the specific porosities tested in this research, plots were created to interpret elastic constants as a function of porosity. The Hashin-Shtrikman, Nielsen and Ramakrishnan and Arunachalam equations for elastic constants, as discussed above, all depend on knowing the solid material properties before calculating their variations as functions of porosity. To compute the elastic constants per the Hashin-Shtrikman, Nielsen and Ramakrishnan and Arunachalam equations for the low and high porosity material, the appropriate Equations from (27) to (33) had to be solved for the pure solid phase value. Additional figures relating the specific material, basalt, SiO_2 or lunar basalt, as well as relating the Hashin-Shtrikman, Nielsen and Ramakrishnan and Arunachalam equations can be found in Appendix A.9.

To compute a porosity relation for the elastic modulus of the low and high porosity sintered lunar regolith simulant, Equation (33) was used and solved for E_o with the computed Poisson's ratio from Table 4-14, using the mean elastic modulus as calculated from Section 4.2. The resulting plots can be seen in Figure 4-16**,** which is cropped between 0% and 20% porosity. Both the low and high porosity values converge

to an elastic modulus of zero at the 50% porosity value. Each porosity curve plotted in Figure 4-16 was calculated using Equation (33) based on one respective data point. The fact that we obtain two different lines is a sign that Equation (33) alone is insufficient for a proper data fit. Thus we obtain two curves rather than one curve upon which both data points should fall.

Figure 4-16 – Calculations were performed to relate the elastic modulus to porosity for the low and high porosity material. This figure was cropped between 0% and 20% porosity to highlight the differences.
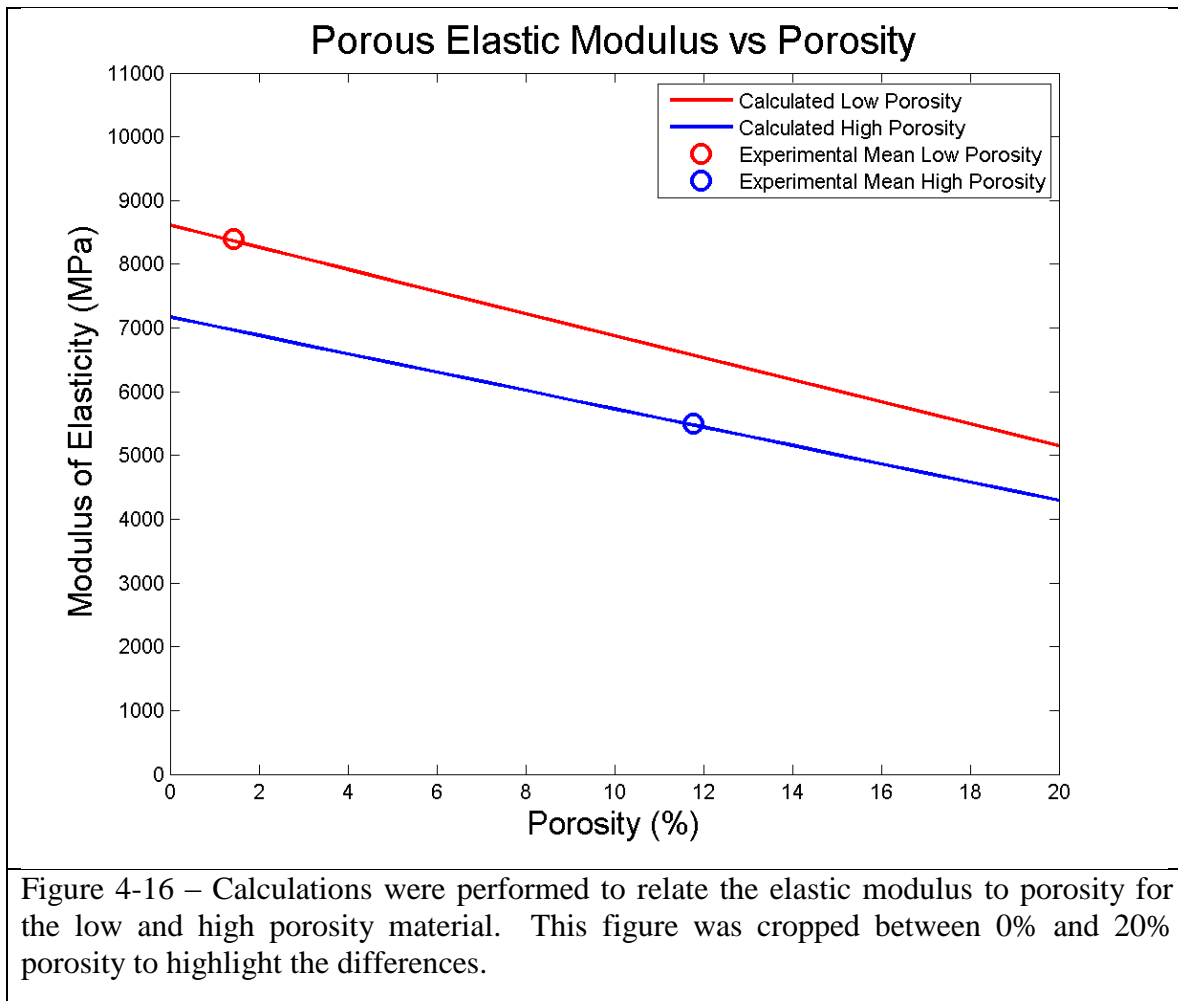
Next, the elastic moduli of the other materials of interest are plotted as functions of porosity in Figure 4-17. The elastic modulus of the lunar basalt sample dominates all other moduli values, raising the concern that the elastic constants for the theoretical lunar basalt may be inaccurate. Comparing the basalt and SiO_2 lines of varying porosity to the

low and high porosity calculations show an order of magnitude difference between the elastic moduli.

Figure 4-17 – Comparing the known material constants with the experimental low and high porosity materials. This figure was cropped between 0% and 20% porosity to highlight the differences.
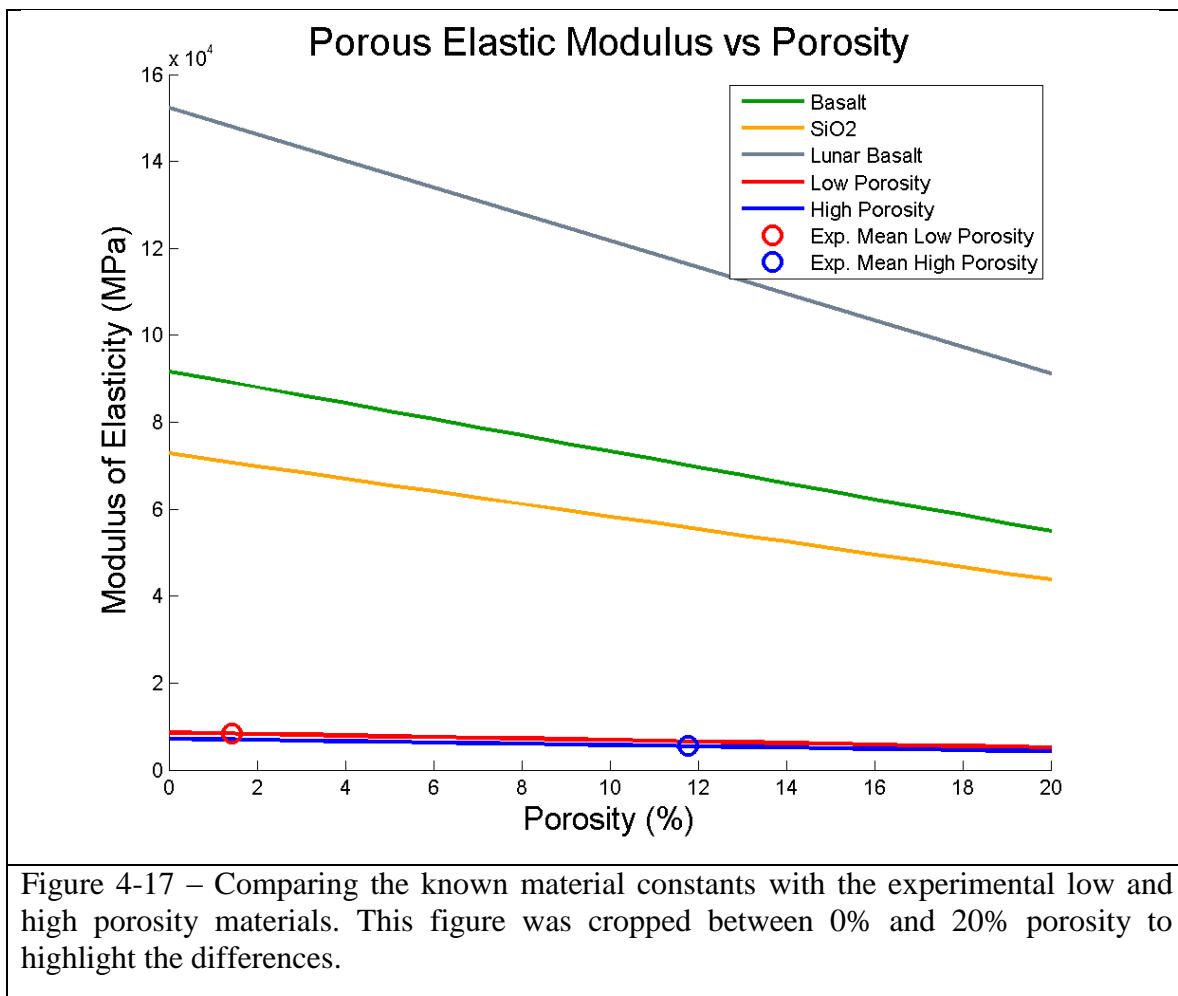
Basalt bulk moduli were computed as functions of porosity. Basalt is regarded to be a very strong terrestrial rock. Basalt material properties were in the middle range of the theoretical lunar basalt and the SiO_2, making it fair for comparison, as it does not occupy the extreme ranges of material properties. In Figure 4-18 three different calculations for bulk modulus were performed across the full range of porosity.

Figure 4-18 – Basalt bulk moduli as functions of porosity using the three methods of calculating porous bulk modulus.
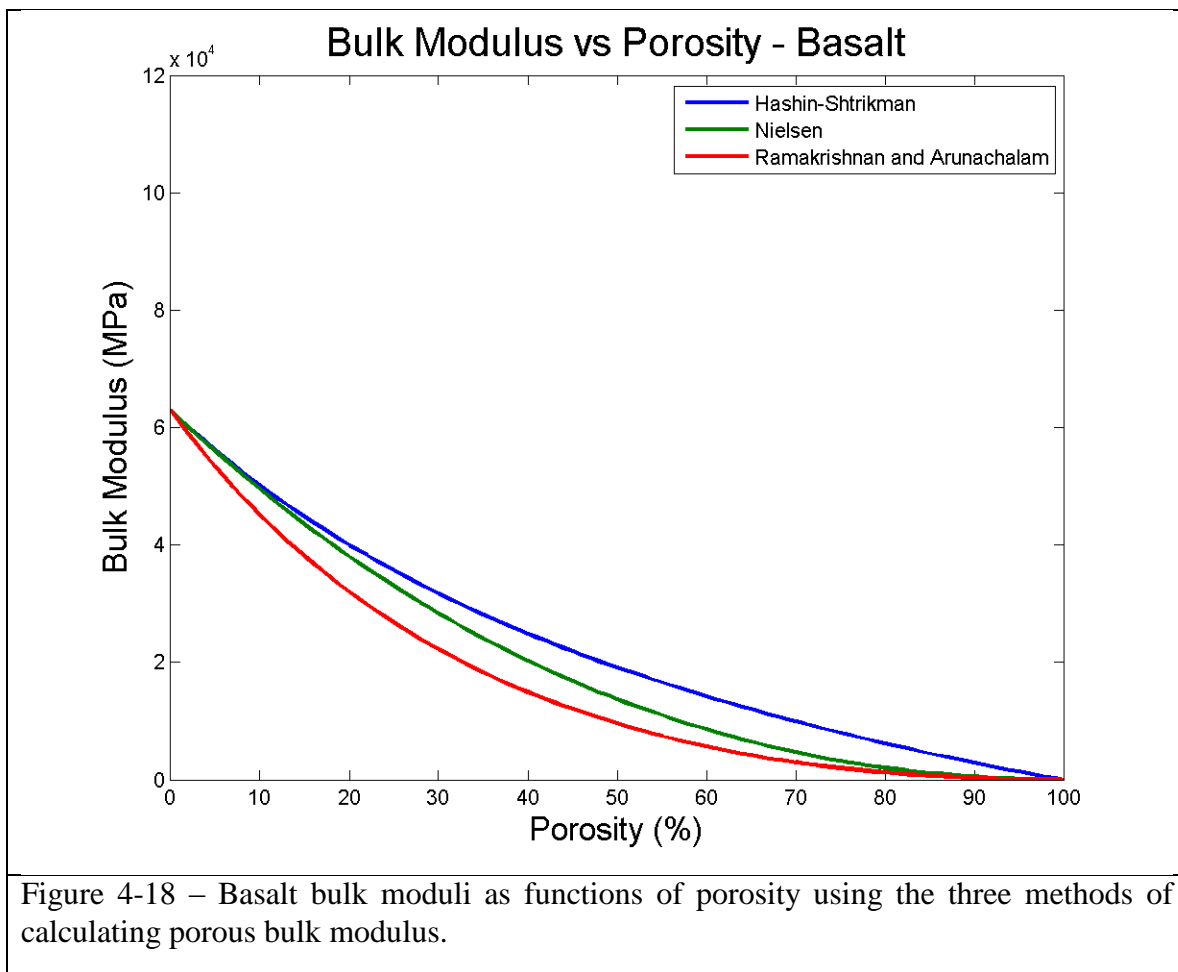
It becomes apparent that the Hashin-Shtrikman bulk modulus calculation provided the highest values for bulk modulus whereas the Ramakrishnan and Arunachalam calculations were the lowest, with the Nielsen bulk modulus values somewhere in-between. This was not unique to the basalt calculations; this pattern of Hashin-Shtrikman calculations providing the maximum values, Nielsen the middle, and Ramakrishnan and Arunachalam the lower values were found across all the materials calculated.

A similar pattern of bulk modulus to porosity calculations appeared for the tested sintered lunar regolith simulant materials and is seen in Figure 4-19. The largest

differences, as compared to Figure 4-18, are the reductions in magnitudes of the bulk moduli. This appears reasonable as the bulk modulus calculations for the low and high porosity sintered materials were significantly less than those of basalt.

Figure 4-19 – Low porosity sintered lunar regolith simulants bulk moduli as functions of porosity using the three methods of calculating porous bulk modulus.
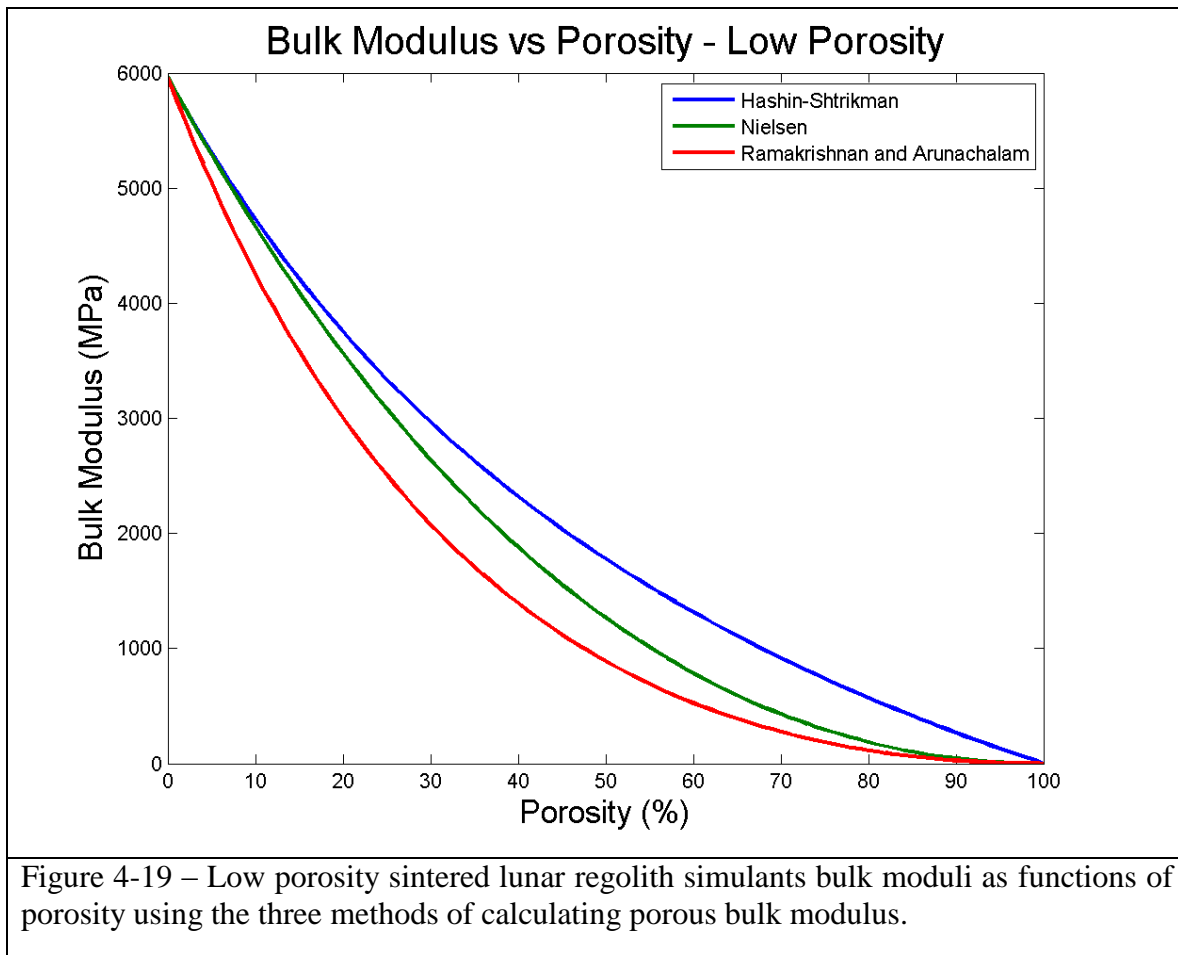
Figure 4-20 shows a comparison of the Nielsen bulk moduli as functions of porosity for basalt, SiO_2 and the theoretical lunar basalt. Nielsen was chosen to display here as it was the calculation that resided between the Hashin-Shtrikman values and the Ramakrishnan and Arunachalam values for bulk modulus. The other figures can be found in Appendix A.9.

Figure 4-20 – Bulk moduli as functions of porosity using the Nielsen calculations are shown here as an example. Both the theoretical lunar basalt and the SiO_2 showed similar patterns in relating bulk modulus to porosity.
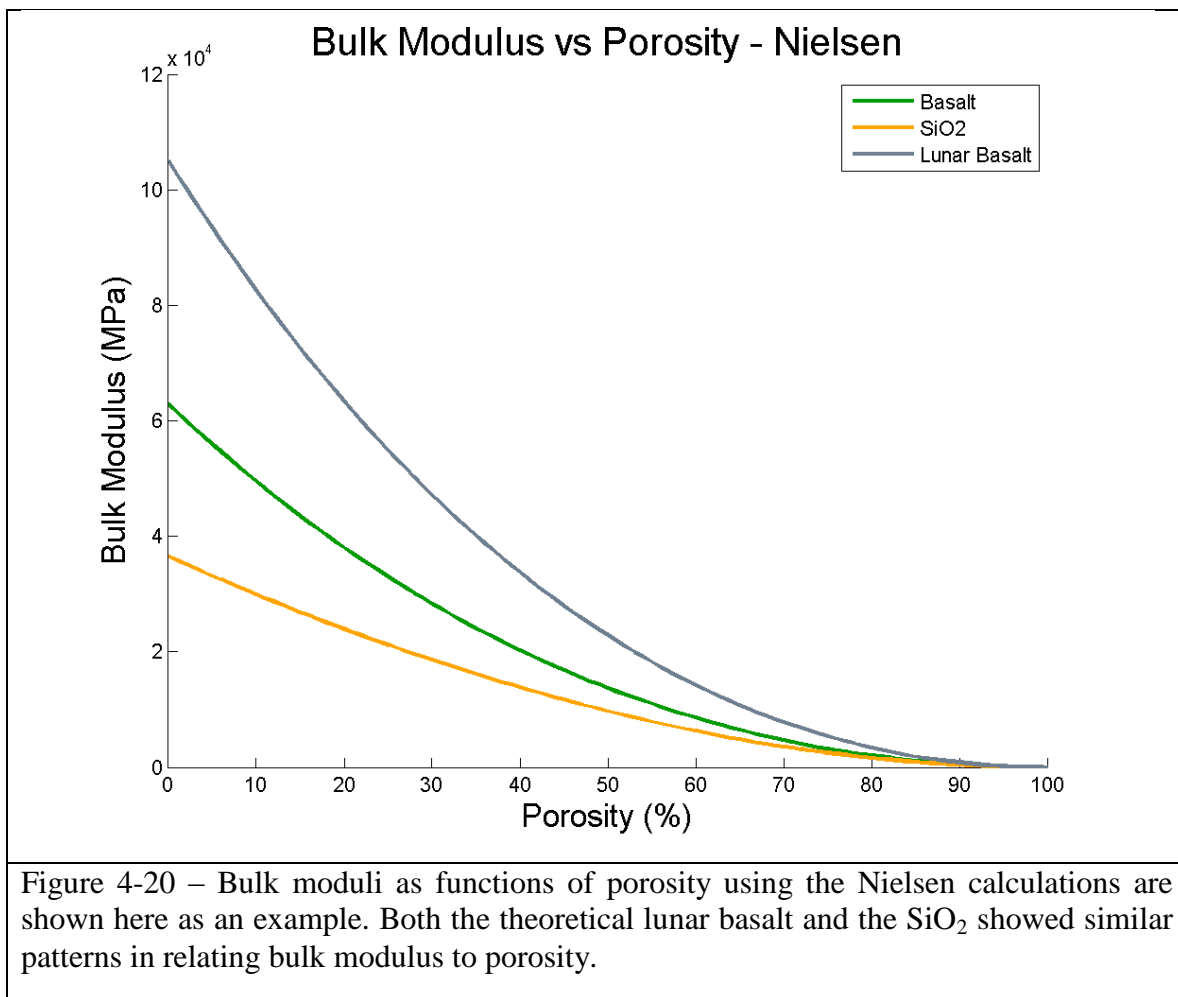
Shear moduli were also calculated as functions of porosity with an example shown in Figure 4-21. Similar patterns as those discerned for the bulk moduli figures also apply for the shear moduli.

Figure 4-21 – Low porosity sintered lunar regolith shear moduli as functions of porosity using the three methods of calculating porous bulk modulus.
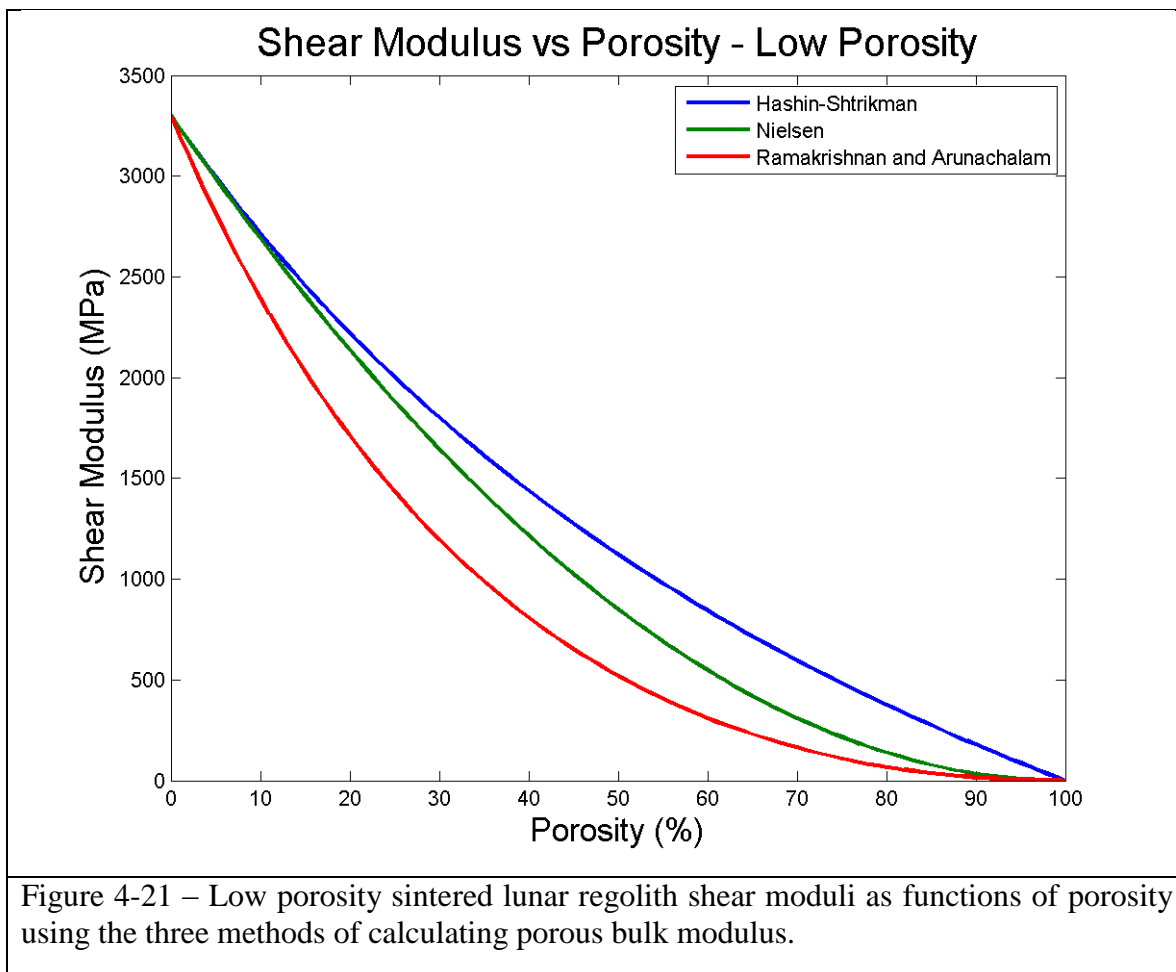
4.10 Comparison to Similar Research

Gualtieri and Bandyopadhyay (2015) were our collaborators who provided the samples used in this testing. Similar compression testing was performed on their samples as was performed in this research. One difference between the two testing series were the porosities of the samples tested, ours were 1.44% and 11.78% where theirs were 0.41% and 8.44% porous. These additional two porosity sets allow for a refined view of the effect of porosity on compressive strength. By having two laboratories perform similar testing, a consistency check on the samples tested is also performed. If both sample sets behave similarly, then the sample's predictability becomes well understood. The

averaged data for both the Gualtieri and the Indyk compression testing can be seen in Table 4-15. The data is organized from low porosity to high porosity for the four sample sets tested, giving the average maximum failure, Young's modulus and the first standard deviation.

			Porosity (%)	Maximum Failure All (MPa)	Maximum Failure Best* (MPa)	E (Gpa)
Low Porosity		Mean of Gualtieri Tests, n>10	0.41	232	-	10.9
		First Standard Deviation	0.24	43.7	-	1.89
		Mean of Indyk Tests, n=8	1.44	202.3	237.2	8.4
		First Standard Deviation	1.91	49.0	10.0	-
High Porosity		Mean of Gualtieri Tests, n>10	8.44	103.2	-	5.98
		First Standard Deviation	1.44	26.7	-	0.71
		Mean of Indyk Tests, n=8	11.78	84.3	100.7	5.5
		First Standard Deviation	3.3	37.0	10.5	-

*n=3

Table 4-15 – A comparison of the sintered lunar simulant sample properties by Gualtieri and Bandyopadhyay (2015) and this research.

It appears that the values for compressive strength and Young's modulus compare well between Gualtieri and Bandyopadhyay and our research. At least ten tests were conducted by Gualtieri and Bandyopadhyay. But it was not stated how many samples were tested exactly or whether poor performing samples were discarded. They may have implemented a more rigorous quality control on the samples tested than in the samples tested in our research. However, inspecting the first standard deviation for the 'Maximum Failure All' column in Table 4-15, there appears to be a similar range of maximum compressive strengths for the two independent compression tests. This points to similar variability of maximum compression strengths from both series of sintered lunar simulant

testing. In the testing by Gualtieri and Bandyopadhyay, no premature compression failures were reported; this is noteworthy as our testing experienced a prevalence of prematurely failure in our samples.

It is unclear if any of the samples in the 'Maximum Failure All' from Gualtieri and Bandyopadhyay experienced premature failure. Also seen in Table 4-15 are 'Maximum Failure Best' which refers to the samples that did not experience premature failures and are the best samples tested in this research. When comparing the 'Maximum Failure All' to the 'Maximum Failure Best,' the first thing to note is the reduction in sample size, 'Maximum Failure Best' only contains three samples each. The 1.44% porous samples without premature failure from 'Maximum Failure Best' exceeded the maximum failure value for the 0.41% porosity samples, but the 11.78% porosity samples were not stronger than the 8.44% samples. The reason low porosity samples in the 'Maximum Failure Best' set performed better than the 0.41% porosity samples is most likely due to the range on standard deviation for both sets. The decreasing strength trend from low porosity to high porosity agrees with findings presented earlier.

Comparing the accuracy of the samples' porosity across the four sample sets highlights that it is more difficult to quantify porosity as the samples become more porous. The samples' porosity becomes less certain as the porosity increases. This can be observed by the increase in the first standard deviation from 0.24% for the 0.41% porous samples to a first standard deviation of 3.3% for the 11.78% % porous samples. Gualtieri and Bandyopadhyay pointed out that it is common for pressed ceramic bodies to have higher porosity towards the edges than the inside. This variation in porosity could become exaggerated as the sample becomes more porous.

The modulus of elasticity was also compared for the two research projects. For the low porosity sets our value for the elastic modulus is on the cusp of the Gualtieri and Bandyopadhyay value. This can be seen as a reasonable comparison as there is also about 1% difference in porosity between the two sets. For the high porosity modulus of elasticity our value is within their first standard. A linear best-fit equation between the four averaged data points is given in Equation (34), where y is the elastic modulus in GPa and x is the porosity in percent,

$$y = -0.42x + 10. \tag{34}$$

Extrapolating to solid lunar simulant, with 0% porosity, yields an elastic modulus of 10 GPa. This can be seen as an upper limit of what the solidified lunar simulant could possibly achieve. This best fit equation compares well with the previously determined elastic modulus average values reported in Section 4.2: the mean modulus of elasticity for low porosity was 8.4 GPa and for high porosity 5.5 GPa. Using Equation (34) for 1.44% porosity results in an elastic modulus of 9.4 GPa, and for 11.78% porosity results in an elastic modulus of 5.5 GPa.

The four maximum failure values for the samples are plotted against porosity using the first standard deviation as error bars in Figure 4-22.

Figure 4-22 – A plot of the maximum failure and porosity values for data from Gualtieri and Bandyopadhyay (2015) and this research. The ~0.4% and ~8.4% porosity data points were from Gualtieri and Bandyopadhyay and the 1.4% and ~12% were from this research. The error bars shown are for one standard deviation from the mean.
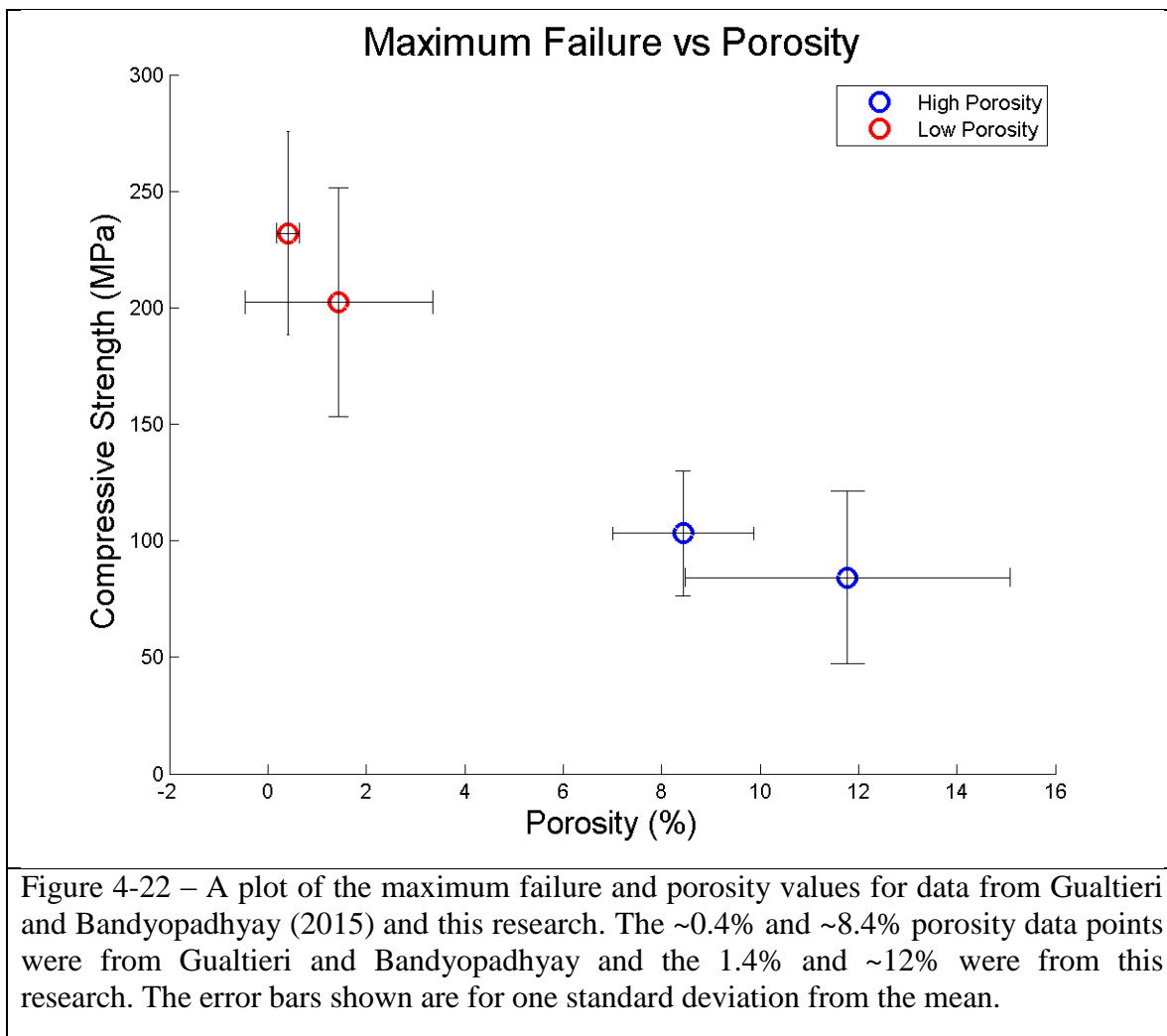
Looking at the four data points, a reevaluation of the linear fits of Section 4.5 should be performed. Remembering that different average porosities were calculated for each set, both high and low porosity values reside within each other's compressive strength error bars. For different porosities, the compressive strength values correlate well. The two sets of data for high porosity both reside inside each other's error bars as well. Since there are four different data points based on different average porosities, should these points be treated as independent porosities or as two, high and low, porosities? The error bars for compressive strength encompass both averaged data points of the high and low porosity

sets. Because of this error range on compressive strength, the four data point averages should be treated as two different porosity sets. There are tighter statistical error bars on the porosity percentages of each sample set, this should argue that the four points should be analyzed independently. However, the resolution of the porosity measuring method should be questioned. Uncertainty also exists in the uniformity of the porosity distribution through each sample as well. The more conservative approach is to continue treating the porosities as a two, low and high porosity, sets. Seeing no convincing argument to attempt a non-linear fit across the four data points, a linear fit between the two low and the two high porosity data points was made and seen in Equation (35), where y is compressive strength in MPa and x is the porosity in percent.

$$y = -13x + 277. \qquad\qquad \textbf{(35)}$$

Next a comparison with an equivalent solid material is made using the linear fit equation and previously calculated solid material properties. These values set the theoretical upper limit for the compressive strength of the solidified lunar simulant material. Extrapolating from the Equation (35), the linear best-fit produces a solid, 0% porosity, compressive strength of 277 MPa.

Comparing this new linear fit value with that from Section 4.5, which, when extrapolated to 0% porosity, resulted in a compressive strength of 219 ± 51 MPa. The 277 MPa value compares well and resides within the first standard of deviation error bound. We thus consider that the two compressive strength linear curve fits from Section 4.5 and Section 4.10 compare very well. Which equation is more accurate or reliable

requires further analysis. Further sample testing should be performed for increased accuracy.

Both research presented here and performed by Gualtieri and Bandyopadhyay attempted to calculate a sintered solid compressive strength value. Gualtieri and Bandyopadhyay used the Ryshkewitch Equation (36) to calculate the sintered solid density compressive strength value.

$$\sigma = \sigma_0 e^{-BP} \qquad\qquad \textbf{(36)}$$

Where σ is the strength of the porous material, σ_0 is the strength of the non-porous body of the same material, P is the porosity expressed as a fraction, and B is the slope of ln σ vs P, a material constant. For σ_0 = 240.7 MPa and 0.123 = B.

The method used in this research to calculate the 0% porosity compressive strength was discussed in more detail in Section 4.5. After taking a linear fit of the averaged low and high porosity compressive strengths then extrapolating to 0% porosity; 219 ± 51 MPa was the calculated to be the 0% porosity compressive strength for sintered lunar simulant from this research. Gualtieri and Bandyopadhyay performed the same calculation using the Ryshkewitch equation to calculated a 0% porosity compressive strength for sintered lunar simulant to be 230.7 MPa. Using two distinctly different methods, and two different sintered sample sets to calculate the 0% porosity compressive strength produced very similar results with only about 10 MPa difference.

In summary, it is indeed very difficult to reliably produce a single porosity sample set. Further investigation is needed to determine the effects of pressing larger scale

samples and if the variation in surface porosity to inner porosity could be a load bearing problem for the material.

Chapter 5.   Application of data

5.1 Summary of Material Properties

Our goal for the data collected and analyzed was to characterize new material properties to be used in designing a lunar structure or other infrastructure such as roadways. Without any access to the lunar materials for testing, simulants were characterized. These material properties can be useful for preliminary designs of lunar structures. Table 5-1 summarizes our results for the low and high porosity. Premature failures occurred during several tests, possibly due to the unground surfaces of the samples prior to compression testing. More experience at preparing such samples would improve their quality.

Material Properties at Maximum Failure	Low Porosity All Data (n=8)		High Porosity All Data (n=8)		Units
	Mean	STD	Mean	STD	
Compressive Strength	202.3	49.0	84.3	37.0	MPa
	29.3	7.1	12.2	5.4	ksi
Bulk Modulus	5961	1693	3586	2062	MPa
	864.6	246	520.2	299	ksi
Elastic Modulus	8358*	748	5475**	782	MPa
	1212	108	794	113	ksi
Torsion Modulus	3300	-	2198	-	MPa
	479	-	319	-	ksi
Average Density†	2.6	0.1	2.2	0.1	g/cm^3
Poisson's Ratio	0.266	-	0.246	-	-

*n=6, **n=5, †From unloaded measurements

Table 5-1 – Summary of the experimental sintered samples material properties. STD is the first standard deviation for each mean value.

Comparing the calculated material properties for the experimental sintered lunar regolith simulant samples to other proposed types of lunar ISRU is difficult for several reasons. First, there are no standards for material property testing of lunar ISRU materials. Simulants are fabricated subject to available resources available and test facility capabilities. Finally statistical sample size of the materials tested should also be clearly stated. The manufacturing and testing of simulants is costly and time consuming, sometimes resulting in sample sizes that are too small for statistically significant results. This can be a limitation of our work, even though the data generated is useful in its own right, but also from a qualitative perspective. Table 5-2 shows compressive strength values for five simulated lunar materials from our literature review.

	Compressive Strength	
	(Mpa)	(psi)
Geothermite, simulant & aluminum[1]	10 - 18	1,450 - 2,611
Additive manufacturing, simulant & binding agent[2]	20	2,951
Lunar sulfur concrete[3]	31	4,500
Lunar concrete[4]	74	10,000
Sintered lunar simulant[5]	203 - 232	29,400 - 33,600
Sintered lunar simulant[6]	77 - 237	11,168 - 34,374

Faierson[1], Cesaretti[2], Houssam[3], Lin[4], Gualtieri[5], Indyk[6]

Table 5-2 – Measured compressive strength values for various lunar resource derived structural materials.

From Table 5-2, three ranges of materials can be identified that also share similar manufacturing techniques. There appears to be a low middle and high range of compressive strength values. On low side are the geothermite and the additive manufactured with binding agent simulants with compressive strengths of about 20 MPa. In the midrange are the lunar concretes. The upper end includes two simulants with an

order of magnitude greater compressive strength. It is noteworthy that the sintered lunar simulants in Table 5-2 were produced by the same process and independently compression tested. The porosity of the sintered lunar simulant can be used to adjust its compressive strength.

Even without increased quality control or refined manufacturing, lower grade high porosity sintered lunar regolith is expected to be stronger than geothermic or concrete based lunar structural materials.

One material of lunar structural importance that is omitted from the above table is cast basalt. Cast basalt was first suggested as a potential lunar structural material by Happel et al. (1992) and has been advocated by Benaroya et al. (2002, 2012) as a main component of an ISRU based lunar structure. Happel et al. (1992) used the assumed cast basalt properties of ultimate compressive strength of 538 MPa (78,000 psi) for his calculations. In the literature review, we could not find testing of cast basalt for ISRU structural material. However promising cast basalt is with a compressive strength in excess of twice the tested sintered lunar simulant, additional work should be performed to confirm its plausibility in the lunar environment and for verification of its material strength. One lunar effect not accounted for in our testing is the reduced lunar gravity. From what is known about sintering in microgravity or reduced gravity, greater levels of distortion of the product can be expected. The specifics of controlling this distortion through forms or finishing work in reduced gravity are yet to be investigated.

Material selection is not as easy as comparing a single material property. The caveat being a single material property is rarely the sole consideration for material selection. Tensile strength, toughness, fracture resistance and other properties all need to

be considered when choosing the composition of load bearing members, especially in as difficult an environment as the Moon's surface.

Aside from the fundamental material properties, fabrication processes need to be considered as well. Reducing initial and post processing time and equipment would be greatly beneficial to making a certain material more attractive for use. All the materials discussed here depend on extracting the lunar regolith from the surface, so excavating equipment will be required regardless of lunar regolith derived ISRU. *Utilizing the regolith in its raw form has the advantage of not requiring refining of the raw minerals out of the regolith. Refining would require additional equipment for this additional step which increases transportation from the Earth to the Moon cost, as well as increase the complexity of manufacturing construction material on the Moon, leading to an increase in the chance of mechanical malfunction and down time of manufacturing in the lunar environment.*

5.2 Application to Lunar Structures

The development of new space capabilities is a difficult task and should be approached as such. Achieving a manned presence on the Moon would mirror such successful space programs as the development and implementation of the Apollo program or the construction of the International Space Station (ISS). For both, incremental steps were taken to prove new technology before proceeding to grander, more advanced challenges involving human lives. The development of a manned lunar outpost or base would have to be implemented in a similar deliberate approach.

Lunar development would be implemented in three major phases as outlined by Happel et al. (1992), Benaroya et al. (2002) and Cohen (2002). The first phase would

consist of transporting prefabricated modules from Earth and assembling them on the Moon over multiple missions. Phase two would allow for a union of terrestrial and lunar fabricated components and modules requiring assembly on the lunar surface. Finally, phase three structures would be comprised significantly of lunar ISRU structural materials. Of course, no specific ISRU based structural material has been selected for the final two phases because of the limited practical understanding of lunar materials that would need to be developed during phases one and two development. This is in part because the technology is not mature enough to make educated decisions on the optimal ISRU manufacturing process. An evaluation period of testing an ISRU manufacturing process and developing structural material could take place during phase one and phase two of lunar development, allowing for actual structural ISRU based material to be ready for phase three. This is regardless of how much terrestrial based lunar simulant testing is performed. Results presented in this research work suggest sintered lunar regolith should warrant early investigation for manufacturing on the lunar surface, possibly during the first phase of establishing a lunar presence.

Deciding which applications may be suitable for an ISRU structural material requires additional consideration. Structural design for the lunar surface is a complex process that depends on many factors. In particular are the $1/6^{th}$ Earth gravity, required internal pressurization for habitability, temperature gradients, radiation shielding, micrometeorite impacts and the effects of lunar dust. Static loading conditions would have the benefit of the reduced lunar gravity. All of these factors can greatly affect the expected and unexpected loading conditions that the structure would need to endure. Cements and ceramics are strongest under compressive loads and weaker for tensile

loading in comparison to other structural materials, such as metals. Terrestrially, structures that are in compression last the longest, but structures in tension are the most efficient. Specific structural members for a phase two or phase three lunar habitat would need to be evaluated on individual merits if sintered lunar regolith would be appropriate. The compressive strength values measured for sintered lunar simulant suggest that sintering actual lunar regolith could form material suitable for very high compressive loads. Offering additional versatility, if a less strong material is desired, this can be accommodated by adjusting the porosity of the sintered lunar regolith. Some examples of structures that are required to handle high compressive loading include static structures that are used for the following: load bearing members, road surfaces, dust mitigation, or launch and landing pads. Terrestrial building and construction codes govern the quality and acceptable methods of constructing these types of structures. Ettouney and Benaroya (1992) initiated the discussion on lunar codes, but no lunar building and construction standards yet exist.

From solely a material strength perspective, a tiered hierarchy can be envisioned where low, medium and high grades of lunar materials are selected for varying demand uses. Geothermic structural lunar material could be at the low end of the scale for applications requiring lower strength. Sintered lunar materials could occupy the high end, satisfying the needs of higher strength applications. If sintered lunar regolith were to prove to be the best all-around material from strength and manufacturing perspectives, then it very well could be the sole material derived from ISRU resources.

Not all structural applications will depend on the strength of the material. Operating in the lunar environment is difficult and demanding. Manufacturing processes

will need to be optimized to use the available resources and consumables sparingly and efficiently.

5.3   *Suggested Manufacturing Processes*

The sintering process for producing the samples tested in this research involved two main actions, pressing the lunar simulant followed by placing the sample into an oven for firing. Both of these steps are possible in the terrestrial environment and both could be implemented on the Moon, though extra considerations will exist for the lunar manufacturing process. Some questions that will need to be addressed are as follows. Is this process to be performed by astronauts? Will the required equipment be transported from Earth or constructed from ISRU? Should this be an autonomous robotic manufacturing process? Will some kind of robotic and human interaction be required to implement this method of manufacturing structural members? The answer to these questions would significantly impact the overall architecture, design and process of the manufacturing machinery.

For small structural members, the manufacturing process here would be effective and efficient. For applications where sintered bricks could be envisioned, possibly foundations or road surfaces, this process could even prove to be ideal. But large structural members would require a large pressing apparatus and a large oven for sintering. This machinery could either be cumbersome to transport from the Earth or difficult to construct on the Moon. A goal should be set to fabricate large sintered structural members with relative ease.

It could be possible to construct large-scale sintered structural components using additive manufacturing processes. Incorporating microwave sintering, additive

manufacturing, pneumatic excavation and autonomous construction could provide a capable method to generate structural ISRU material. Incorporating the previous research reviewed in Section 1.4 a system could be envisioned to construct either members or complete structures.

Several systems have already been tested and analyzed which could be integrated to form large-scale sintered structural components. Alternative sintering methods have already been tested. Examples include microwave sintering of actual lunar regolith by Taylor and Meek (2005) and sintering simulant through a Fresnel lens by Cardiff and Hall (2008). The architecture of additive manufacturing would be similar in configuration to the D-Shape printer used by Cesaretti et al. (2013) or LENS used by Balla et al. (2012). The additive manufacturing work plane should meet the scale of the structural members. Ruess et al. (2006) envisioned segments in length of 2.5 m (8.2 ft) that would be assembled together in segments to construct a lunar structure capable of supporting six astronauts. The D-Shape printer has a work plane of 6 m by 6 m (19.7 ft by 19.7 ft) and should be expected fabricate the full member lengths required in the Ruess et al. (2006) calculations. With an additive manufacturing process chosen, a preferred sintering method selected, and a scale requirement set, a large-scale additive manufacturing system can be envisioned.

A fixed system similar in appearance and scale to the D-Shape printer but with a microwave 'printer head' could be used. The working structural material would be unrefined lunar regolith. The base work plane would be a leveled segment of the Moon's lunar regolith with walls to encompass the ends of the build area. This leveling could be performed with a vibratory roller or a vibratory blade to ensure the lunar regolith surface

is flat and compact. After the flat surface has been established, the 'printer head' of the microwave could be passed across the surface and sinter the desired cross-sectional shape of the component to be fabricated. Next, a layer of lunar regolith would be deposited on the previously sintered surface at a slightly elevated level, then made flat and the 'writing' process would repeat, sintering the freshly deposited lunar regolith to the previously sintered lunar regolith. This would continue until the component was formed in its entirety. The next step would be to extract the component that would now be buried in lunar regolith. A novel method of excavating lunar regolith has been proposed by Zacny et al. (2010), where a nozzle is inserted into lunar regolith and injects a gas. This gas then disperses outward due to the vacuum and kicks out the surrounding regolith. A similar method could be implemented to remove the non-sintered lunar regolith, gaining access to the now sintered component.

Chapter 6.   Summary and Future Work

This research heavily depends on the notion that developing fundamental material properties of a new lunar regolith derived structural material will allow its proliferation for lunar structure design. For any new medium, material properties and elastic constants open the gateway to engineers to create and evaluate new structures and concepts. For this research, quantifying the material properties of sintered lunar simulant served as an analogue to sintered lunar regolith. Sixteen manufactured sintered samples of two different porosities created for this research underwent compression testing. The load and deflection were recorded and analyzed with material properties evaluated.

The effect of porosity on these properties was investigated and it was found that lower porosity percentages resulted in a stronger material. The modulus of elasticity and bulk modulus were calculated for low and high porosity sintered lunar simulant. Additional material properties evaluated included: compressive strength, stress, strain, toughness, and Poisson's ratio. Compressive strength histograms were created, as well as compressive strength as a function of porosity.

The three qualities of the lunar surface, the lunar regolith being a granular medium, the vacuum and a virtually limitless supply of thermal energy from the Sun, make the Moon an ideal place to utilize sintering as a manufacturing method. Incorporating these resources, a method of fabricating sintered lunar regolith by means of additive manufacturing was also proposed. Sintering lunar regolith simulant produces a structurally strong material that can be used as an analogue to what could be formed on the lunar surface with actual lunar regolith.

One difficulty was the premature failures that occurred during some of the tests and how to handle the data from those tests. It is believed that by refining the manufacturing quality control and the testing process of the samples of sintered lunar regolith, these premature failures could be greatly reduced. However, even using the data from initial failure data sets provided impressively strong compressive strengths. In comparison to other terrestrial concretes and lunar structural materials, sintered lunar simulant proved to have the highest experimentally tested compressive strength. This bodes well for comparable sintered lunar regolith that is expected to be similar if not stronger on the Moon since the lunar environment provides better conditions for the sintering process.

From measurements taken on actual lunar samples, almost three-quarters of one lunar regolith sample studied was composed of particles less than 150 μm in size. The highest compressive strength values were produced by the low porosity sintered samples that were sieved to be less than 215 μm in particle size. We expect that on the Moon, very strong low porosity sintered material is ubiquitous due to the effects of constant meteor bombardment. Future work should evaluate if un-sieved lunar simulant could produce usable and reliable samples with high compressive strengths. In addition to proposing further research work, additional improvement to the data presented in this research could also be made.

The data quality collected and presented in this research can be improved in several ways. First, by testing more samples, larger number of compression tests could be performed. This would increase the accuracy of the average and standard deviation of the maximum compression strength of the two porosity sample sets. Second, ensuring the top

and bottom of the sample surfaces are flat and smooth. The surfaces which mate with the compression plates must be flat to ensure no pressure concentration points occur. Loading the sample unevenly could reduce the maximum possible loading and may allow for premature failures of the sample. Creating a flat surface can be accomplished through grinding or milling the samples. Extra care must be taken as the samples can be very brittle and may be prone to fracture or crumbling if grinding is performed incorrectly, ruining the sample for compression testing. Third, by refining the manufacturing process for creating the samples, a higher quality with fewer imperfections can be expected. With more experience in manufacturing the samples and better quality control over the ones produced, fewer faults should be expected during manufacture. This should translate to an overall better quality sample, able to produce a narrower and more consistent range of loading data. Fourth, to gather better information on the overall effect of porosity on sintered lunar simulant, a wider range of porosities could be manufactured and tested. However, we can also say that even with the above issues, our samples showed remarkable strength.

For equal comparisons across various lunar materials, a standard for testing lunar samples should be created to ensure accurate comparisons. Better testing criteria are also needed. The terrestrial equivalents can be found in standards such as ASTM C39 'Standard Test Method for Compressive Strength of Cylindrical Concrete Specimens.' Lunar materials could have standards fashioned in a similar format.

Sintering lunar regolith is a process expected to take place on the Moon. Manufacturing testing can take place in an environment that better mimics the actual lunar environment. Sintering in a vacuum or in a microgravity environment should be

expected to produce samples with different elastic constant values, but the question of how different remains to be investigated. Additionally, by conducting manufacturing tests in a simulated environment, it is possible to gain a better understanding of the challenges faced in manufacturing. It would be very interesting to see how material properties for an oven-sintered sample, as produced for this research, would compare to a sample produced by an additive manufacturing process, such as selective laser sintering. Some questions to answer would be: do the variable thermal conditions between the two processes produce similar or different sintering results? Could additive manufacturing potentially repair sintered components that have fractured?

Further knowledge could be gained about sintered lunar regolith if reinforcement can be added during the fabrication process. With steel reinforcement, similar to reinforced concrete, tension loads would be handled much better, lending greater flexibility to structural member usage.

A complete design of a lunar structure using the material properties for the sintered lunar simulant presented here could be created. This would provide a better understanding of how much lunar regolith would be needed to construct a usable structure. This information would be valuable in providing criteria for excavation and manufacturing equipment needed to process and form the regolith into sintered material. An excellent starting point for this structural design would be the structure in the work by Ruess et al. (2006).

Impact resistance of porous material could be valuable and studied further. Though not investigated in this research, the ability for porous sintered regolith to absorb micrometeorite impacts should be promising. During the 1702 siege of Fort Castillo De

San Marcos in St. Augustine, Florida by English warships, the stone use to construct the fort was credited with saving it. This stone is called the coquina, similar to limestone but comprised of ancient seashells that had bonded together and is full of voids. It allowed the cannon balls to be cushioned and softened the impact, subsequently minimizing any cannonball damage. *Micrometeorite impacts could be mitigated or better controlled by a similar porous outer structural layer.* This outer layer could be comprised of a high porosity sintered lunar regolith. If sintered lunar regolith proved useful for micrometeorite shielding, it could be envisioned that the more stable sintered material replace mounds of raw lunar regolith on top of lunar structures for shielding. This could be one more suitable application of this new material.

Sintered lunar regolith has shown great potential to become a staple for lunar ISRU structural material due to its impressive material properties, ease of production and its readily available source material. In order to further explore and develop the Moon, future long-duration surface missions will increasingly depend on ISRU. With further research into the relevant applications of materials such as sintered lunar regolith, there is hope that establishing a permanent presence on the Moon could occur in the near future.

Appendix A   Additional Figures

A.1 Tables of Computed Data

Test numbers 1 through 8 were low porosity samples, and tests 9 through 16 were high porosity samples.

Test Number	Porosity Group	Mass (grams)	Height 1 (mm)	Height 2 (mm)	Height 3 (mm)	Average Height (mm)	Diameter 1 (mm)	Diameter 2 (mm)	Diameter 3 (mm)	Diameter 4 (mm)	Diameter 5 (mm)	Average Diameter (mm)
1	<212	5.43	19.589	19.626	19.54	19.585	11.632	11.645	11.546	11.522	11.514	11.5718
2	<212	5.35	19.02	19.02	19.024	19.02133	11.619	11.645	11.705	11.76	11.738	11.6934
3	<212	5.39	19.353	19.346	19.378	19.359	11.831	11.789	11.687	11.662	11.642	11.7222
4	<212	5.65	20.531	20.536	20.547	20.538	11.79	11.723	11.648	11.58	11.571	11.6624
5	<212	5.49	19.391	19.463	19.418	19.424	11.773	11.708	11.721	11.741	11.703	11.7292
6	<212	4.72	16.837	16.905	16.983	16.90833	11.744	11.703	11.674	11.672	11.629	11.6844
7	<212	5.25	18.945	18.875	18.859	18.893	11.679	11.791	11.883	11.87	11.827	11.81
8	<212	5.44	20.365	20.171	19.99	20.17533	12.171	12.161	12.115	12.033	11.923	12.0806
9	>212	5.09	19.474	19.412	19.329	19.405	12.042	12.142	12.161	12.182	12.151	12.1356
10	>212	4.18	16.581	16.521	16.626	16.576	12.448	12.499	12.508	12.538	12.595	12.5176
11	>212	4.94	18.767	18.757	18.835	18.78633	12.08	12.156	12.165	12.172	12.144	12.1434
12	>212	5.11	19.905	19.847	19.808	19.85333	12.041	12.104	12.172	12.222	12.332	12.1742
13	>212	5.11	19.128	19.16	19.163	19.15033	12.048	12.132	12.172	12.177	12.16	12.1378
14	>212	5.05	18.802	18.785	18.755	18.78067	12.059	12.094	12.134	12.127	12.134	12.1096
15	>212	5.00	19.217	19.265	19.335	19.27233	12.556	12.546	12.532	12.508	12.51	12.5304
16	>212	4.56	17.683	17.704	17.764	17.717	12.285	12.343	12.375	12.347	12.384	12.3468

Test Number	Porosity Group	Load Initial (kN)	Load 0.2 mm (kN)	Load Intial Failure (kN)	Load Maximum (kN)	Height Initial (mm)	Height 0.2 mm (mm)	Height Intial Failure (mm)	Height Maximum (mm)	Deflection Initial (mm)	Deflection 0.2 mm (mm)	Deflection Maximum (mm)
1	<212	0.063	5.911	26.352	26.352	19.585	19.380	18.990	18.990	0.205	0.595	0.595
2	<212	0.618	6.249	20.929	21.369	19.021	18.816	18.491	18.366	0.205	0.530	0.655
3	<212	0.328	4.844	24.431	24.431	19.359	19.149	18.694	18.694	0.210	0.665	0.665
4	<212	0.011	3.589	15.166	20.078	20.538	20.333	20.068	19.948	0.205	0.470	0.590
5	<212	0.556	5.934	20.567	26.054	19.424	19.214	18.899	18.694	0.210	0.525	0.730
6	<212	0.272	3.975	25.150	25.150	16.908	16.703	16.238	16.238	0.205	0.670	0.670
7	<212	3.715	11.218	15.980	21.026	18.893	18.688	18.548	18.318	0.205	0.345	0.575
8	<212	0.212	2.404	3.207	9.916	20.175	19.975	19.910	19.250	0.200	0.265	0.925
9	>212	0.192	2.588	10.755	10.755	19.405	19.200	18.885	18.885	0.205	0.520	0.520
10	>212	0.063	0.773	3.317	4.379	16.576	16.371	15.996	15.801	0.205	0.580	0.775
11	>212	1.501	8.945	15.775	16.082	18.786	18.586	18.431	18.411	0.200	0.355	0.375
12	>212	0.241	4.738	10.895	10.895	19.853	19.643	19.428	19.428	0.210	0.425	0.425
13	>212	1.262	5.353	13.374	13.374	19.150	18.950	18.705	18.705	0.200	0.445	0.445
14	>212	0.838	6.215	8.907	13.115	18.781	18.576	18.496	18.376	0.205	0.285	0.405
15	>212	0.305	1.720	4.924	5.231	19.272	19.072	18.822	18.682	0.200	0.450	0.590
16	>212	0.196	2.335	3.739	4.988	17.717	17.512	17.387	17.222	0.205	0.330	0.495

Test Number	Porosity Group	Volume Initial (mm^3)	Volume 0.2 mm (mm^3)	Volume Intial Failure (mm^3)	Volume Maximum (mm^3)	Density Initial (g/mm^3)	Density 0.2mm (g/mm^3)	Density Intial Failure (g/mm^3)	Density Maximum (g/mm^3)
1	<212	0.0021	0.0020	0.0020	0.0020	2636310	2664196	2718911	2718911
2	<212	0.0020	0.0020	0.0020	0.0020	2617033	2645545	2692043	2710365
3	<212	0.0021	0.0021	0.0020	0.0020	2580477	2608776	2672272	2672272
4	<212	0.0022	0.0022	0.0021	0.0021	2575492	2601459	2635811	2651668
5	<212	0.0021	0.0021	0.0020	0.0020	2615085	2643666	2687730	2717204
6	<212	0.0018	0.0018	0.0017	0.0017	2605504	2637481	2713008	2713008
7	<212	0.0021	0.0020	0.0020	0.0020	2536075	2563895	2583247	2615682
8	<212	0.0023	0.0023	0.0023	0.0022	2350943	2374481	2382233	2463908
9	>212	0.0022	0.0022	0.0022	0.0022	2269155	2293383	2331637	2331637
10	>212	0.0020	0.0020	0.0020	0.0019	2048876	2074532	2123166	2149368
11	>212	0.0022	0.0022	0.0021	0.0021	2269395	2293815	2313105	2315618
12	>212	0.0023	0.0023	0.0023	0.0023	2209478	2233099	2257811	2257811
13	>212	0.0022	0.0022	0.0022	0.0022	2304346	2328666	2359167	2359167
14	>212	0.0022	0.0021	0.0021	0.0021	2333698	2359453	2369658	2385133
15	>212	0.0024	0.0024	0.0023	0.0023	2104897	2126970	2155221	2171371
16	>212	0.0021	0.0021	0.0021	0.0021	2147505	2172644	2188264	2209229

Test Number	Porosity Group	Pressure Initial (KPa)	Pressure 0.2 mm (KPa)	Pressure Intial Failure (KPa)	Pressure Maximum (KPa)	Bulk Modulus 0.2 mm (MPa)	Bulk Modulus Intial Failure (MPa)	Bulk Modulus Maximum (MPa)
1	<212	600932	56205	250570	250570	5370	8248	8248
2	<212	5752902	58190	194885	198980	5399	6994	5778
3	<212	3039134	44882	226378	226378	4138	6590	6590
4	<212	107233	33595	141977	187956	3366	6204	6543
5	<212	5142421	54917	190343	241128	5080	7042	6416
6	<212	2539621	37074	234550	234550	3058	5919	5919
7	<212	33909523	102410	145877	191937	9438	7989	6307
8	<212	1845697	20977	27976	86511	2116	2130	1887
9	>212	1658163	22372	92984	92984	2118	3470	3470
10	>212	510944	6282	26954	35581	508	770	761
11	>212	12961019	77238	136207	138860	7255	7208	6956
12	>212	2068421	40699	93597	93597	3848	4372	4372
13	>212	10907960	46265	115581	115581	4430	4974	4974
14	>212	7277359	53960	77333	113874	4943	5096	5281
15	>212	2473011	13945	39934	42419	1344	1710	1386
16	>212	1637074	19505	31231	41661	1686	1677	1491

A.2   Load vs. Deflection - All Data
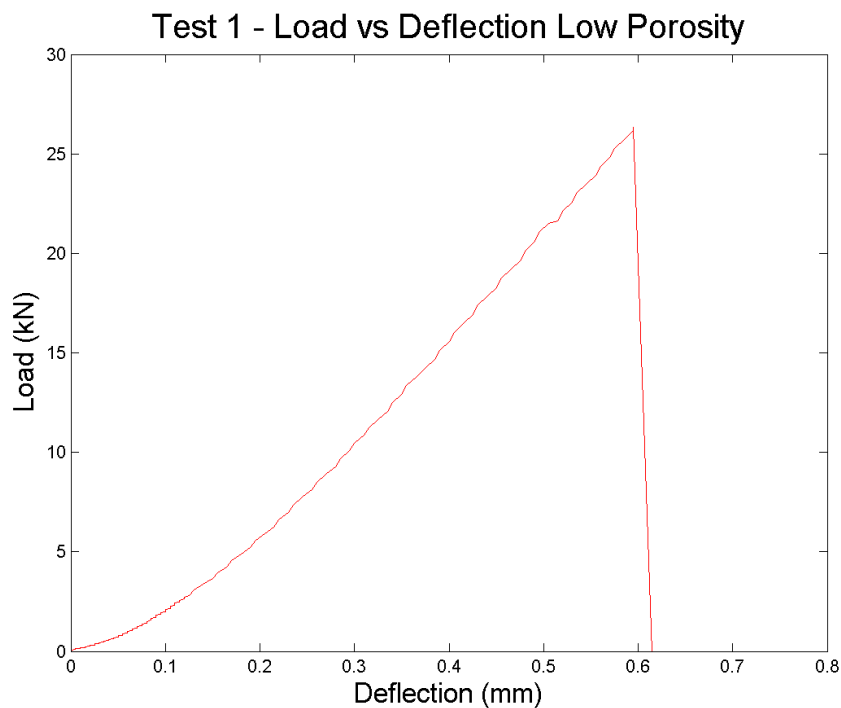
Test 1: This was a textbook example test, non-linear ramping before the start point, linear loading and deflection until the specimen failure. This was a very good test.
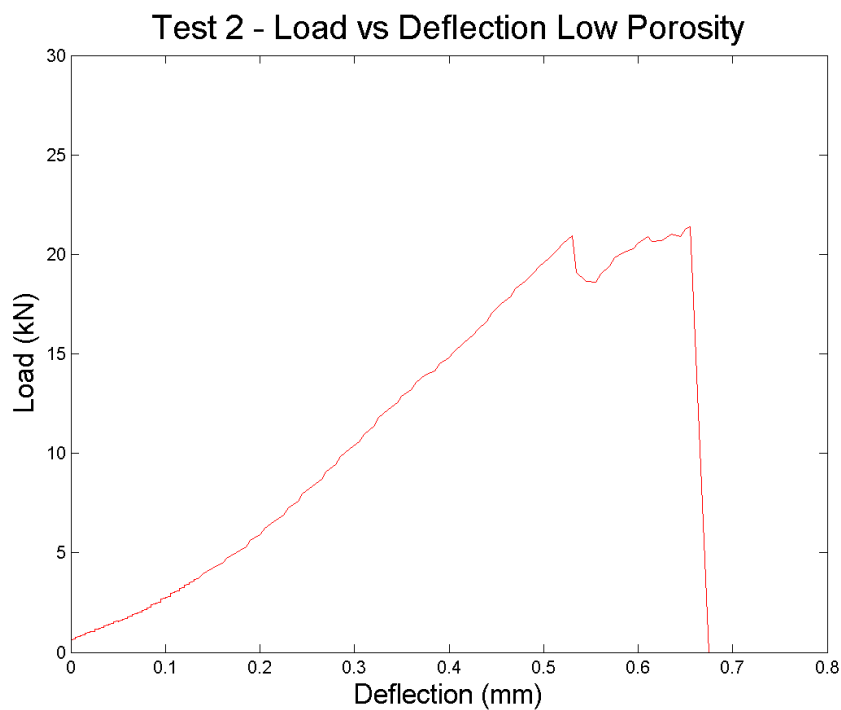
Test 2: The test experienced an initial failure but was able to recover to an about equal loading as the initial failure.

Test 3 - Load vs Deflection Low Porosity
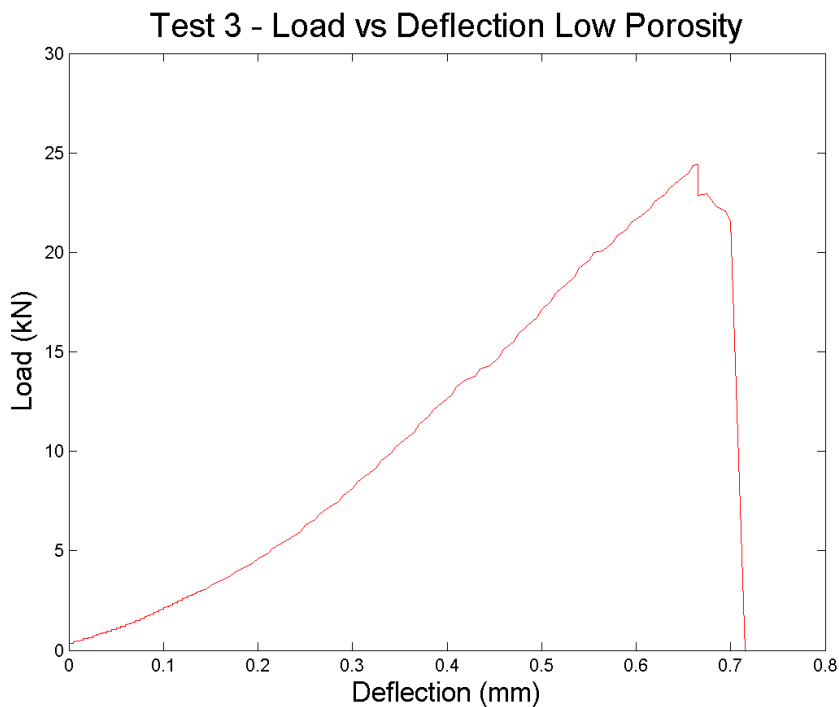
Test 3: A good test that did not recover after failure, obtaining one of the highest loading values measured. This test was similar in loading characteristics to Test 6.

Test 4 - Load vs Deflection Low Porosity
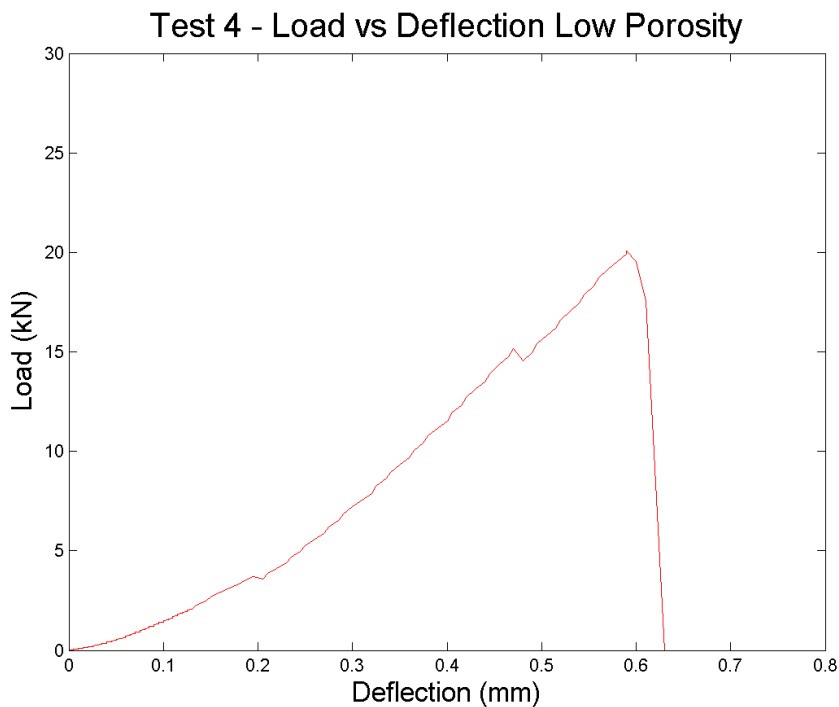
Test 4: A good test in which the specimen was able to recover from an initial failure and display a high load value. This test was similar to Test 5.
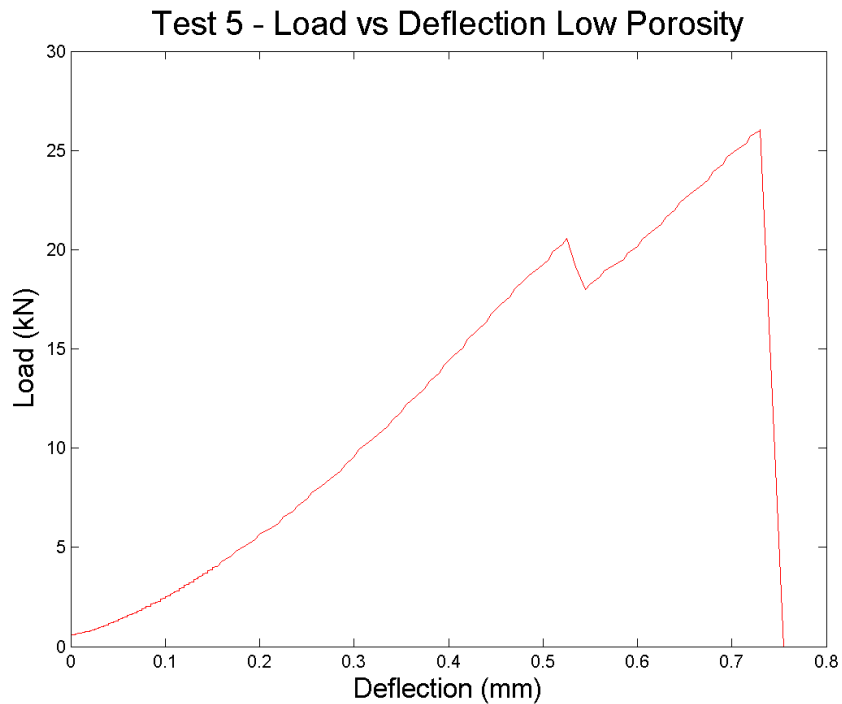
Test 5: A good test in which the specimen was able to recover from an initial failure and display a high load value. This test was similar to Test 4.
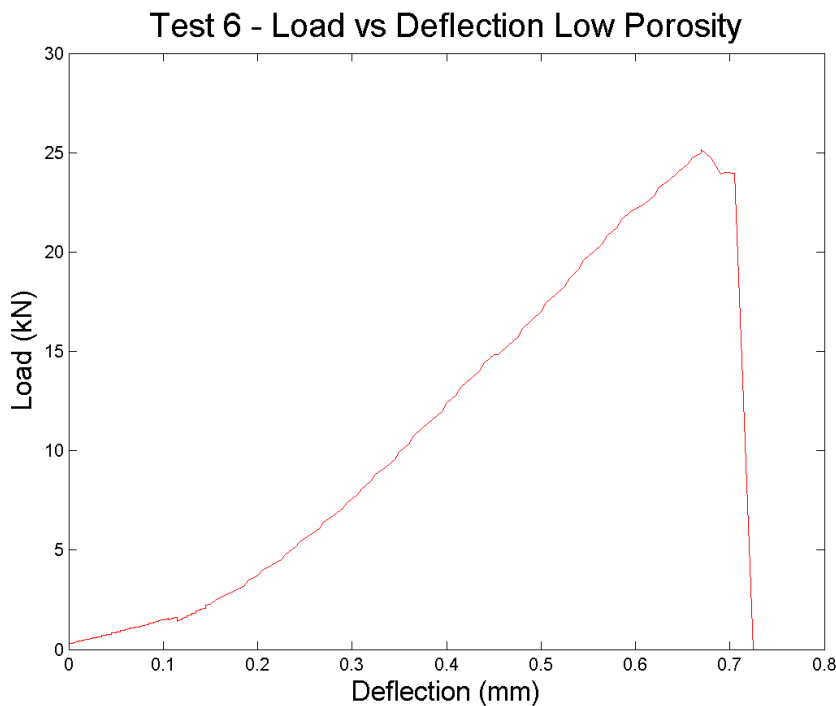
Test 6: A good test that did not recover after failure, obtaining one of the highest loading values measured. This test was similar in loading characteristics to Test 3.

Test 7 - Load vs Deflection Low Porosity
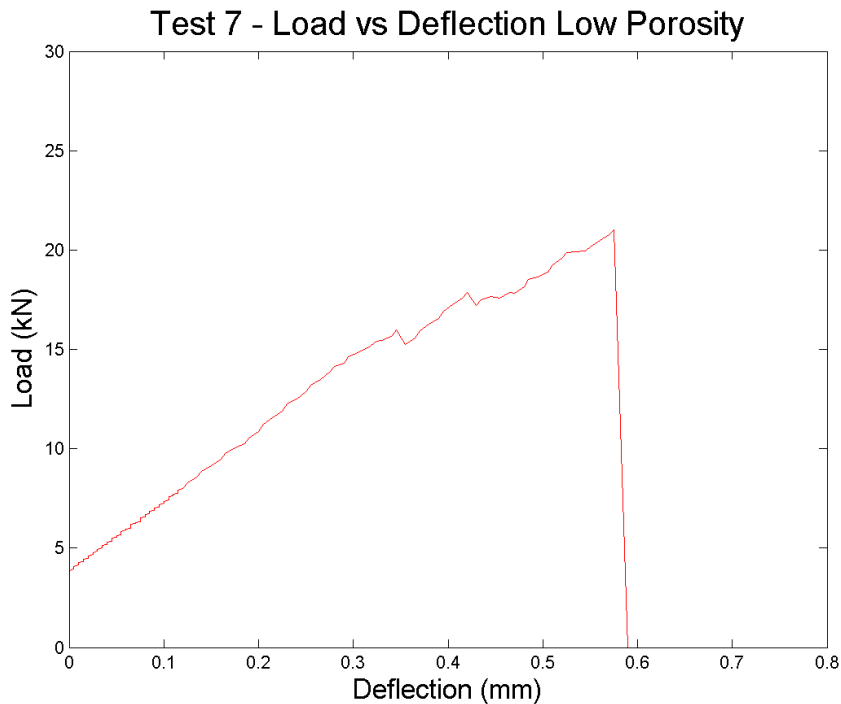
Test 7: A fair test where several initial failures occurred leading up to the maximum failure. Regardless of the initial failures, the specimen was still able to reach a high loading value.

Test 8 - Load vs Deflection Low Porosity
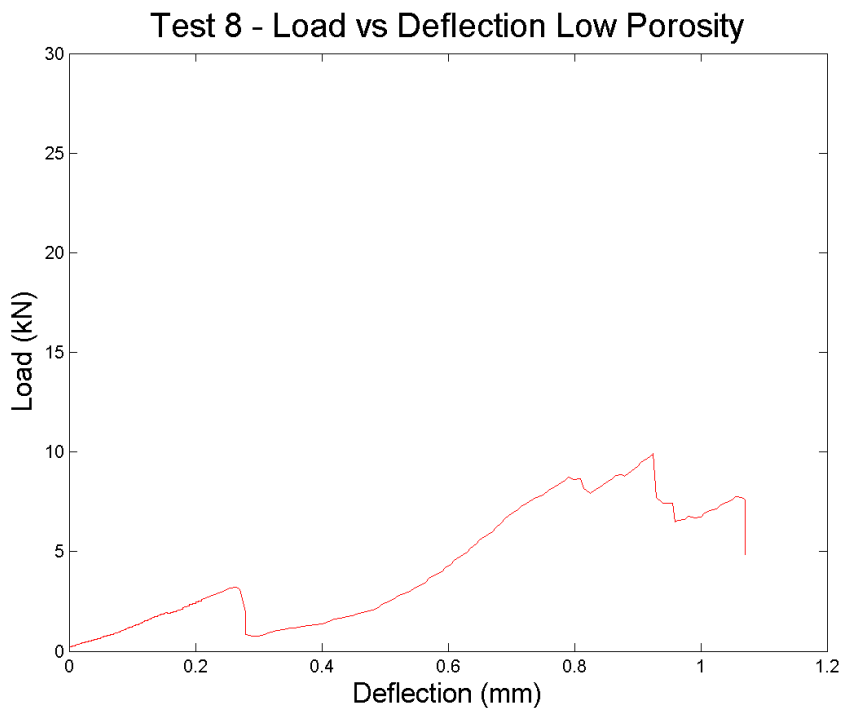
Test 8: A poor test in which the specimen crumbled during the test. A low loading value was recorded after a fracture midway through the specimen, contributing to a high deflection of the specimen.
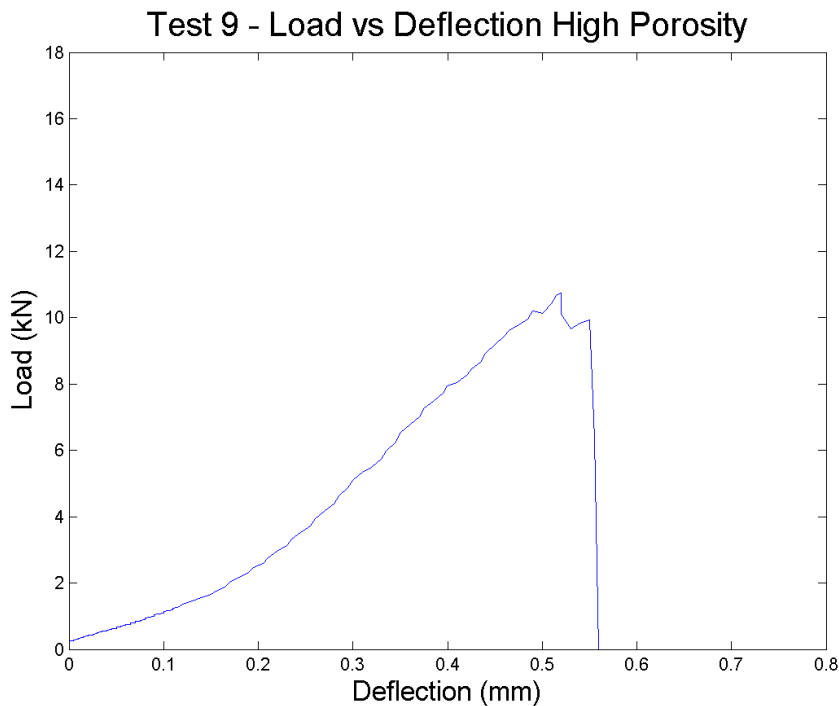
Test 9: A good test that did not recover after maximum failure. This test was similar to Test 13 in loading.
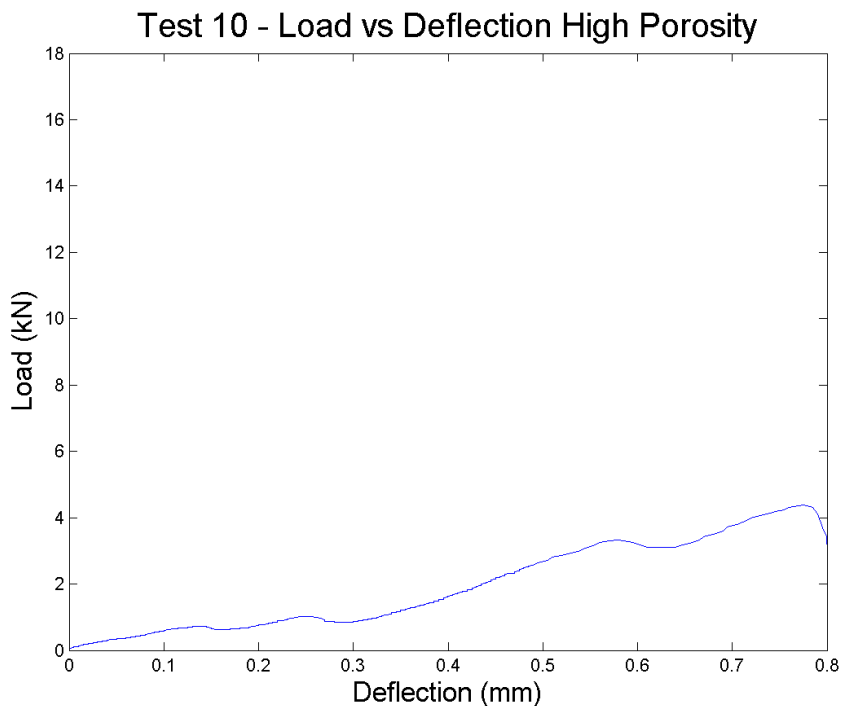
Test 10: A poor test in which the specimen crumbled during the test. A low loading value was recorded. High deflection was observed due to the specimen fracturing. This test was similar to Tests 15 and 16.
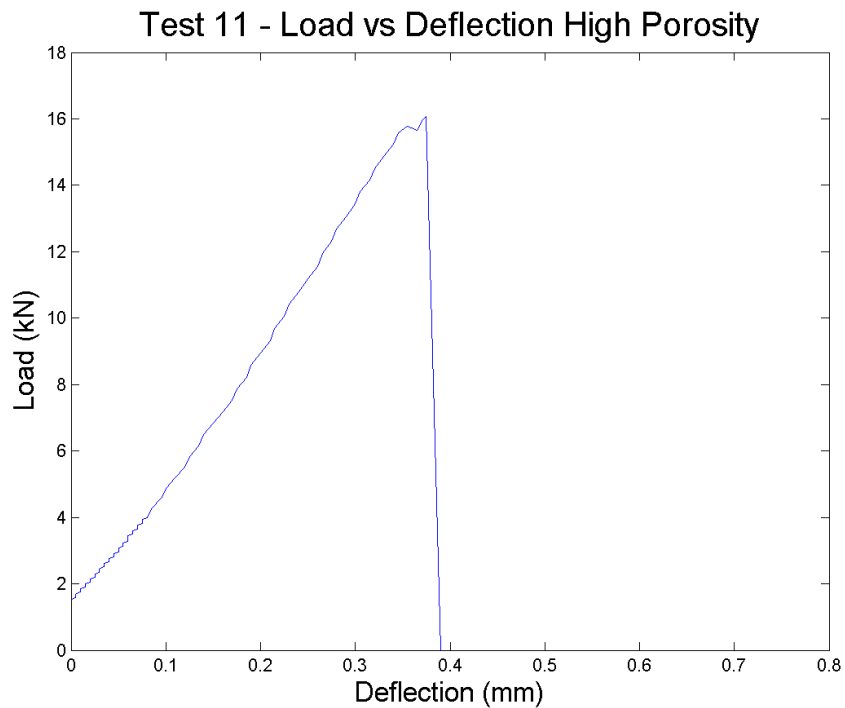
Test 11: A good test which exhibited a small initial failure towards the upper end of its loading.
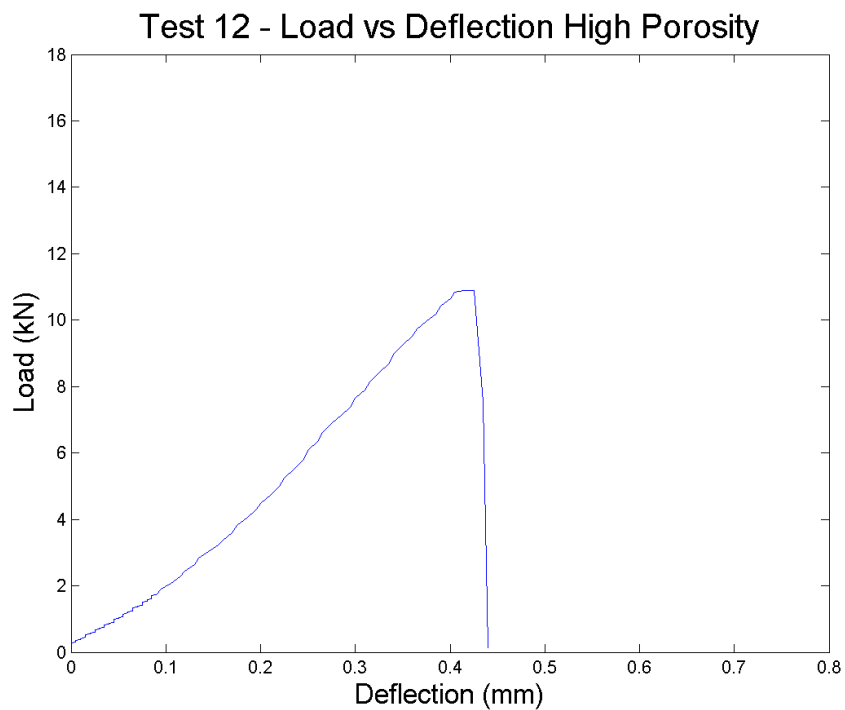
Test 12: A good test that only experienced a maximum.

Test 13 - Load vs Deflection High Porosity
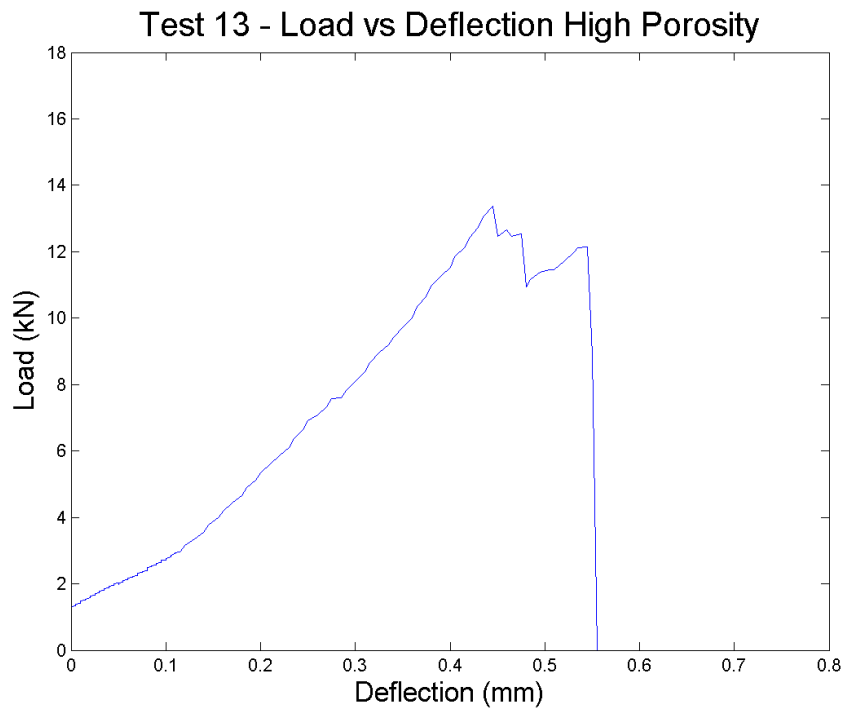
Test 13: A good test that did not recover after maximum failure. This test was similar to Test 9 in loading.

Test 14 - Load vs Deflection High Porosity
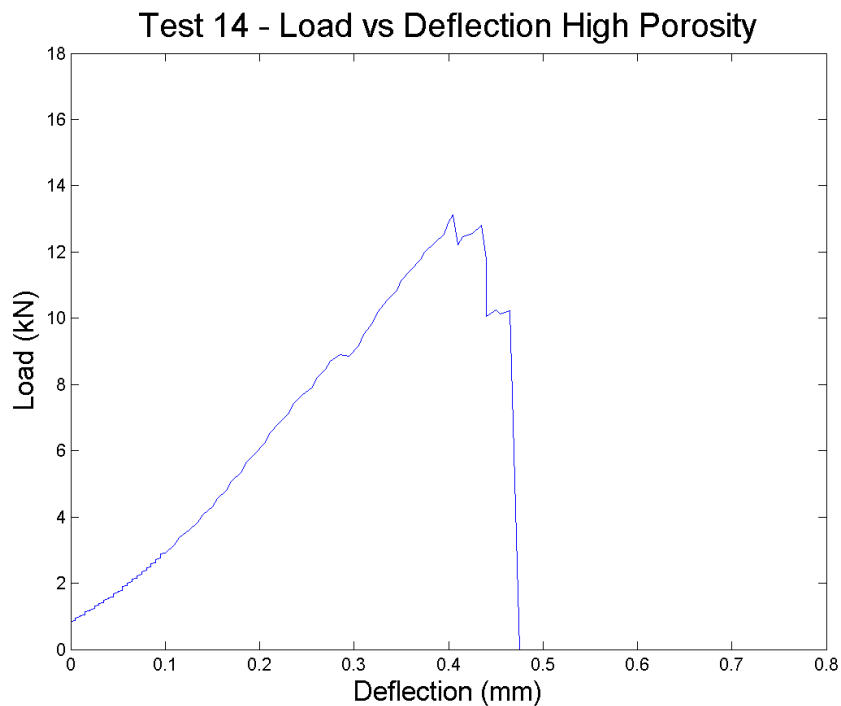
Test 14: A good test that did not recover after failure. This test was similar in loading characteristics to Test 9.
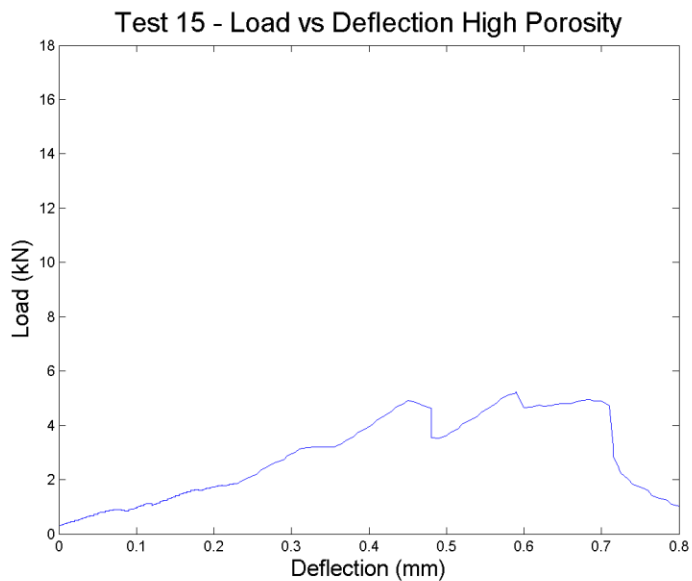
Test 15: A poor test in which the specimen crumbled during the test. A low loading value was recorded. High deflection was observed due to the specimen fracturing. This test was similar to tests 10 and 16.
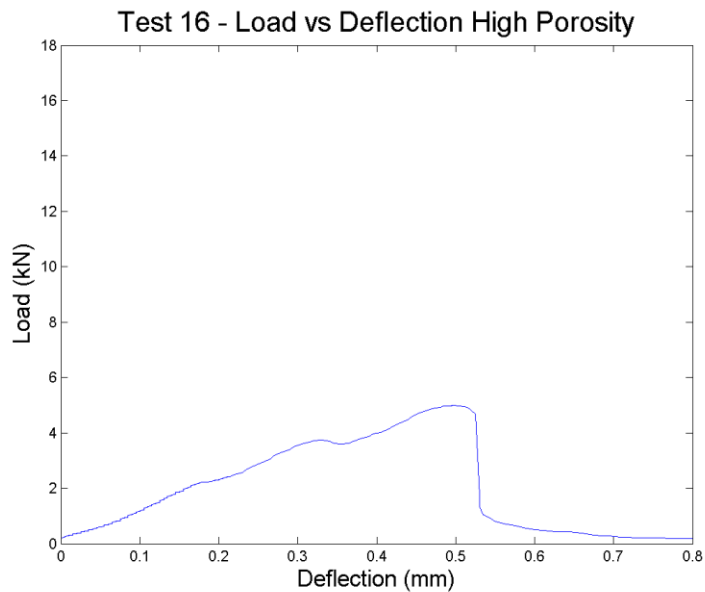
Test 16: A poor test in which the specimen crumbled during the test. A low loading value was recorded. High deflection was observed due to the specimen fracturing. This test was similar to tests 10 and 15.

A.3 Load vs. Deflection - Cut Data

The data presented in these figures are cut from the original data set. The initial load ramping up to the first 0.02 mm of compression is removed and data after the maximum failure of the sample is removed.

Test 1 - Load vs Deflection Low Porosity - start to max
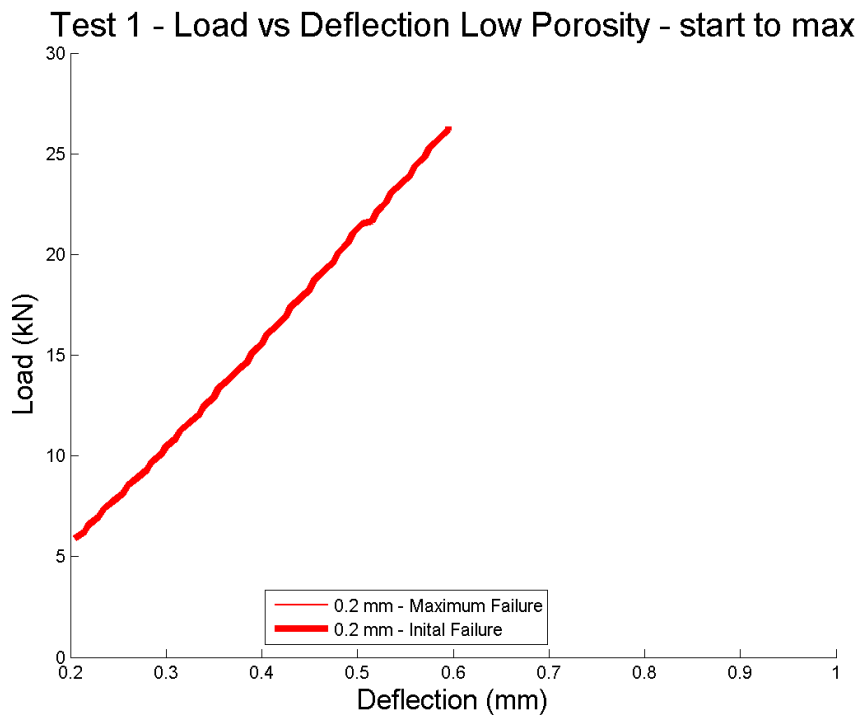
Test 2 - Load vs Deflection Low Porosity - start to max
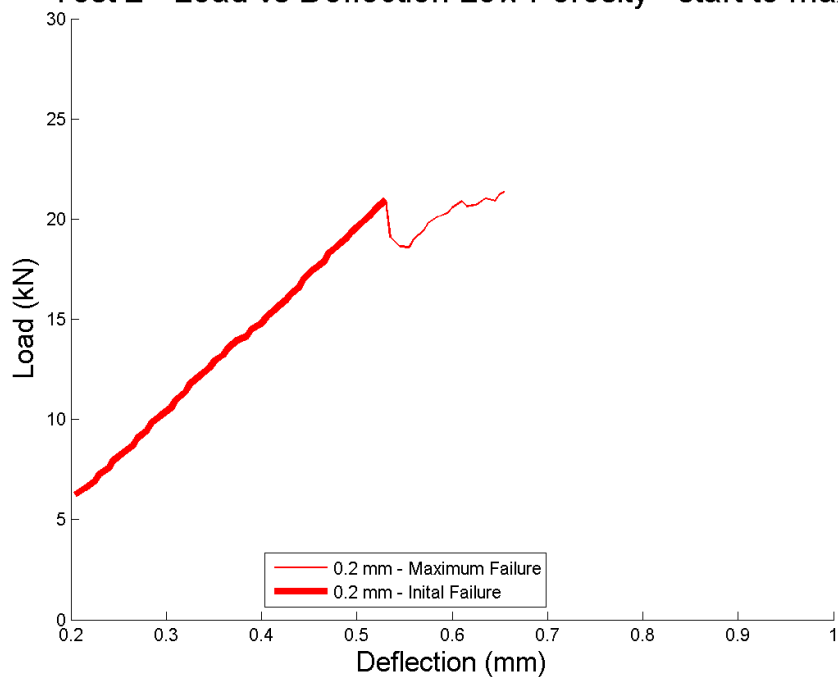
Test 3 - Load vs Deflection Low Porosity - start to max
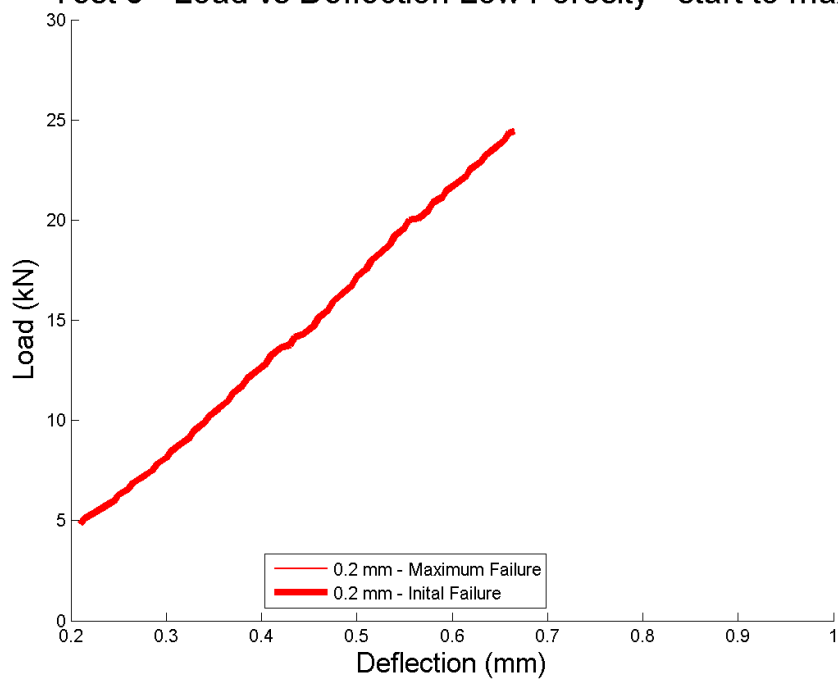
Test 4 - Load vs Deflection Low Porosity - start to max
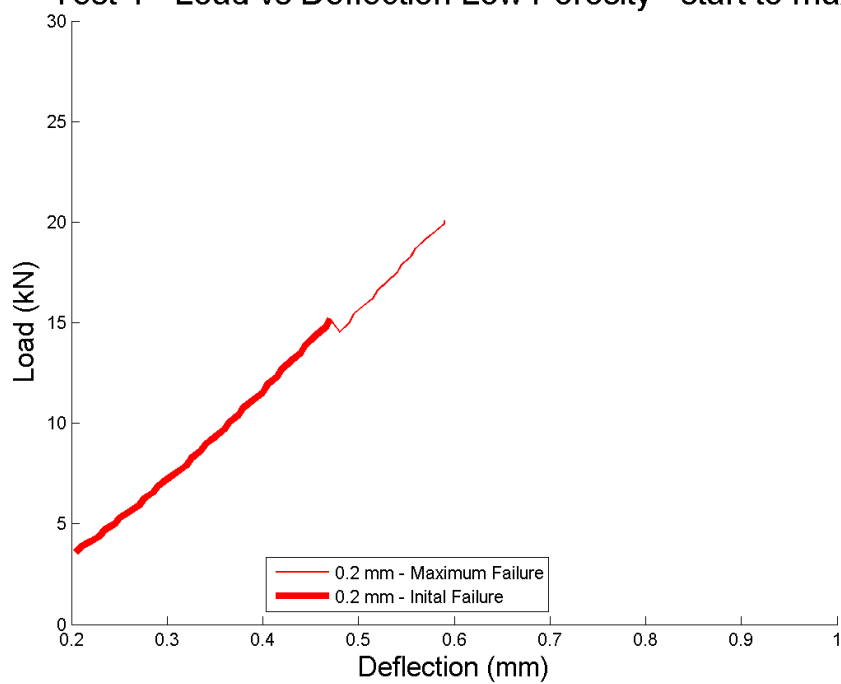
Test 5 - Load vs Deflection Low Porosity - start to max
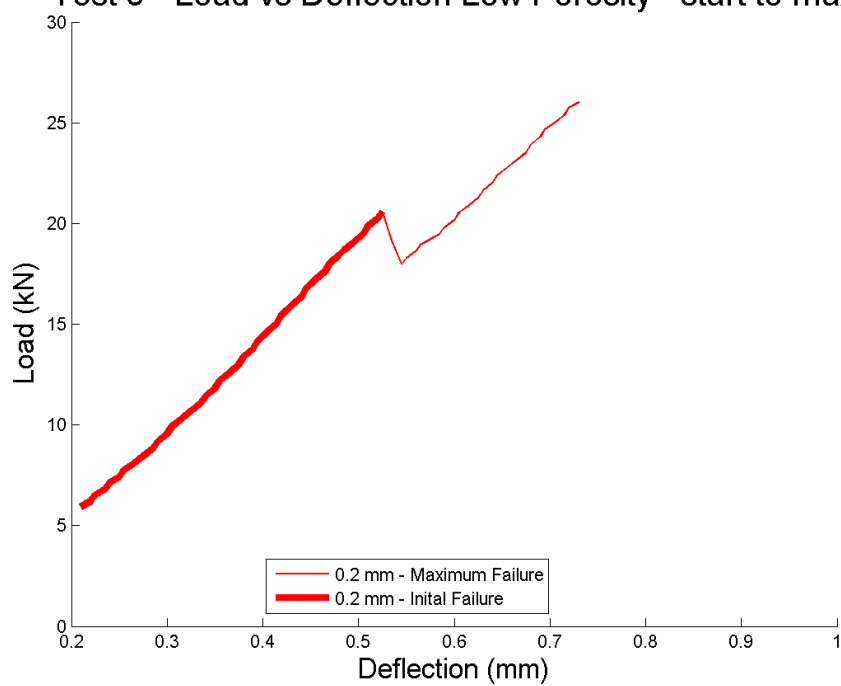
Test 6 - Load vs Deflection Low Porosity - start to max
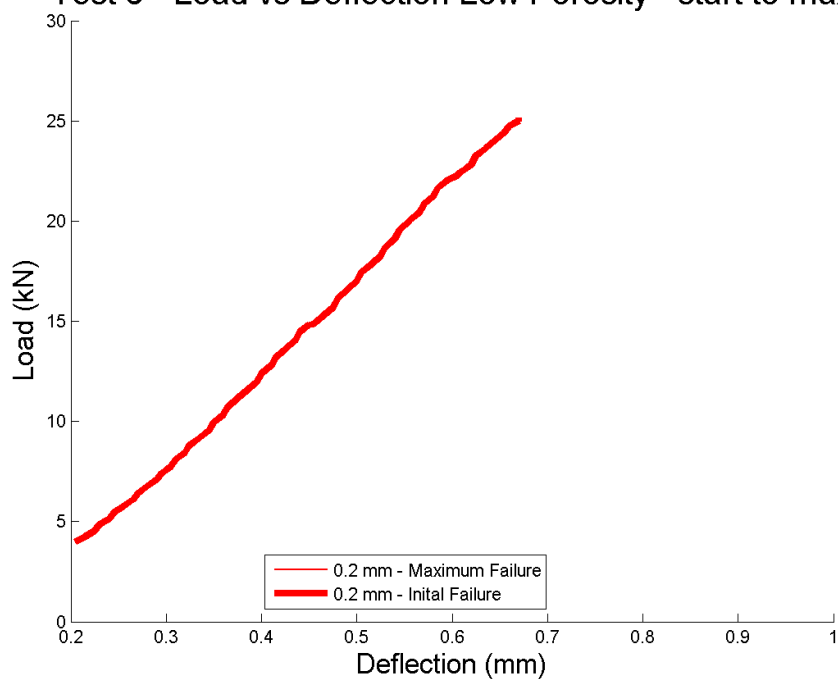
Test 7 - Load vs Deflection Low Porosity - start to max
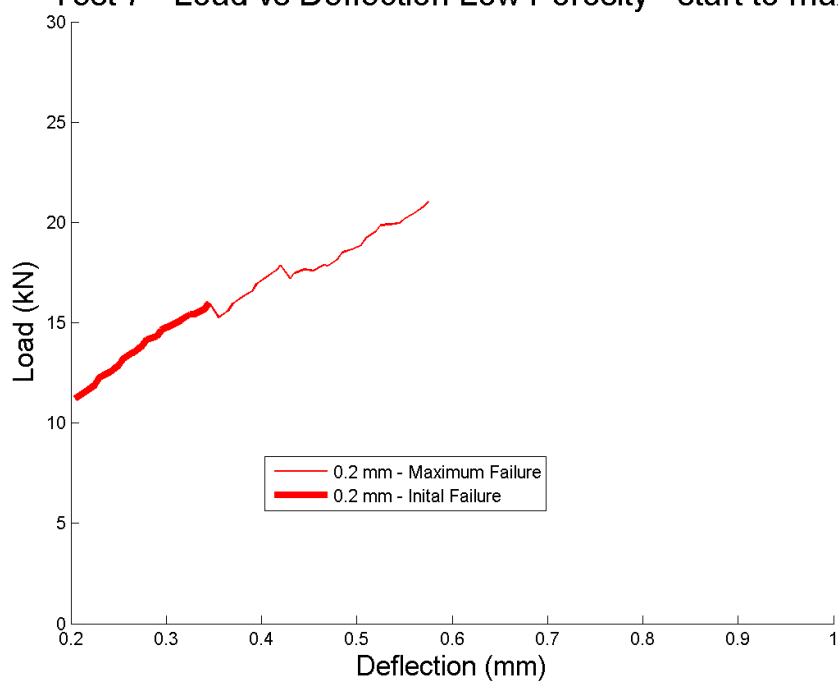
Test 8 - Load vs Deflection Low Porosity - start to max
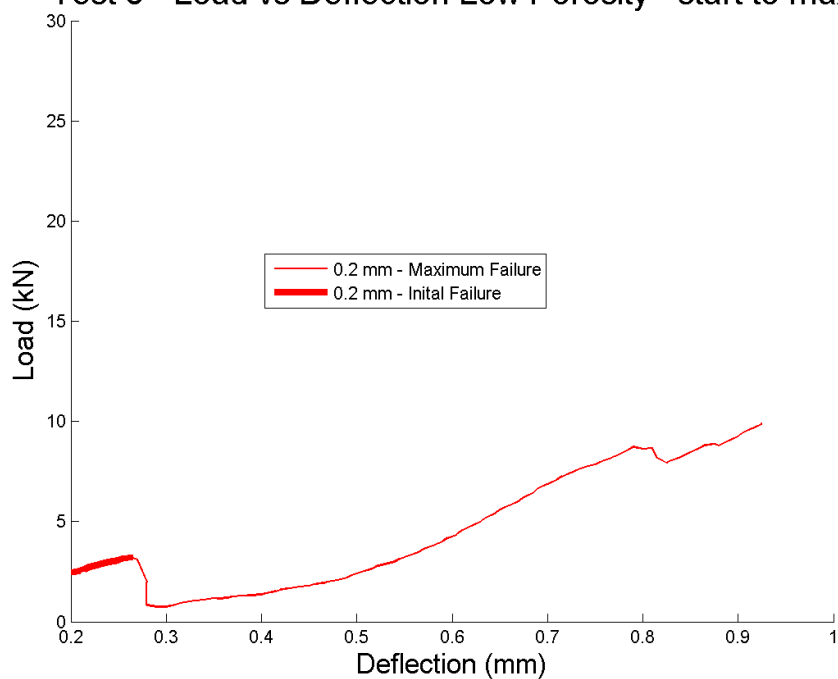
Test 9 - Load vs Deflection High Porosity - start to max
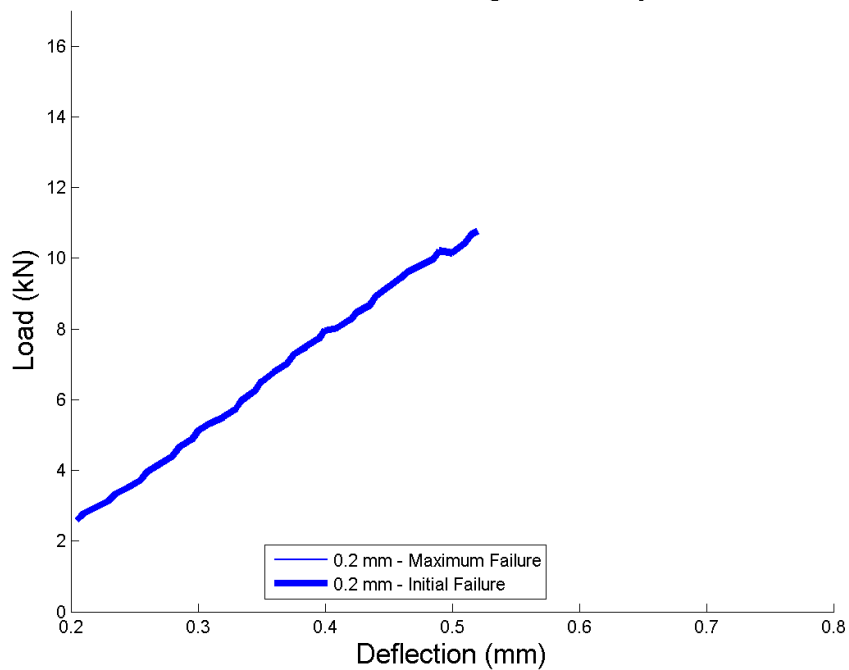
Test 10 - Load vs Deflection High Porosity - start to max
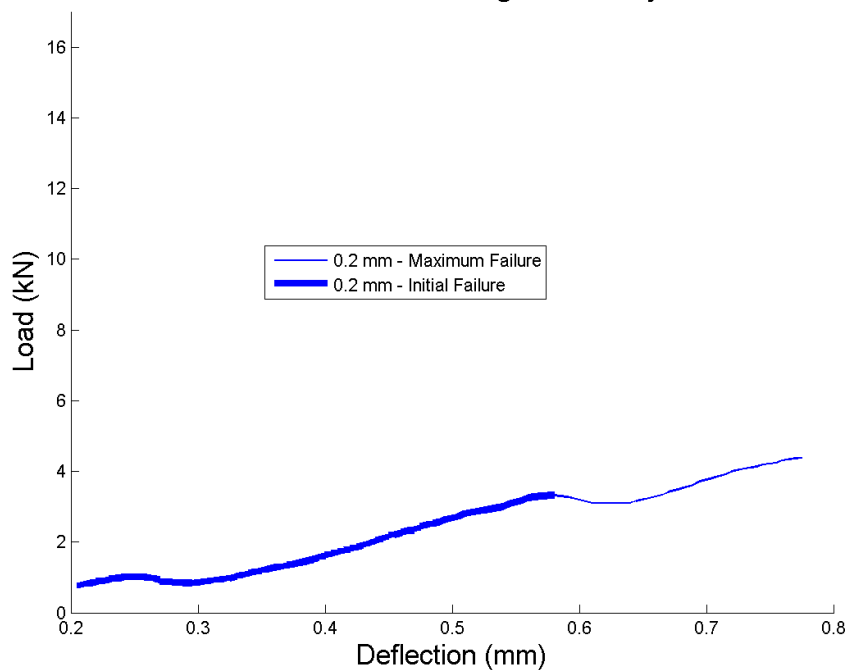
Test 11 - Load vs Deflection High Porosity - start to max
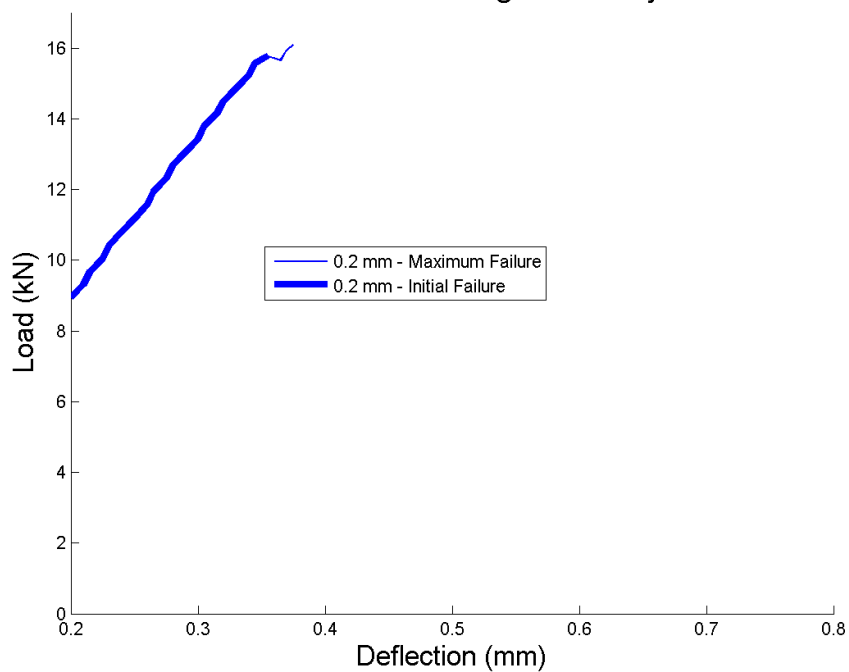
Test 12 - Load vs Deflection High Porosity - start to max
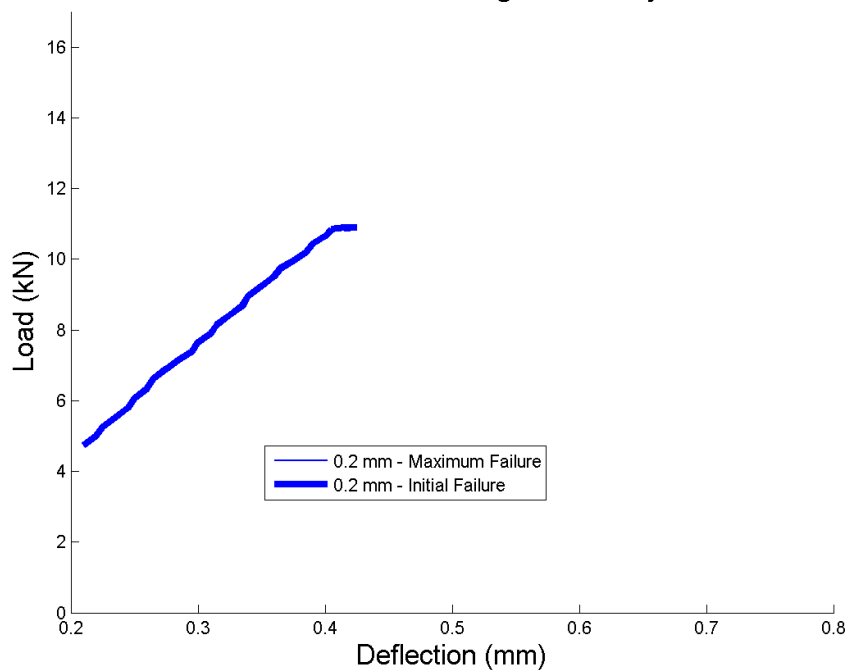
Test 13 - Load vs Deflection High Porosity - start to max
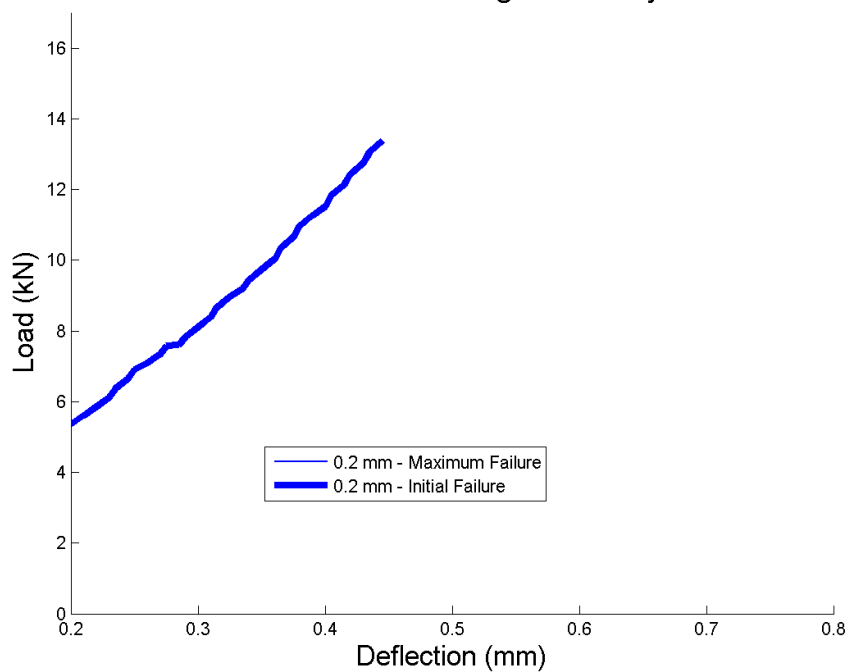
Test 14 - Load vs Deflection High Porosity - start to max

Legend:
- 0.2 mm - Maximum Failure
- 0.2 mm - Initial Failure

Load (kN) vs Deflection (mm)

Test 15 - Load vs Deflection High Porosity - start to max

Legend:
- 0.2 mm - Maximum Failure
- 0.2 mm - Initial Failure

Load (kN) vs Deflection (mm)
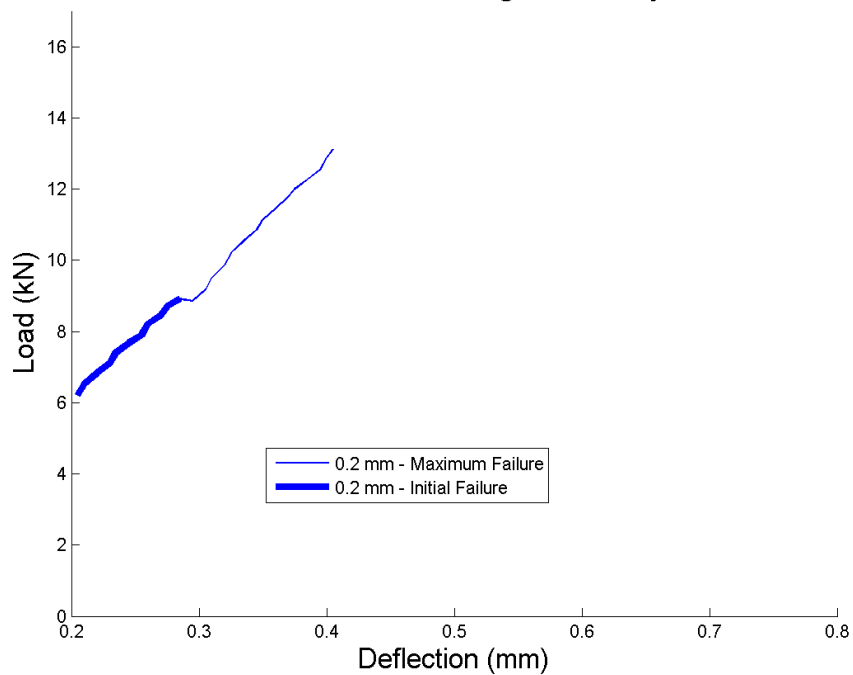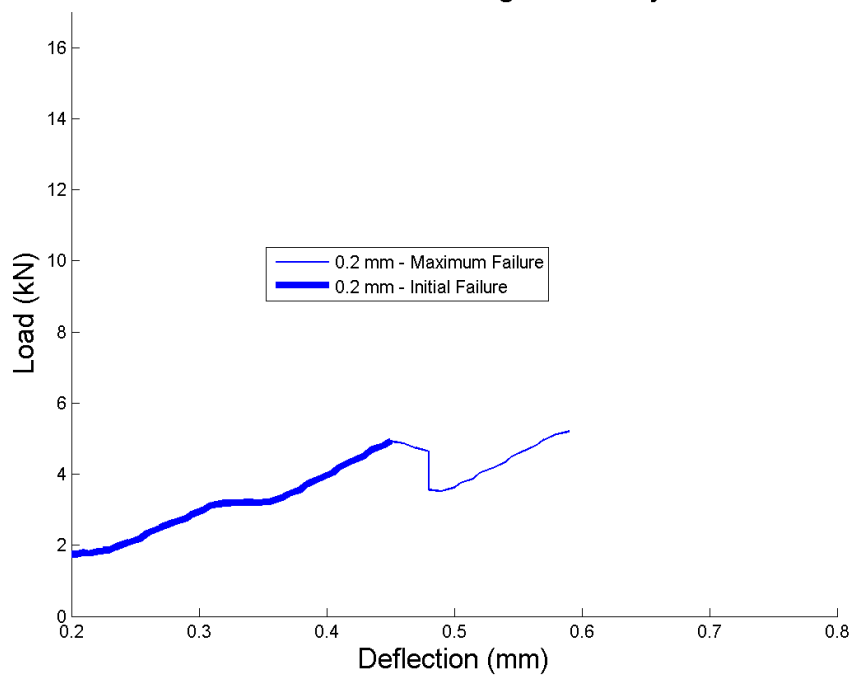
Test 16 - Load vs Deflection High Porosity - start to max
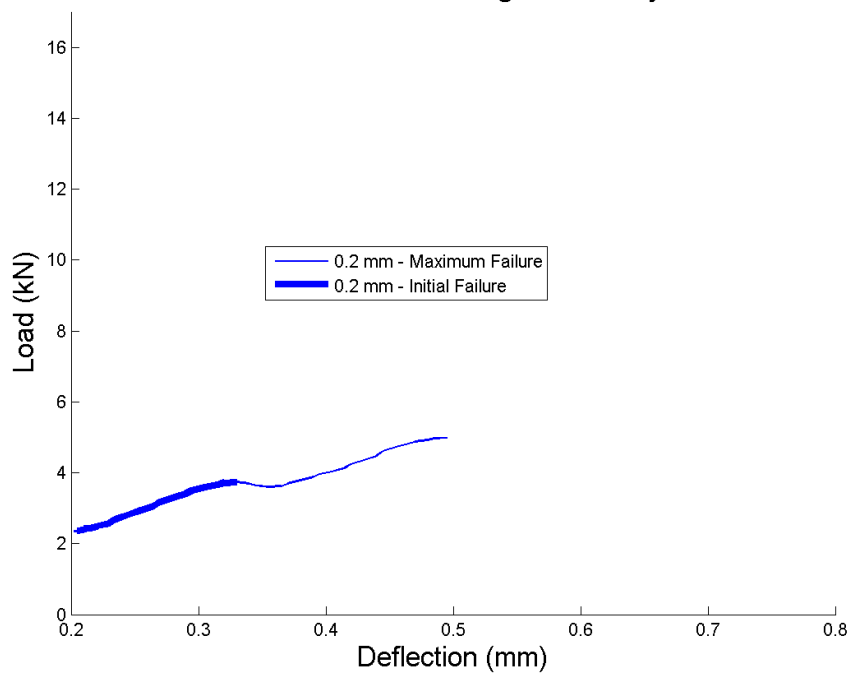
A.4 *Cumulative Data Overlay*
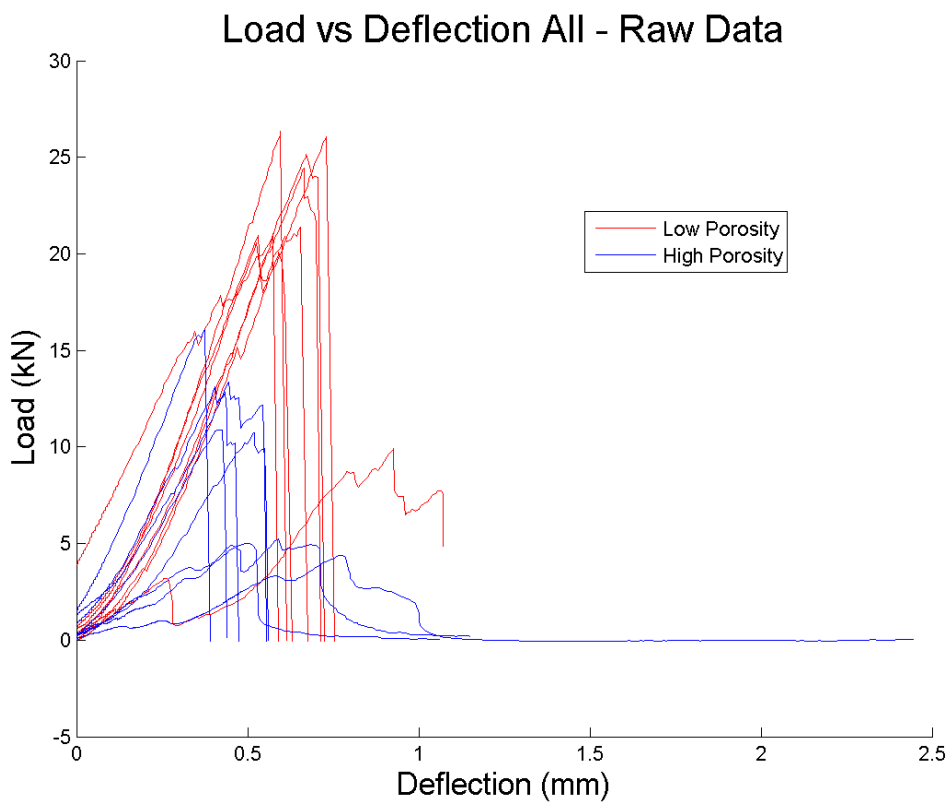
This is an overlay plot of all data from all the compression tests. It becomes evident that the low porosity samples were able to sustain the highest loading conditions where the high porosity samples were able to sustain loads about half the magnitude of the low porosity samples.

Stress vs Strain - All Tests
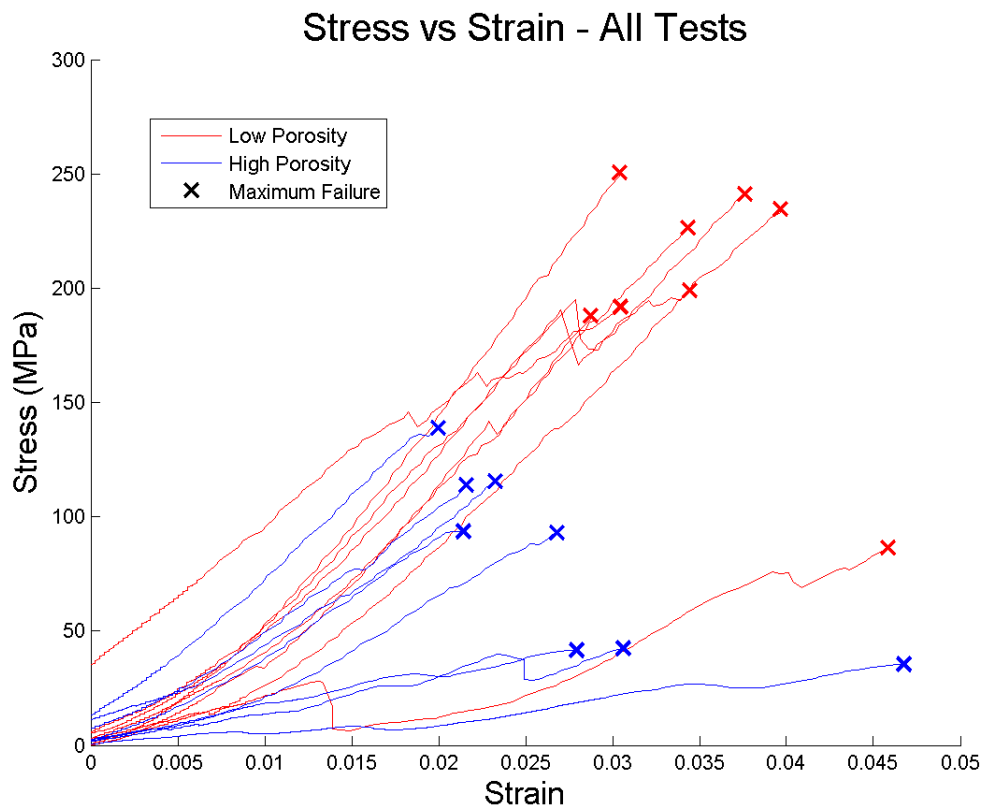
The clustering of low porosity maximum failure data points becomes apparent in the ~240 MPa range where the high porosity maximum failure data points becomes apparent at ~120 MPa. Four data points were from samples which crumbled during testing, three high porosity and one low porosity samples all below the ~100 MPa value. The three high porosity samples which crumbled all had a very consistent maximum stress value.

A.5 *Stress vs. Strain*

The data presented in these figures are cut from the original data set. Data after the maximum failure of the sample is removed. Maximum and local failures of the specimen are noted on each figure.

Test 1 - Stress vs Strain - start to max
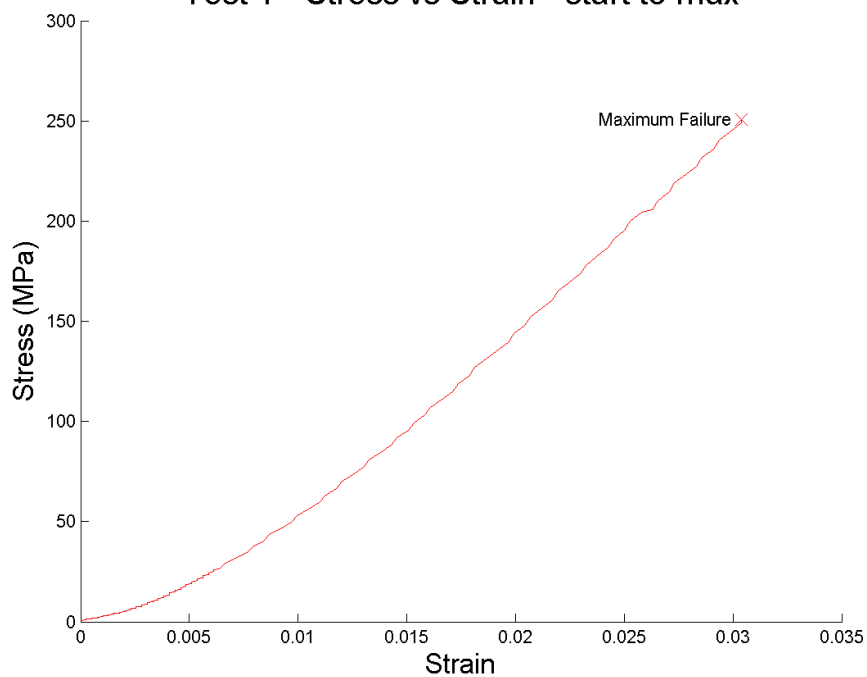
Test 2 - Stress vs Strain - start to max
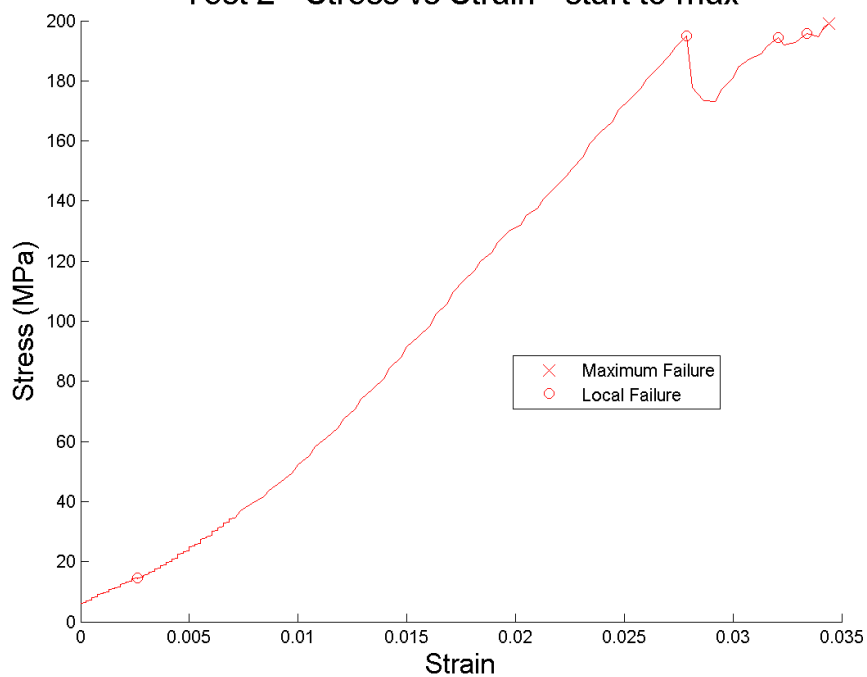
**Test 3 - Stress vs Strain - start to max**
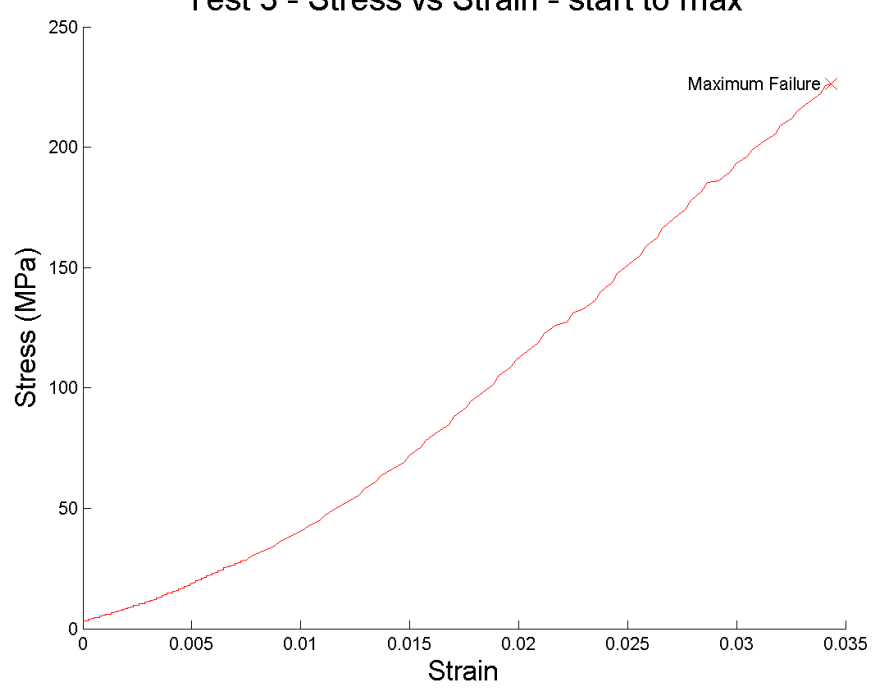
Test 4 - Stress vs Strain - start to max
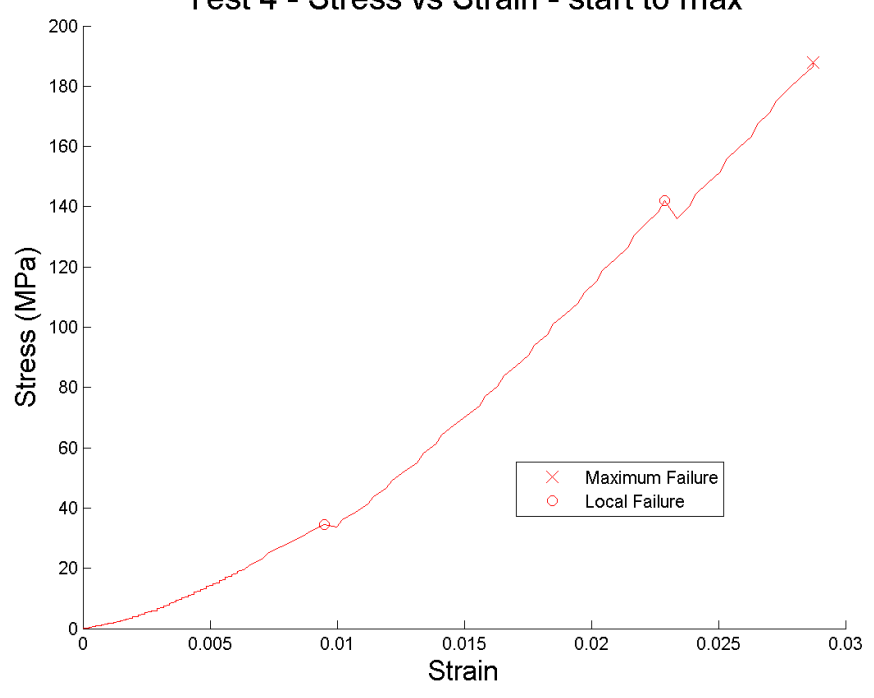
Test 5 - Stress vs Strain - start to max
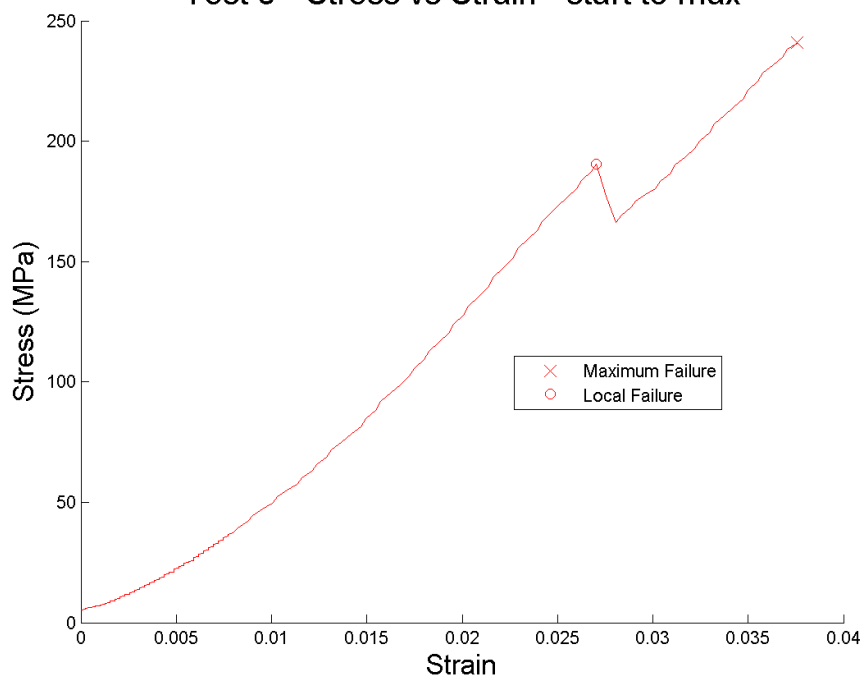
Test 6 - Stress vs Strain - start to max
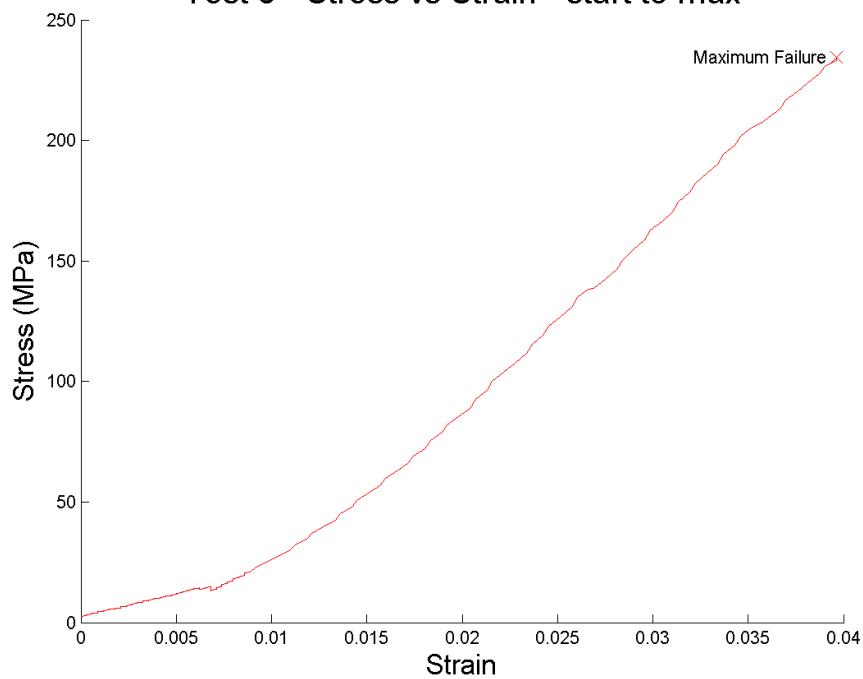
Test 7 - Stress vs Strain - start to max
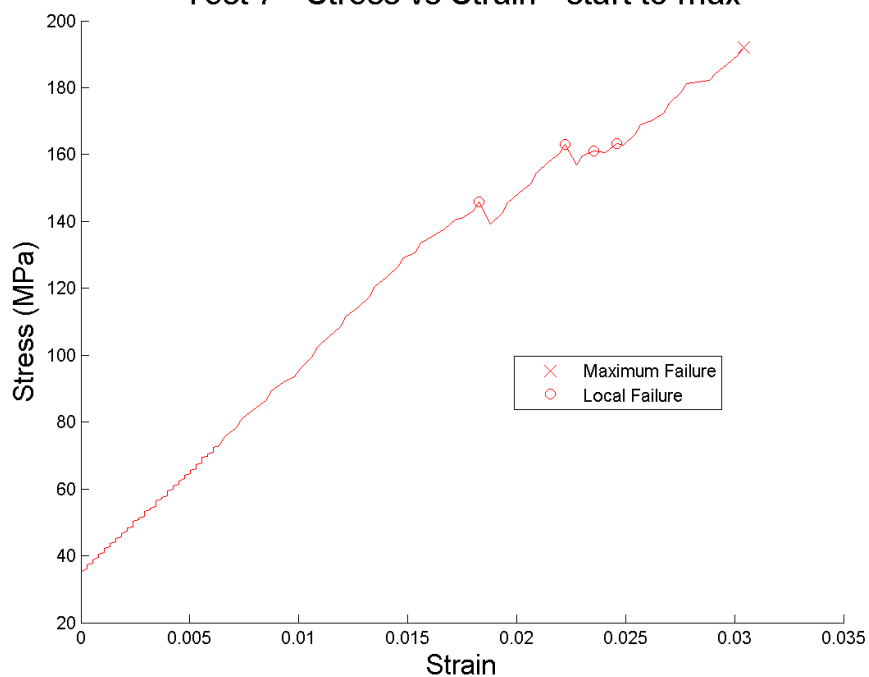
Test 8 - Stress vs Strain - start to max
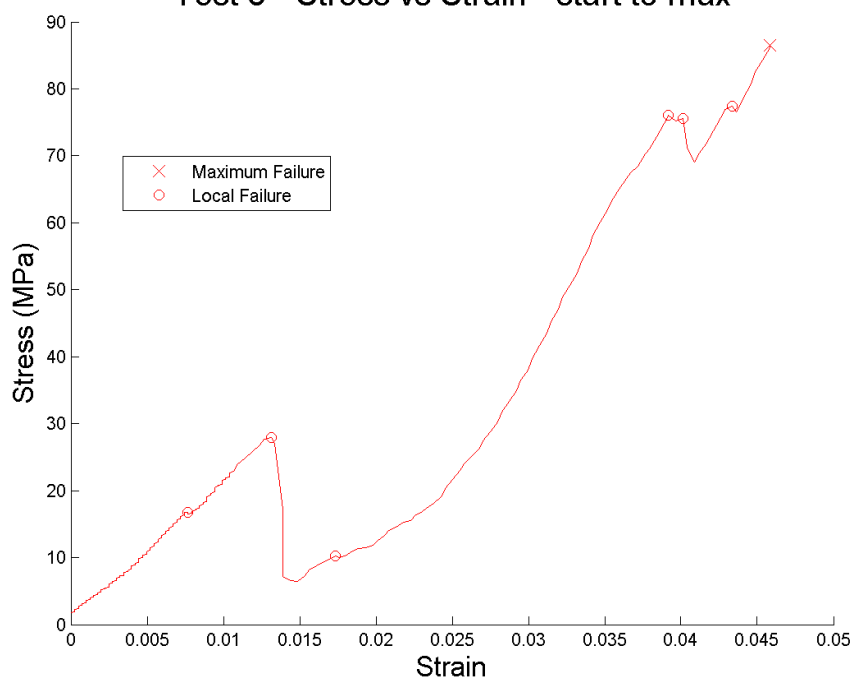
Test 9 - Stress vs Strain - start to max
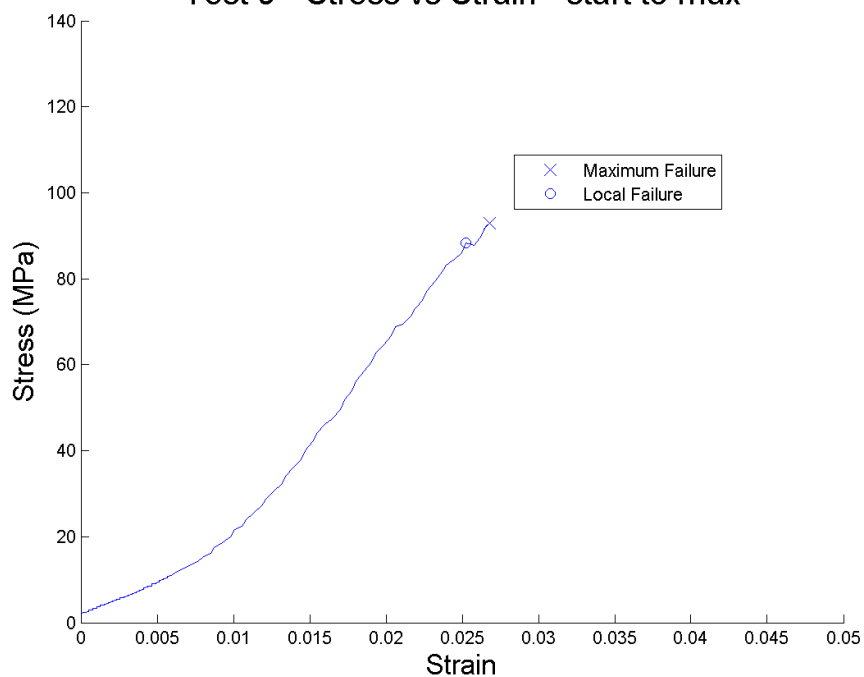

Test 10 - Stress vs Strain - start to max

Test 11 - Stress vs Strain - start to max

Test 12 - Stress vs Strain - start to max
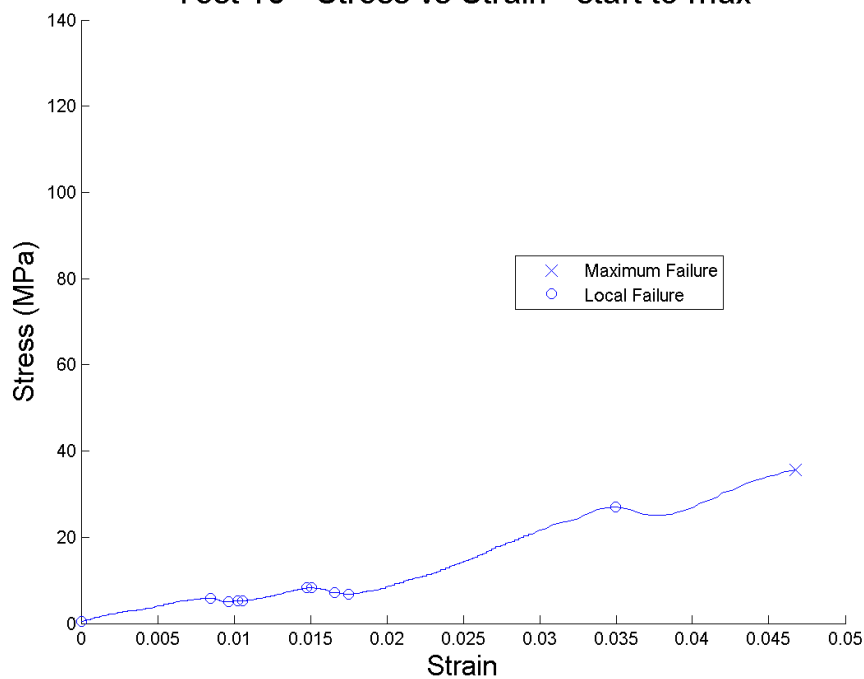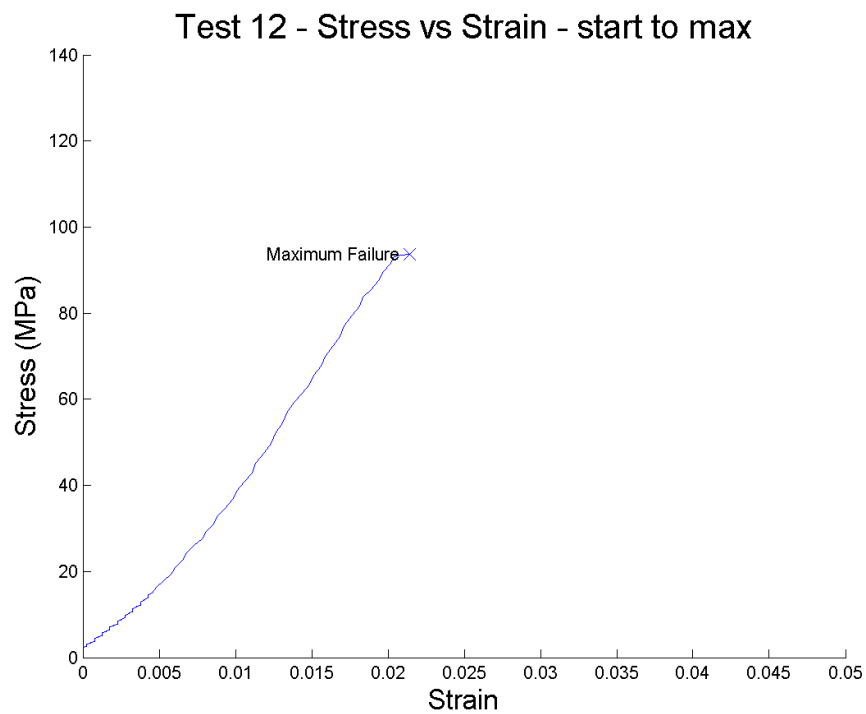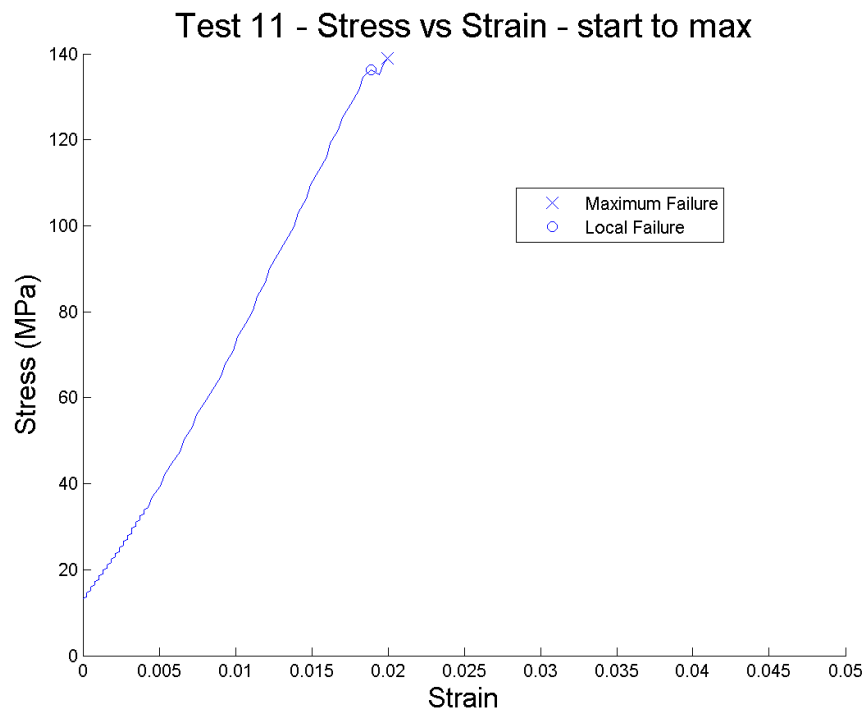
Test 13 - Stress vs Strain - start to max
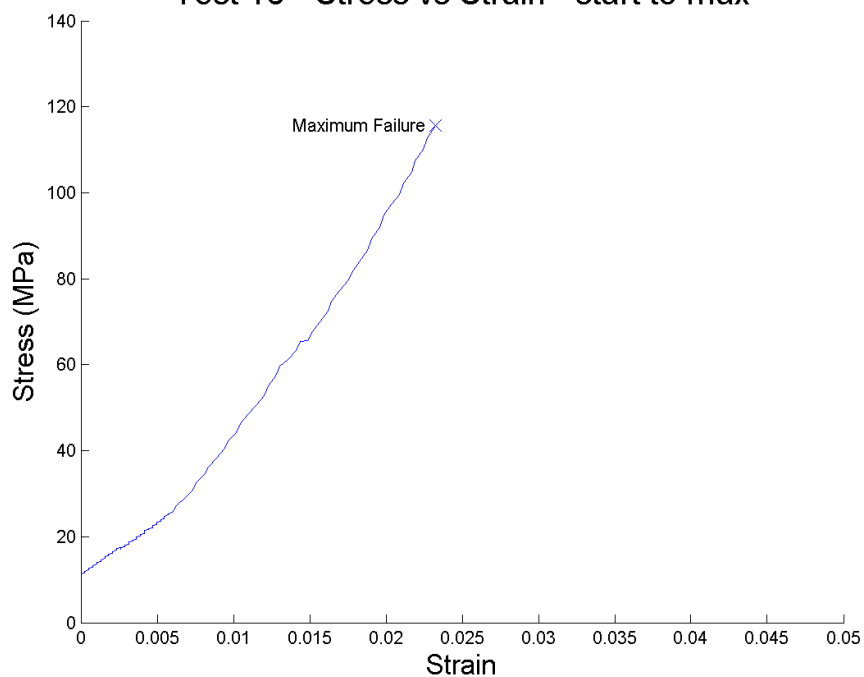
Test 14 - Stress vs Strain - start to max
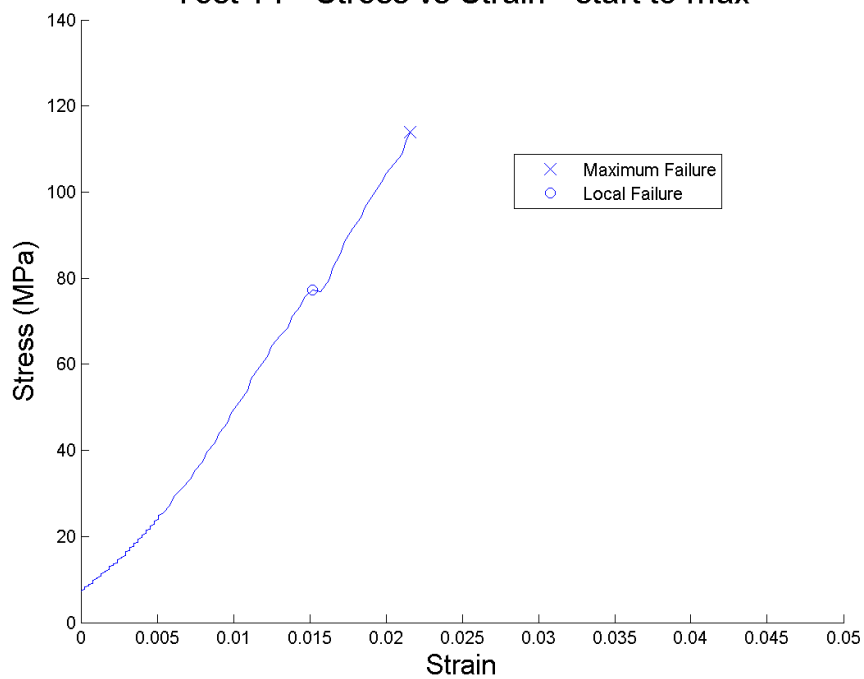
Test 15 - Stress vs Strain - start to max
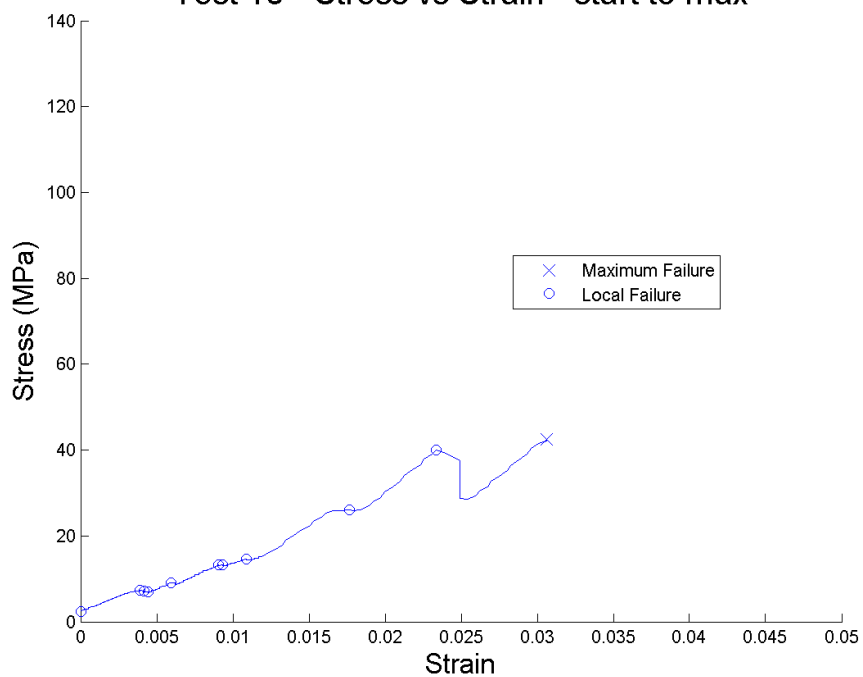
Test 16 - Stress vs Strain - start to max
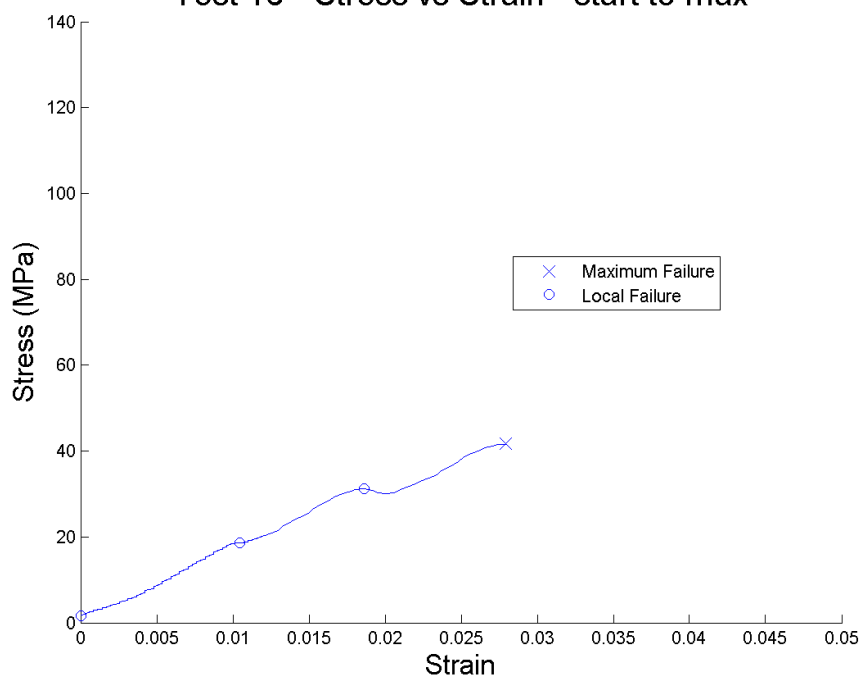
A.6 Toughness

The data presented in these figures were from the start of the test to the maximum failure of the sample.


Test 1 - Toughness - start to final

Test 2 - Toughness - start to inital

Test 3 - Toughness - start to final


Test 4 - Toughness - start to inital

## Test 5 - Toughness - start to inital

## Test 6 - Toughness - start to final

Test 9 - Toughness - start to initial

Test 10 - Toughness - start to initial
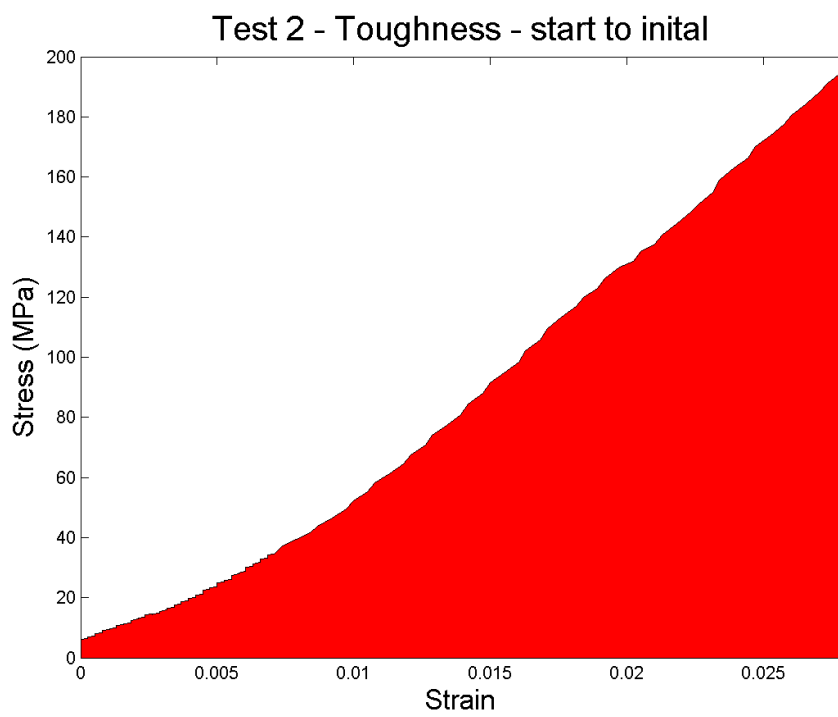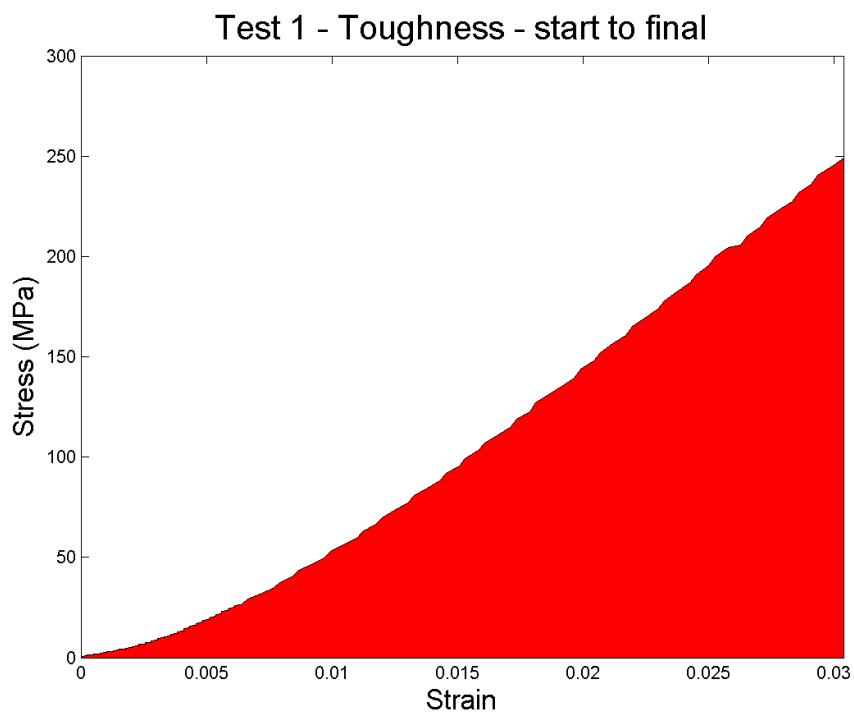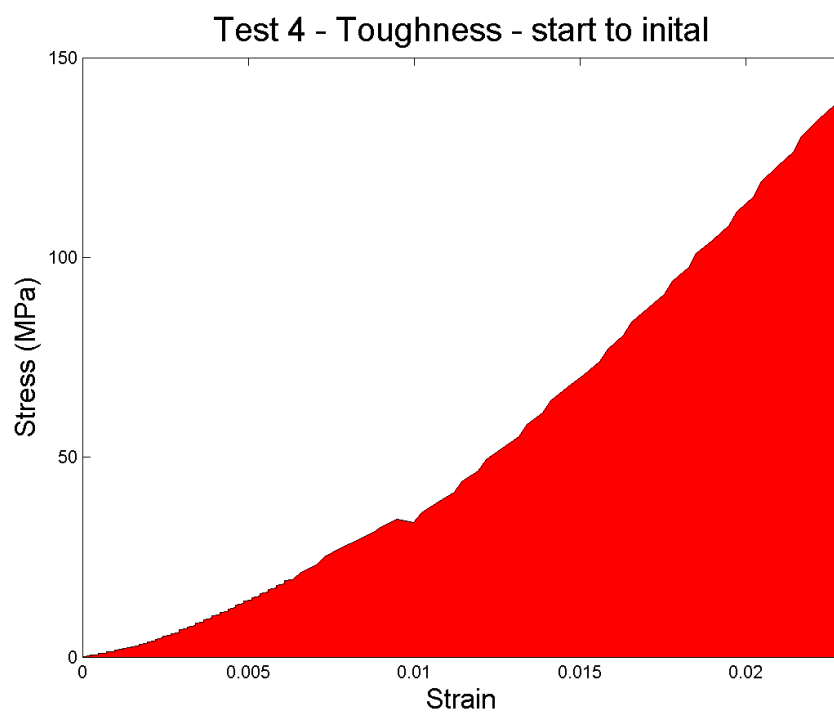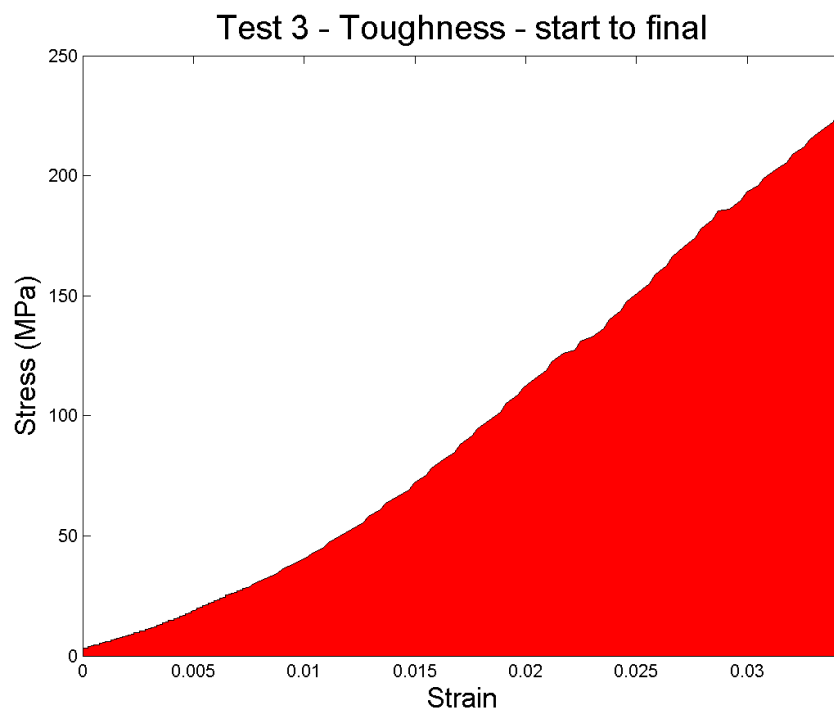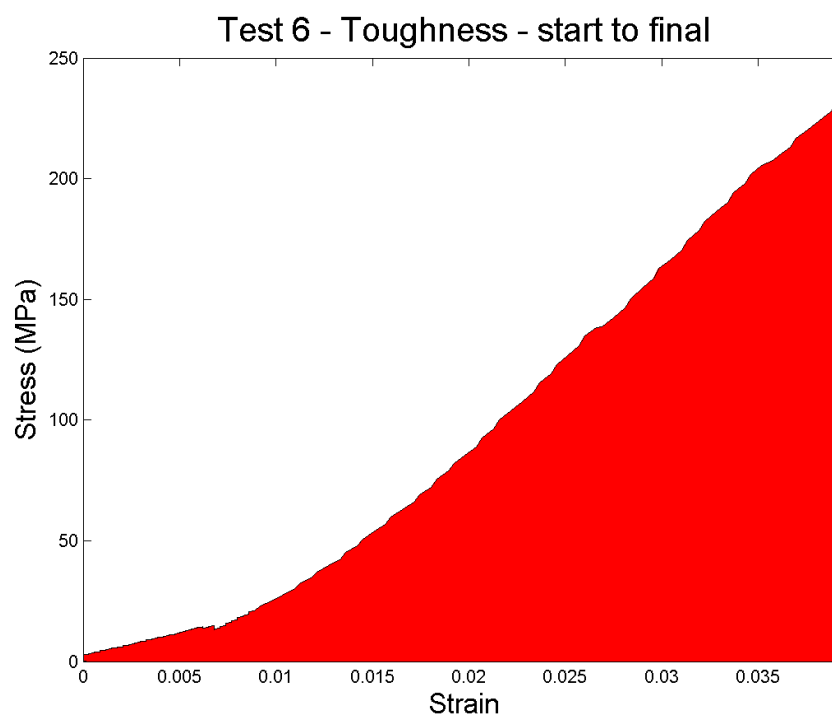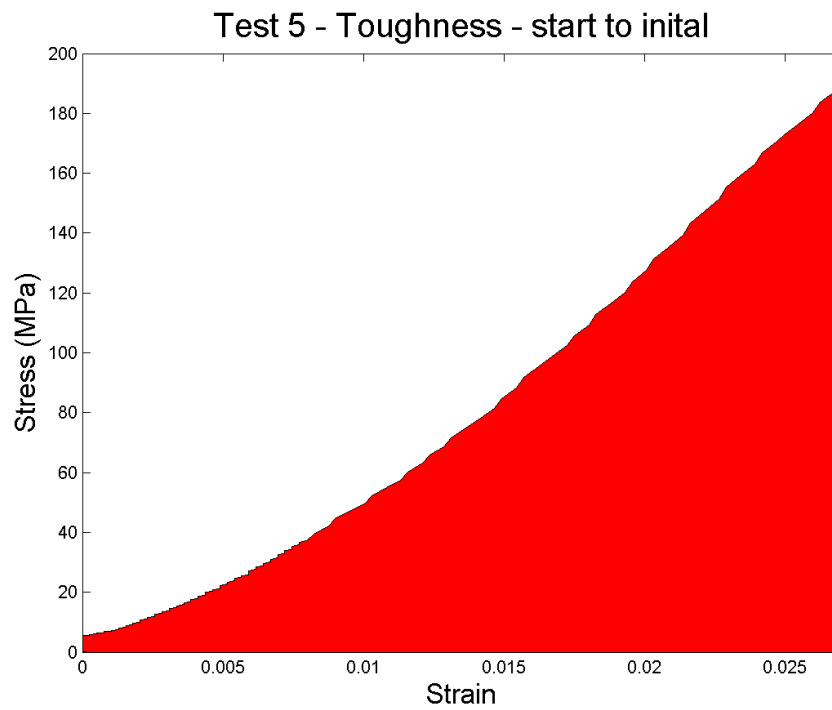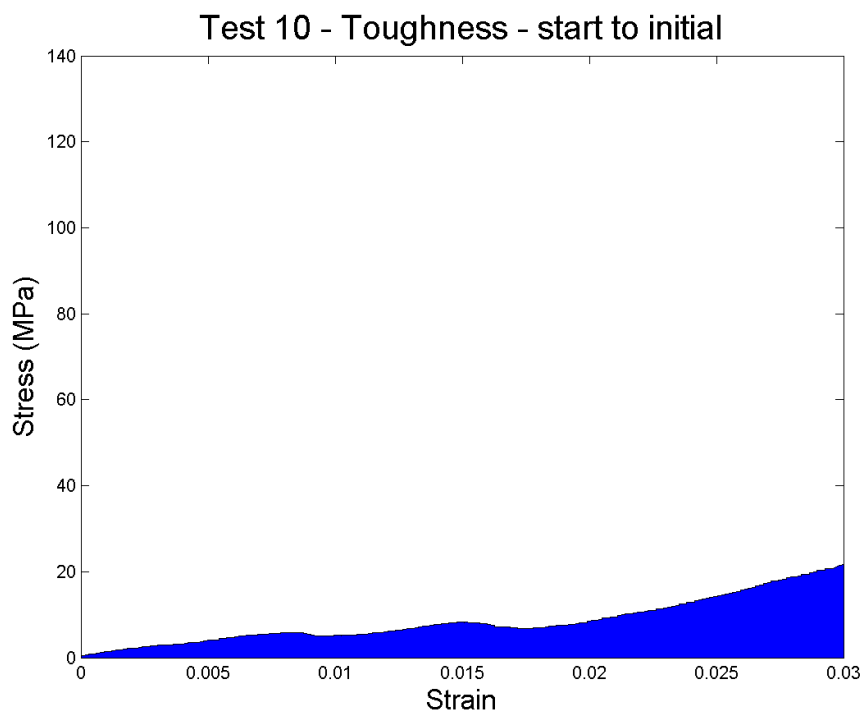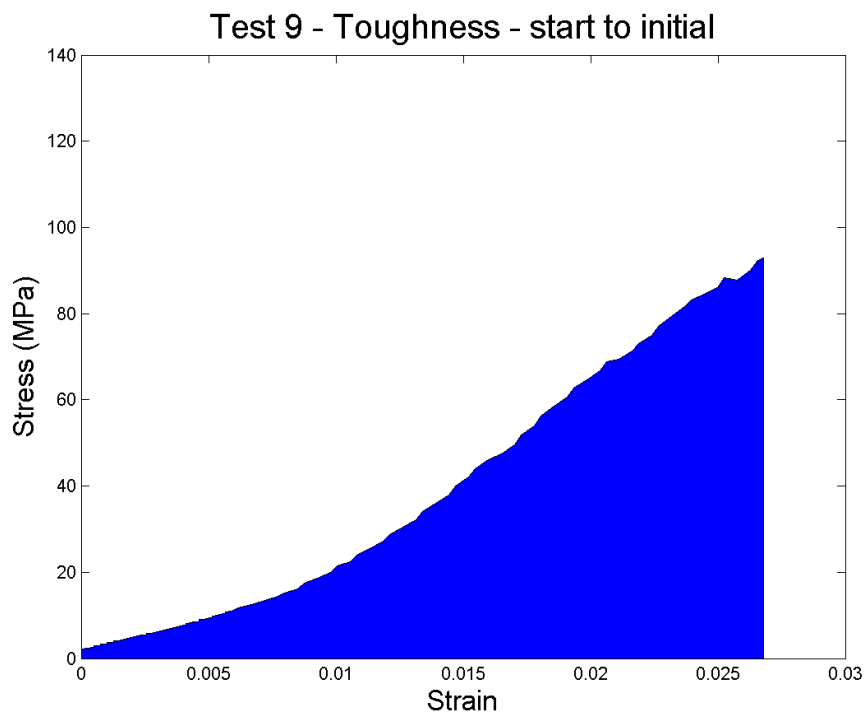
Test 11 - Toughness - start to initial
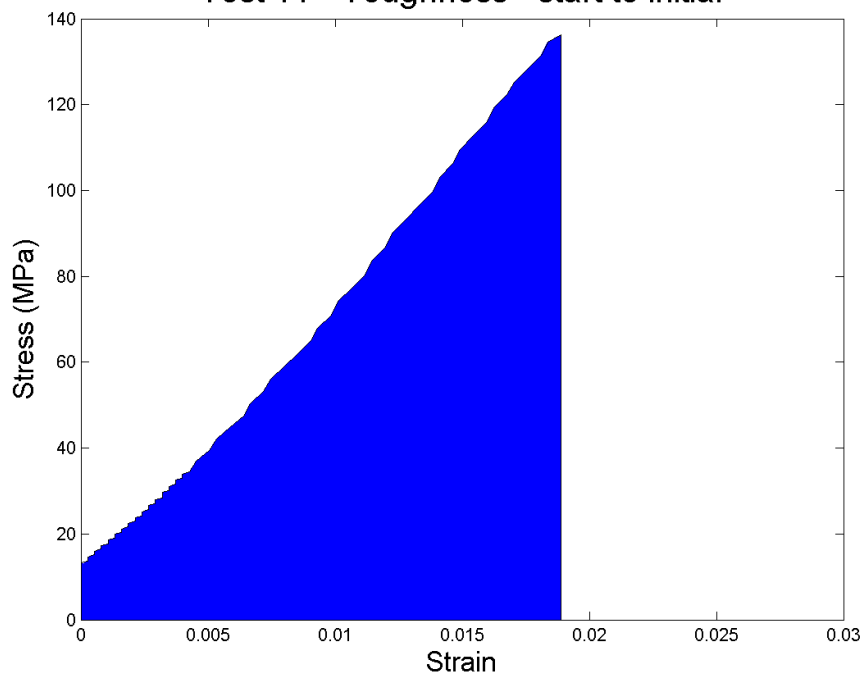

Test 12 - Toughness - start to initial
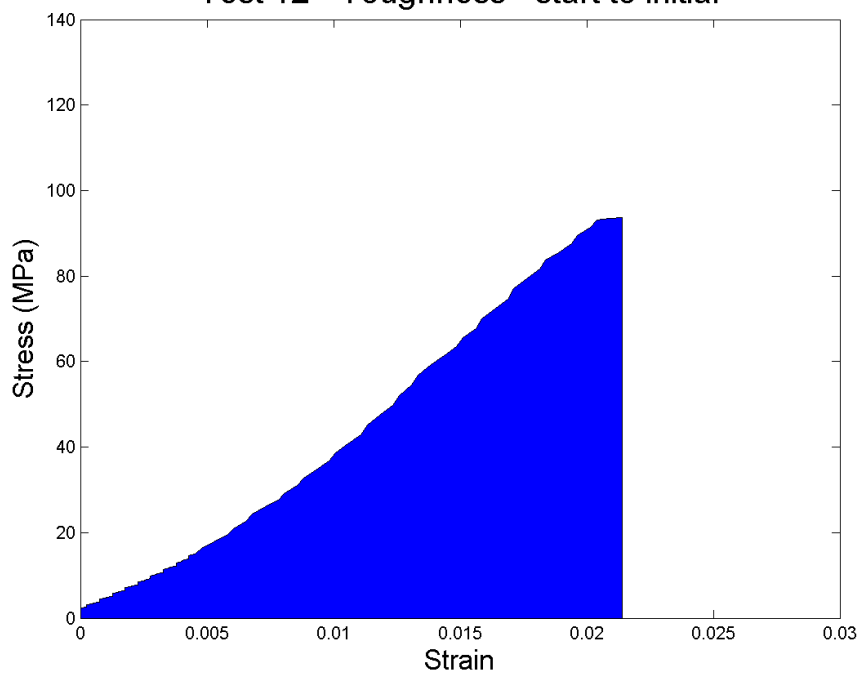
Test 13 - Toughness - start to initial
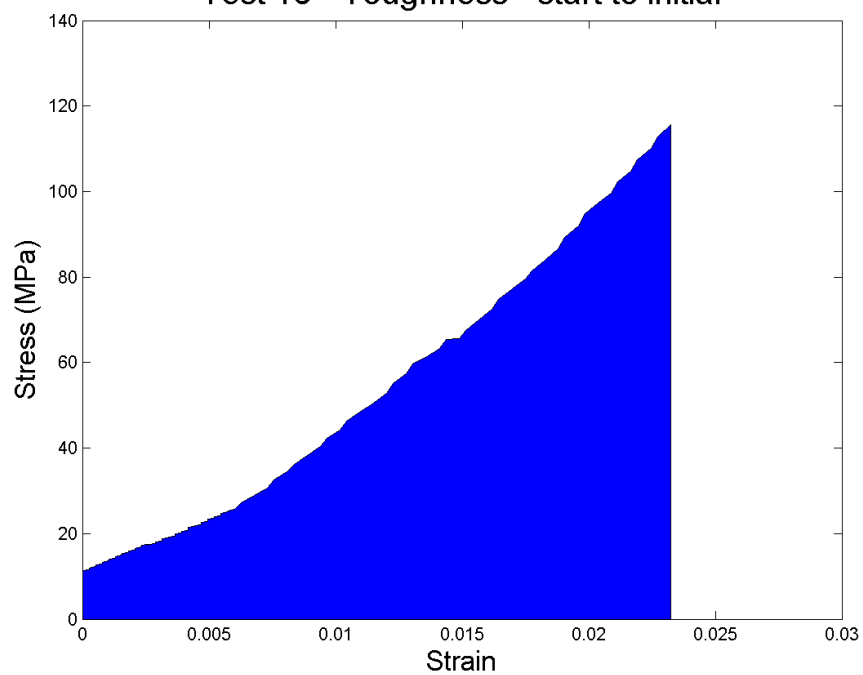
Test 14 - Toughness - start to initial
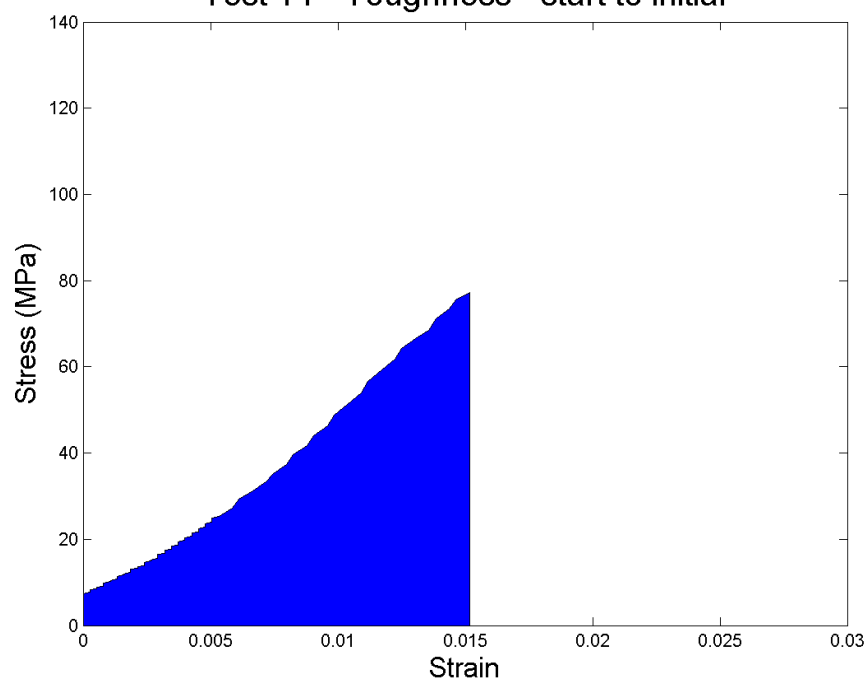
Test 15 - Toughness - start to initial
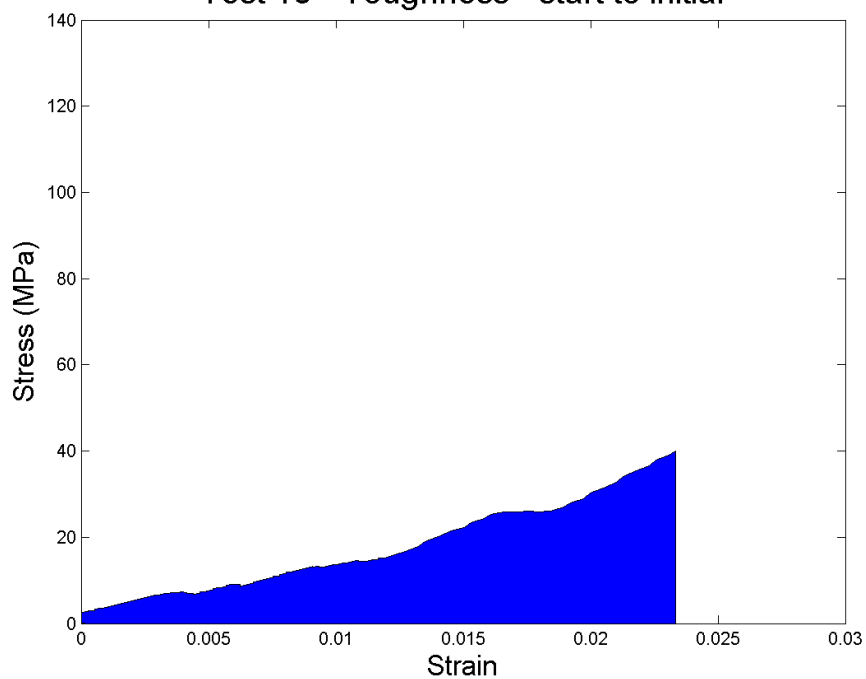
Test 16 - Toughness - start to initial
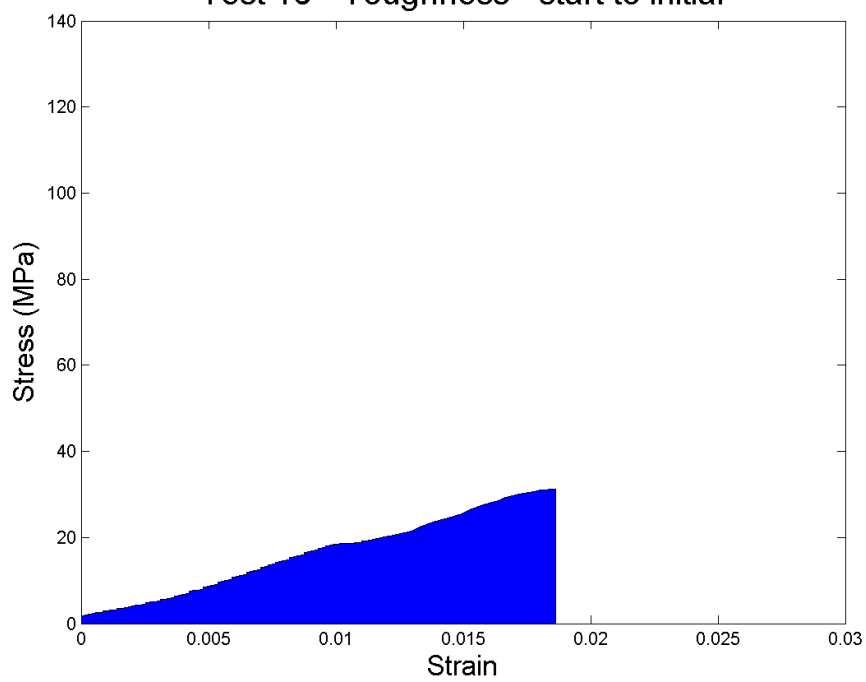
A.7   Stress vs. Strain with Linear Fit

Test 1 - Stress vs Strain - start to final
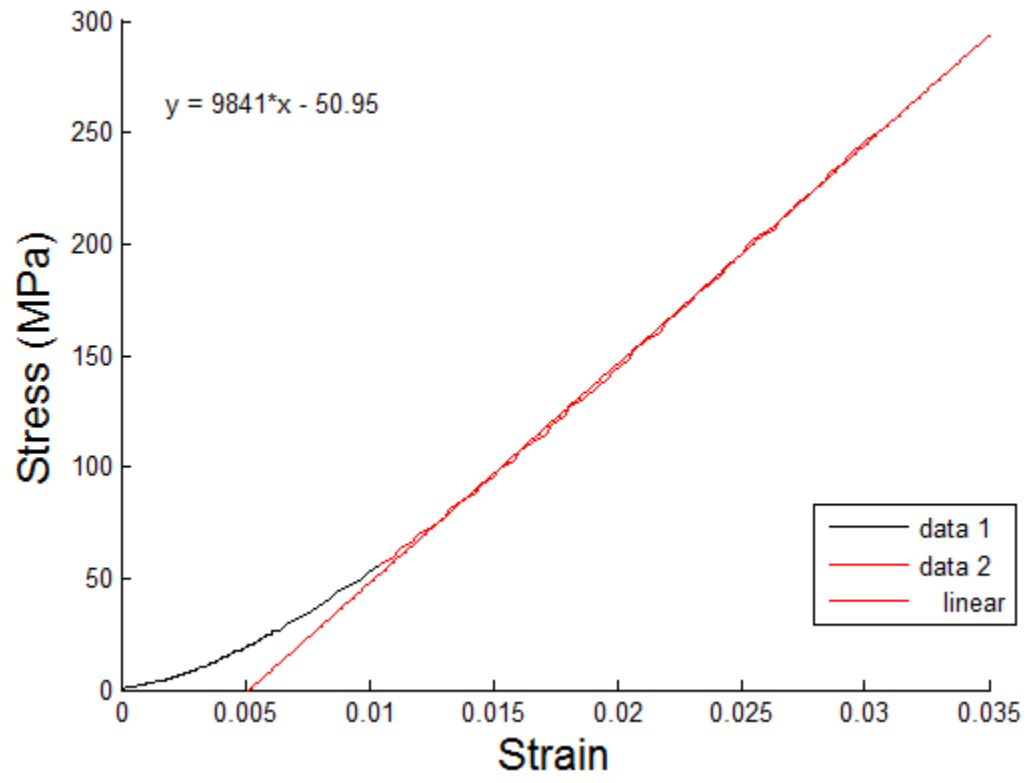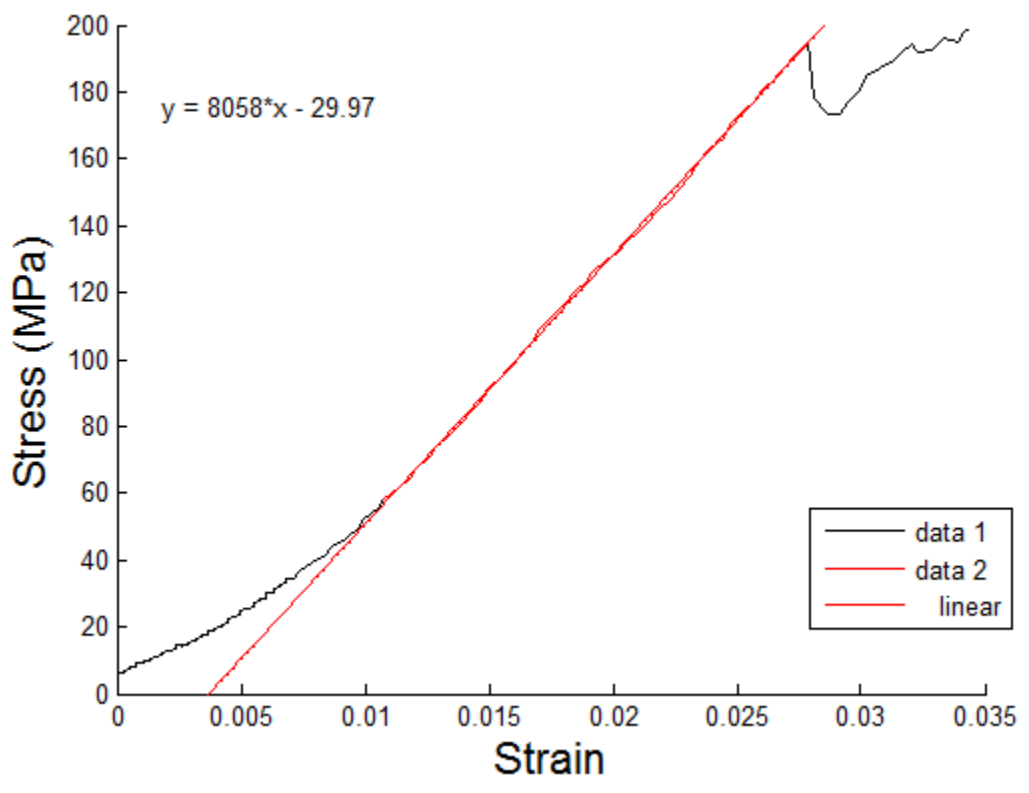
y = 9841*x - 50.95

Test 2 - Stress vs Strain - start to initial

y = 8058*x - 29.97

Test 3 - Stress vs Strain - start to final

y = 7924*x - 45.82

Test 4 - Stress vs Strain - start to inital

y = 8365*x - 53.41

Test 5 - Stress vs Strain - start to inital

y = 8525*x - 41.61

Test 6 - Stress vs Strain - start to inital

y = 7433*x - 59.5

Test 9 - Stress vs Strain - start to inital

y = 4477*x - 25.4

Stress (MPa)

Strain

data 1
data 2
linear

Test 11 - Stress vs Strain - start to inital

y = 6882*x + 5.408

Stress (MPa)

Strain

data 1
data 2
linear

Test 12 - Stress vs Strain - start to inital

y = 5203*x - 13.47

Test 13 - Stress vs Strain - start to inital

y = 5384*x - 12.4

Test 14 - Stress vs Strain - start to end

$y = 5430 \cdot x - 5.077$

A.8 Compressive Strength Histograms

Low Porosity Samples at Maximum Failure, Bin = 10

Low Porosity Samples at Initial Failure, Bin = 10
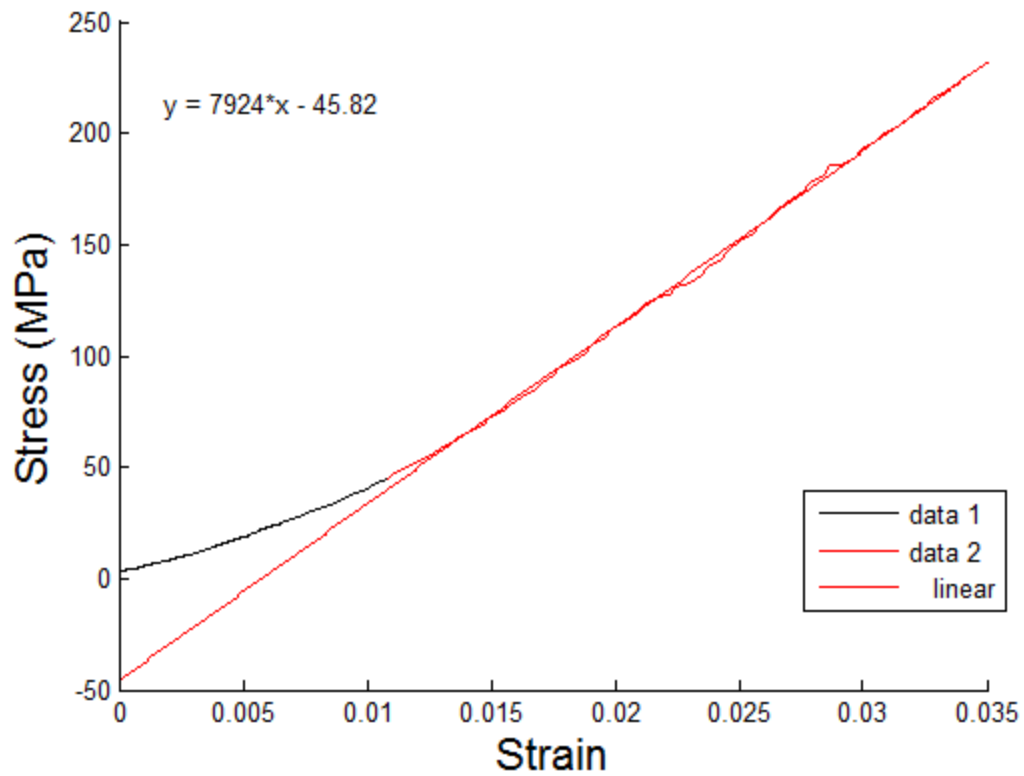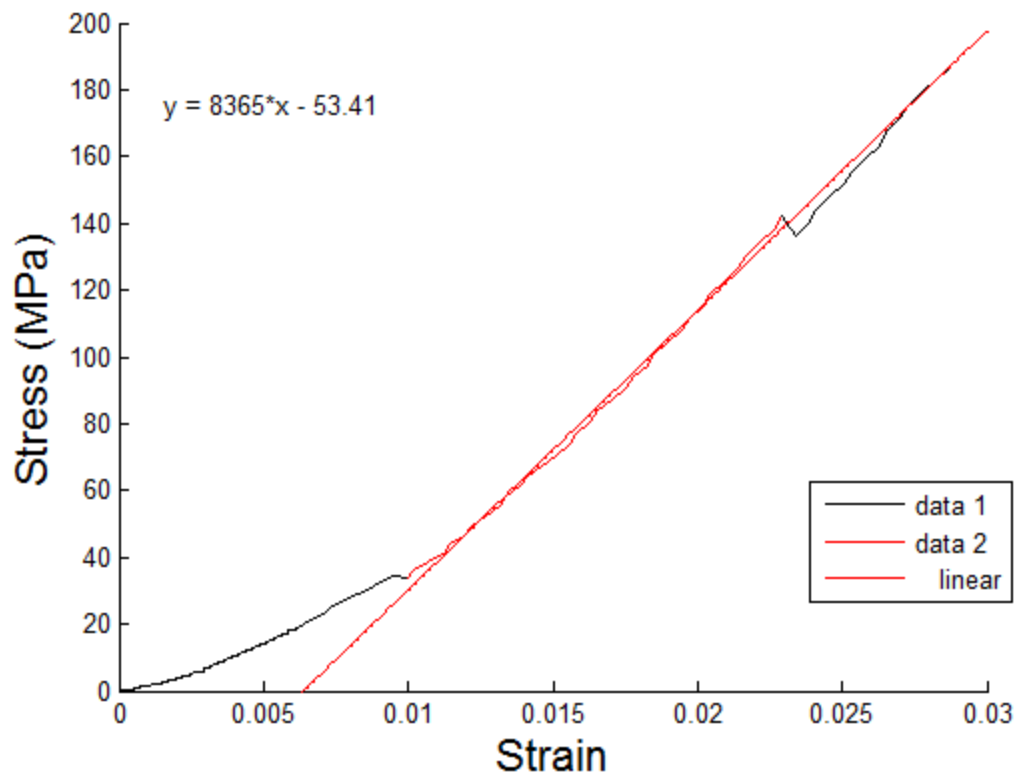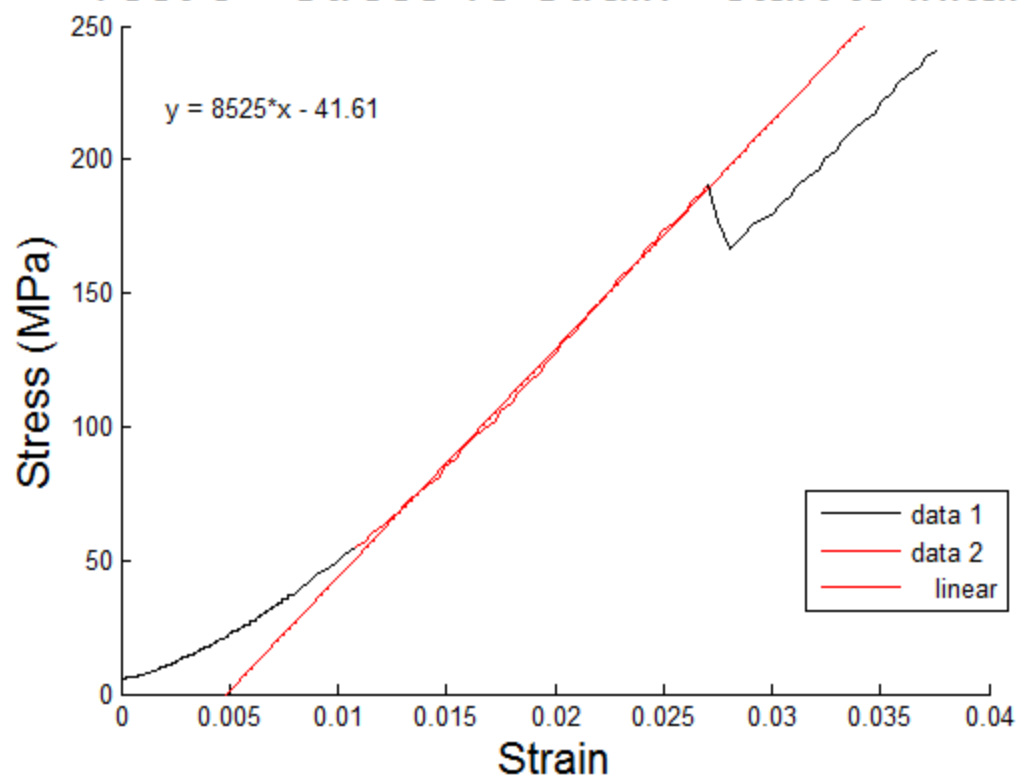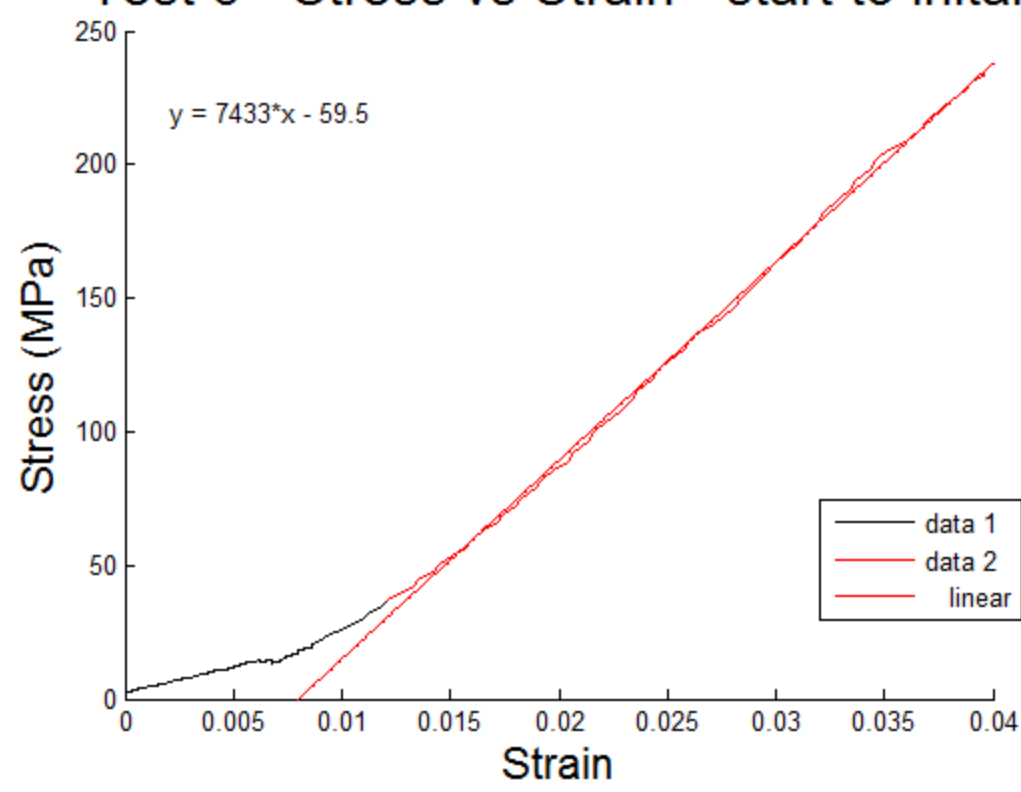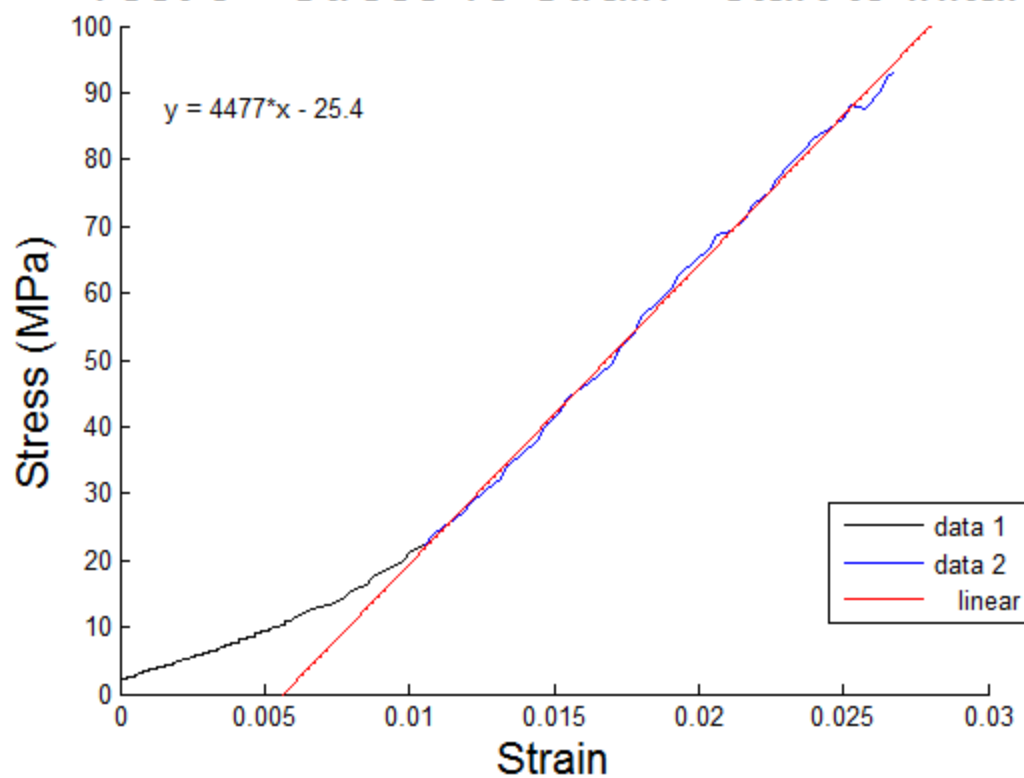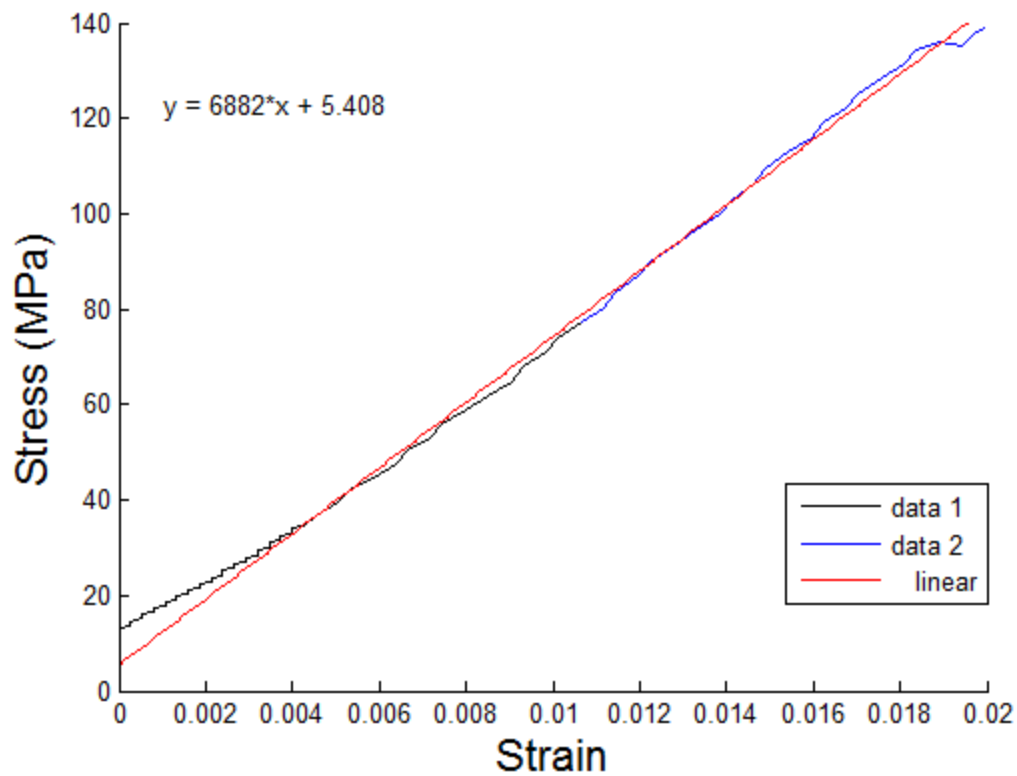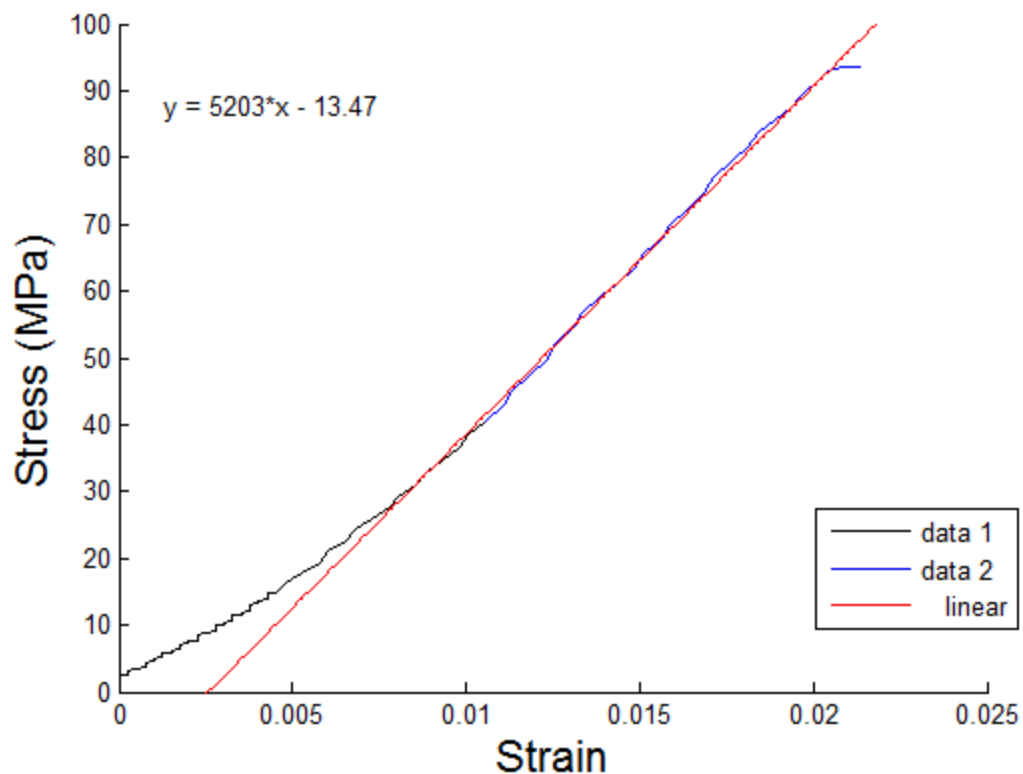
This data set appears different from the compiled histogram showing all 4 data sets. The reason for this difference is that the range of values here is between 27 and 136 MPa and divided into ten bins, where the other 3 data sets are between about 28 to 250 MPa, a larger range containing larger bins. Contains narrow bins in comparison to the other data set histograms.

High Porosity Samples at Initial Failure, Bin = 10
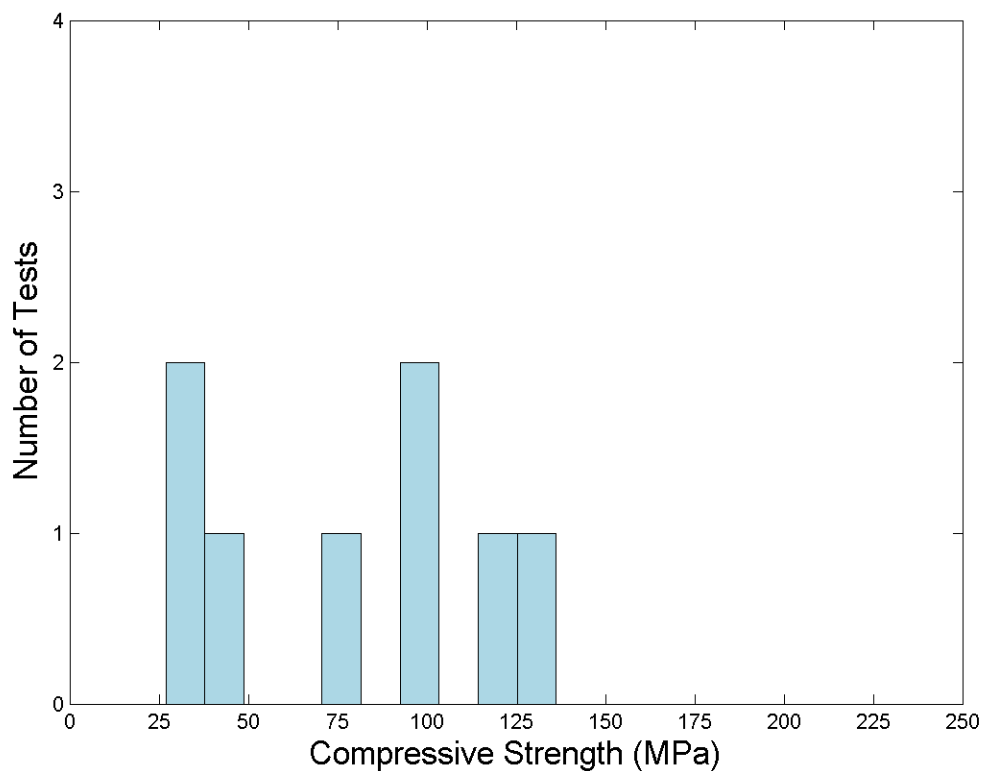
High Porosity Samples at Maximum Failure, Bin = 10
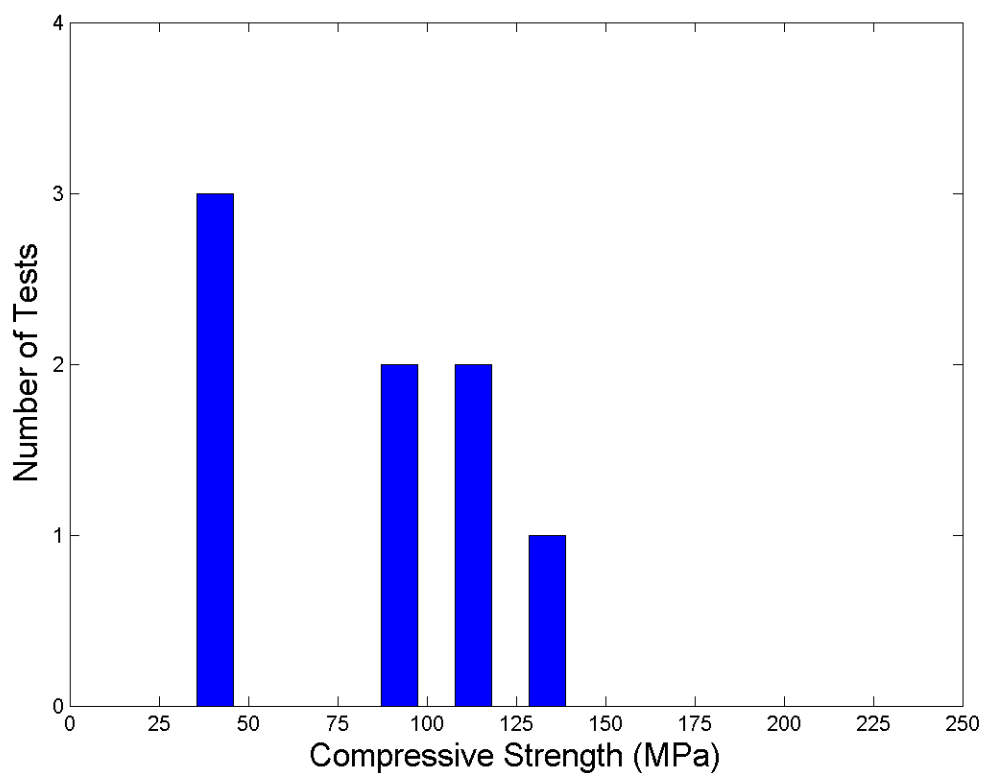
All Samples at Maximum Failure, Bin = 10
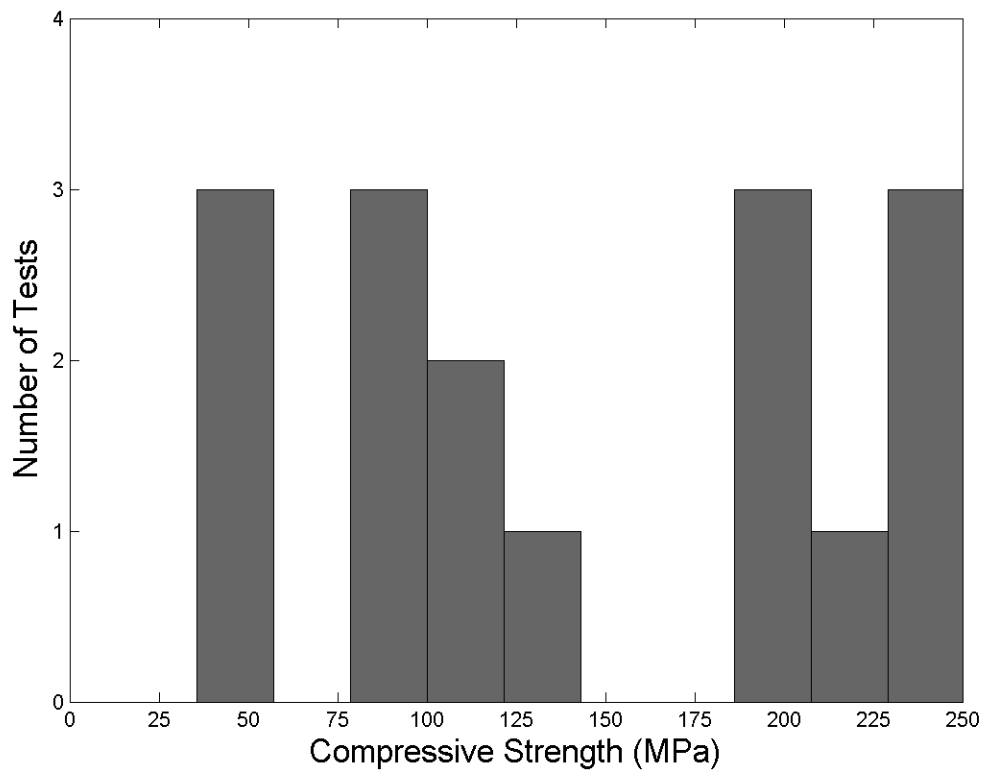
All Samples at Initial Failure, Bin = 10
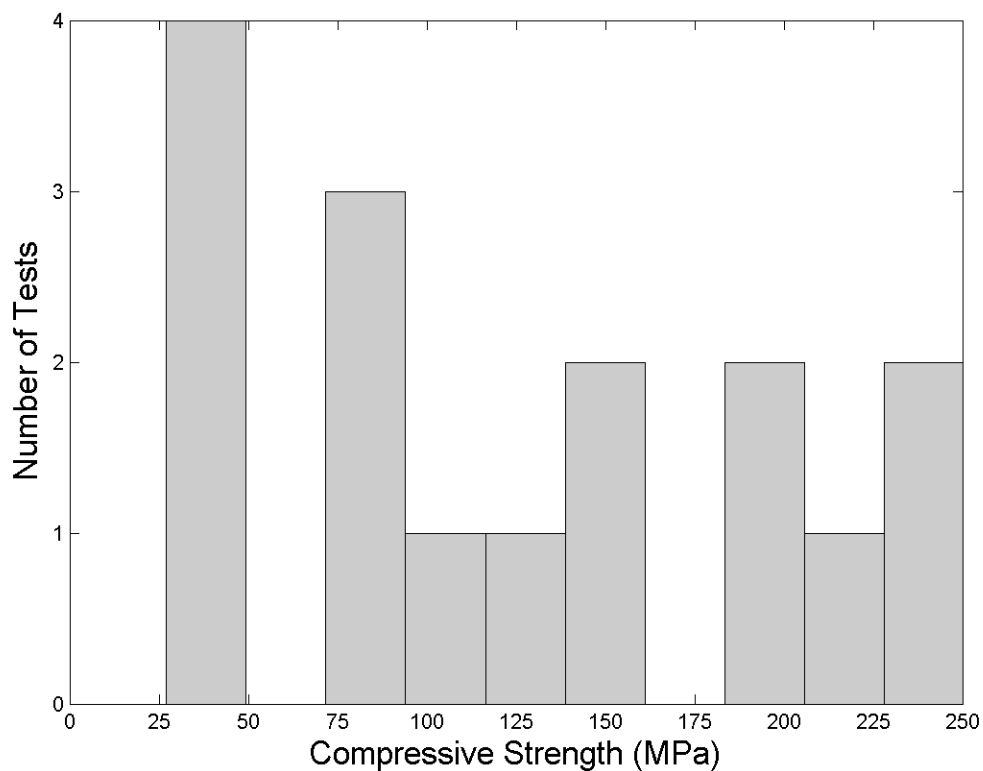
All Samples at Failures, Bin = 10
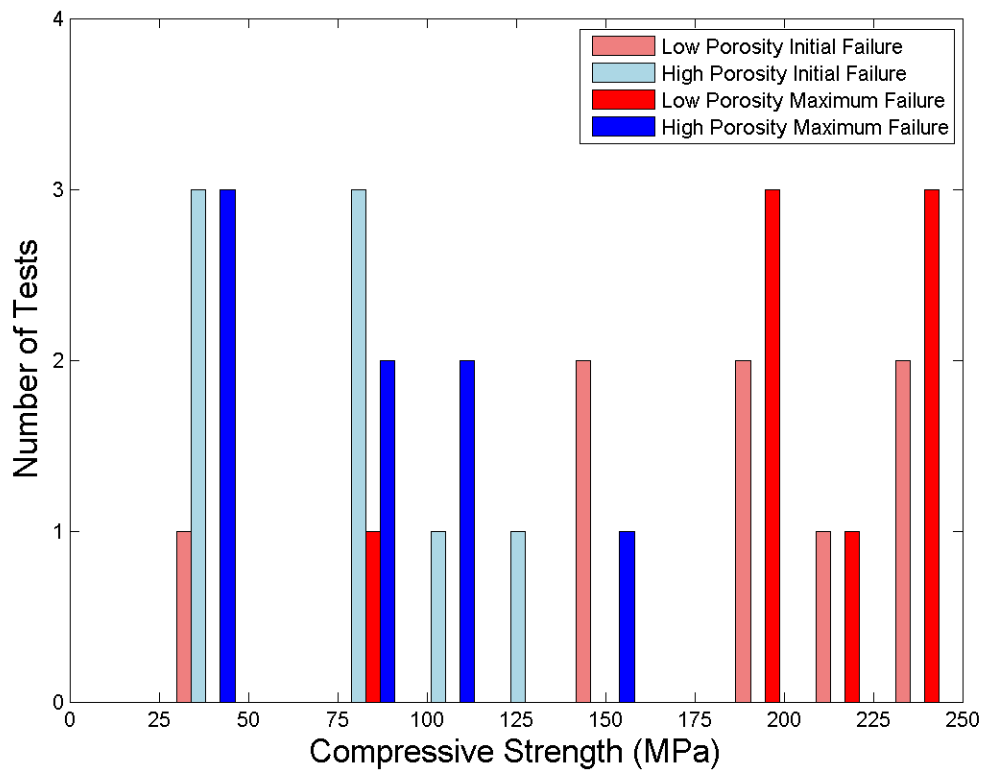
A.9 Elastic Constants as a Function of Porosity

Bulk Modulus vs Porosity - Ramakrishnan and Arunachalam

Bulk Modulus vs Porosity - Basalt

Bulk Modulus vs Porosity - SiO2

Bulk Modulus vs Porosity - Lunar Basalt 12065

Bulk Modulus vs Porosity - High Porosity

Bulk Modulus vs Porosity - Low Porosity

Shear Modulus vs Porosity - Hashin-Shtrikman

Shear Modulus vs Porosity - Nielsen
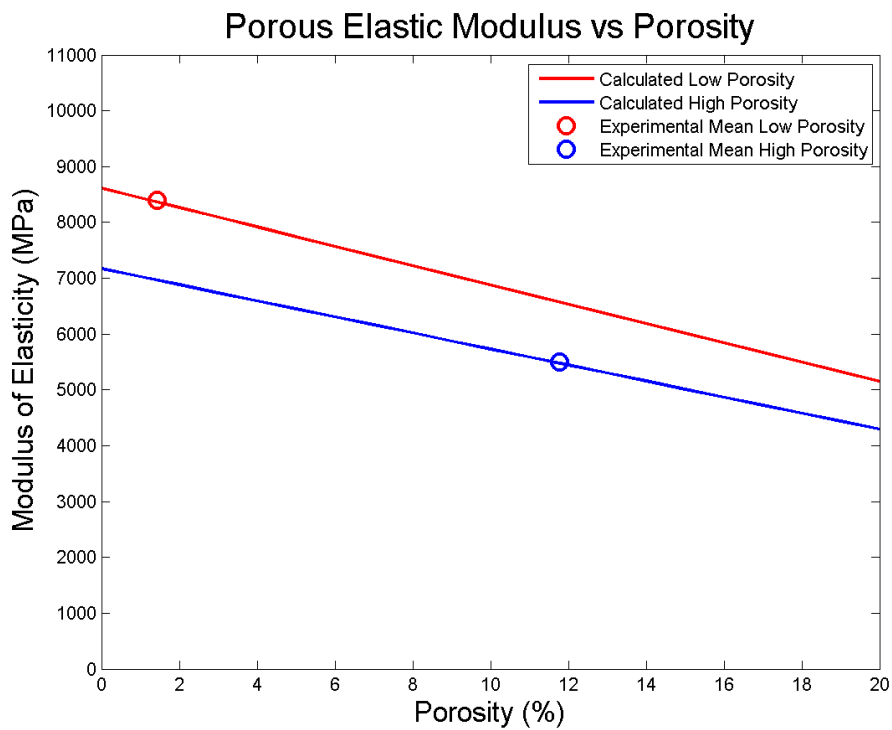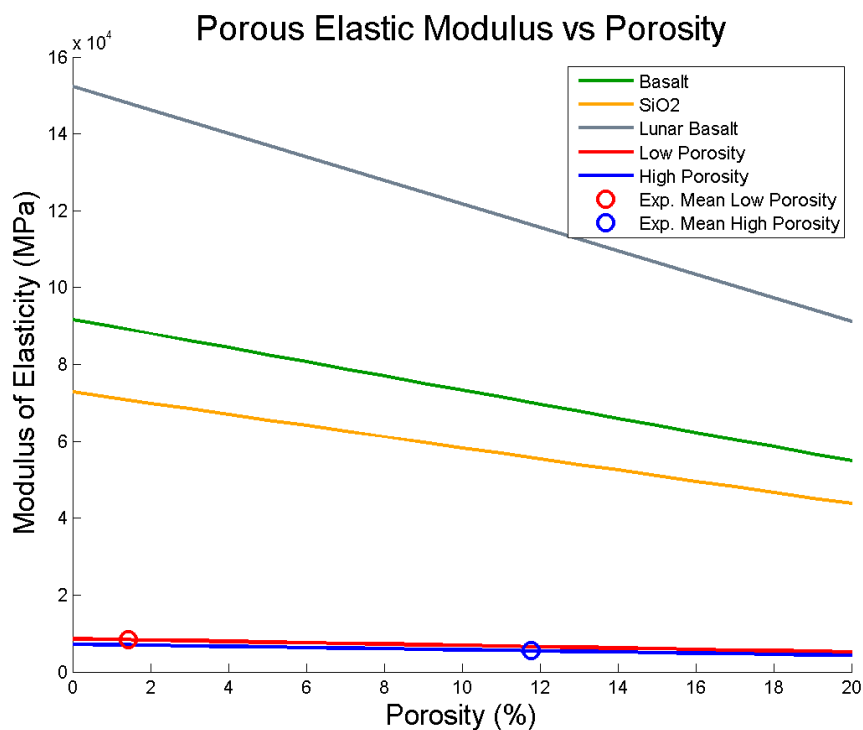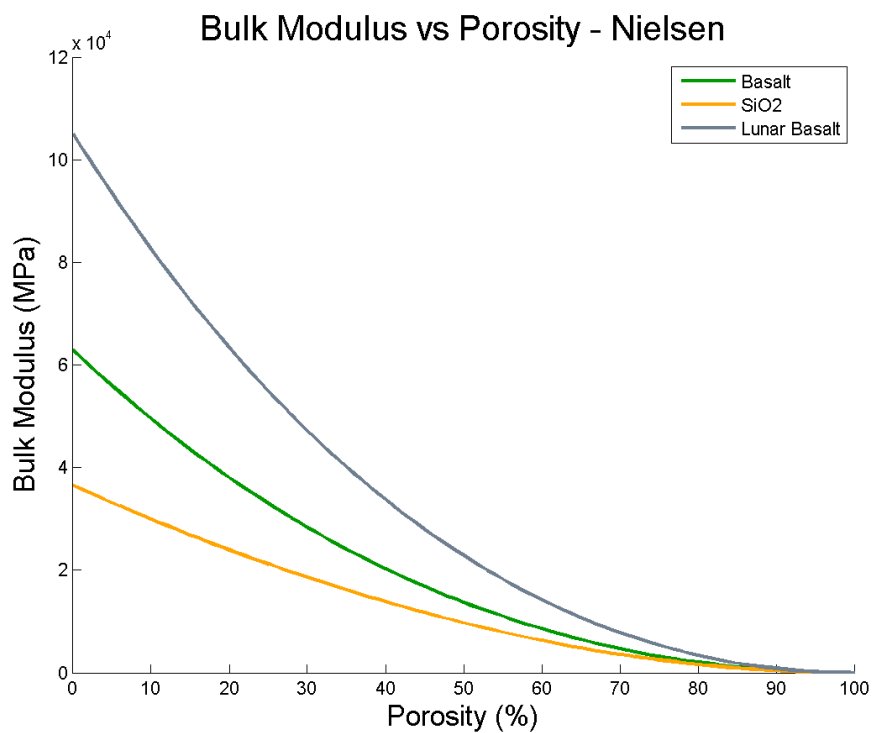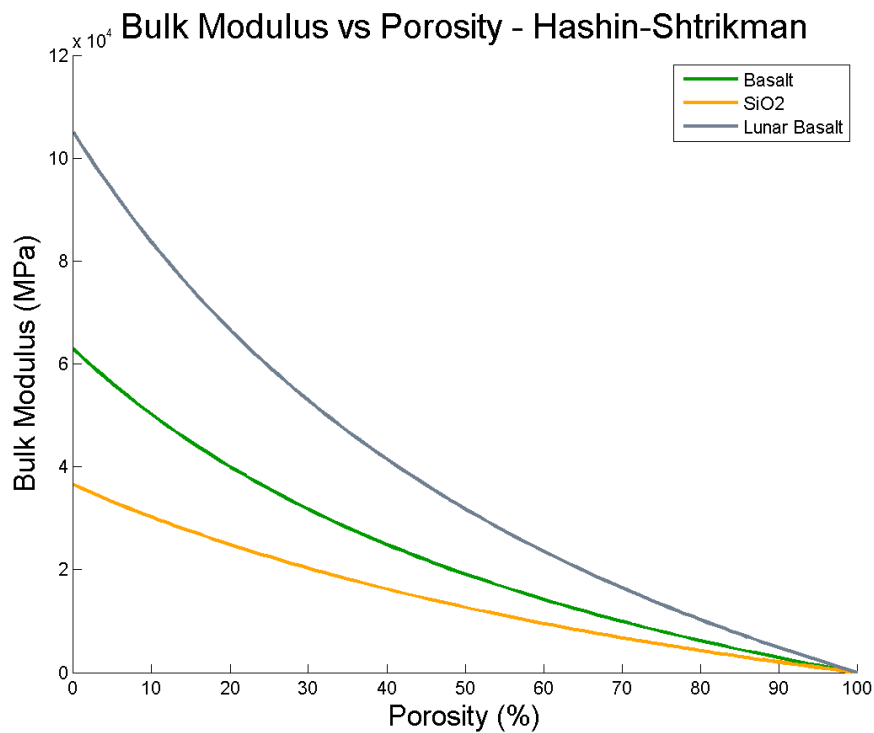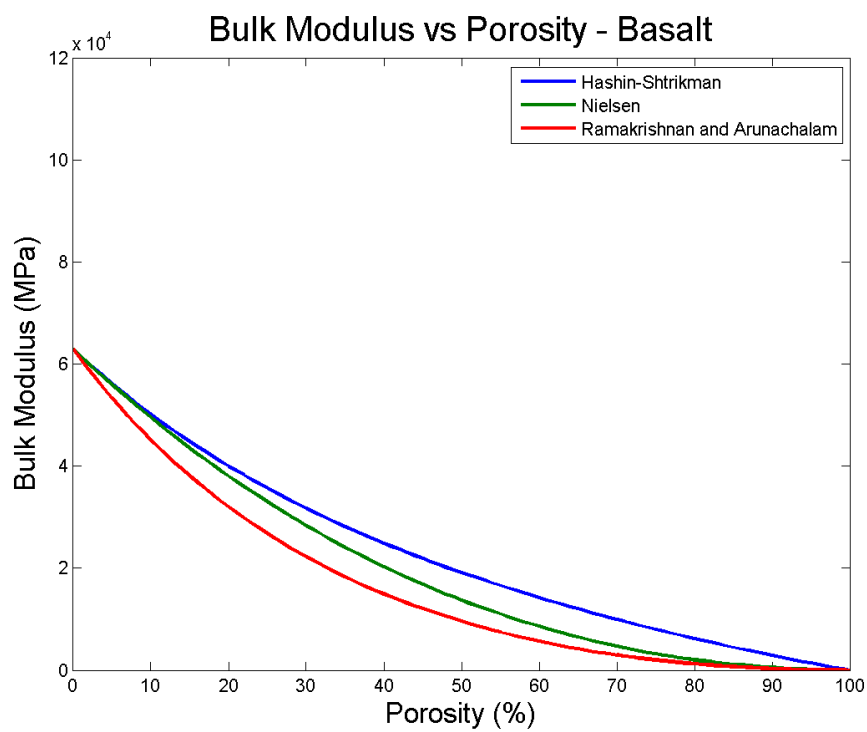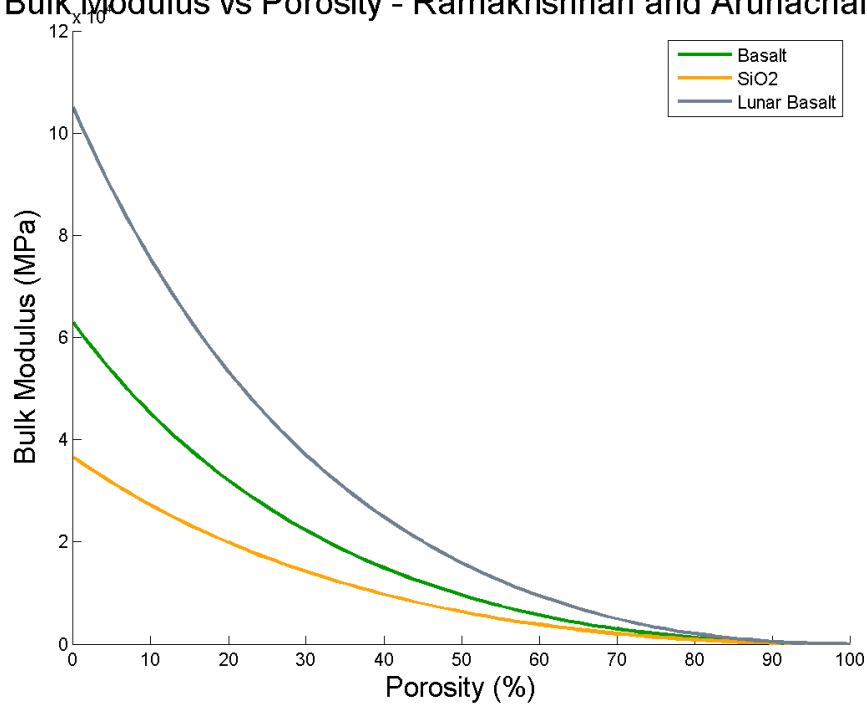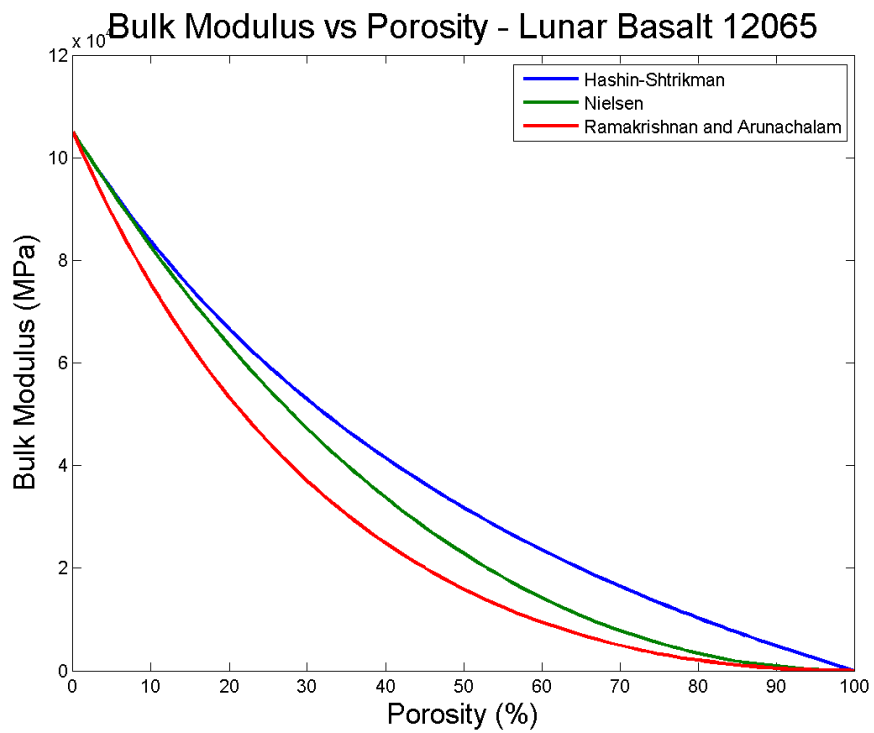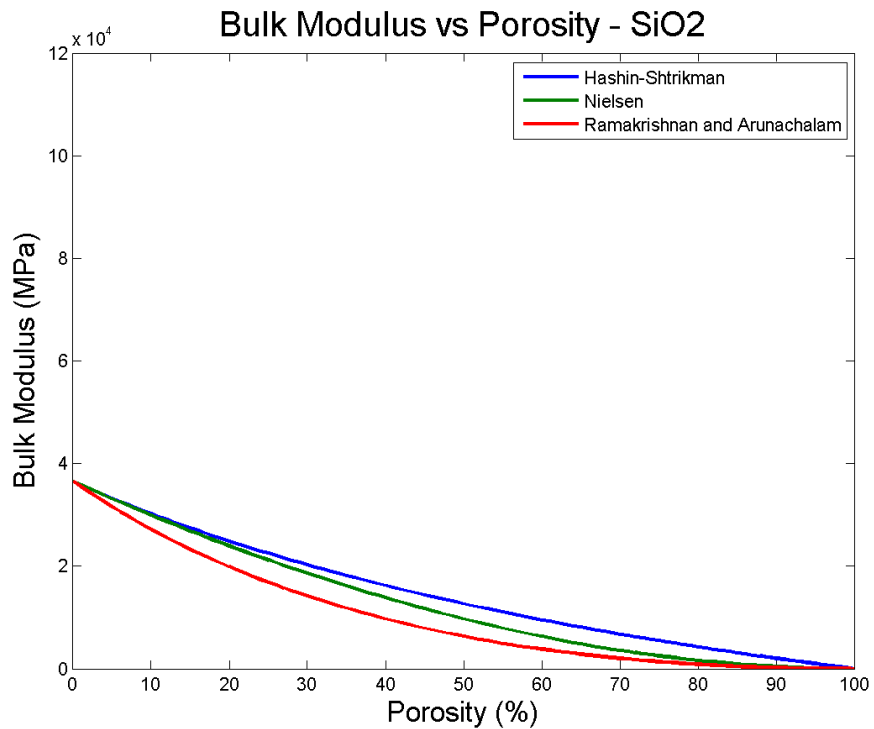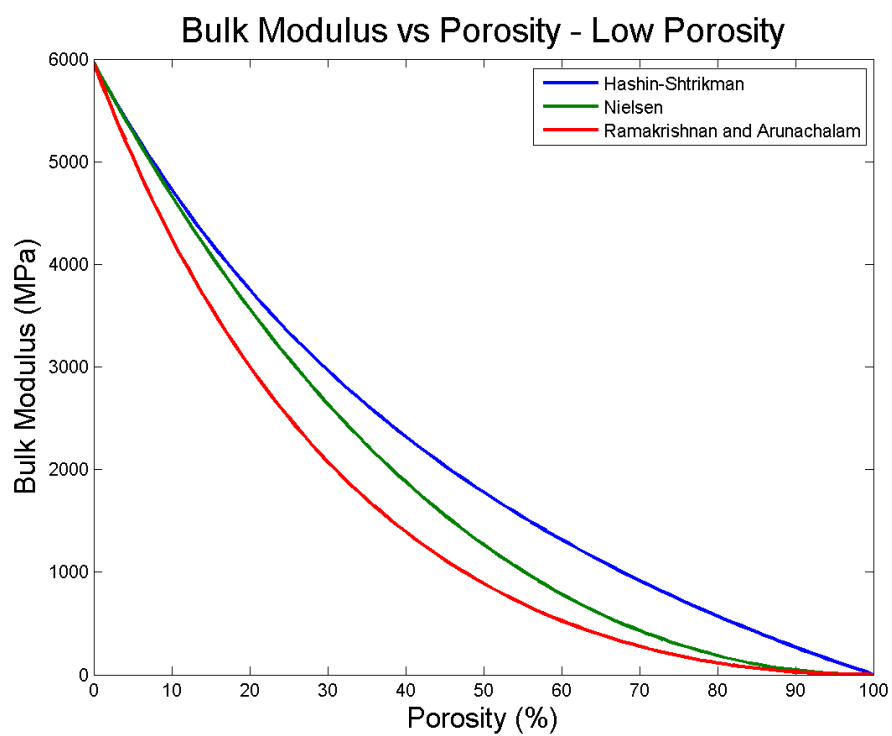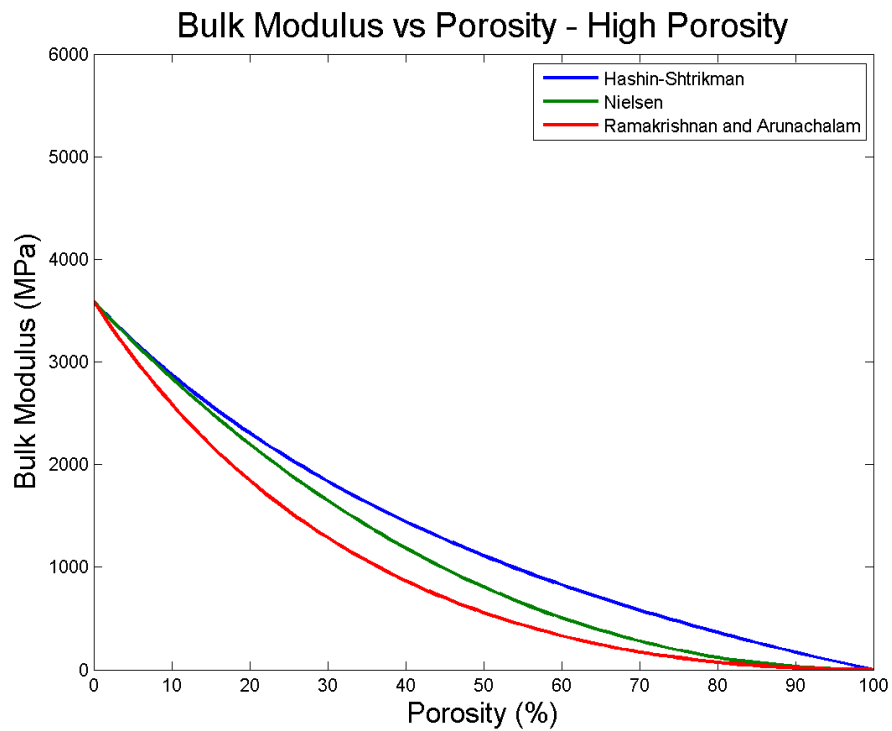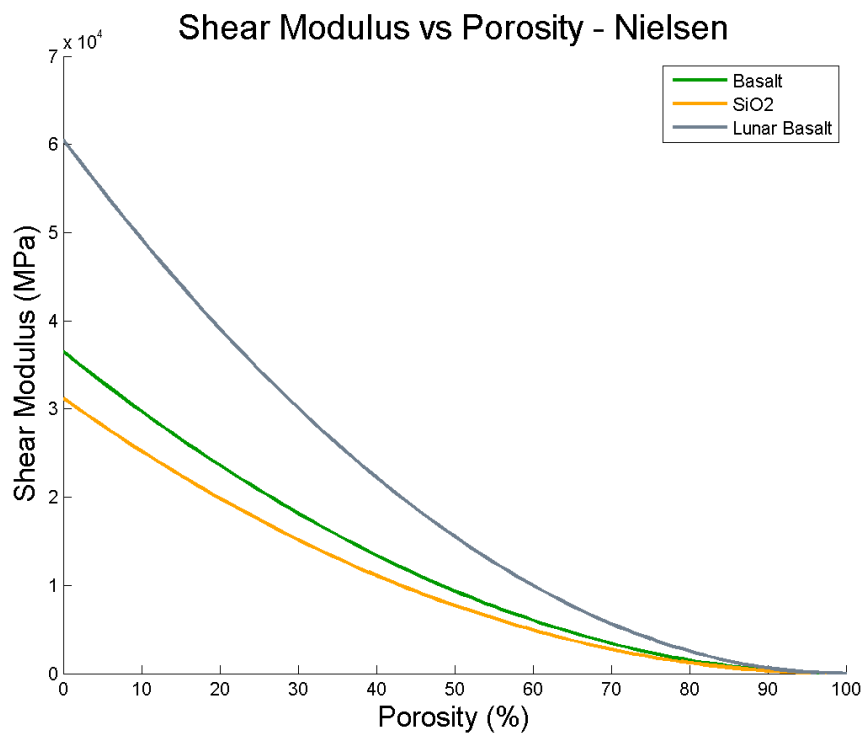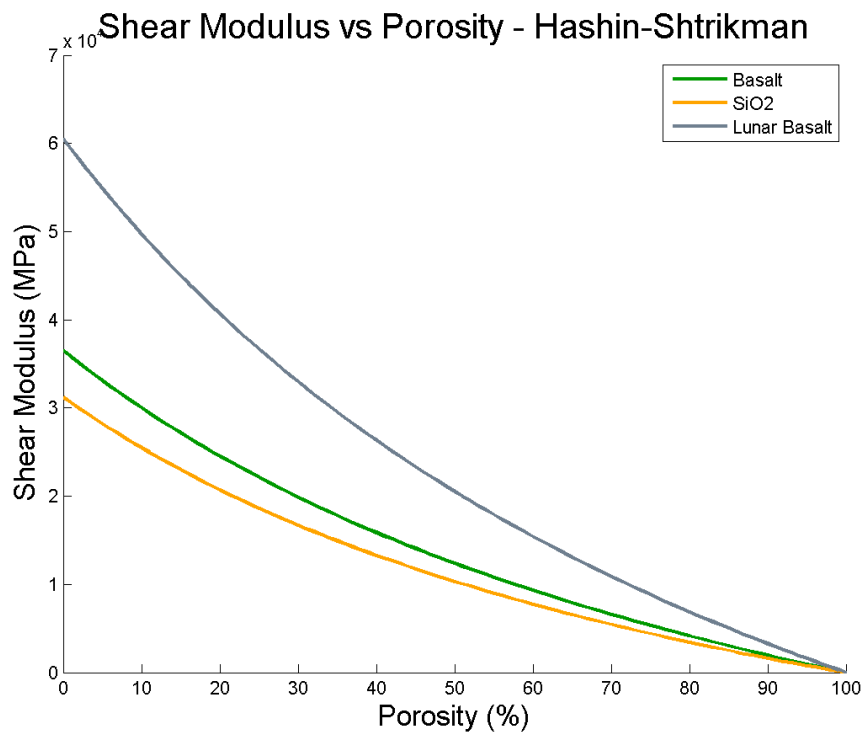
Shear Modulus vs Porosity - Ramakrishnan and Arunachalam

Shear Modulus vs Porosity - Basalt

Shear Modulus vs Porosity - SiO2

Shear Modulus vs Porosity - Lunar Basalt 12065

Shear Modulus vs Porosity - High Porosity
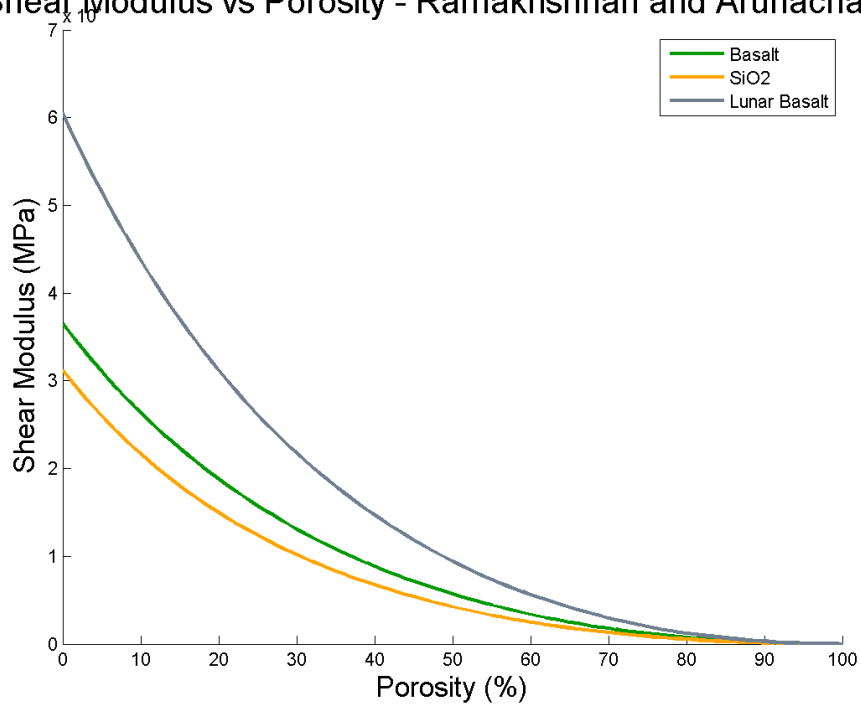
Shear Modulus vs Porosity - Low Porosity
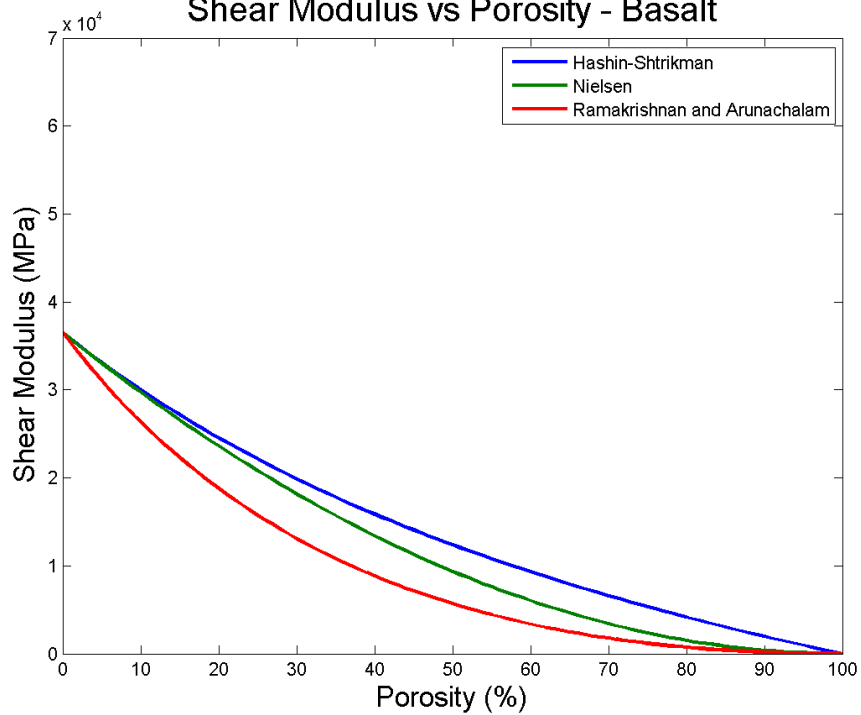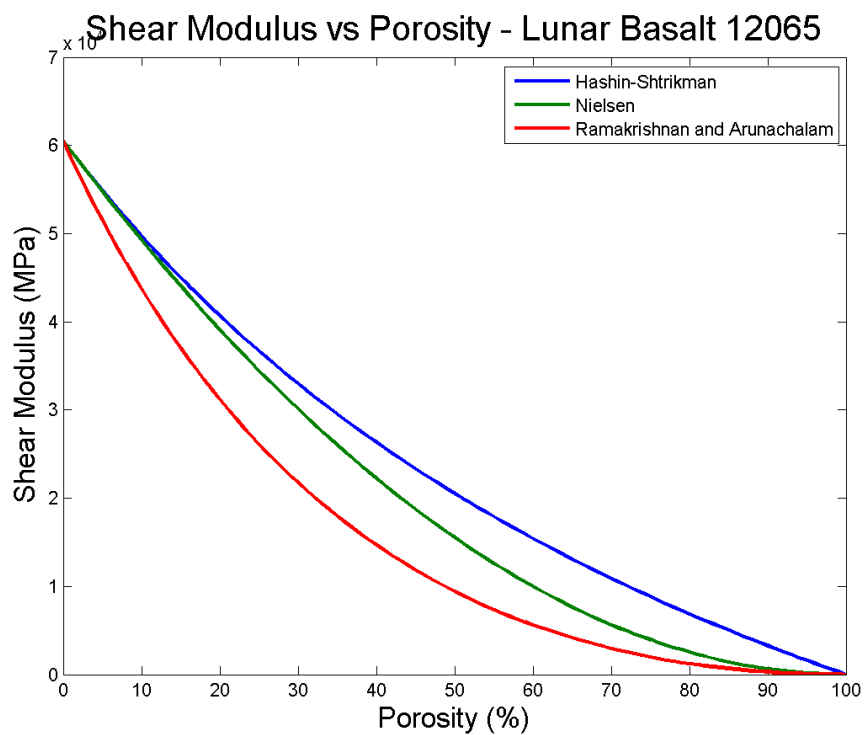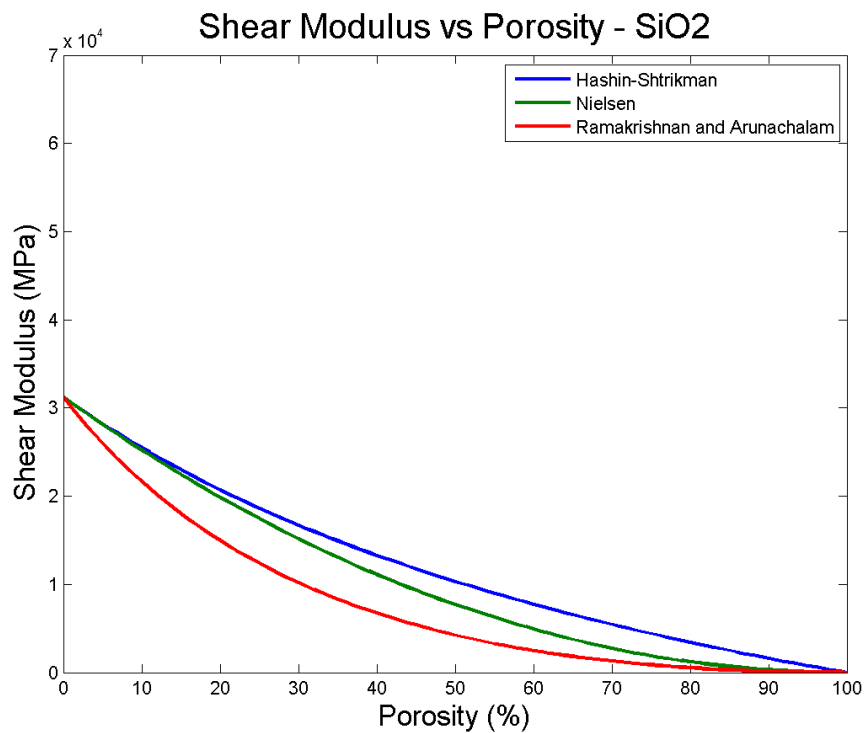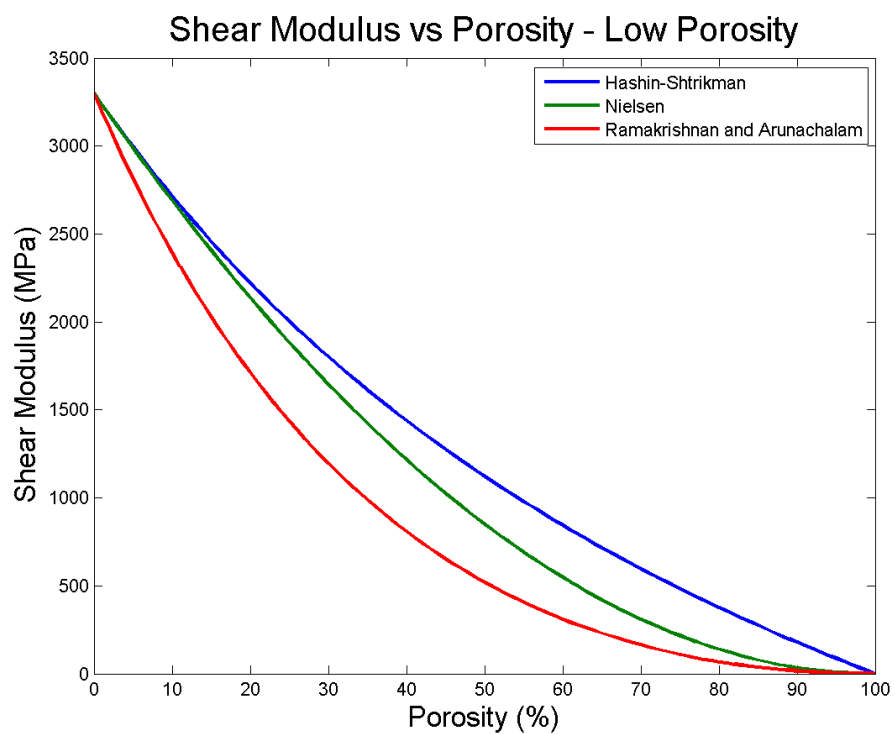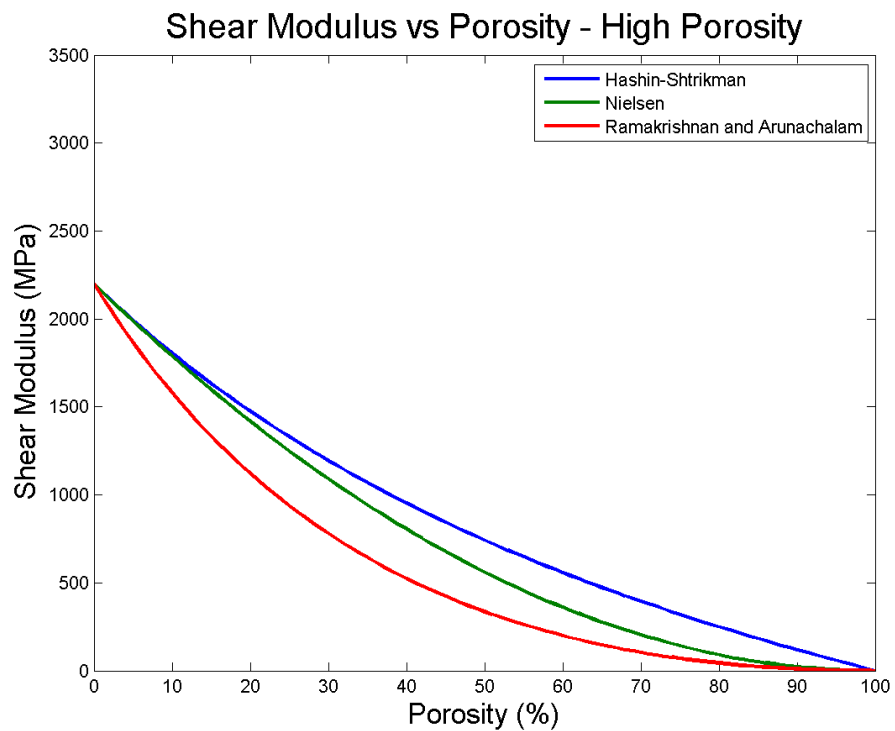
Appendix B   JSC-1A Sample Processing Procedure

JSC-1A Processing Procedure

W.M. Keck Biomedical Materials Research Center

School of Mechanical and Materials Engineering

Washington State University, Pullman WA 99164 USA

Email: amitband@wsu.edu & thomas.gualtieri@email.wsu.edu

This is the account of the development of a process to produce cylinders of JSC-1A that were sintered to exhibit the highest compression strength of the material. I will explain how both batches of the samples were made, and also give details why some of the steps were taken.

1. The powder was sifted using a No.70 sift which separated out any powder that was larger than 212μm. Initially the samples were pressed from the powder that was given. It was found that when pouring the powder into the cylinder mold, the larger grain powder had a tendency of falling in first, Then when it was packed, it was visibly noticeable that one end of the sample had larger powder size, which would lead to a difference of porosity across the specimen. By sifting the powder, there was a more consistent size of powder, which resulted in more homogeneous porosity across the sample.

2. 6 grams of the powder was measured out and poured into a 12mm wide cylinder mold. It was found through trial and error that when 6 grams of powder was pressed it produced a sample that had a height to width ratio of 2:1.

3. The powder was then pressed up to a pressure of 4MPa. It was let sit at this pressure for a minute and then removed. It should be noted that this step caused the most trouble. The powder is very dry and does not have very good adhesion to itself. Upon removal the packed cylinders would break apart frequently. A lot of time the fine powder would get in between the plug that was used to press and eject the cylinder, and the walls of the mold. This would cause the mold to vibrate when the sample was being pressed out. When the mold would vibrate, the pressed powder would shake apart and cause the cylinder to collapse. The samples were very fragile in this stage and any small touch or movement had the possibility of causing it to break apart. This made transporting the pressed samples a very fragile operation that usually resulted in at least one cylinder breaking.

4. The samples were then put in a furnace where they were sintered. Below is a table and graph of the process. It was found that at 1125°C the powder would start to melt and not retain its cylinder shape. Once this was found the temperature was lowered and the sintering times were played with until a process was found that produced a seemingly strong sample that retained its shape. Though this process worked well, there are still a lot of processes that could be explored and tested.

Temp. (°C)	Room Temp. - 350		350	350-750	750	750 - 1120	1120	End
Time (min)		350	60	400	60	370	15	Cool Down

JSC-1A Sintering Process
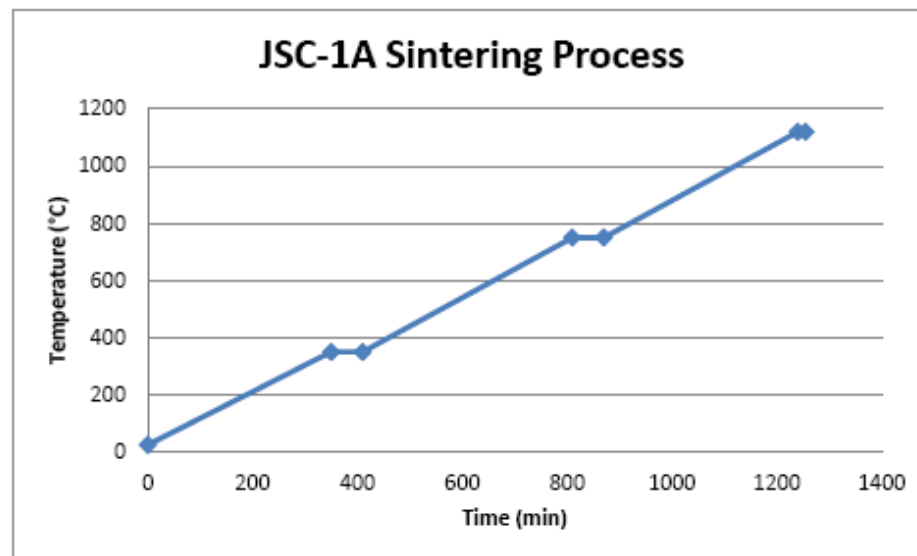
5. Once this was done the samples were observed to see if they retained their shape, and if the ends of the cylinder were flat. A lot of times powder would fall away from the ends leaving non-flat surfaces. If this was the case, which it was most the time, the end of the sample was cut away to the point where there were no visible defects at the end and a flat surface could be made. The end was then grinded as flat.

One batch of sample was made using the powder that made it through the No.70 sift. This resulted in a ≈1.4% porosity measurement using Archimedes method. The other set was made using the powder that did not pass through the No.70 sift. This resulted in samples that had ≈12% porosity. The results are listed in the table below.

Sintering Temp.	Sintering Time	Powder Size	Porosity (Average)
1120°C	15min	< 212µm	1.44%
1120°C	15min	> 212µm	11.78%

Appendix C   Sample Matlab Code

```matlab
createplot  =1;  % create plot output if =1, do not if =0
createexcel =0;  % create excel output if =1, do not if =0
maxdeflection=0;
TOUGHNESS=0;
        testno=                 [2 4 5 6 7 8 10 11 13 14 15 16];
        testinitialmaxindex=[2 2 1 3 1 2 11  1  2  1 10  3];
        counter=1;

% import test log file
titlefile=sprintf('Compression Test Log 5-20-2014.xlsx');
[lognum,logtxt,lograw]=xlsread(titlefile,'A6:R21');
 cd('C:\HRFiles\MATLAB\RUResearch');
titlefile=sprintf('CompressionTestDataCut.xlsx'

for j=1:16
    fprintf('Loop Iteration Number: %0.0f \n',j);

    % read excel with imported test data products
    [num]=xlsread(titlefile,j); % deflection (mm)

    % Setup - locating basic data information
    deflection=num(:,2);                    % mm
    deflection=deflection-num(1,2);     % mm zero deflection
    load=num(:,3);                          % kN
    Load_F=max(load);                       % kN
    maxdeflection=deflection(find(Load_F==(num(:,3))));  % mm
    datapointtotal=length(num(:,1));

    % Find overall maximum value
        [locsALL,pksALL]=peakseek(load);
        quantityofmaximaALL=length(pksALL);
        deflecpksALL=deflection(locsALL)';
        l_Load_F=find(locsALL==find(Load_F==(num(:,3))));
        deflecpksALL=deflecpksALL(1:l_Load_F);
        l_localmaximums=locsALL(1:l_Load_F);
        d_start=find(deflection>=0.2);
        d_start=d_start(1);
        l_end=find(load==max(load));

        if j==testno(counter)
            l_initial=locsALL(testinitialmaxindex(counter));
            Load_1=pksALL(testinitialmaxindex(counter));
            initialfailurelength=deflection(l_initial);

            counter=counter+1;
        else
            Load_1=load(l_end);
            l_initial=l_end;
            initialfailurelength=deflection(l_end
        end
```

```matlab
        hephzibah=zeros(1,length(deflecpksALL));  % create zero array
        if length(deflecpksALL)>1
            for k=1:length(deflecpksALL)
                if deflecpksALL(k)>0.2
                    hephzibah(k)=1;
                end
            end
            quantityofmaximaOVER2 =sum(hephzibah);  % sum number of
values greater than 0.2 mm,
        else
            hephzibah=[0];
            quantityofmaximaOVER2 =1;                  % quantity of peaks
above 0.2 mm deflection


        end

    CS_Area=(pi*(lognum(j,15)/1000)^2)/4;   % m^2
    CS_Area_small=(pi*lognum(j,15)^2)/4;    % mm^2

    Load_I=load(1);                            % kN
    Height_I=lognum(j,9);                      % mm
    Diameter_I=lognum(j,15);                   % mm
    Mass_I=lognum(j,5);                        % g
    Volume_I_small=CS_Area_small*Height_I;     % mm^3
    Volume_I=CS_Area*Height_I/1000;            % m^3
    Density_I_small=lognum(j,5)/Volume_I_small;   % g/mm^3
    Density_I=(lognum(j,5)/1000)/Volume_I;     % kg/m^3
    Pressure_I=(Load_I/CS_Area)/1000;          % MPa   1 Pa =1 N/m^2
    EngStress_I=(Load_I/CS_Area)/1000;         % MPa

    % 0.2 mm Sample Measurements and Values
    Load_02=load(d_start);                     % kN
    Height_02=lognum(j,9)-deflection(d_start); % mm
    Deflection_02=deflection(d_start);         % mm
    Volume_02_small=CS_Area_small*Height_02;   % mm^3
    Volume_02=CS_Area*Height_02/1000;          % m^3
    Density_02_small=lognum(j,5)/Volume_02_small;   % g/mm^3
    Density_02=(lognum(j,5)/1000)/Volume_02;        % kg/m^3
    Pressure_02=(Load_02/CS_Area)/1000;             % MPa
    BulkModulus_02=Pressure_02/((Volume_I-Volume_02)/Volume_I);  % Mpa
    EngStress_02=(Load_02/CS_Area)/1000;       % MPa
    EngStrain_02=((lognum(j,9)-deflection(d_start))-
lognum(j,9))/lognum(j,9);

    % Initial Failure Sample Measurements and Values
    Load_1=Load_1;                             % kN
    Height_1=lognum(j,9)-initialfailurelength;    % mm
    Deflection_1=initialfailurelength;         % mm
    Volume_1_small=CS_Area_small*Height_1;     % mm^3
    Volume_1=CS_Area*Height_1/1000;            % m^3
    Density_1_small=lognum(j,5)/Volume_1_small;   % g/mm^3
    Density_1=(lognum(j,5)/1000)/Volume_1;     % kg/m^3
    Pressure_1=(Load_1/CS_Area)/1000;          % MPa
    BulkModulus_1=Pressure_1/((Volume_I-Volume_1)/Volume_I);  % MPa
    EngStress_1=(Load_1/CS_Area)/1000;         % MPa
```

```matlab
    EngStrain_1=((lognum(j,9)-initialfailurelength)-
lognum(j,9))/lognum(j,9);


     % Final Sample Measurements and Values
    Load_F=max(load);                             % kN
    Height_F=lognum(j,9)-maxdeflection;       % mm
    Deflection_F=maxdeflection;                % mm
    Volume_F_small=CS_Area_small*Height_F;  % mm^3
    Volume_F=CS_Area*Height_F/1000;           % m^3
    Density_F_small=lognum(j,5)/Volume_F_small;    % g/mm^3
    Density_F=(lognum(j,5)/1000)/Volume_F;         % kg/m^3
    Pressure_F=(Load_F/CS_Area)/1000;         % MPa       1 Pa =1 N/m^2
    BulkModulus_F=Pressure_F/((Volume_I-Volume_F)/Volume_I);   % MPa
    EngStress_F=(Load_F/CS_Area)/1000;        % MPa
    EngStrain_F=((lognum(j,9)-maxdeflection)-lognum(j,9))/lognum(j,9);

    Height_live=Height_I-deflection(1:l_end);   % mm
    Deflection_live=deflection(1:l_end);        % mm
    Volume_live_small=CS_Area*Height_live(1:l_end);   % mm^3
    Volume_live=CS_Area*Height_live(1:l_end)/1000;    % m^3
    Density_live_small=lognum(j,5)/Volume_live;        % g/mm^3
    Density_live=(lognum(j,5)/1000)/Volume_live;       % kg/m^3
    Pressure_live=load(1:l_end)/CS_Area;               % KPa
    BulkModulus_live=Pressure_live./((Volume_I-
Volume_live)/Volume_I)/1000;        % MPa
    EngStress_live=((load(1:l_end))/CS_Area)/1000;    % MPa
    EngStrain_live=((lognum(j,9)-deflection(1:l_end))-
lognum(j,9))/lognum(j,9); % unitless, strain values across the entire
data set

time=(linspace(1,length(EngStress_live),length(EngStress_live)))/10;

    % create a set for live date up to initial failure
        length_shrinking=lognum(j,9)-deflection;   % mm
    length_shrinking=length_shrinking(1:l_end);     % mm
    bulk_modulus_live=-EngStress_live./ EngStrain_live;
    BulkModulusAtMaxFailure=bulk_modulus_live(end);

    % Cut and calculate data sets END
    % Plot all 16 data sets in full START

    % plot output of data set
    if createplot==1

        if j<=8
           strname=sprintf('Test %d - Load vs Deflection Low
Porosity',j);
           h1=plot(deflection,load,'r');
           if j==8 % since test 8 has a little different bounds
               xlim([0 1.2]); ylim([0 30]);
           else
               xlim([0 0.8]); ylim([0 30]);
           end

        else
```

```matlab
            strname=sprintf('Test %d - Load vs Deflection High
Porosity',j);
            h2=plot(deflection,load,'b');
            xlim([0 0.8]); ylim([0 18]);
        end

        set(gcf,'color','w');
        title(strname,'FontSize',20);
        xlabel('Deflection (mm)','FontSize',16);
        ylabel('Load (kN)','FontSize',16);
        legend([h1 h2], 'Low Porosity','High
Porosity','Location','Best');
        cd('C:\HRFiles\MATLAB\RUResearch\Plots\All');
        saveas(gcf,strname,'png');
        close(gcf);

% Plot all 16 data sets in full END
% Plot all 16 data sets cut after initial failure START

data from 0.2 then .2 mm in deflection to maximum load condition

        end point locsALL(1)

        if j<=8
            strname=sprintf('Test %d - Load vs Deflection Low Porosity
- Initial Failure',j);
            h1=plot(deflection(d_start:l_end),load(d_start:l_end),'r');
            %xlim([0.2 1]); ylim([0 30]);

        else
            strname=sprintf('Test %d - Load vs Deflection High Porosity
- Initial Failure',j);
            h2=plot(deflection(d_start:l_end),load(d_start:l_end),'b');
            %xlim([0.2 0.8]); ylim([0 17]);
        end

        set(gcf,'color','w');
        title(strname,'FontSize',20);
        xlabel('Deflection (mm)','FontSize',16);
        ylabel('Load (kN)','FontSize',16);
        cd('C:\HRFiles\MATLAB\RUResearch\Plots\Cut');
        saveas(gcf,strname,'png');
        close(gcf);

% Plot all 16 data sets cut after initial failure END
% plots the dataset from 0.2 mm to maximum load, plots are overlaid
START

        if j<=8
            strname=sprintf('Test %d - Load vs Deflection Low Porosity
- start to max',j);
            hold on

h1=plot(deflection(d_start:l_end),load(d_start:l_end),'r','LineWidth',1
);
```

```matlab
h2=plot(deflection(d_start:l_initial),load(d_start:l_initial),'r','Line
Width',4);
            xlim([0.2 1]); ylim([0 30]);
            legend([h1 h2], '0.2 mm - Maximum Failure','0.2 mm - Inital
Failure','Location','Best');
            hold off
        else
            strname=sprintf('Test %d - Load vs Deflection High Porosity
- start to max',j);
            hold on

h1=plot(deflection(d_start:l_end),load(d_start:l_end),'b','LineWidth',1
);

h2=plot(deflection(d_start:l_initial),load(d_start:l_initial),'b','Line
Width',4);
            xlim([0.2 0.8]); ylim([0 17]);
            legend([h1 h2], '0.2 mm - Maximum Failure','0.2 mm -
Initial Failure','Location','Best');
            hold off
        end

        set(gcf,'color','w');
        title(strname,'FontSize',20);
        xlabel('Deflection (mm)','FontSize',16);
        ylabel('Load (kN)','FontSize',16);
        cd('C:\HRFiles\MATLAB\RUResearch\Plots\Cut');
        saveas(gcf,strname,'png');
        close(gcf);

% plots the dataset from 0.2 mm to maximum load, plots are overlaid END
% plot engineering stress vs engineering strain START

        clear h1 h2 h3
        hold on

        EngStrain_live=-EngStrain_live;
        snl=EngStrain_live(l_localmaximums);
        ssl=EngStrain_live(l_localmaximums);

        if j<=8
            strname=sprintf('Test %d - Stress vs Strain - start to
max',j);
            h1=plot(EngStrain_live,EngStress_live,'r');

h2=plot(max(EngStrain_live),max(EngStress_live),'rX','MarkerSize',10);
            if quantityofmaximaOVER2 >1
                 h3= plot(snl(1:end-1),ssl(1:end-1),'ro');
            end
        else
            strname=sprintf('Test %d - Stress vs Strain - start to
max',j);
            h1=plot(EngStrain_live,EngStress_live,'b');

h2=plot(max(EngStrain_live),max(EngStress_live),'bX','MarkerSize',10);
```

```matlab
            if quantityofmaximaOVER2 >1
                h3= plot(snl(1:end-1),ssl(1:end-1),'bo');
            end
            xlim([0 0.05]); ylim([0 140]);
        end
        hold off
        set(gcf,'color','w');
        title(strname,'FontSize',20);
        xlabel('Strain','FontSize',16);
        ylabel('Stress (MPa)','FontSize',16);

        if exist('h3') ==1
            legend([h2 h3], 'Maximum Failure','Local
Failure','Location','Best');
        else
            text(max(EngStrain_live),max(EngStress_live),'Maximum
Failure  ','HorizontalAlignment','right');
        end

        cd('C:\HRFiles\MATLAB\RUResearch\Plots\Stress Vs Strain');
        saveas(gcf,strname,'png');
        close(gcf);
        clear h1 h2 h3

% plot engineering stress vs engineering strain END
% plot engineering stress vs engineering strain Cut between 0.02 and
initial failure START

        clear h1 h2 h3
        hold on

        EngStrain_live=-EngStrain_live;
        snl=EngStrain_live(l_localmaximums);
        ssl=EngStrain_live(l_localmaximums);
        h1=plot(EngStrain_live,EngStress_live,'k');

 % used for test 1-6
        if j<=8 && (j==1 ||j==3)
            strname=sprintf('Test %d - Stress vs Strain - start to
final',j);

h2=plot(EngStrain_live(d_start:l_end),EngStress_live(d_start:l_end),'r'
);
            % xlim([0 0.05]); ylim([0 260]);
        elseif j<=8 && (j==2 || j==4 || j==5|| j==6)
            strname=sprintf('Test %d - Stress vs Strain - start to
inital',j);

h3=plot(EngStrain_live(d_start:l_initial),EngStress_live(d_start:l_init
ial),'r');

        if j<=9
            strname=sprintf('Test %d - Stress vs Strain - start to
initial',j);
```

```matlab
h4=plot(EngStrain_live(d_start:l_initial),EngStress_live(d_start:l_init
ial),'c','LineWidth',4);
            xlim([0 0.05]); ylim([0 140]);

        if j>=9
            strname=sprintf('Test %d - Stress vs Strain - start to
end',j);

h5=plot(EngStrain_live(d_start:l_initial),EngStress_live(d_start:l_init
ial),'b');
        else
        end

        hold off
        set(gcf,'color','w');
        title(strname,'FontSize',20);
        xlabel('Strain','FontSize',16);
        ylabel('Stress (MPa)','FontSize',16);
         pause
        cd('C:\HRFiles\MATLAB\RUResearch\Plots\Stress Vs Strain CUT');
        saveas(gcf,strname,'png');

        close(gcf);
        clear h1 h2 h3

% plot engineering stress vs engineering strain Cut between 0.02 and
initial failure END
% plot Toughness area charts START

        hold off

         clear h1 h2 h3

        EngStrain_live=-EngStrain_live;
        snl=EngStrain_live(l_localmaximums);
        ssl=EngStrain_live(l_localmaximums);
        h1=plot(EngStrain_live,EngStress_live,'k');

        if j<=8% && (j==1 ||j==3)
            strname=sprintf('Test %d - Toughness - start to final',j);

h2=area(EngStrain_live(1:l_end),EngStress_live(1:l_end),'FaceColor','r'
);

        elseif j>=9
            strname=sprintf('Test %d - Toughness - start to
initial',j);

h4=area(EngStrain_live(1:l_initial),EngStress_live(1:l_initial),'FaceCo
lor','b');
            xlim([0 0.03]); ylim([0 140]);

        end
```

```matlab
Toughness=trapz(EngStrain_live(1:l_end),EngStress_live(1:l_end));
        TOUGHNESS(j)=Toughness;


        hold off
        set(gcf,'color','w');
        title(strname,'FontSize',20);
        xlabel('Strain','FontSize',16);
        ylabel('Stress (MPa)','FontSize',16);
        cd('C:\HRFiles\MATLAB\RUResearch\Plots\Good\Toughness');
        saveas(gcf,strname,'png');

        close(gcf);
        clear h1 h2 h3

% plot Toughness area charts END

        cd('C:\HRFiles\MATLAB\RUResearch');

    end
% Plot all 16 data sets cut after initial failure END
% Create and export compiled calculations in excel START
    if createexcel==1

        cd('C:\HRFiles\MATLAB\RUResearch');

        HEADER1={        'Test File Name',...
                         'Test Operator',...
                         'Test Date',...
                         'Test Number',...
                         'Sample Number',...
                         'Porosity Group',...
                         'Mass (grain)',...
                         'Mass (grams)',...
                         'Height 1 (mm)','Height 2 (mm)','Height 3
(mm)',...
                         'Average Height (mm)',...
                         'Diameter 1 (mm)','Diameter 2 (mm)','Diameter 3
(mm)','Diameter 4 (mm)','Diameter 5 (mm)',...
                         'Average Diameter (mm)'};

        HEADER2={        'Number of Data Points',...
                         'Quantity of peak values during test, entire
data set',...
                         'Quantity of peak values during test, greater
then 0.2 mm, and less then max load',...
                         'Area of Sample Cross Section Averaged
(m^2)',...
                         'Area of Sample Cross Section Averaged
(mm^2)',...
                         'Sample Volume (m^3)',...
                         'Sample Volume (mm^3)',...
                         'Sample Density (kg/m^3)',...
                         'Sample Density (g/mm^3)',...
```

```matlab
                        'Maximum Load (kN)',...
                        'First Local Max Value Load (kN)',...
                        'Maximum Deflection (mm)',...
                        'First Local Max Value Deflection (mm)',...
                        'Engineering Stress Max (MPa)'...
                        'Engineering Stress First Local Max (MPa)',...
                        'Engineering Strain Max',...
                        'Engineering Strain First Local Max'...
                        'Bulk Modulus at Max Failure (MPa)'};

        MASTER1=lograw;
        MASTER2(j,:)=[  datapointtotal...
                        quantityofmaximaALL...
                        quantityofmaximaOVER2...
                        CS_Area...
                        CS_Area_small...
                        Volume_I...
                        Volume_I_small...
                        Density_I...
                        Density_I_small...
                        Load_F...
                        Load_1...
                        maxdeflection...
                        initialfailurelength...
                        EngStress_F...
                        EngStress_1...
                        EngStrain_F...
                        EngStrain_1...
                        BulkModulusAtMaxFailure];

        cd('C:\HRFiles\MATLAB\RUResearch\Export Excel');

        xlswrite('Compression Test Compiled
Data.xlsx',HEADER1,'Sheet1','A1')
        xlswrite('Compression Test Compiled
Data.xlsx',HEADER2,'Sheet1','S1')
        xlswrite('Compression Test Compiled
Data.xlsx',MASTER1,'Sheet1','A2')
        xlswrite('Compression Test Compiled
Data.xlsx',MASTER2,'Sheet1','S2')


    HEADER3={       'Diameter (mm)'...
                    'Circular Cross Section Area (mm^2)'...
                    'Mass (g)'...
                    'Load Initial (kN)',...
                    'Load 0.2mm (kN)',...
                    'Load Int. Failure (kN)',...
                    'Load Final (kN)',...
                    'Height Initial (mm)',...
                    'Height 0.2mm (mm)',...
                    'Height Int. Failure (mm)',...
                    'Height Final (mm)',...
                    'Deflection Initial (mm)',...
                    'Deflection 0.2mm (mm)',...
                    'Deflection Final (mm)',...
```

```matlab
                        'Volume Initial (mm^3)',...
                        'Volume 0.2mm (mm^3)',...
                        'Volume Int. Failure (mm^3)',...
                        'Volume Final (mm^3)',...
                        'Density Initial (g/mm^3)',...
                        'Density 0.2mm (g/mm^3)',...
                        'Density Int. Failure (g/mm^3)',...
                        'Density Final (g/mm^3)',...
                        'Pressure Initial (MPa)',...
                        'Pressure 0.2mm (MPa)',...
                        'Pressure Int. Failure (MPa)',...
                        'Pressure Final (MPa)',...
                        'Bulk Modulus 0.2mm (MPa)',...
                        'Bulk Modulus Int. Failure (MPa)',...
                        'Bulk Modulus Final (MPa)',...
                        'Engineering Stress Initial (MPa)',...
                        'Engineering Stress 0.2mm (MPa)',...
                        'Engineering Stress Int. Failure (MPa)',...
                        'Engineering Stress Final (MPa)',...
                        'Engineering Strain 0.2mm',...
                        'Engineering Strain Int. Failure',...
                        'Engineering Strain Final'};

    MASTER3(j,:)=[  Diameter_I...
                    CS_Area_small...
                    Mass_I...
                    Load_I...
                    Load_02...
                    Load_1...
                    Load_F...
                    Height_I...
                    Height_02...
                    Height_1...
                    Height_F...
                    Deflection_02...
                    Deflection_1...
                    Deflection_F...
                    Volume_I_small...
                    Volume_02_small...
                    Volume_1_small...
                    Volume_F_small...
                    Density_I_small...
                    Density_02_small...
                    Density_1_small...
                    Density_F_small...
                    Pressure_I...
                    Pressure_02...
                    Pressure_1...
                    Pressure_F...
                    BulkModulus_02...
                    BulkModulus_1...
                    BulkModulus_F...
                    EngStress_I...
                    EngStress_02...
                    EngStress_1...
                    EngStress_F...
                    EngStrain_02...
```

```
                    EngStrain_1...
                    EngStrain_F];

        cd('C:\HRFiles\MATLAB\RUResearch\Export Excel');

        xlswrite('Compression Test Compiled
Data3.xlsx',HEADER1,'Sheet1','A1')
        xlswrite('Compression Test Compiled
Data3.xlsx',HEADER3,'Sheet1','S1')
        xlswrite('Compression Test Compiled
Data3.xlsx',MASTER1,'Sheet1','A2')
        xlswrite('Compression Test Compiled
Data3.xlsx',MASTER3,'Sheet1','S2')

        cd('C:\HRFiles\MATLAB\RUResearch');
    end

end
```

References

Allen, C.C., Graf, J.C. and McKay, D.S. (1994), Sintering bricks on the Moon, in Galloway, R.G. and Lokaj, S. (Eds), *Proceedings of the ASCE Specialty Conference (Space'94)*, Albuquerque, NM, 26 February-3 March, ASCE, New York, NY.1220-1229.

Ashby, M., and Jones, D. (1999). *Engineering materials 2 an introduction to microstructures, processing, and design* (2nd ed.). Oxford: Butterworth-Heinemann.

Askeland, D., Fulay, P. and Wright, W. (1994). *The science and engineering of materials* (3rd ed.). Boston: PWS.

Bart, G., Nickerson, R., Lawder, M., and Melosh, H. (2011). Global survey of lunar regolith depths from LROC images. Icarus, 485-490.

Benaroya, H., Indyk, S. and Mottaghi, S. (2012). Advanced systems concept for autonomous construction and self-repair of lunar surface ISRU structures. In Badescu, V. (Ed.), *Moon prospective energy and material resources* (pp. 641-660). Berlin: Springer.

Benaroya, H. and Bernold, L. (2008). Engineering of lunar bases. *Acta Astronautica, 62*, 277-299.

Benaroya, H., Mottaghi, S. and Porter, Z. (2012). Magnesium as an ISRU-derived resource for lunar structures. *Journal of Aerospace Engineering,* 152-159.

Benaroya, H., Bernold, L., and Chua, K. M. (2002). Engineering, design, and construction of lunar bases." *Journal of Aerospace Engineering*, 15(2), 33–45.

Balla, V., Roberson, L., Connor, G., Trigwell, S., Bose, S. and Bandyopadhyay, A. (2012).First demonstration on direct laser fabrication of lunar regolith parts. *Rapid Prototyping Journal,* Vol. *18*, 451-457.

Bridgford, E. and Eustes, A., (1999) Physical properties of basalt, ice, and permafrost report in support of the Martian subsurface explorer. Colorado School of Mines. JPL Contract #961494.

Cambou, B., Jean, M. and Radjai, F. (2009). *Micromechanics of granular materials*. London: ISTE.

Cao, G. and Wang, Y. (2004). *Nanostructures & nanomaterials synthesis, properties & applications*. London: Imperial College Press.

Cardiff E.H. and Hall, B.C. (2008). A dust mitigation vehicle utilizing direct solar heating. *Joint Annual meeting of LEAG-IECUM-SRR.* October 28-31, 2008.

Cohen, M.M. (2002). Selected precepts in lunar architecture. *Tech.*

Rep., 53rd Int. Astronautical Congress, The World Space Congress, Houston.

DeGarmo, E., Paul, E., Black, J. and Kohser, R. (2003). *Materials and processes in manufacturing* (9th ed.). New York: Wiley.

Duke, M.B., Gaddis, L.R., Cesaretti, G., Dini, E., Kestelier, X., Colla, V. and Pambaguian, L. (2013). Building components for an outpost on the lunar soil by means of a novel 3D printing technology. *Acta Astronautica, 93*, 430-450.

Elasticity of Minerals, Glasses, and Melts. (1995). In T. Ahrens (Ed.), Mineral physics & crystallography: A handbook of physical constants (p. 56). Washington, DC: American Geophysical Union.

Ettouney, M., and Benaroya, H. (1992). Regolith Mechanics, Dynamics, and Foundations. *Journal of Aerospace Engineering,* 214-229.

Faierson, E., Logan, K., Stewart, B. and Hunt, M. (2010). Demonstration of concept for fabrication of lunar physical assets utilizing lunar regolith simulant and a geothermite reaction. *Acta Astronautica,* Vol. *67*, 38-45.

German, R.M. (2003). Gravitational effects on liquid phase sintering - distortion observations. Unpublished manuscript. Retrieved from: https://www.cavs.msstate.edu/publications/docs/2003/07/2003-17.pdf

German, R.M. (1996). *Sintering theory and practice*. New York: Wiley.

Gualtieri, T. and A. Bandyopadhyay. (2015). Compressive deformation of porous lunar regolith. Materials Letters, Vol. 143, 276-278.

Happel, J.A., Willam, K. and B. Shing. (1992). Prototype Lunar Base Constructing Using Indigenous Materials, SPAE 92 Engineering, Construction, and Operations in Space, Proceedings of the ASCE, New York, 112-122.

Heiken, G., Vaniman, D. and B. French. (1991). *Lunar sourcebook: A user's guide to the Moon*. Cambridge: Cambridge Univ. Press.

Hintze, P., Curran, J. and T. Back. (2009). Lunar surface stabilization via sintering or the use of heat cured polymers. *47th AIAA Aerospace Sciences Meetings Including the New Horizons Forum and Aerospace Exposition.*

Hobosyan, M.A. and K.S. Marturosyan. (2012). Sintering of regolith by activated thermites: a novel approach for lunar in situ resource utilization. *43ed Lunar and Planetary Science Conference.*

Hung, Ching-cheh, and Jeremiah McNatt (24 Feb. 2010). Lunar dust simulant containing nanophase iron and method for making the same. Patent 20110204185A1.

Kingery, W. and Bowen, H. (1976). *Introduction to ceramics* (2nd ed.). New York: Wiley.

Lamond J.F. and Pielert, J.H. *Significance of tests and properties of concrete and concrete-making materials.* Bridgeport, NJ. ASTM International. 2006.

Lin, T.D., Love, H., and Stark, D. (1987). Physical properties of concrete made with Apollo 16 lunar soil sample. American Institute of Aeronautics and Astronautics, Proceedings, October 1987.

Landis, G.A. (2007). Materials refining on the Moon. *Acta Astronautica* 60, 906-915.

Marshal Space Flight Center (2010). In Situ Resource Utilization (ISRU) Element. Unpublished Source. http://isru.msfc.nasa.gov/lib/Documents/Simulant-listing.pdf

McLemore, C., Fikes, J., McCarley, K., Good, J. E., Gilley, S. D. and Kennedy, J. P. (2008). From Lunar Regolith to Fabricated Parts: Technology Developments and the Utilization of Moon Dirt. Retrieved July 21, 2015, from http://ntrs.nasa.gov/search.jsp?R=20080018923

National Ready Mixed Concrete Association. (2003). *What, why & how? testing compressive strength of concrete, concrete in practice.*

Nickerson, R.D., Bart, G.D., Lawder, T. and Melosh, H.J. (2011). Global lunar regolith depths revealed. *Lunar and Planetary Science Conference 2011.*

Pabst, W., and Gregorvá, E. (2009). The Poisson Ratio of Porous Materials. In S. Kaskel, P. Llewellyn, F. Reinoso, and N. Seaton (Eds.), *Characterisation of porous solids VIII proceedings of the 8th International Symposium on the Characterisation of Porous Solids,* 424-431. Cambridge, UK: RSC Publishing.

Park, S. J., Chung, S.H., Johnson J. L., and German, R. M. (2006). Distortion simulation of liquid phase sintering on Earth on the Moon and mars and in space. *Metal Powder Industries Federation.*

Reed, J. (1988). *Introduction to the principles of ceramic processing* (2nd ed.). New York: Wiley.

Rickman, D., Edmunson, J. and McLemore, C. (2013). Functional comparison of lunar regoliths and their simulants. *Journal of Aerospace Engineering,* Vol. 26, 176-182.

Rickman, D., McLemore, C., and Fikes, J. (2007, June 28). Characterization summary of jsc-1a bulk lunar mare regolith simulant. Retrieved January 6, 2015, from http://www.orbitec.com/store/JSC-1A_Bulk_Data_Characterization.pdf

Taylor, G.J., and Schmitt, H.H. (2006). Development of the Moon. *Reviews in Mineralogy & Geochemistry* 60, 597-656.

Taylor, L.A., and Meek, T.T. (2005). Microwave sintering of lunar soil: properties, theory, and practice. *Journal of Aerospace Engineering,* Vol. *18*, 188-196.

Toutanji, H., Evans, S. and Grugel, R. (2012). Performance of lunar sulfur concrete in lunar environments. *Construction and Building Materials, 29*, 444-448.

Ulamec, S., Biele, J., and Trollope, E. (2010). How to survive a lunar night. *Planetary and Space Science,* 1985-1995.

Upadhyaya, A and German, R. (2001). Gravitational effects during liquid phase sintering. *Materials Chemistry and Physics, 67*, 25-31.

Warren, N., Trice, R., Soga, N., and Anderson, O. (1973). Rock physics properties of some lunar samples. Proceedings of the Lunar Science Conference, vol. 4, 2611. Retrieved April 29, 2015, from http://articles.adsabs.harvard.edu//full/1973LPSC....4.2611W/0002612.000.html

Wilson, T. L. and K. B. Wilson. (2005). Regolith sintering a solution to lunar dust mitigation. *Lunar and Planetary Science XXXVI.*

Zacny, K., Craft, J., Hedlund, M., Chu, P., Galloway, G. and Muller, R. (2010). Investigating the efficiency of pneumatic transfer of JSC-1A lunar regolith simulant in vacuum and lunar gravity during parabolic flights. *AIAA SPACE 2010 Conference & Exposition*.